Metal and Gas Adsorption on High-surface-area Catalyst Support Materials: Energetics by Calorimetry and Adsorbate Structure

Wei Zhang

A dissertation

submitted in partial fulfillment of the

requirements for the degree of

Doctor of Philosophy

University of Washington

2020

Reading Committee:

Charles T. Campbell, Chair

Dan Fu

David J. Masiello

Program Authorized to Offer Degree:

Chemistry

University of Washington

Abstract

Metal and Gas Adsorption on High-surface-area Catalyst Support Materials: Energetics by Calorimetry and Adsorbate Structure

Wei Zhang

Chair of the Supervisory Committee:

Prof. Charles T. Campbell

Department of Chemistry

Along with the increase in the world population and global economy, the world primary energy consumption is also growing year by year, which in turn has brought about energy shortage and global warming. Developing renewable energy and increasing its total fraction in the world energy portfolio is one of the strategies to tackle the energy and environmental hurdles. The forward progression can be seen in that 14.8% of the increase in primary energy in 2017 was provided by renewable energy (including biofuels), which grew rapidly driven by robust growth in both wind and solar power. However, the total fraction of world energy portfolio from all renewables is expected to amount to just 8% according to the report published by National Research Council in 2008 and fossil fuels will be a major part of the world primary energy portfolio for the next few

decades to come. Therefore, accelerating the pace of improvement in energy productivity (i.e., the amount of energy needed to produce a unit of output), especially the utilization of fossil fuels, becomes an urgent task. In order to complete this task, this dissertation brings two strategies into attention, (1) developing highly active, selective, and thermodynamically stable heterogeneous catalysts for the chemicals and energy industries and (2) developing and applying porous adsorbent materials for the capture of CO_2 and other toxic gases and for the storage and utilization of cleaner, high-energy-density, and lower-carbon fuels such as hydrogen and methane.

Heterogeneous catalysis has been at the center of the chemicals and energy industries since more than 90% of chemical manufacturing processes utilize catalysts. Late transition metal nanoparticles supported on high area oxide surfaces are the key ingredients of many catalysts and electrocatalysts with numerous applications in the energy, chemical, and environmental industries. The catalytic activity and selectivity of these catalysts often varies dramatically with the size and shape of the metal nanoparticles, and with the support materials. In many cases, the supported metal nanoparticles are rendered inactive due to particle sintering (i.e., coarsening into fewer, larger particles), which also depends strongly on the particle size and support materials. These properties have been proven to be closely correlated with the strength of bonding of the metal atom and nanoparticles to the support surface. To clarify structure–activity relationships in such catalysts and their sintering kinetics, our group has been measuring the strength of the interaction between metal nanoparticles and the support surfaces using metal vapor adsorption calorimetry.

Chapter 2 describes the standard procedure and experimental setup for metal vapor adsorption calorimetry and equilibrium adsorption isotherm (EAI). The metal vapor adsorption calorimeter described in Section 2.1 has been applied to drop-cast films of metal–organic frameworks (MOFs) NU-1000 described in Chapter 3. The Brunauer–Emmett–Teller (BET)

system described in Section 2.2 has been used to measure equilibrium adsorption isotherms for many small gases on NU-100 in Chapter 6.

A Zr-based metal–organic framework (MOF) NU-1000 as a heterogeneous catalyst support onto which transition metal nanoparticles can be deposited is introduced in **Chapter 3**. The nature and energy of the reactions between Ca vapor and the internal surfaces of the NU-1000 have been studied by adsorption microcalorimetry, low energy He^+ ion scattering spectroscopy (LEIS), X-ray photoelectron spectroscopy (XPS), and Kohn−Sham density functional theory (DFT).

Chapter 4 introduces a novel calorimeter design to study metal vapor adsorption calorimetry on surfaces of nanomaterials that are deposited from liquid solutions, as is typical when preparing industrial catalyst materials. It uses a $LiTaO_3$ crystal for heat detection, which has a Curie point of 893 K, thus theoretically allowing samples to be heated up to ~890 K to clean before use. Its capability has been demonstrated by measuring the bond energies of Ag vapor onto the clean surfaces of high-surface-area TiO_2 powdered support materials.

Mixed or binary metal oxides (i.e., oxides with two metal elements) are often used as supports in catalysis with considerable improvement on various aspects of catalyst performance. **Chapter 5** proves that we can measure adsorption energies, using the new metal vapor adsorption calorimeter introduced in Chapter 4, on any atomically smooth well-ordered mixed-oxide surface and demonstrates that thin Langmuir-Blodgett (LB) films of layered perovskite nanosheets provide a powerful new approach to study surface chemistry on single-crystal mixed-oxide surfaces.

A shift away from coal and oil into cleaner, high-energy-density, and lower-carbon fuels such as hydrogen and methane, is considered as another strategy to increase energy efficiency and alleviate greenhouse effect. While hydrogen and methane have so many ubiquitous merits, the biggest challenge for large-scale transportation and utilization is to develop a safe, lightweight,

and economical gas storage technique. The Zr-based MOF NU-1000 is a particularly interesting adsorbent material for gas storage and separation because it is water- and temperature-stable, has a high BET surface area and large pore volumes that allow NU-1000 to efficiently trap various gas molecules inside its framework. Its application as a storage media for gas molecules depends on the adsorption capacity and selectivity for the adsorbates of interest. As such, **Chapter 6** reports the combined experimental and theoretical study of small gases adsorption on NU-1000, which make NU-1000 perhaps the best understood MOF in terms of gas adsorption properties and serve as a prototype system for studying the surface chemistry of MOFs in general, thus guiding most applications on MOFs.

To sum up, this dissertation provides deeper and systematic understandings of metal and gas adsorption on high-surface-area catalyst support materials, in the fields of heterogeneous catalysis and gas storage and separation relevant to energy and environmental industries. Here, I want to emphasize the importance of the new metal adsorption calorimeter introduced in **Chapter 4**. To clarify the structure–activity relationships in supported metal nanoparticle catalysts and their sintering kinetics, researchers have adopted a model catalysts approach whereby structurally well-defined samples are prepared by vapor deposition of the metal onto single-crystal oxide surfaces, which encounters the well-known "materials gap" with respect to real industrial catalysts. To bridge this materials gap, this calorimeter allows one to measure the strength of metal atom bonding and the adhesion energy of metal nanoparticles to clean surfaces of technologically relevant catalyst support materials. This opens up new opportunities for discovering better support materials and for basic scientific study of structure / function relationships with respect to metal / support bond energies.

TABLE OF CONTENTS

LIST OF FIGURES

Figure 6.18. Calculated (DFT) heat of adsorption at zero coverage and 77 K ($<Q>_{0,DFT}$) from ref. [94], measured differential Isosteric heat of adsorption at 0 and 0.1 ML coverage ($Q_{st}(0)$ and $Q_{st}(0.1)$) from this experiment, and $Q_{st}(0.1)$ from ref. [94] (labelled with "(a)") for all four gases studied here, plotted as a function of increasing Lennard-Jones well depth. Inset is the ratio between $Q_{st}(0)/<Q>_{0,DFT}$ as a function of increasing Lennard-Jones well depth.171

LIST OF TABLES

ACKNOWLEDGEMENTS

Firstly, I would like to express my sincere gratitude to my supervisor Prof. Charles T. Campbell for his continuous support of my Ph.D. study, for his wisdom, patience, and especially cultural inclusiveness. His guidance helped me to acquire knowledge and overcome the obstacles in all the time of my Ph.D. research. He has been a better advisor and mentor than I could have imagined. I would also like to thank my group members for their knowledge, insightful comments, and a lot of help. I would especially like to thank Spencer Carey for getting me trained on his UHV system and teaching me the basics of single-crystal adsorption calorimetry, James Lownsbury for mentoring me on the Ca on NU-1000 project and getting me prepared for my first metal adsorption calorimetry project, and John Eichler for being a quick-learning and reliable apprentice and helping me with maintaining and troubleshooting my UHV system and collecting data.

Besides the Campbell group, I would like to thank Professor Emeritus Oscar Vilches at Department of Physics for his knowledge, motivation, and guidance in completing the van der Waals adsorption on NU-1000 project. After being retired for many years, Oscar still works several days per week in the lab. His passion for fundamental research has given me a lot of encouragement. I would like to thank Yuanyuan Ma, Graeme Vissers, Iván A. Santos-López, and James Lownsbury for helping collect adsorption isotherm data for the van der Waals adsorption on NU-1000 project.

I would like to thank our collaborators, the groups of Joseph Hupp and Omar Farha at Northwestern University for providing the NU-1000 samples, the group of Donald Truhlar and Christopher Cramer at the University of Minnesota for their computational work for the Ca on NU-1000 project, the group of Donald Truhlar at the University of Minnesota for computational

work for the van der Waals adsorption on NU-1000 project, and the group of Thomas Mallouk (now at University of Pennsylvania) especially Ritesh Uppuluri at Pennsylvania State University for preparing us high-quality calcium niobate nanosheet samples and meeting our tons of stringent requirements for the samples. I would like to say millions of thanks to Ritesh for all the time and efforts he spent to communicate, tackle all the issues, and get the sample preparation done very nicely.

I have been super lucky to work with many brilliant engineers within and outside academic setting. I would like to thank Eric Strakbein, Kevin Soderlund, and Brian Wadey from the Chemistry Machine Shop and for taking care of the lab facilities to create a safe and comfortable working environment. I would especially like to thank Eric Strakbein for being available to help whenever I needed him. I would like to thank Bob Scott and Larry Stark from the Physics Machine Shop for their expertise in building my first new sample platen and many other parts. I would also like to express my sincere thanks to Lon Buck, Roy Olund, and Bill Beaty from the Chemistry Electronics Shop for their endless efforts to help me repair many of my old-fashioned problematic electronics, for their expertise in designing new circuits and software to make my experimental operation easier and smoother, and for their insightful comments and advice to my inscrutable queries. I enthusiastically thank Lon Buck for always being available to give invaluable advice and provide technical guidance when I was designing and testing my new sample platen and sample heater. Besides all the engineers I have worked with at UW, I would like to thank George Krizek from Vacuum Systems Ltd. for his knowledge, patience, and instruction and for all the time he had spent with me either in person or through countless email and Skype conversations in order to get my hemispherical energy analyzer back to work.

Last but not the least, I would like to thank my family and my friends, especially my parents and Angela for supporting me spiritually and in life. Without you, I wouldn't be where I am today.

Chapter 1. Introduction

Associated with increase in the world population and the global economy, the world primary energy consumption has been growing up gradually in recent years (Figure 1.1),[1] which brings about the problem of fuel exhaustion and global warming. For example, the CO_2 level has steadily risen by 40% since the beginning of the industrial revolution.[2] In dealing with the energy and environmental hurdles, there would not be a single solution; rather, multiple technologies will be developed and implemented.[3] For example, the total fraction of world energy portfolio from all renewables is expected to amount to just 8%, so increased utilization will not be sufficient to meet the increasing energy demand. According to the report published by National Research Council in 2008, fossil fuels will be a major part of the world primary energy portfolio for the next few decades to come.[2] To lead to a sustainable future, new strategies are required for the utilization the fossil fuels in the most efficient and environmentally friendly manner.

Heterogeneous catalysis has been at the center of the chemicals and energy industries since more than 90% of chemical manufacturing processes utilize catalysts.[4] In the early 1900s, the development of the Haber-Bosch process (i.e., synthesis of ammonia from its elements in the presence of iron at high temperatures and pressures) has illustrated the huge potential impact of heterogeneous catalysis on human society; in this case, the lives of almost half of the world population were made possible by Haber–Bosch nitrogen in 2008.[5,6] That the 2007 Nobel Prize in Chemistry was awarded to Prof. Ertl for his studies of chemical processes on solid surfaces[7-10] demonstrates a huge amount of interest in heterogeneous catalysis both from a scientific and an industrial perspective.[11] Hence, developing highly active, selective, thermodynamically stable, and energy efficient heterogeneous catalysts is one of the strategies leading to a sustainable future.

Transition metal nanoparticles dispersed across the surface of oxide supports are key ingredients in many heterogeneous catalysts, electrocatalysts, and photocatalysts of importance in energy technologies, fuel cells, pollution prevention, and chemical processing.[12,13] For example, they are used extensively for ammonia synthesis, steam reforming, methanol synthesis, the hydrogenation of sulfur-containing organics from crude oil, selective oxidation of alcohols, etc.[14-18] Many experimental studies have shown the catalytic activity and selectivity of supported metal nanoparticles can vary dramatically with particle size and the support materials on which they are deposited.[19-22] In addition, under catalytic reaction conditions (e.g., high temperatures and pressures), these metal nanoparticles can sinter (i.e., coalesce to fewer, larger particles), resulting in loss of activity and selectivity, and the sintering kinetics also depends strongly on the particle size and support materials.[23-25] These properties have been proven to be closely correlated with the strength of bonding of the metal atom and nanoparticles to the support surface.[12] Clearly, for the purpose of more rational catalyst design, there is a strong motivation to develop a fundamental and systematic understanding of the key parameters that control catalyst activity, selectivity, and stability.

To clarify these structure–activity relationships in such catalysts and their sintering kinetics, our group has previously measured the strength of the interaction between metal nanoparticles and the support surfaces using metal vapor adsorption calorimetry.[12,26-28] These metal adsorption calorimetry studies have been performed on thin, single-crystal oxide films grown on thin, single-crystal metal substrates and cleaned in ultra-high vacuum (UHV), in order to have very well-defined surface structures where the fundamental aspects of metal / support bonding can most easily be elucidated.[12,26-28] However, this "model catalyst" approach encounters the well-known "materials gap" with respect to the real industrial catalysts.[29,30] That is, these flat and well-ordered

surfaces are quite different from the atomically-rough surfaces typically present on the high-surface-area materials needed for real industrial catalyst supports. To bridge this materials gap, we demonstrate here that we can calorimetrically measure metal atom adsorption energies and metal nanoparticle adhesion energies now on support materials (e.g., metal−organic frameworks, metal oxide nanoparticles, and lamellar perovskite nanosheets) with large specific surface areas instead.

Metal−organic frameworks (MOFs) are an extensive class of nanoporous crystalline materials composed of small metal, metal oxide, or mixed-metal−oxide nodes connected by organic linker groups of a fixed length and conformation; the linkers bind to nodes via reactive binding sites such as ionized carboxylic acid groups.[31-33] MOFs have attracted great research interest due to a unique combination of properties, such as structural homogeneity that makes MOFs amenable to X-ray diffraction,[34,35] large surface areas[36,37] and pore sizes,[38,39] framework flexibility,[38,40] opportunities for rational design and tunability,[35,41,42] and almost limitless compositional diversity.[33]

MOFs have numerous current and potential applications in catalysis.[43-48] Because metal–organic framework (MOF) nodes can be oxide clusters of controllable sizes near ∼1 nm in diameter, they can be thought of as very well-defined and homogeneous oxide "nano-supports" to which catalytic metals (like Pt, Ag, Pd, etc.) could be attached to achieve improvement in activity or simply to provide a more homogeneous structure to facilitate fundamental studies of supported metal clusters. The organic linker groups effectively isolate these nodes (and the supported metals) from each other, thus possibly preventing sintering of the metal centers. Additionally, due to the highly ordered nature of MOFs, their structures can be easily determined with X-ray diffraction (XRD).[34,35,49]

The Zr-based MOF NU-1000[50,51] is a particularly promising MOF for catalysis because it is water- and temperature-stable,[52] has a Brunauer–Emmett–Teller (BET) surface area of >2000 m^2/g,[50,52] and has 31 Å hexagonal pores that allow large molecules to penetrate into the bulk of the MOF crystallites. NU-1000 contains transition metal oxide nodes[51] of formula $[Zr_6(\mu_3\text{-}OH)_4(\mu_3\text{-}O)_4(OH)_4(OH_2)_4]$ isolated by pyrene-based linkers[53] (see Figure 3.1). Each node has six Zr atoms in its structure connected by Zr-O-Zr bonds, so it resembles a tiny cluster of zirconium oxide and can be thought of as well-defined, homogeneous oxide nanosupports for catalytic metals of interest. Thus, the bonding of metal atoms and metal clusters to the oxide nodes of MOFs like NU-1000 is a subject of considerable interest.

Chapter 3 describes the bonding energetics of calcium vapor adsorption onto clean NU-1000 at 300 K in UHV using metal vapor adsorption calorimetry, the growth mechanism and surface morphology of the evolving Ca film using low energy He^+ ion scattering spectroscopy (LEIS) and X-ray photoelectron spectroscopy (XPS), and modeled reactions between calcium atoms and the internal surfaces of NU-1000 using density functional theory (DFT). The reaction enthalpies of calcium with NU-1000 are high below 2 monolayers (ML) (570-366 kJ/mol), attributed to calcium first reacting with carboxylic acid groups, free water impurities, or both on the internal surfaces (these reactions proceed to ~20 nm below the external surface), then with the aquo or hydroxyl groups on the Zr_6 nodes. Beyond 2 ML, the exothermicity decreases asymptotically to the sublimation enthalpy of bulk Ca (178 kJ/mol), mainly attributed to the formation of Ca(solid) nanoparticles on the external surface. This is the first adsorption calorimetry of metal atoms on the homogeneous oxide cluster nodes of any MOF, and it provides an experimental benchmark with respect to reaction energetics for validating the accuracy of DFT calculations used to model metal bonding to oxide clusters in general.

Many important catalysts and electro-catalysts for energy and environmental technologies involve late transition metal atoms and nanoparticles dispersed across the surface of some high-surface-area support materials, for example, metal oxide nanoparticles. TiO_2 nanoparticles have been used in wide-ranging catalytic studies.[54-57] For example, Christopher's group has recently reported a single Pt atom catalyst with high thermal stability by depositing isolated Pt atoms onto 5-nanometer-diameter anatase TiO_2 nanoparticles, and this catalyst exhibited a 2-fold greater turnover frequency for CO oxidation than the 1 nm pre-reduced Pt clusters on the same TiO_2 nanoparticles.[57] Therefore, the strength of bonding of transition metal atoms and nanoparticles to these surfaces of these TiO_2 nanoparticles is of significant interest.

Chapter 4 introduces a novel calorimeter to measure the strength of metal bonding to clean surfaces of high-surface-area catalyst support materials, which extends metal adsorption calorimetry to surfaces of nanomaterials that are deposited from liquid solutions, as is typical when preparing industrial catalyst materials. This calorimeter implements $LiTaO_3$ single crystals as the heat detectors, which maintain high pyroelectric heat-signal response after heating to high temperatures (up to ~890 K theoretically),[58] while the pyroelectric polymer heat detectors used for previous calorimetry studies (including Ca adsorption on NU-1000) in this calorimetry apparatus could only be heated up to ~350 K.[59,60] In Chapter 4, I demonstrate this new calorimetry capability by depositing thin films of the 5-nm-diameter anatase TiO_2 nanoparticles *directly* onto the $LiTaO_3$ crystals, cleaning these materials after deposition by heating to high temperatures (up to ~890 K theoretically)[58] in UHV or in controlled gases (e.g., O_2) to remove impurities present after deposition, and studying the heat of adsorption of Ag vapor as a function of coverage on clean surfaces of these TiO_2 films. The XPS results show that there is no or negligible oxidation state change of the TiO_2 support after being heated. The measured sticking probability is above 0.988

for all Ag coverages. The heat of adsorption is ~206 kJ/mol in the limit of zero Ag coverage, and then increases asymptotically to the heat of sublimation of bulk Ag(s), 285 kJ/mol,[61] at higher Ag coverages. To our knowledge, this is the only metal vapor adsorption calorimeter capable of measuring metal adsorption energies on the surfaces of solution-prepared high-surface-area catalyst support materials.

As mentioned above, our group has previously reported many adsorption calorimetry studies of metal atoms on thin, single-crystal oxide films grown on thin, single-crystal metal substrates,[12,26-28] but those are all oxides of a single metal element. Mixed or binary metal oxides (i.e., oxides with two metal elements) are often used as supports in catalysis with considerable improvement on various aspects of catalyst performance, with ceria-zirconia in automotive exhaust treatment and other reactions[62-65] being the best-known example. Unfortunately, growing atomically smooth single-crystal surfaces of mixed oxides in well-defined composition and structure has never been reported on samples that would be applicable in our metal vapor adsorption calorimetry in the literature.

Perovskite, with the general formula ABO_3 (A and B being two cations and O being an oxygen anion), represents probably the most studied mixed-oxide system in the field of heterogeneous catalysis. They are low-cost, easy to synthesize, and show a large variation in their composition and structure allowing tailoring of their chemical and physical properties to better target their applications. Since 2000, a significant amount of research has been done on new synthesis techniques and applications of perovskites, and they are indeed considered as potential alternatives for platinum-group metals (PGMs) today. On the other hand, since both perovskites and noble metals have their unique merits, simultaneous use of those two materials could offer a tremendous advantage for catalytic processes, i.e., perovskites could be used as a suitable mixed-

oxide support for noble metal nanoparticles to both improve their catalytic efficiency and expand their life span.[66,67]

Chapter 5 proves that we can use the new calorimeter described in Chapter 4 to measure metal adsorption energies on a single-crystal mixed-oxide support prepared in a simple new way that offers many exciting new possibilities for surface science studies. A class of lamellar calcium niobate perovskite, $HCa_2Nb_3O_{10}(001)$, can be dispersed in solution as single-crystalline flat sheets which are only one layer thick but extend laterally from several hundred nanometers to a few micrometers.[68-73] Each nanosheet consist of three NbO_6 octahedral layers, with Ca^{2+} in the center of the cube formed by Nb^{5+} and half of the surface O atoms in surface OH groups (see Figure 1.2). These nanosheets can be simply deposited in a layer-by-layer fashion on flat substrates using Langmuir-Blodgett (LB) techniques to make a thin, single-crystal mixed-oxide film.[69,71,74-76] The long lateral dimension indicates that these nanosheets have very high surface area and a huge ratio of terrace sites to sheet-edge sites, making them promising model mixed-oxide supports with very homogeneous surface sites for studying adsorption, for example of metal atoms and nanoparticles. We use this LB-film method to deposit such perovskite thin films *directly* onto the $LiTaO_3$ heat detectors. We verify the sheet-like morphology of the $HCa_2Nb_3O_{10}$ nanosheets using atomic force spectroscopy (AFM). We report calorimetric measurements of the heat of adsorption and sticking probability of Ag atoms as a function of coverage on clean dehydrated ("dh") $HCa_2Nb_3O_{10}(001)$ surface. We also elucidate the particle-growth mechanism and surface morphology of the evolving Ag nanoparticles using low-energy He^+ ion scattering spectroscopy (LEIS) and the charge transfer associated with the strong chemical reaction between the Ag atoms and the dh-$HCa_2Nb_3O_{10}(001)$ nanosheets using X-ray photoelectron spectroscopy (XPS). The results show surprisingly strong bonding between Ag and dh-$HCa_2Nb_3O_{10}(001)$ with a very high adhesion energy of 4.33 J/m^2.

This is the first adsorption calorimetry study of metal atoms on single-crystal mixed oxide surfaces, and such layered perovskite nanosheets provide a powerful new approach for us to study surface chemistry on mixed-oxide surfaces.

Besides exploring highly active, selective, thermodynamically stable, and energy efficient heterogeneous catalysts, a shift away from coal and oil into cleaner, high-energy-density, and lower-carbon fuels such as hydrogen and methane, is considered as another strategy to increase energy efficiency and alleviate greenhouse effects. Hydrogen has long been regarded as an ideal clean energy carrier generating "zero emission" because it is carbon free, combustion of hydrogen produces only water as a product, and has an inexhaustible resource of water. What's more, hydrogen has a very high energy density which nearly triples that of gasoline per mass unit. While hydrogen has so many ubiquitous merits, the biggest challenge of hydrogen utilization is to develop a safe, lightweight, and economical hydrogen storage technique.[77-79] Natural gas, whose main component is methane, is another clean energy gas and appears to be more promising to replace petroleum as the world's primary fuel for transportation. It has the highest H to C ratio of any fossil fuel and lower sulfur and nitrogen contents, thus resulting in much less CO, CO_2, SO_x, and NO_x emission.[80-82] In addition, recent engineering advances in horizontal drilling and hydraulic fracturing have led to the discovery and mining of large quantities of global natural gas reserves, reducing the price of natural gas below that of gasoline in many countries.[83,84] As with hydrogen, methane storage is one of the biggest challenges for large-scale transportation and utilization since methane is in its gaseous state at ambient temperature and pressure. Conventional methane storage techniques such as compression and liquefaction have unavoidable drawbacks. Compressed natural gas (CNG) requires costly multi-stage compressors and high-pressure tanks which are heavy and potentially explosive, while liquefied natural gas (LNG) needs complicated

and energy-consuming cryogenic cooling system for storage.[85,86] Apparently, the development of viable method to store hydrogen and methane gas molecules in a confined space has to be put on the urgent agenda.

As a class of coordination polymers, metal−organic frameworks (MOFs) are composed of inorganic nodes consisting of small metal, metal oxide, or mixed metal oxide clusters connected by various types and lengths of organic linkers. They have drawn great research interest in the field of gas storage and separation due to a unique combination of properties such as large nanoscale porosity (up to 90% free volume),[37] high surface areas (up to 7,000 m^2/g),[36] low densities (down to 0.13 g/cm^3),[87] and extraordinary degree of variability for both the organic and inorganic components of their structures.[33] The most intriguing property of porous MOFs is their unprecedented high surface area which makes them stand out from other porous materials, and the nanospace inside their pores makes them an excellent adsorbent for various gas molecules. In this respect, employing MOFs as a storage media are a viable and promising method for transportation and utilization of the aforementioned clean energy carriers.[77] Besides the storage of clean gases (H_2 and CH_4), MOFs are also implemented for CO_2 capture to alleviate greenhouse effect,[88,89] the removal of toxic gases (e.g., CO, NO_x, SO_x, H_2S),[90-92] and the synthesis of industrial chemicals.[93]

The aforementioned Zr-based MOF NU-1000 is a particularly interesting MOF for gas storage and separation because it is water- and temperature-stable,[52] has a Brunauer–Emmett–Teller (BET) surface area of ~2,580 m^2/g and large pore volumes (e.g., the hexagonal channels seen in Figure 6.1(a) have a diameter of about 31 Å; and the pores seen in Figure 6.1(b) have diameters of 8.5 Å) that allow NU-1000 to efficiently trap various gas molecules inside its framework.[94] NU-1000 contains transition metal oxide nodes,[51] which resemble hydrated ZrO_2 clusters, and pyrene-based linkers (TBAPy, H_4TBAPy is the 1,3,6,8-tetrakis(p-benzoic-

acid)pyrene)),[53] both offering several kinds of adsorption sites for gases.[94,95] Its application as a storage media for gas molecules depends on the adsorption capacity and selectivity for the particular adsorbate or adsorbates of interest. As such, the measurement of adsorption isotherms and the determination of isosteric heats of adsorption as a function of coverage are of great research interest.

Chapter 6 reports the measurements of adsorption isotherms and the determination of isosteric heats of adsorption of many small gases (H_2, D_2, Ne, N_2, CO, CH_4, C_2H_6, Ar, Kr, and Xe) on NU-1000. We correlate the adsorption energies as functions of coverage with the Lennard-Jones well depth (ε) where possible, compare the experimental results to the density functional theory (DFT) calculations of the single-atom/single-molecule adsorption enthalpies, and propose a sequential-site-filling model (assuming gases are filled in a sequential order from the strongest to the weakest DFT-calculated adsorption site) to help understand gas adsorption on NU-1000 at low coverages. With these results, NU-1000 becomes perhaps the best understood MOF in terms of gas adsorption properties and serves as a prototype system for studying the surface chemistry of MOFs in general, thus guiding most applications on MOFs. Also, the excellent agreement between experimental measurements and DFT calculations provides confidence in the ability of DFT to predict relative adsorption enthalpies at different sites in MOFs when van der Waals interactions dominate.[94,95]

Table 1.1 lists the publications reprinted in this dissertation and their corresponding chapters. To sum up, this dissertation provides deeper and systematic understandings of metal and gas adsorption on high-surface-area catalyst support materials, in the fields of heterogeneous catalysis and gas storage/separation relevant to energy and environmental industries. **Chapter 2** provides a brief overview of the experimental setup and measurement procedures for metal vapor

adsorption calorimetry and equilibrium adsorption isotherm. (More details are provided in Chapters 3-6.) **Chapter 3** describes the adsorption calorimetry study of calcium atoms on the homogeneous zirconium oxide cluster nodes of MOF NU-1000, which provides an experimental benchmark with respect to reaction energetics for validating the accuracy of DFT calculations used to model metal bonding to oxide clusters in general. **Chapter 4** introduces a novel calorimeter to measure the strength of metal bonding to clean surfaces of high-surface-area catalyst support materials, of the type used industrially, the capability of which is demonstrated by measuring the bond energies of Ag vapor onto the clean surfaces of high-surface-area TiO_2 powdered support materials. **Chapter 5** reports for the first time the adsorption calorimetry of metal gas atoms on any atomically smooth well-ordered mixed-oxide surface and demonstrates that thin LB films of layered perovskite nanosheets provide a powerful new approach to study surface chemistry on single-crystal mixed-oxide surfaces. **Chapter 6** describes the combined experimental and theoretical study of gas adsorption on the Zr-based MOF NU-1000, which make NU-1000 perhaps the best understood MOF in terms of gas adsorption properties and serve as a prototype system for studying the surface chemistry of MOFs in general, thus guiding most applications on MOFs.

1.1 FIGURES AND TABLES

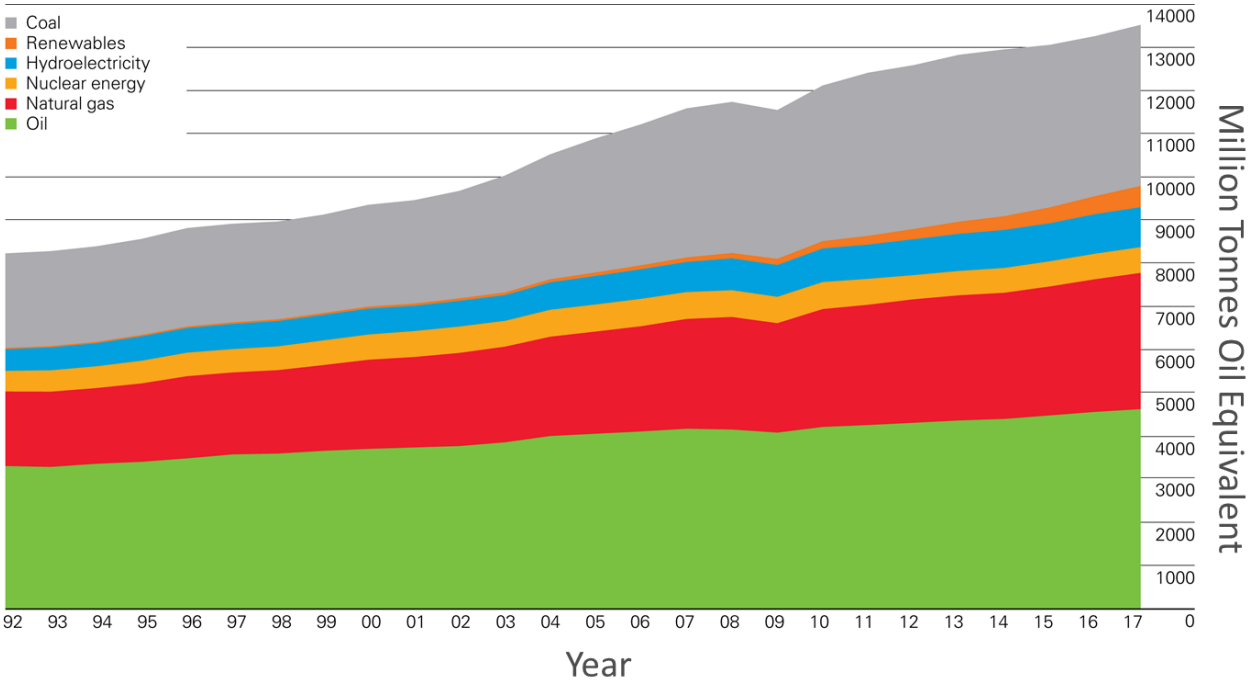

Figure 1.1. World primary energy consumption by fuel in million tonnes oil equivalent (mtoe) versus year. Reprinted with permission from ref. [1].

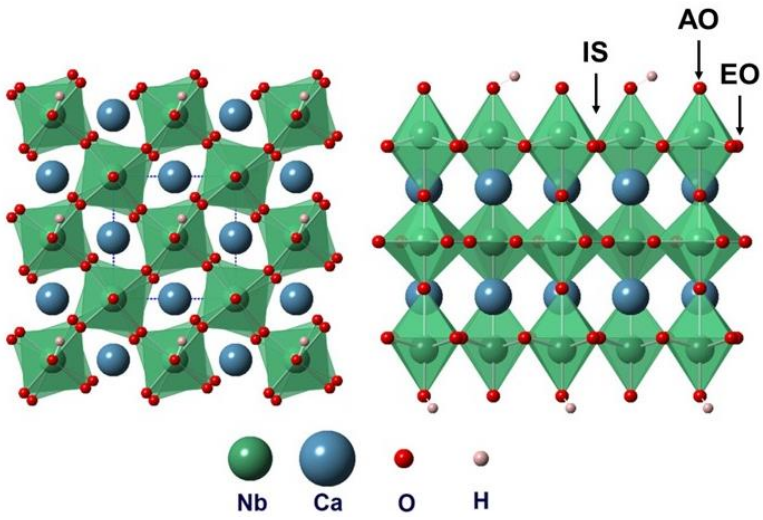

Figure 1.2. Polyhedral representations of the $HCa_2Nb_3O_{10}$ nanosheet structure, viewed from the [001] (left) and [010] (right) directions. The structure at left is the top view of the (001) surface being studied here. The dashed blue line indicates the unit cell. There are 6.74×10^{14} O atoms/cm^2 on this (001) surface, half of which are in the surface OH groups. The right structure shows one complete 'layer' of the nanosheet, which has a thickness (or repeat distance in the 3D bulk) of 1.44 nm. Labels indicate AO: axial oxygen, EO: equatorial oxygen, IS: interstitial space. The structural parameters used to draw the structure are from ref. [96].

Table 1.1. Publications Reprinted in This Dissertation and Their Corresponding Chapters*

Chapter	Publication
Chapter 3	Lownsbury, J. M.; Santos-Lopez, I. A.; Zhang, W.; Campbell, C. T.; Yu, H. Y. S.; Liu, W. G.; Cramer, C. J.; Truhlar, D. G.; Wang, T.; Hupp, J. T.; Farha, O. K. Calcium Vapor Adsorption on the Metal-Organic Framework NU-1000: Structure and Energetics. *J. Phys. Chem. C* **2016**, *120*, 16850-16862.
Chapter 4	Zhang, W.; Campbell, C. T. Calorimetric Metal Vapor Adsorption Energies for Characterizing Industrial Catalyst Support Materials. *ACS Catal*. submitted.
Chapter 5	Zhang, W.; Uppuluri, R.; Mallouk, T. E.; Campbell, C. T. Silver Adsorption on Calcium Niobate(001) Nanosheets: Calorimetric Energies Explain Sinter-Resistant Catalyst Support. *J. Am. Chem. Soc*. submitted.
Chapter 6	Zhang, W.; Ma, Y.; Santos-López, I. A.; Lownsbury, J. M.; Yu, H.; Liu, W.-G.; Truhlar, D. G.; Campbell, C. T.; Vilches, O. E. Energetics of van der Waals Adsorption on the Metal–Organic Framework NU-1000 with Zr_6-oxo, Hydroxo, and Aqua Nodes. *J. Am. Chem. Soc.* **2018**, *140*, 328-338. Vissers, G. O.; Zhang, W.;Vilches, O. E.; Liu, W.-G.; Yu, H. S.; Truhlar, D. G.; Campbell, C. T. Heats of Adsorption of N_2, CO, Ar, and CH_4 versus Coverage on the Zr-Based MOF NU-1000: Measurements and DFT Calculations. *J. Phys. Chem. C* **2019**, *123*, 6586-6591.

* Publications based on research as a PhD student at the University of Washington that were not included in this dissertation:

Carey, S. J.; Zhao, W.; Harman, E.; Baumann, A.-K.; Mao, Z.; Zhang, W.; Campbell, C. T. Energetics of Adsorbed Methanol and Methoxy on Ni(111): Comparisons to Pt(111). *ACS Catal.* **2018**, *8*, 10089-10095.

Publications based on research prior to enrolling at at the University of Washington:

Zhang, W.; Wang, S.; Wang, Y.; Zhu, Z.; Gao, X.; Yang, J.; Zhang, H. ZnO@ZnS core/shell microrods with enhanced gas sensing properties. *RSC Adv.* **2015**, *5*, 2620−2629.

Mei, L.; Zhang, X.; Wang, Y.; Zhang, W.; Lu, Z.; Luo, Y.; Zhao, Y.; Li, C. Multivalent Polymer-Au nanocomposites with cationic surfaces displaying enhanced antimicrobial activity. *Polym. Chem.* **2014**, *5*, 3038−3044.

Mei, L.; Lu, Z.; Zhang, W.; Wu, Z.; Zhang, X.; Wang, Y.; Luo, Y.; Li, C.; Jia, Y. Bioconjugated nanoparticles for attachment and penetration into pathogenic bacteria. *Biomaterials* **2013**, *34*, 10328−10337.

Chapter 2. Instrumentation

Heats of adsorption are heats generated over the course of an adsorption reaction on a surface, and they are the most important ingredient in understanding the thermodynamics of surface reactions. These provide direct information regarding the binding strength between the adsorbate and adsorbent. Therefore, there is a great motivation to measure these adsorption enthalpies to better understand important surface reactions in catalysis and electrocatalysis, gas storage and separation, photovoltaics, and microelectronics.

This chapter introduces two experimental techniques to measure adsorption enthalpies, metal vapor adsorption calorimetry and equilibrium adsorption isotherm (EAI). Section 2.1 includes a brief introduction to the metal vapor adsorption calorimetry technique and the sample platen used for studying Ca adsorption on a Zr-based metal–organic frameworek (MOF) NU-1000 in Chapter 3. Section 2.2 covers the basics of the EAI technique and introduces a Brunauer–Emmett–Teller (BET) system which has been used to measure adsorption isotherms included in Chapter 6.

We recently introduced a novel calorimeter, which implements a $LiTaO_3$ single crystal as the heat detector and allows samples to be heated up to ~890 K for the first time, extending our calorimetric technique to surfaces of nanomaterials that are deposited from liquid solutions, as is typical when preparing industrial catalyst materials. This calorimeter will be introduced separately in Chapter 4.

2.1 METAL VAPOR ADSORPTION CALORIMETRY

Adsorption enthalpies have been measured on single-crystalline metal and oxide surfaces using metal vapor adsorption calorimetry, equilibrium adsorption isotherm (EAI), and temperature programmed desorption (TPD). Unlike EAI and TPD which cannot provide adsorption enthalpies for the species of interest in many cases where the adsorbate dissociates, restructures or diffuses into the bulk before desorption, metal vapor adsorption calorimetry allows *direct* calorimetric measurements of adsorption enthalpies on various surfaces irrespective of the structure the adsorbates might assume or the reversibility of adsorption.[28]

Our metal vapor adsorption calorimeter was described in detail by Stuckless et al. in a 1998 article published in *Review of Scientific Instruments*.[60,97] The sample platen was later modified as described in detail by Diaz et al. for studying spin-coated polymers.[97] We used that same sample platen design here to study the NU-1000 samples, and performed the study of Ca adsorption on NU-1000 described in detail in Chapter 3. In this section, I will introduce the standard procedures of our metal vapor adsorption calorimetry technique using the Ca on NU-1000 project as an example.

The schematic diagram of the metal vapor adsorption calorimeter and details of the sample platen for NU-1000 samples are shown in Figure 2.1 and Figure 2.2, respectively. The calorimeter uses a pyroelectric β-polyvinylidene fluoride (PVDF) sheet for heat detection. The PVDF sheet is 28 μm thick and pre-coated on each side with 70 nm Cu and topped with 10 nm Ni for electrical contact. It was cut into ~1.3 cm diameter disks from a large sheet using a ceramic scissor to avoid face-to-face shorts. Thin films of NU-1000 were prepared by drop-casting from an agitated NU-1000 solution (0.5 wt % in acetone) directly onto the heat detector disks. The sample-coated heat detector disks were then mounted onto sample platens and stored in a sample suitcase. (Up to 11

samples could be stored in the sample suitcase.) The sample suitcase was baked at 350 K under vacuum overnight to remove trace solvent and physisorbed water from the samples and finally reached a base pressure of 2×10^{-9} Torr.

To perform adsorption calorimetry and surface analysis, the samples were transferred from the sample suitcase to the ultra-high vacuum (UHV) analysis chamber with a base pressure of 2×10^{-10} mbar. In the calorimetry stage, Ca atom beam was produced from 99.5% purity Ca granules (purchased from Alfa Aesar), which was evaporated from a Knudsen cell containing an alumina-lined tungsten crucible. The flux of the beam at the sample position was firstly measured by a quartz crystal microbalance (QCM). The beam was then chopped into 102 ms long pulses at 1/2 Hz and collimated to provide a 4.18 mm diameter deposition area on the NU-1000 sample. The heat released from the adsorption of metal atoms was transferred by thermal diffusion to the heat detector. The resulting peak-to-peak voltage response across the PVDF sheet was then calibrated using the voltage response to pulses of known energy of stabilized He-Ne laser with 632.8 nm wavelength. (The reflectivity of the sample at the He-Ne laser wavelength 632.8 nm was measured *ex situ* using an integrating sphere in a second He-Ne laser of the same type.) The typical operating temperature of the Knudsen cell was ~950 K for Ca, which generates extra thermal radiation that impinges on the sample surface. This radiation contribution was also measured by translating a BaF_2 window into the path of the Ca beam, which blocked all the Ca atoms before they impinged onto the sample but passed a known fraction (~92%) of the radiation. This radiation contribution was finally subtracted from the total calorimetric heat.

The sticking probability was measured simultaneously with a modified King-Wells method[60] using a line-of-sight quadrupole mass spectrometer (QMS) positioned at a polar angle of 35° (known as the "magic angle")[98] from the surface normal to measure the fraction of metal atoms

which strike the surface but do not stick. The QMS signal was calibrated by a "zero-sticking" reference provided by measuring the integrated desorption of a known amount of multilayer metal atoms on a heated Ta foil. A -500 V bias voltage was applied between the sample and the mass spectrometer to avoid electron damage to the sample surface.

The UHV analysis chamber is also equipped with a hemispherical electron energy analyzer (Leybold-Heraeus EA 11/100), ion gun (Leybold-Heraeus IQE 12/38), and Mg/Al Kα dual anode X-ray source (VG Scienta XR3E2) for low-energy He^+ ion scattering spectroscopy (LEIS) and X-ray photoelectron spectroscopy (XPS). The growth of Ca on NU-1000 was studied by LEIS using He^+ ions with 1.00 keV primary energy. The sample was positioned perpendicular to the energy analyzer axis, and the ion beam was directed at 45° with respect to the surface normal. Ion fluxes were typically 15 nA/cm^2, and the sample was exposed to the He^+ ions only during spectrum acquisition. Each deposition of Ca atoms followed previous depositions consecutively, starting with a sample that had no adsorbed Ca atoms on its surface. XPS spectra were collected using either Al Kα ($h\upsilon$ = 1486.6 eV, 130 W) or Mg Kα ($h\upsilon$ = 1253.6 eV, 130 W) as the excitation source, with detection of photoelectrons normal to the surface.

2.2 EQUILIBRIUM ADSORPTION ISOTHERM

The use of equilibrium adsorption isotherms to determine the isosteric (constant coverage) heat of adsorption (Q_{st}) and the entropy change (ΔS_{ad}) upon adsorption of a gas is given by Eq. $Q_{st} = RT^2[\partial(lnP)/\partial T] = -R[\partial(lnP)/\partial(1/T)]$ (6.5. The needed data (pairs of P and T at several constant coverages) was extracted from horizontal lines drawn across isotherms like those of Figure 6.4 and Figure 6.5. The plots of ln P versus $1/T$ over a reasonably narrow range of T (such that Q_{st} is constant) yield straight lines. The slope of each of these lines gives $-Q_{st}/R$ and the y-intercept is equal to $-\Delta S_{ad}/R$, where both values correspond to that specific coverage.

Adsorption isotherms included in Chapter 6 were measured using two slightly different point-by-point approaches described in ref [94]. Figure 6.4 and Figure 6.5 show measured isotherms of CO and CH_4 to illustrate these two approaches. For the CO isotherms in Figure 6.4, the temperatures were set and all data points were taken by keeping the temperature constant. For the CH_4 isotherms in Figure 6.5, the higher T (99.0 K, 106.5 K, 113.5 K) isotherms started at constant temperatures and were continued only to about half a monolayer to get to low coverages at equilibrium pressures accessible with the 10 Torr pressure gauge, after which the temperature was lowered in steps. When the desired lower T (67.0 K, 83.5 K, 74.5 K) was reached, the isotherm was then continued to the bulk vapor pressure. The single equilibrium points obtained at each lower T were used to check reproducibility.

Our NU-1000 samples were prepared at Northwestern University using a procedure described in ref [49] and kindly given to us by J. T. Hupp and O. K. Farha. Each NU-1000 sample with a mass of approximately 10 mg was loaded into the glass tube (see Figure 2.3) and baked at 350 K under vacuum overnight to remove trace solvent and physisorbed water. No sample was further exposed to air after baking.

2.3 FIGURES

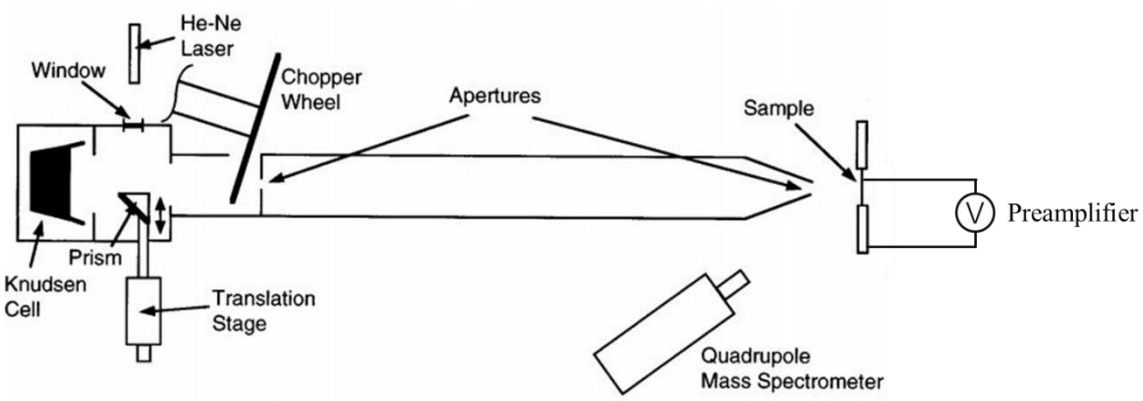

Figure 2.1. Schematic diagram of the UHV metal vapor adsorption calorimeter. It includes a Knudsen cell and associated molecular beam path with rotating chopper to generate pulsed, collimated metal atom beams. It also includes a moveable prism used for calorimeter calibration by directing a diffused He–Ne laser beam down the molecular beam path. The samples were directly deposited onto the heat detector as thin films. Details of the sample platens housing the PVDF detectors are shown in Figure 2.2. The heat released from the adsorption of metal atoms was transferred by thermal diffusion to the heat detector, generating a voltage response which was then amplified by the preamplifier. Reprinted and modified with permission from ref. [60].

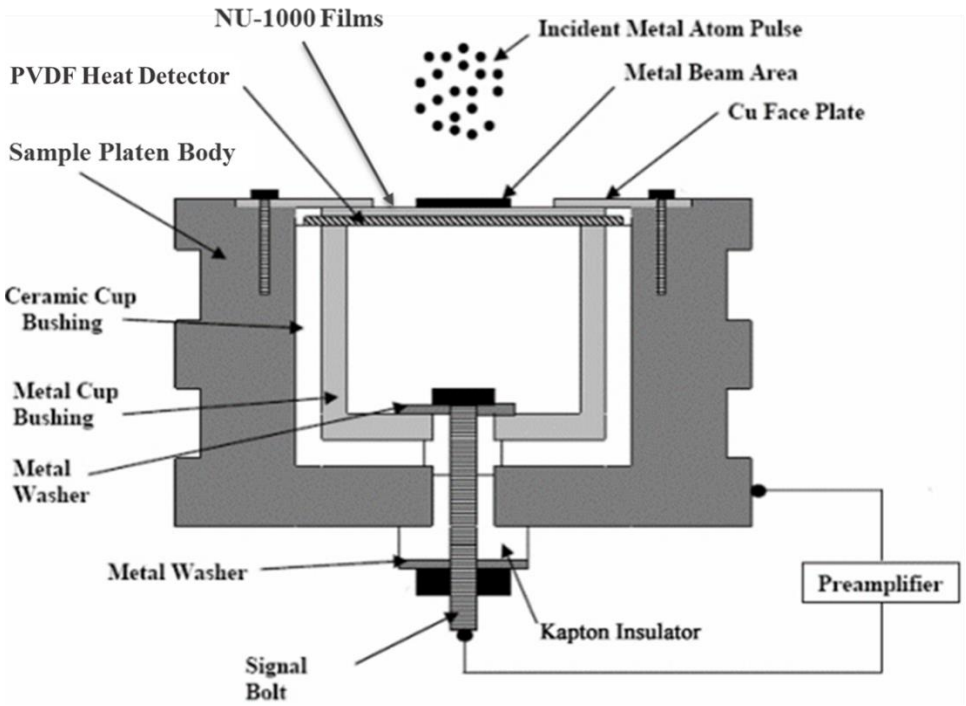

Figure 2.2. A cross-sectional view of the sample platen for the NU-1000 samples. The entire sample platen is circularly symmetric when viewed from above or below. The pyroelectric PVDF heat detector sheet was cut into ~1.3 cm diameter disks from a large sheet of metal-coated PVDF. The NU-1000 sample was drop-casted onto its front face. Each sample-coated disk was clamped between a copper face plate and copper cup bushing. The copper cup bushing was held in the ceramic cup bushing by a signal bolt which was isolated from the body of the sample platen. The metal films on the front and back face of the PVDF are thus electrically isolated from each other, and the signal bolt and sample platen body act as the electrical leads from these metal-film electrodes to the preamplifier. A 4-mm diameter area centered on the front face of NU-1000 sample was exposed to the pulsed metal atom beams. Reprinted and modified with permission from ref. [97].

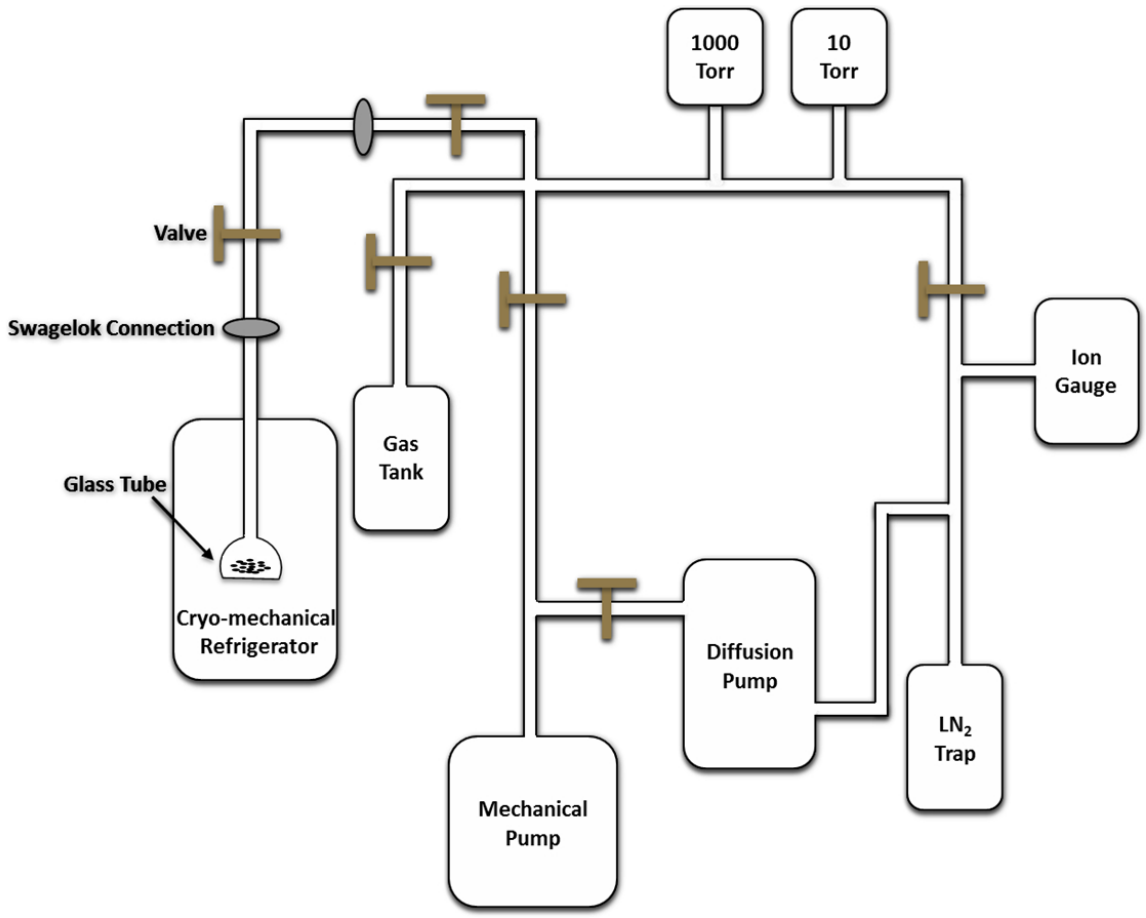

Figure 2.3. Diagram of the BET system which was used to measure equilibrium adsorption isotherms included in Chapter 6. The NU-1000 samples were placed in a 4 mm ID Pyrex glass tube with a wider (about 10 mm) flared flat bottom to make better thermal contact with the cooling system and to prevent powder migration when baked and/or pumped. The sample temperature was regulated by a cryo-mechanical refrigerator within a temperature range 11 K < T < 300 K, ± 0.1 K. The glass tube was attached to a vacuum and gas handling manifold capable of pumping to 3×10^{-7} Torr and pressurizing up to 1 atm. The dosing system had a calibrated volume of 87 cm^3 and two MKS Baratron capacitance absolute pressure gauges with 1000 Torr and 10 Torr ranges. The dead volume of the empty adsorption cell was calibrated between 12 K and room temperature using helium gas.[94]

Chapter 3. Calcium Vapor Adsorption on the Metal−Organic Framework NU-1000: Structure and Energetics

This chapter is reprinted with permission from reference [99]:

Lownsbury, J. M.; Santos-Lopez, I. A.; Zhang, W.; Campbell, C. T.; Yu, H. Y. S.; Liu, W. G.; Cramer, C. J.; Truhlar, D. G.; Wang, T.; Hupp, J. T.; Farha, O. K. Calcium Vapor Adsorption on the Metal-Organic Framework NU-1000: Structure and Energetics. *J. Phys. Chem. C* **2016**, *120*, 16850-16862.

ABSTRACT

The nature and energy of the reactions between calcium vapor and the internal surfaces of the metal−organic framework (MOF) NU-1000 have been studied by adsorption microcalorimetry, low energy He^+ ion scattering spectroscopy (LEIS), X-ray photoelectron spectroscopy (XPS), and Kohn−Sham density functional theory (DFT). NU-1000 is one of the most stable MOFs with transition-metal-oxide nodes, and thus it is of interest as a potential catalyst or catalytic support when modified with other metals. The reaction heats of Ca with NU-1000 are high below 2 monolayers (ML) Ca coverage (570−366 kJ/mol), attributed (based on DFT) to Ca reacting first with free benzoic acid functionalities or water impurities, then with H_2O and OH groups on the Zr_6 nodes to produce $Ca(OH)_2$ clusters. With higher Ca doses, the heat of Ca reaction decreases asymptotically to the sublimation enthalpy of bulk Ca (178 kJ/mol), attributed to the formation of Ca(solid) nanoparticles on the external surface, which only occurs after all of the H_2O and OH groups are titrated deeply enough (∼20 nm) such that slow Ca diffusion prevents further reaction.

3.1 INTRODUCTION

Metal−organic frameworks (MOFs) are an extensive class of nanoporous crystalline materials composed of small metal, metal oxide, or mixed-metal−oxide nodes connected by organic linker groups of a fixed length and conformation; the linkers bind to nodes via reactive binding sites such as ionized carboxylic acid groups.[31-33] MOFs have attracted great research interest due to a unique combination of properties, such as structural homogeneity that makes MOFs amenable to X-ray diffraction,[34,35] large surface areas[36,37] and pore sizes,[38,39] framework flexibility,[38,40] opportunities for rational design and tunability,[35,41,42] and almost limitless compositional diversity.[33] Predictive modeling has been used effectively to screen vast numbers of node/linker combinations to select high-performance MOFs for experimental study.[100,101] MOFs have numerous current and potential applications, including gas separation[102,103] and storage,[104-107] catalysis,[43-48] sensing,[108,109] and drug delivery.[110] The Zr-based NU-1000[50,51] is a particularly promising MOF for catalysis because it is water- and temperature-stable,[52] has a BET surface area of >2000 m^2/g,[50,52] and has 31 Å hexagonal pores that allow large molecules to penetrate into the bulk of the MOF crystallites. See Figure 3.1 for the structure of NU-1000.

Because metal–organic framework (MOF) nodes can be oxide clusters of controllable sizes near ∼1 nm in diameter, they can be thought of as very well-defined and homogeneous oxide "nano-supports" to which catalytic metals (like Pt, Ag, Pd, etc.) could be attached to achieve improvement in activity or simply to provide a more homogeneous structure to facilitate fundamental studies of supported metal clusters. The organic linker groups effectively isolate these nodes (and the supported metals) from each other, thus possibly preventing sintering of the metal centers. Additionally, due to the highly ordered nature of MOFs, their structures can be easily

determined with X-ray diffraction (XRD).[34,35,49] Thus, the binding of metal atoms and metal clusters to the oxide nodes of MOFs like NU-1000 is a subject of considerable interest.

Loading MOF nodes with metals has been demonstrated via chemical vapor deposition,[111] solution phase impregnation,[112,113] and even solid grinding.[114] The large pore size and water/temperature stability of NU-1000 also allow for metal loading via atomic layer deposition (ALD)[49,115,116] and metal exchange[117] that would otherwise be severely limited by framework degradation and vapor-phase mass transport. Mondloch et al.[49] used XRD to show that the crystallinity of NU-1000 was not significantly altered by loading the nodes with Al and Zn via ALD, and they used diffuse reflectance infrared Fourier transform spectroscopy to confirm that Al and Zn react with free hydroxyl groups on the Zr_6 nodes. Kim et al.[115] used XRD and X-ray pair distribution function analysis to show similar results for loading NU-1000 nodes with indium via ALD.

Here, we study the bonding energetics of calcium vapor adsorption onto clean NU-1000 at 300 K in ultrahigh vacuum using adsorption microcalorimetry, surface spectroscopies, atomic beam/surface scattering, and Kohn–Sham density functional theory (DFT). As shown below, the Ca atoms are transiently adsorbed in a weakly held precursor state that allows them to diffuse deeply (~10-20 nm) into the NU-1000. Thus, we probe here mainly the internal surfaces of the NU-1000. These have a BET surface area of 2,040 -2,320 m^2/g.[50,52] Calcium is chosen as the probe metal here to study the metal-binding properties of NU-1000 because we already know a lot about how Ca binds to the surfaces of bulk metal oxides,[118,119] pure hydrocarbon surface functionalities,[120] and organic carboxylate and ester groups in the surfaces of polymers.[121-124] Specifically, Ca has a very weak interaction with pure hydrocarbon groups,[120] so it is not expected to interact strongly with the fused benzene rings of the linkers. Thus, it is expected to react only at

the zirconium oxide nodes or at the carboxylate groups that bind the linkers to these nodes. We elucidate the film-growth mechanism and surface morphology of the evolving Ca film using low-energy He^+ ion scattering spectroscopy (LEIS) and X-ray photoelectron spectroscopy (XPS). Simultaneous measurement of the heat of adsorption and sticking probability of the metal atoms as a function of coverage provides the interfacial bonding energies for Ca on NU-1000 as a function of Ca coverage. The reactions are modeled with DFT and interpreted in that light. These results show a strong tendency for Ca metal to diffuse into the pores of NU-1000 and react with either −OH and $-OH_2$ groups on the Zr_6 node, free carboxylic acid on the external surface, or residual weakly bonded water in kinetic competition with Ca(solid) particle nucleation and growth on the surface and in the pores, and eventually Ca(s) film growth across the MOF surface. These reactions occur extensively to a depth of ∼20 nm beneath the NU-1000 surface.

3.2 EXPERIMENTAL METHODS

NU-1000 was prepared solvothermally and then activated, as described previously.[49] Activation removes synthesis solvent and replaces benzoate ligands (nonstructural ligands) on the nodes with aqua and hydroxo ligands. ^1H NMR of the digested material confirmed that activation was complete, with the only carbon-containing component being the tetra-acid of the MOF organic linker, pyrene-tetraphenylcarboxylate. Nitrogen adsorption measurements of the activated MOF yielded the BET surface area, the pore volume, and the isotherm shape expected for a clean and undamaged sample. Powder X-ray diffraction measurements yielded the pattern expected for NU-1000, with no evidence of the formation of polymorphs such as NU-901.[125] The MOF crystallites are necessarily terminated with linkers, nodes, or both, with the identity of the terminating units possibly being crystal-face dependent. A linker-terminated face will present unreacted carboxylic acid groups. We have been unable to observe these by DRIFTS, which is not unexpected even if

they are present, as the detection limit is about 1%. A node-terminated face will present excess aqua and hydroxo ligands. These additional ligands, if present, are likely to be indistinguishable by DRIFTS from aqua and hydroxo ligands present within the crystallites.

Thin NU-1000 films were prepared by drop-casting from an agitated NU-1000 solution (0.5 wt % in acetone) directly onto the heat detector, a metal-coated foil of the pyroelectric polymer β-polyvinylidene fluoride (PVDF, see below). Three ∼6 μL aliquots were drop-cast onto the substrates, which were covered by a small upturned cup with a hole in the center to slow the evaporation rate of acetone. This yielded NU-1000 films ∼1.5 μm thick that uniformly coat the PVDF with low surface roughness confirmed using a microscope. We typically prepared 10 NU-1000-coated heat detectors at a time, and transferred them to the sample preparation chamber via a stainless steel "suitcase" equipped with a gate valve. With the suitcase attached, the preparation chamber was evacuated to its base pressure of 2×10^{-9} mbar and heated at 348 K for ∼10 h to outgas the samples and remove trace solvent and physisorbed water. The samples were then transferred into the ultrahigh vacuum (UHV) analysis chamber for surface characterization and calorimetry as needed.

The heat detectors were ∼1.3 cm diameter disks cut from 28 μm thick sheets of PVDF, precoated on each side with 70 nm Cu and topped with 10 nm Ni for electrical contacts (purchased from Measurement Specialties). These heat detector disks were coated with NU-1000 as described above. After coating with NU-1000, these "samples" were mounted onto sample platens specially designed such that the sample disks are fixed in place by a thin copper washer and the front and back contacts are electrically isolated from each other by a ceramic bushing, as described elsewhere.[97,123] The reflectivity of these NU-1000 films at the He–Ne laser wavelength (632.8 nm)

was measured ex situ using an integrating sphere and was found to be 0.737 ± 0.018. The standard deviation of the reflectivity measurement for an individual sample was less than 3%.

The surface analysis chamber, its adsorption calorimeter, and its pulsed metal atom beam have been described previously.[60] Briefly, the UHV chamber used for these experiments had a base pressure of 3×10^{-10} mbar and was equipped with a hemispherical energy analyzer (Leybold-Heraeus EA 11/100) for LEIS and XPS, ion gun (Leybold-Heraeus IQE 12/38), Mg/Al Kα dual anode X-ray source (VG Scienta XR3E2), quartz crystal microbalance (QCM, Inficon), quadrupole mass spectrometer (QMS, UTI 100C), and adsorption microcalorimeter.

The calorimetric method used here has been described previously.[60,97] Briefly, the NU-1000-coated sample platens were heated in the preparation chamber vacuum at 348 K for at least 1 h prior to each experiment, then transferred to the analysis chamber. The sample platen was then mounted on a large Cu thermal reservoir where electrical connections were made to its heat-detector electrodes. A collimated 4 mm diameter beam of Ca gas atoms was chopped into 100 ms long pulses containing 0.009 monolayers (ML) of Ca at a rate of 0.5 Hz. One ML of Ca is defined here as 7.4×10^{14} atoms per cm^2 of geometric (projected flat) area, which is the packing density of the Ca(111) crystal face. The energy from gas adsorption generates a transient temperature rise in the NU-1000 sample, which is transferred by thermal diffusion to the pyroelectric PVDF detector it coats. The resulting peak-to-peak voltage response was calibrated using the voltage response to pulses of known energy from a stabilized He–Ne laser with 632.8 nm wavelength. A sensitivity of ~350 V per joule of heat absorbed by NU-1000 was commonly found. Because the calorimeter sensitivity and laser power at the sample are constant throughout the experiment, we can determine the change in optical reflectivity of the samples at the He–Ne wavelength due to addition of Ca by measuring the heat signal of the laser before and after dosing Ca. The heat signal

for the laser increased by an average of 29% to ~450 V/J. That is, more light was absorbed by the sample after Ca was adsorbed on the NU-1000 surface. The average calculated reflectivity after experiments was 0.663 ± 0.020. This is approximately the reflectivity of 632.8 nm light reported for thick Ca films.[126] The operating temperature of the Ca beam source was ~923 K, which generates thermal optical radiation that impinges on the sample along with the Ca metal atoms. This thermal radiation was measured by translating a BaF_2 window into the path of the beam, allowing ~95% of the optical radiation to pass through to the sample, while blocking the metal atoms. This radiation contribution was subtracted from the total measured signal. To convert the measured internal energy changes into the standard heat change at the surface temperature (300 K), the excess translational energy of the metal gas atoms at the oven temperature above that for a 300 K Maxwell–Boltzmann distribution was subtracted, and a small pressure–volume work term (RT) was added, as described elsewhere.[60]

The sticking probability for Ca on NU-1000 was determined using the QMS with the modified King–Wells method described previously.[60,98] A metal grid positioned between the QMS and the sample was biased at -500 V to prevent damage to the samples from electrons emitted by the QMS filaments. The growth of Ca on NU-1000 was studied by LEIS using He^+ ions with a primary energy of 1 keV and an angle of 45° between the ion gun and analyzer axes (i.e., 135° scattering angle). Ion fluxes were typically 15 nA/cm^2, and the sample was exposed to the He^+ beam for 2 min to measure the C and Ca signal at each coverage. A two-point experiment also confirmed that beam damage is not a significant factor during LEIS. For XPS experiments, 260 W Mg Kα X-rays ($h\nu$ = 1253.6 eV) were used, and the spectra were referenced to the C 1s peak of NU-1000. The samples used in LEIS, XPS, and calorimetry experiments were baked at 348 K in the preparation chamber vacuum for at least 1 h prior to experiments to ensure the samples were

free of water. Calorimetry was also performed on samples baked for 10 min at 378 K in the preparation chamber vacuum, then cooled to 348 K prior to experiments. Baking to higher temperatures removes any remaining physisorbed water in the MOF channels, as well as structural $-OH_2$ groups from the Zr_6 node.[115] All experiments were performed at 300 K.

3.3 COMPUTATIONAL METHODS

The experimental crystal structure of NU-1000[49] was used as the initial structure in our study. We also built a cluster model ($Zr_6C_{56}O_{32}H_{56}$, see below) that has one Zr_6 core and eight benzoates attached to it; the geometry of the cluster was optimized with all carbons fixed to their positions that were optimized in a periodic calculation from previous work.[51] The Gaussian 09[127] and CRYSTAL14[128] software suites were used for the cluster and periodic calculations, respectively. All theoretical calculations, both cluster and periodic, were performed with Kohn–Sham density functional theory (DFT) with atom-centered Gaussian basis functions. We used the M06-L[129] exchange-correlation functional for geometry optimization (and Hessian calculation in the case of clusters), followed by a single-point energy with the M06-2X[130] functional, which has been previously validated as giving an accurate energy for the formation of a Ca–O bond.[131] We used the 6-31G(d,p)[132-136] basis set for H, C, and O. The SDD effective core potential and corresponding basis set were used for Zr[137,138] and Ca.[139]

An ultrafine integration grid was used for all cluster calculations. Enthalpies were calculated at 300 K. The vibrational contributions were calculated by the quasiharmonic approximation, which means using the harmonic oscillator formulas but with scaled frequencies that account for anharmonicity and systematic errors in the density functional calculations, as explained elsewhere.[140] The scale factor used was 0.978 for M06-L, as calculated by the Freqscale program.[141]

In periodic calculations, the lattice constants and atomic positions were both optimized except in the slab calculations, in which the lattice constants were fixed to values optimized in the bulk calculations. For geometry optimization in the periodic model, the Gaussian basis functions with exponents smaller than 0.06 and the polarization p function of H were removed. In the following single-point calculation, the basis functions of Ca with exponent smaller than 0.06 but greater than 0.03 and the polarization p functions of H were added back to better describe the reactions involving H and Ca. Default settings were used in CRYSTAL14 except that Itol5 was increased to 35 to facilitate convergence of the M06-2X calculations. All enthalpies from periodic calculations are approximated by adding the reaction energy at 0 K (neglecting zero-point energies) from the periodic calculation to the difference from the cluster calculations between the enthalpy of reaction at 300 K and the energy of reaction at 0 K (neglecting zero-point energies).

3.4 RESULTS

3.4.1 *Sticking Probability*

The amount of Ca vapor that actually adsorbs on the NU-1000 surface must be known to determine the true Ca coverage from the Ca flux and to convert enthalpies of adsorption/reaction measured by calorimetry into units of kJ per mole adsorbed. Figure 3.1 shows the sticking probability of Ca atoms on NU-1000 (outgassed at 348 K) as a function of Ca coverage at 300 K. In the limit of zero coverage, the sticking probability of Ca on NU-1000 was 0.91 and increased steadily to within 1% of unit sticking by 3 ML coverage. Multilayer Ca films are known to have near unit sticking probability for Ca at 300 K.[119] The flux of the Ca atom beam was measured with the calibrated QCM at 300 K, precoated with a multilayer of vapor-deposited Ca to ensure unit sticking probability. Coverage was determined by time-integrating the product of the Ca flux and the sticking probability.

3.4.2 *Low-Energy Ion Scattering Spectroscopy*

LEIS with He^+ ions is useful for determining the location of the adsorbed Ca because it provides element-specific information while probing only the topmost atomic layer of the solid.[142,143] Figure 3.2 shows the evolution of the Ca and C LEIS signals, both normalized to their maximum values, as a function of Ca coverage on NU-1000 at 300 K, with the inset depicting the low coverage region in more detail. Effects of beam damage by He^+ ions were determined to be negligible by comparing the signal intensity versus coverage to a control experiment, which exposed the surface to ~5 times fewer ions but yielded identical results within the data scatter. The Ca signal grows much more slowly with Ca coverage than predicted by a layer-by-layer growth model on a flat substrate, and even more slowly than on flat films of several organic semiconductors we investigated previously,[120,123,124,144-146] where the Ca was shown to diffuse deeply below the external surface at 300 K (down to at least 3 nm and up to 12 nm, depending on the material) before reacting with internal surface functional groups that contain heteroatoms. However, the curve is similar in shape to the Ca growth curves on phenyl-C_{61}-butyric acid methyl ester (PCBM)[123] and the polyfluorenes poly(9,9-di-n-hexyl-2,7-fluorene) (PDHF) and poly(9,9-di-n-hexyl-2,7-fluorene vinylene) (PDHFV),[120] which contain very few heteroatoms (none in the case of the polyfluorenes). In general, the very slow growth of Ca LEIS signal in those cases was due to a combination of (1) Ca diffusing below the surface and reacting with internal surface groups, followed by (2) Ca atoms nucleating clusters of Ca(solid) on the surface, which grow into thick 3D Ca particles that cover only a small fraction of the surface initially (but eventually make a continuous overcoating). This second step has a heat of adsorption very similar to the heat of sublimation of bulk Ca(s), 178 kJ/mol.[61] It appears in Figure 3.2 that a similar behavior occurs here, so that Ca initially (up to >5 ML here) is reacting with sites below the external surface and thus is binding to the internal surfaces of the NU-1000, where it is invisible to LEIS.

The carbon LEIS signal increases over the first 2 ML of Ca coverage. This could be explained by changes to the amount of C exposed at the surface due to Ca reacting within the pores of the MOF, perhaps releasing aromatic groups that segregate to the surface, or a decrease in the He^+ ion neutralization probability at the surface due to adsorption of Ca, which probably lowers the work function, or both. Beyond 2 ML of Ca coverage, the Ca LEIS increase is mirrored by a slow decrease in the C signal toward zero.

3.4.3 *X-ray Photoelectron Spectroscopy*

The ratio of the integrated areas of the Ca 2p XPS peak at increasing Ca coverage to the initial C 1s peak at 300 K is shown in Figure 3.3. This Ca/C^0 ratio increases very slowly below 1 ML Ca coverage, consistent with the diffusion of Ca below the XPS probe depth. The growth of the Ca/C^0 ratio is much slower than is predicted by the layer-by-layer growth model on a flat surface, also shown in Figure 3.3. The tabulated inelastic mean free path of C 1s electrons (λ_C) is 26.2 Å when excited with Mg Kα X-rays ($h\nu$ = 1253.6 eV).[147] For the layer-by-layer model calculations, following Ertl and Küppers,[148] we increased λ_C by a factor of 1.8 to account for the large void density in NU-1000. The density of NU-1000 was estimated to be 0.85 g/cm^3 (i.e., 1.8-fold smaller than 1.5 g/cm^3, a typical density for materials of similar composition used to determine λ_C). The sensitivities for C and Ca were taken from Wagner et al.[149] The experimental peak area ratio also grows more slowly than was found previously for Ca deposition on PCBM (a functionalized C_{60} buckyball), where Ca was shown to diffuse and react at depths greater than 10 nm below the PCBM surface.[123] Sample charging precluded a more thorough XPS analysis of the chemical state of NU-1000 with increasing Ca coverage, but there was qualitative evidence of oxygen being involved in some reaction as the O 1s peak shape was altered much more than the C 1s and Zr 3d peaks with increasing Ca coverage. These pieces of evidence suggest that the porous

structure of NU-1000 promotes extensive diffusion of Ca below the external surface and its reaction with internal surfaces, prior to nucleation of Ca(s) at or near the external surface.

3.4.4 *Calorimetric Enthalpies of Adsorption*

Figure 3.4 shows the differential enthalpy of adsorption of Ca on NU-1000 samples that had been outgassed in vacuum at 348 and 378 K as a function of total Ca coverage at 300 K. For pulses containing ~0.009 ML of Ca, the pulse-to-pulse standard deviation of the enthalpies of adsorption at high coverages, where the enthalpy is independent of coverage, is approximately 10 and 32 kJ/mol for samples baked at 348 and 378 K, respectively. The increase in noise may be due to the fact that the pyroelectric response of PVDF begins to degrade at temperatures above ~353 K, and this degradation increases with temperature.[59] Additionally, three experiments were averaged on samples baked at 348 K, as compared to only two experiments on samples baked at 378 K. For samples baked at 348 K, the enthalpy of adsorption in the limit of zero coverage is ~ -513 kJ/mol. Outgassing the NU-1000 to 378 K for 10 min increased the initial enthalpy of adsorption to ~ -570 kJ/mol. It is not obvious why the exothermicity of reaction(s) with the initially deposited Ca atoms is slightly greater for those samples outgassed at higher temperature as compared to lower temperature. However, it has recently been shown that local node structural changes, which do not affect overall crystal order, can occur in bulk NU-1000 as temperatures are elevated above roughly 400 K.[150] It may be that in the thin films, such changes can also occur in the samples heated to only 378 K, and that such local node structural changes generate sites that are still more exothermic in their reactions with Ca than are those described and computed below. As detailed structural data are not available for these local node distortions, we cannot construct specific examples, particularly as they are likely associated with the dangling carboxylic acid functionalities at the film terminus and their potential changes in orientation associated with node

distortions, but we speculate that this is a reasonable explanation for the reproducible variation in initial enthalpies of reaction/adsorption as a function of outgassing temperature. Note that the sticking probability (S) versus coverage was not measured for the samples outgassed at 378 K. Because S was so close to unity at all coverages for NU-1000 samples outgassed at 348 K (Figure 3.1), and the enthalpy versus coverage was so similar for both outgassing temperatures, we assumed it was the same for 378 K as at 348 K.

Figure 3.4 shows that the very negative reaction enthalpies (>-250 kJ/mol) extend to Ca coverages of >2 ML, or 1.48×10^{15} Ca atoms per cm^2. The DFT calculations below, and the general trend from our earlier measurements that Ca does not react strongly with pure hydrocarbon moieties,[120,123] show that the high-enthalpy-release reactions are due to reactions with nodes and reactive, dangling carboxylic acid groups. Given the low density of these node sites, this 2 ML Ca coverage corresponds to a reacted depth of >10 nm (see below). This means that, just as with Ca adsorption on polymer films,[120,123,124,144-146] Ca is initially bound in a weakly held state that diffuses rapidly into the NU-1000 and thus can react quite deeply within the internal surface area.

3.4.5 *Computational Results*

In this section, we discuss the results from periodic and cluster calculations and compare them to experiment. To make the presentation unambiguous and easier to follow, we adopt the convention of following each numerical value for energies or enthalpies by "[C]" if it is an enthalpy from a cluster calculation, by "[P]" if it is an approximated enthalpy from a periodic calculation, and by "[T]" if it is an enthalpy from tabulated experimental numbers in references.

As shown in Figure 3.5, the cluster model of the nodes studied here ($Zr_6C_{56}O_{32}H_{56}$) has one Zr_6 core and eight benzoates attached to it, in the geometry optimized from previous periodic calculations.[51] As a strong reducing agent, Ca reacts with acidic hydrogens to produce H_2. In the

absence of protons, Ca can also react with H_2 to give calcium hydride.[151] In NU-1000, the possible sources of protons are uncoordinated benzoic acid moieties on the external surface, $-OH_2$ or $-OH$ groups of the Zr_6 nodes, and residual water that is solvating nodes otherwise fully saturated with aquo and hydroxo ligands. We show below that the dominant reactions are with $-OH_2$ and $-OH$ groups of the Zr_6 nodes (i.e., on the internal surfaces of the MOF), as shown for the cluster model in Figure 3.5. We calculated the energies and enthalpies of Ca reacting with these and the other types of functional groups on the internal and external surfaces of NU-1000 by both cluster and periodic DFT, as listed in Table 3.1.

There are terminal uncoordinated carboxylic acid sites at the external surface of the NU-1000. Thus, the following reaction between Ca and unreacted carboxylic acid groups of the linkers may occur:

$$\mathrm{Ca(g)} + 2\mathrm{ROOH} \rightarrow (\mathrm{ROO})_2\mathrm{Ca} + \mathrm{H_2(g)} \qquad (3.1)$$

Because the external surface has $\sim 3.5 \times 10^{13}$ nodes per cm^2 of area (see below) and each such surface node may contribute two such benzoic acid groups, this reaction could occur for a maximum of 3.5×10^{13} Ca atoms per cm^2, or less than 0.05 ML of Ca. The calculated enthalpy of reaction in the gas phase for R = Ph (benzoic acid) is -531 kJ/mol [C]. (For comparison, the experimental reaction enthalpy for R = methyl is -695 kJ/mol, from thermodynamic tables of heats of formation [T].[61,152]) To calculate the reaction between Ca and uncoordinated benzoic acid moieties on the surface, we built a periodic slab model of the [001] surface of NU-1000 containing a single layer of three Zr_6 nodes (1 unit cell), terminating with 12 pyrene linkers in total, each of which has two benzoic acids on either the top or the bottom surface, as shown in Figure 3.6A. We considered Ca reacting with different percentages of surface benzoic acid to form H_2: 50% (one benzoic acid reacted per pyrene) and 100% (two benzoic acids reacted per pyrene). For the 50%

case, we found two benzoate and one unreacted benzoic acid groups to coordinate Ca^{2+}, as shown in Figure 3.6B, with the net reaction energy per Ca being -538 kJ/mol [P]. The extra coordination from the C═O bond of an unreacted benzoic acid to Ca^{2+} may account for the slightly more exothermic reaction as compared to the gas-phase reaction$Ca(g) + 2ROOH \rightarrow (ROO)_2Ca + H_2(g)$ (3.1. The large exothermicity also agrees with the high initial enthalpy release measured experimentally, because the external surface of NU-1000 is the first to make contact with deposited Ca. For the 100% case, we found that each Ca^{2+} is chelated by two benzoates, as shown in Figure 3.6C. The enthalpy of reaction (-500 kJ/mol [P]) is not only lower than the 50% case, but also lower than the enthalpy of Ca reacting with two free benzoic acids, that is, benzoic acids in the gas phase (-531 kJ/mol [C]); this may be attributed to the more constrained geometry for two benzoates binding to Ca at the surface.

There is one unsatisfactory feature of a model where the initial reaction of Ca is with dangling benzoic acid-type groups on the external surface of the MOF, as discussed above. The Ca LEIS signal is undetectable in the first 1 ML of coverage (see Figure 3.2), and certainly far below that expected for 10% of a ML of Ca bound on the external surface to benzoic acids. If this reaction does occur to the extent of 10% of a ML of Ca (twice the maximum estimated above), the reacted Ca must somehow get below the benzene rings so they are hidden from the He^+ ions.

The Zr_6 node in NU-1000 has 16 protons distributed on four faces: three each on two faces in the large pore (diameter d = 31 Å), three each on two faces in the small pore (d = 10 Å), and four present as −OH groups of the node itself.[52] Each face has the most stable proton topology[51] as shown in Figure 3.7. To model Ca reacting with an OH_x groups on a Zr_6 node, we replaced different numbers of H atoms for OH_x functionality on the Zr_6 node by Ca in the unit cell. We surveyed the reactions shown in Figure 3.7 to assess the following cases in Figure 3.8: (A and B)

one Ca in the large or small pore, (C–F) two Ca in the large or small pore, (G–L) four Ca, one Ca per face or two Ca per face in the large or small pore, and (M) eight Ca replacing all H atoms on the node. To reduce the computational cost, C_2 or C_i node symmetry is imposed on these geometries where possible; further differentiation of the cases is provided in the caption of Figure 3.8, which shows the optimized structures.

The calculated enthalpies of reaction per Ca found in the reactions leading to the products in Figure 3.8 are given in Table 3.1. The first Ca has similar exothermicity to react with the OH_x groups in the large pore or small pore (-421 kJ/mol [P]), and this value is greater than found for the cluster calculation (-395 kJ/mol [C]), indicating the effect of relaxation of linkers that are fixed in the cluster calculation. A higher enthalpy of reaction per Ca atom (-436 kJ/mol [P]) is found for placing two Ca atoms in the large pore with C_i symmetry. In this optimized structure, two benzoates dissociate one O atom from a Zr ion and coordinate the two Ca ions with the PhC(O)O–Ca distance being 2.23 Å. The dissociation and recoordination of benzoate are more prominent for cases with C_i symmetry, such as two Ca in the large or small pore, as shown in Figure 3.8C and E, and for cases with high Ca loading (equal to or greater than 4 Ca per node). The most exothermic case (per Ca) is when four Ca react with the most acidic protons ($-OH_2$) and μ_3-OH on each face (-459 kJ/mol [P]); Ca reacting with the remaining protons releases less enthalpy, as reflected by the smaller enthalpy of reaction per Ca in the case of 8 Ca per node (-393 kJ/mol [P]). This type of reaction should account for the middle range of the experimentally measured enthalpies of reaction as Ca diffuses into the pores of NU-1000.

Another proton source is from the residual weakly bonded water that may remain within the NU-1000 samples after outgassing. We estimated the reaction enthalpy between Ca and residual water by checking tabulated heats of formation for the following reaction at 298 K:

$$\mathrm{Ca(g) + 2H_2O(l) \rightarrow Ca(OH)_2(s) + 2H_2(g)} \quad (3.2)$$

which has an enthalpy of reaction of −679 kJ/mol [T]. To estimate the amount of physisorbed water remaining in the MOF under UHV, we calculated the bonding strength between the water and the node. Two different conformations were examined, as shown in Figure 3.9.

Let us estimate the coverage of surface sites by weakly held residual water by assuming that every water molecule that strikes the surface sticks and equate that adsorption rate at 300 K and 2×10^{-9} mbar water with a desorption rate given by the product of a typical desorption prefactor for water (10^{13} s^{-1}), the saturation number of water sites per unit area ($\sim 10^{15}$ cm^{-2}), the fractional coverage of water sites (θ), and $\exp(-E_{des}/RT)$, where E_{des} is the activation energy for desorption. We estimate E_{des} from the binding enthalpy for conformation A in Figure 3.9 to be -66.7 kJ/mol. These values give a steady-state population of $\theta = 3 \times 10^{-5}$. If such residual water molecules and the Ca itself were so rapidly diffusing that incoming Ca atoms could be found by water molecules that diffused from ∼60 nm below the surface, this could explain 0.1 ML of reacting Ca with the very high initial heat observed. We show evidence below that diffusing Ca atoms probe down to >20 nm below the surface in their reaction with immobile water and −OH groups that are intrinsic to the nodes.

In the absence of other protons, Ca might react with a Zr–OH group in a single step to form a hydride (in the form of Zr–O–Ca–H). This hydride can exist as a reaction intermediate for Ca reacting with an −OH group or as a stable product when protons are almost depleted. We calculated the enthalpy of reaction for one representative case to form a Ca–H bond, as shown in Figure 3.8N; this reaction has an enthalpy of reaction of -311 kJ/mol [P], which is less than that for reactions that produce H_2 but still comparable.

Calcium gas can also react with the gaseous H_2 product of the above reactions to produce calcium hydride (presumably as solid clusters within the NU-1000 pores) with an enthalpy of -359 kJ/mol [T] based on standard enthalpies of formation.[61] This would need to occur before the H_2 escapes the NU-1000 (as it would otherwise be pumped away), and may even occur with the H atoms they release before any H−H bond is formed. Despite never making H_2 itself, the heat released per mole of Ca by the net reaction to CaH_2 can be estimated by averaging this 359 kJ/mol with the calculated heat from any one of the above reactions which produce H_2.

Once all protons are consumed, the incoming Ca nucleates and grows nanoparticles of solid Ca in a pore of NU-1000 at or near its external surface; therefore, the reaction enthalpy approaches the negative of the enthalpy of sublimation of bulk Ca(solid). To study the nucleation step, we first placed two Ca on 1,3,6,8-tetrakis(phenyl)pyrene in the cluster model. After optimization, the flat pyrene becomes slightly bent toward two Ca, and the enthalpy of reaction per Ca is -62 kJ/mol [C]. The CM5 partial atomic charge[153] on each Ca in this case is 0.37 and the Mulliken partial atomic charge[154] is 0.39; these values indicate that Ca dimer donates electrons to pyrene to form a charge-transfer complex [$Ca^{2+}\cdots pyrene^{-}$]. To study how the geometry constraint on pyrene in NU-1000 affects the enthalpy of reaction, we also placed two Ca on pyrene in a periodic calculation (inside or outside the triangular channel, as shown in Figure 3.10A and B, respectively). For the in-channel and out-of-channel configurations, the Ca–Ca distance is 3.81 and 3.87 Å, respectively, with Mulliken charges on each Ca of 0.52 and 0.46, respectively, indicating more charge transfer in the condensed phase. The enthalpies of reaction for both conformations are slightly lower (-49 and -45 kJ/mol [P]) than those in the gas-phase calculations (see Table 3.1), reflecting the condition that both linker conformations in the periodic calculation are constrained. When protons are

depleted, this reaction can make the first Ca–Ca bond for the nucleation step in forming Ca(solid) clusters.

3.5 DISCUSSION

The experimental results can be summarized as follows: (a) the exothermicity of Ca adsorption on NU-1000 is initially very high (~513 and ~570 kJ/mol in the limit of zero coverage for samples baked at 348 and 378 K, respectively) and much greater than the bulk enthalpy of Ca sublimation (ΔH_{sub} = 178 kJ/mol); (b) the exothermicity of Ca adsorption approaches ΔH_{sub} by ~5 ML coverage; (c) the Ca LEIS intensity increases much more slowly with Ca coverage than is predicted by a layer-by-layer growth model, only reaching complete layer coverage by ~40 ML; and (d) the Ca/C^0 XPS peak area ratio increases much more slowly on NU-1000 than is predicted for a layer-by-layer growth model.

In the following, we will describe a model for the progress of the reaction of Ca with the NU-1000 interface/film that is consistent with these results.

As shown in Figure 3.2, the Ca LEIS signal intensities remain near zero for the first ~2 ML of Ca, where the exothermicity of Ca adsorption drops slowly from its initial value (above 500 kJ/mol) to ~280 kJ/mol, still ~100 kJ/mol larger than ΔH_{sub}. This, together with the very weak Ca XPS signal, is consistent with nearly all of the adsorbing Ca atoms diffusing below the external surface at coverages below 2 ML, where they undergo much more exothermic reaction(s) than depositing pure Ca(solid). Above 5 ML, however, the Ca LEIS signal starts to grow rapidly, and the exothermicity has dropped to within 20 kJ/mol of that for formation of Ca(s) and continues to asymptotically approach that value. In this regime, Ca must be mainly forming Ca(s) nanoparticles on or near the topmost atomic layers of the NU-1000. Between these low- and high-coverage regimes, the exothermicity and Ca LEIS signals make a transition wherein there is kinetic

competition for incoming Ca atoms. They can either diffuse below the external surface to undergo a highly exothermic reaction on internal surfaces, or they can nucleate and grow 3D Ca(s) nanoparticles on or near the external surface with a much lower heat. If growth were limited only to the formation of 3D Ca(s) particles from the beginning, the measured exothermicity of adsorption should be approximately equal to the bulk enthalpy of Ca sublimation of 178 kJ/mol (or less in the case of small clusters, due to the Kelvin effect[155]). The high exothermicity below 1 ML (570 to 350 kJ/mol) indicates a much more aggressive reaction initially at internal surface sites within the MOF. Because Ca has only very weak interactions with pure hydrocarbon polymers and hydrocarbon functional groups in polymers,[120] but reacts highly exothermically with oxygen-containing functional groups,[123,124,145] we attribute this high exothermicity to Ca reacting in some way with oxygen atoms associated with the Zr_6 nodes, either at their terminal $-OH$ or $-OH_2$ groups, at the impurity of unreacted benzoic acid groups on linkers, or with noncrystalline residual water.

The DFT calculations above show that these large enthalpies below 1 ML (-570 to -350 kJ/mol) could include any combination of Ca reactions with RCOOH groups on the external surface or with $-OH_x$ on the nodes. Figure 3.4 can be explained by a kinetic competition between three reactions: (1) Initially (up to 0.05 ML of Ca), Ca reacts with RCOOH on the external surface to account for the high initial heat release (520-570 kJ/mol). (2) Next, Ca reacting with $-OH_x$ on the nodes becomes most important, which accounts for the intermediate amount of heat released ($\sim$420-500 kJ/mol). (3) Finally, the nucleation and formation of Ca(s) dominates, with heats approaching the final exothermicity of $\sim$178 kJ/mol.

It is not obvious why the exothermicity of reaction(s) with the initially deposited Ca atoms is slightly greater for those samples outgassed at higher temperature as compared to lower

temperature. However, it has recently been shown that local node structural changes, which do not affect overall crystal order, can occur in bulk NU-1000 as temperatures are elevated above roughly 400 K.[150] It may be that in the thin films, such changes can also occur in the samples heated to only 378 K, and that such local node structural changes generate sites that are still more exothermic in their reactions with Ca than are those described and computed above. As detailed structural data are not available for these local node distortions, we cannot construct specific examples, particularly as they are likely associated with the dangling carboxylic acid functionalities at the film terminus and their potential changes in orientation associated with node distortions, but we speculate that this is a reasonable explanation for the reproducible variation in initial enthalpies of reaction/adsorption as a function of outgassing temperature.

The carbon LEIS signal increases over the first 2 ML of Ca coverage. This could be explained by changes to the amount of C exposed at the surface due to Ca reacting within the pores of the MOF, perhaps releasing aromatic groups that segregate to the surface, or a decrease in the He^+ ion neutralization probability at the surface due to adsorption of Ca, which probably lowers the work function, or both. Beyond 2 ML of Ca coverage, the Ca LEIS increase is mirrored by a slow decrease in the C signal toward zero.

The XPS Ca/C^0 peak area ratio increases to only a very small ratio over the first 1 ML of Ca coverage, indicating that Ca atoms diffuse below the external surface to react in NU-1000 beyond the XPS probe depth ($\lambda_C \approx 4.7$ nm). The Ca/C^0 peak area ratio increases even more slowly than seen for Ca growth on PCBM,[123] a system that saw diffusion of Ca atoms to a depth of >10 nm below the surface. Sample charging precluded a more thorough XPS analysis of the chemical state of NU-1000 with increasing Ca coverage, but there was qualitative evidence of oxygen being involved in some reaction as the O 1s peak shape was altered much more than the C 1s and Zr 3d

peaks with increasing Ca coverage. These pieces of evidence suggest that the porous structure of NU-1000 promotes extensive diffusion of Ca below the external surface and its reaction with internal surfaces, prior to nucleation of Ca(s) at or near the external surface.

The enthalpy curve in Figure 3.4 can be interpreted in terms of a simple two-step mechanism: (I) a highly exothermic reaction of Ca with oxygen-containing species associated with the Zr_6 nodes within the MOF, and (II) growth of Ca(s) clusters and nanoparticles on or near the external surface with an enthalpy change of about -178 kJ/mol.

A similar exponential-like decay in enthalpy with coverage as that seen here has always been observed for Ca adsorption on organic semiconducting polymers and molecules,[120,123,124,144-146,156] and we attribute it to the same type of kinetic competition here as was used to explain those data. It reflects the decreasing probability for an incoming Ca atom to diffuse further below the external surface to find unreacted sites (oxygen-containing species) and its increasing probability to instead find a growing cluster of Ca(s) to which it attaches. Reaction I slows as these oxygen-containing groups near the surface get titrated by Ca. The density of nodes is very small (~0.23 nodes per nm^3), so the reaction proceeds to >10 nm depth (see below) before diffusion becomes too slow to compete effectively. Meanwhile, reaction II gets faster as the fraction of the external surface and near-surface covered with Ca(s) clusters increases. The enthalpy for reaction II dominates after 5 ML, and perhaps already by ~2 ML. The LEIS data in Figure 3.2 show that only ~1% of the surface is covered by Ca(s) by 2 ML. We show below that nodes have already been reacted down to a depth of >10 nm at this 2 ML coverage.

We use this simple two-state model to explain the enthalpy data in Figure 3.4 for samples baked to 348 K, and from this estimate the extent of reaction with internal-surface oxygen-containing groups on the nodes. This model assumes that the measured enthalpy changes in Figure

3.4 result from only two contributing reactions: one with an enthalpy change equal to the initial enthalpy release of 513 kJ/mol and the other due to the formation of Ca(s) with an enthalpy release equal to ΔH_{sub} (178 kJ/mol). In this model, the measured differential enthalpy of adsorption at any Ca coverage (ΔH_{ad}) is the sum of the fraction of Ca atoms in the pulse that reacts via node oxygen (f) multiplied by -513 kJ/mol and the remaining fraction (1 – f), which makes Ca(s) particles, multiplied by $-\Delta H_{sub}$ (-178 kJ/mol):

$$\Delta H_{ad} = f(-513\,kJ/mol) + (1-f)(-178\,kJ/mol) \tag{3.3}$$

Solving for f at every Ca coverage results in the curve of *f* versus coverage shown in the top graph of Figure 3.11, which is identical in shape to the enthalpy curve in Figure 3.4, except $f = 1$ corresponds to -513 kJ/mol and $f = 0$ corresponds to -178 kJ/mol. Multiplying *f* by the Ca coverage added per pulse gives the amount of reacted Ca per pulse in ML, which reacts at the node oxygens. Summing pulses from zero coverage up to any other coverage gives the total amount of "reacted Ca" (i.e., the amount that reacts with oxygen-containing groups at the nodes) at that coverage. This is plotted versus Ca coverage in the bottom graph of Figure 3.11. As seen, this amount increases gradually until saturating at 1.77 ML of "reacted Ca" at coverages above 7 ML.

We converted this "reacted Ca" coverage to the effective "reacted depth" by calculating the volume of the unit cell of NU-1000 (one hexagonal pore plus two triangular pores, two layers deep) to be 12.8 nm^3. Each unit cell contains 3 nodes, which gives the number density of nodes mentioned above (0.23 nodes per nm^3). Using the Ca ML definition of 7.4×10^{14} atoms/cm^2 and assuming a reaction stoichiometry of 4 Ca per node, we thus calculated the reacted depth of NU-1000 from the reacted Ca coverage, which saturates at ~14 nm. The progression of this reaction depth with coverage is also shown in the bottom graph of Figure 3.11. If instead we assume a

reaction stoichiometry of 8 Ca per node, as seen for Al deposition via ALD,[49,115] we calculate a total reaction depth of ~7 nm.

Of course, there are several types of oxygen-containing functional groups at each node, so there may be a range of reaction enthalpies for Ca with these nodes, and not just this single value of -513 kJ/mol, equal in magnitude to the maximum (initial) enthalpy change assumed in Eq. $\Delta H_{ad} = f(-513\,kJ/mol) + (1-f)(-178\,kJ/mol)$ (3.3. If we instead assume that the enthalpy for the "reacted Ca" has a range of values between -513 and -366 kJ/mol, which is the average enthalpy for the first 2 ML of Ca coverage and very close to the DFT enthalpies for Reaction $\mathrm{Ca(g) + 2ROOH \rightarrow (ROO)_2Ca + H_2(g)}$ (3.1 and $\mathrm{Ca(g) + 2H_2O(l) \rightarrow Ca(OH)_2(s) + 2H_2(g)}$ (3.2, the "reacted Ca" amount and depth increases. Replacing -513 kJ/mol in Eq. $\Delta H_{ad} = f(-513\,kJ/mol) + (1-f)(-178\,kJ/mol)$ (3.3 with a value greater than or equal in magnitude to -366 kJ/mol leads to the results in Figure 3.12. This is quite similar to Figure 3.11, but extends to higher coverages and larger reacted amounts and depths (saturating instead at ~23 nm depth). On the basis of the DFT calculations, this modified two-state model in Figure 3.12 better represents the real situation, with Ca reactions with RCOOH occurring initially (with exothermicity of 520 kJ/mol), followed by Ca reactions with $-OH_x$ on the nodes (with exothermicity of ~400 kJ/mol).

On the basis of its bulk crystal structure, the density of nodes in NU-1000 is 2.34×10^{20} nodes per cm^3. This gives a density of roughly 3.5×10^{13} nodes per cm^2 in the closest-packed layer (assuming close-packed spheres) and a layer-to-layer separation (layer thickness) of ~1.5 nm. Thus, the reacted depth of 23 nm corresponds to ~15 layers of nodes whose $-OH_2$ and $-OH$ groups react highly exothermically with Ca at saturation, after which the Ca only grows as Ca(solid) on the external surface.

3.6 CONCLUSIONS

Calcium vapor reacts initially with a high exothermicity (~ -513 and ~ -570 kJ/mol for samples outgassed at 348 and 378 K, respectively), attributed to Ca reacting with carboxylic acid groups, free water, or both on the internal surfaces. The exothermicity slowly drops to −280 kJ/mol by 2 ML, attributed to a gradual switch to reaction of Ca with $-OH_x$ on Zr_6 nodes deep below the external surface, with an average enthalpy of reaction equal to -366 kJ per mole of Ca. These reactions with the internal surfaces of the MOF nodes produce calcium salts. The very slow growth of Ca LEIS and XPS signals shows that these reactions proceed to ~20 nm below the external surface before the diffusion of transiently adsorbed Ca atoms becomes too slow to find unreacted sites on the internal surfaces. Beyond 2 ML, the exothermicity of adsorption decreases exponentially to the sublimation enthalpy of Ca (178 kJ/mol), reaching this limit by 5 ML; this is attributed to the formation of Ca(solid) nanoparticles near and on the MOF's external surface.

3.7 FIGURES AND TABLES

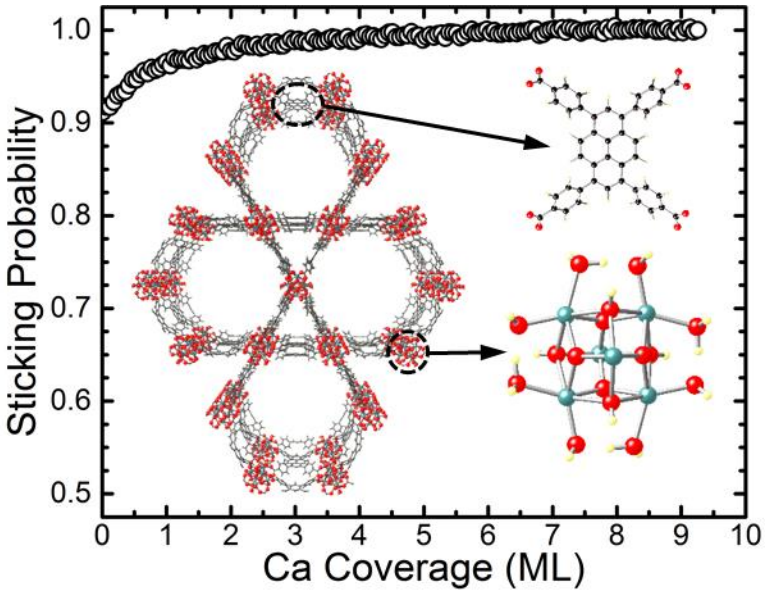

Figure 3.1. Measured sticking probability of Ca gas atoms on NU-1000 (outgassed at 348 K) as a function of Ca coverage at 300 K. Each data point represents a pulse of ~0.009 ML with a pulse frequency of 0.5 Hz. Monolayer coverage (1 ML) is defined as the Ca(111) packing density (7.4×10^{14} Ca atoms per cm^2). The inset shows the NU-1000 structure with the following color scheme: Zr, turquoise; O, red; C, black; H, cream.

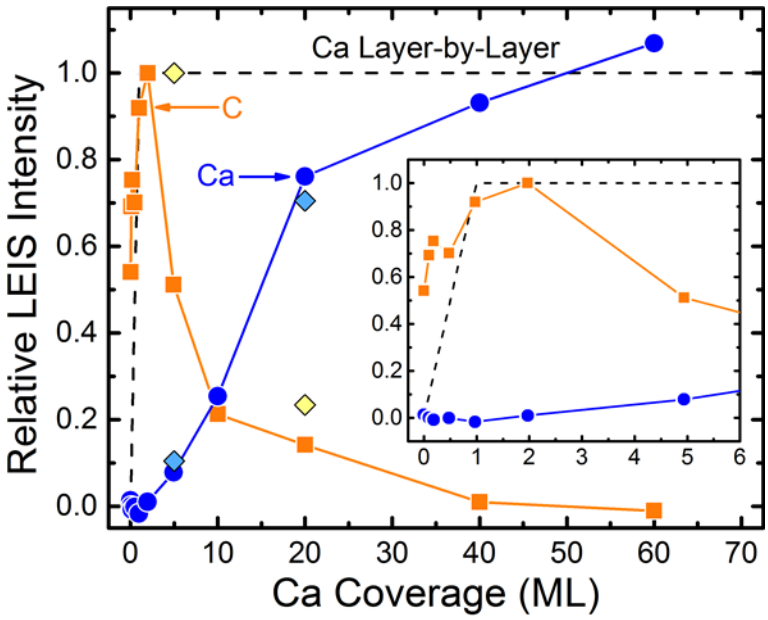

Figure 3.2. He^+ LEIS measurements of Ca growth on NU-1000 (outgassed at 348 K) at 300 K. The relative integrated LEIS peak intensities for Ca (blue ●) and C (orange ■) are displayed as a function of Ca coverage. Calcium intensities are normalized with respect to the saturation signal obtained for very high Ca coverages. Carbon intensities are normalized with respect to the signal obtained from a pristine NU-1000 sample. The dashed line indicates the Ca signal growth curve expected for a layer-by-layer growth model on a flat surface, such that the signal saturates at completion of the first ML. The inset shows a close-up of the low-coverage region. Diamond points were measured using 5-fold larger Ca coverage steps than round points, so that the sample was exposed to only 20% of the typical He^+ dose. Their agreement shows that ion-beam damage does not affect the data at the low ion doses used for normal data acquisition.

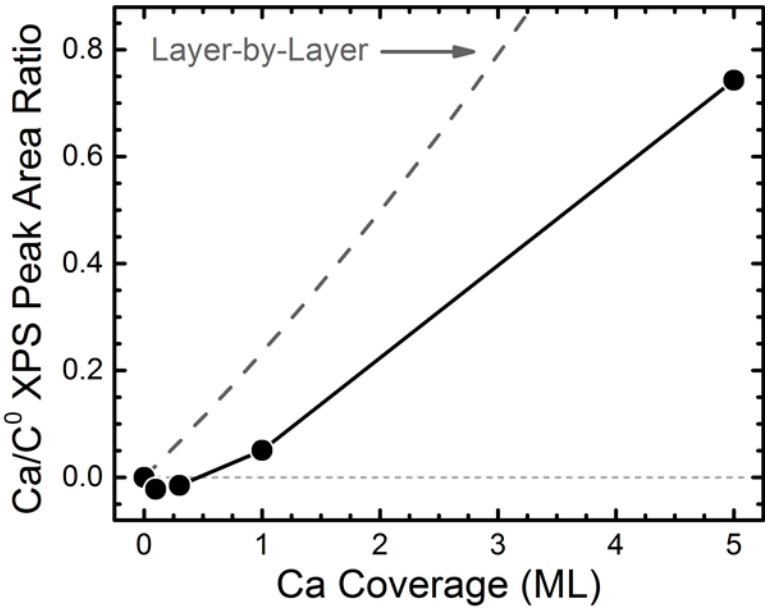

Figure 3.3. Ratio of the integrated area of the Ca 2p XPS peak to the initial C 1s peak as a function of Ca coverage on NU-1000 (outgassed at 348 K) at 300 K. The dashed line indicates the Ca/C^0 peak area ratio expected for layer-by-layer growth on a flat surface.

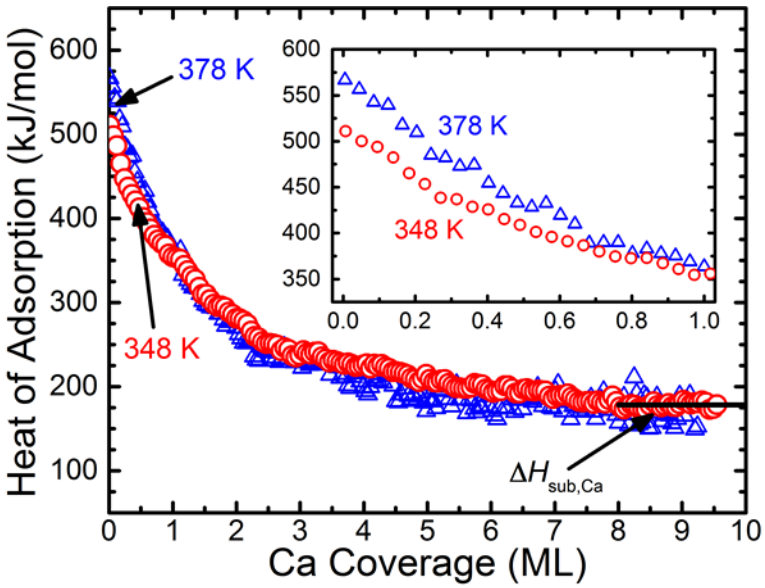

Figure 3.4. Differential heat of adsorption of Ca on NU-1000 at 300 K after baking at 348 and 378 K in a preparation chamber with a base pressure of 2×10^{-9} mbar, plotted as a function of total Ca coverage. The heat of adsorption plotted here is the negative of the standard enthalpy of adsorption at 300 K. The inset shows a close-up of the region up to 1 ML Ca coverage.

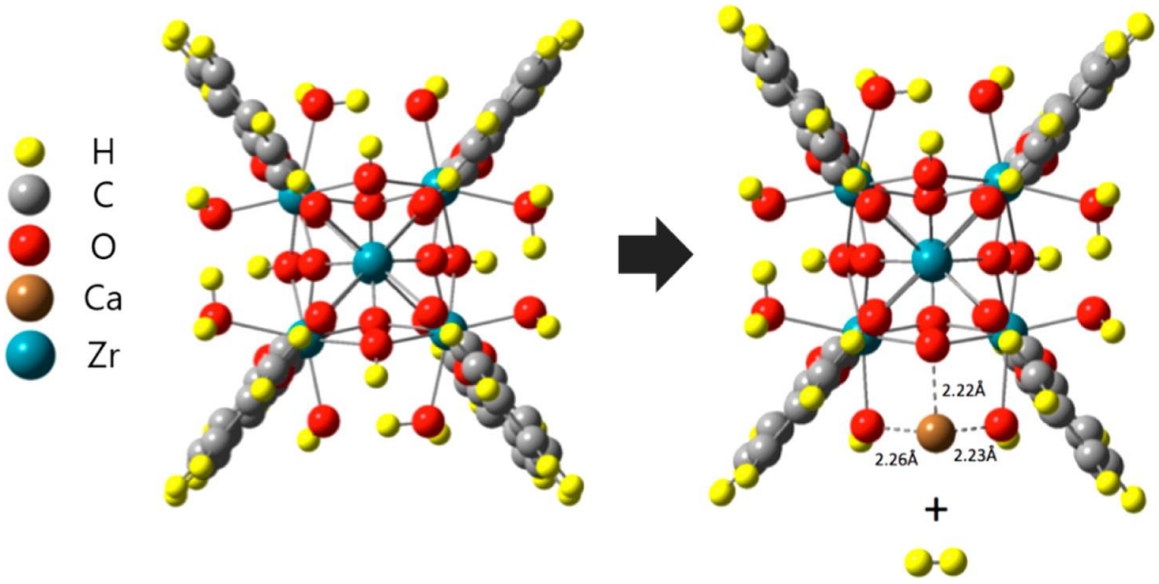

Figure 3.5. Predicted structures optimized in the cluster calculations but with the carbon coordinates frozen at their values from ref [51]. (Left) The initial Zr_6 node with 8 attached benzoates (to model linkers), giving the cluster formula $[Zr_6(\mu_3\text{-}O)_4(\mu_3\text{-}OH)_4(OH)_4(OH_2)_4]^{8+}$. (Right) Final product, $[Zr_6(\mu_3\text{-}O)_5(\mu_3\text{-}OH)_3(OH)_5(OH_2)_3Ca]^{8+}$, formed during the reaction of Ca with a node-bound water-hydroxyl complex, which releases hydrogen, shown here in the form of dihydrogen (similar to the reactions in Figure 3.8A and B; see below). The released hydrogen may instead react with another Ca to make CaH_2 clusters (see text).

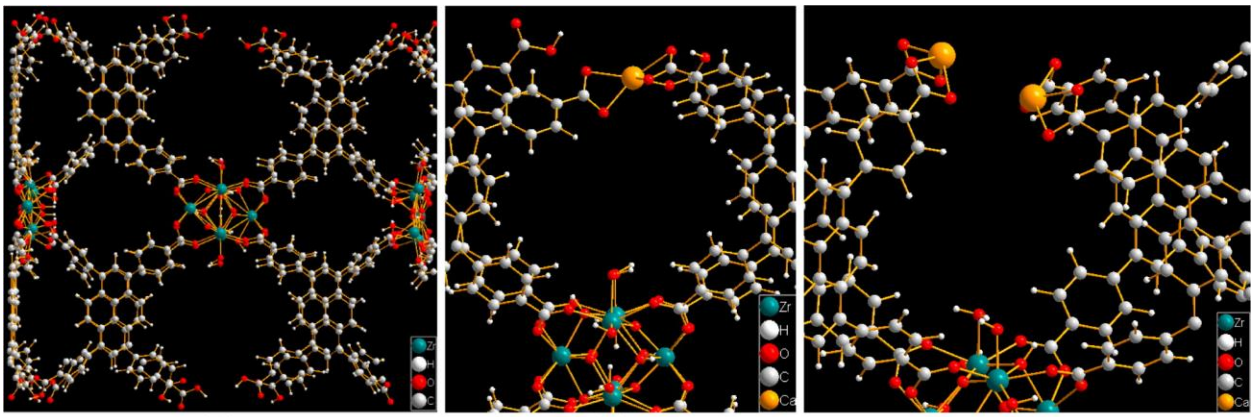

Figure 3.6. (A) The slab model of (001) surface of NU-1000 optimized in the periodic calculation with lattice constants constrained at bulk values. (B) 50% of surface benzoic acid reacting with Ca. (C) 100% of surface benzoic acid reacting with Ca.

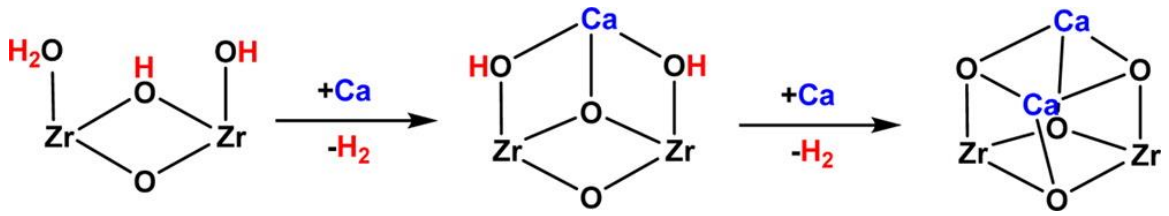

Figure 3.7. Most stable proton topology on the face of the Zr_6 node of NU-1000 and the proposed products of Ca reacting with protons. Only one of four faces of the Zr_6 node with $-OH_x$ is shown.

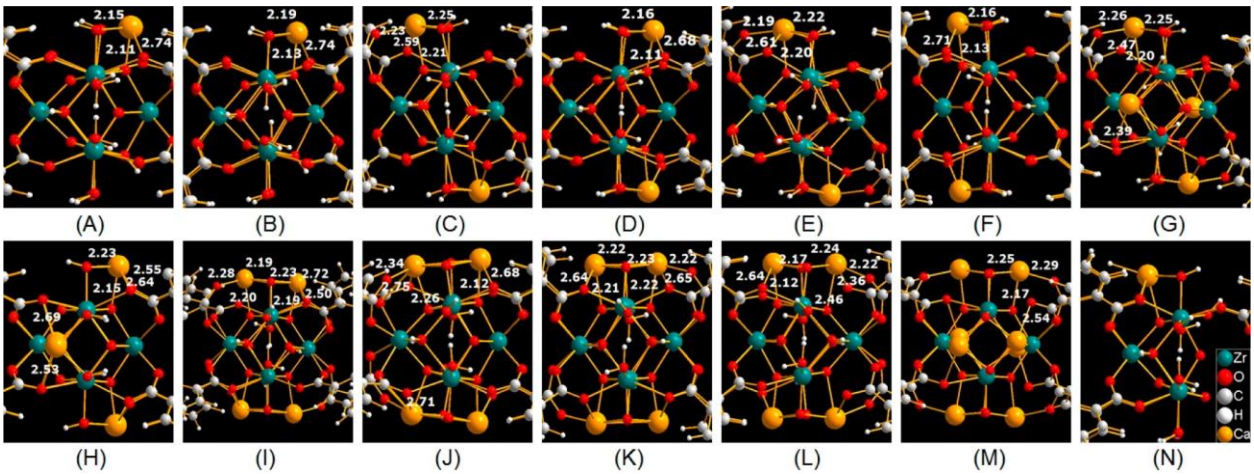

Figure 3.8. Product of Ca reacting with different numbers of protons on the Zr_6 node optimized in the periodic calculation (as listed in Table 3.1). Some Ca–O distances are marked. (A) 1 Ca in the large pore; (B) 1 Ca in the small pore; (C) 2 Ca atoms in the large pore with C_i symmetry; (D) 2 Ca in the large pore with C_2 symmetry; (E) 2 Ca in the small pore with C_i symmetry; (F) 2 Ca in the small pore with C_2 symmetry; (G) 4 Ca, 1 Ca per face with C_i symmetry; (H) 4 Ca, 1 Ca per face with C_2 symmetry; (I) 4 Ca in the large pore with C_i symmetry; (J) 4 Ca in the large pore with C_2 symmetry; (K) 4 Ca in the small pore with C_i symmetry; (L) 4 Ca in the small pore with C_2 symmetry; (M) 8 Ca in both pores; and (N) hydride formation in large pore.

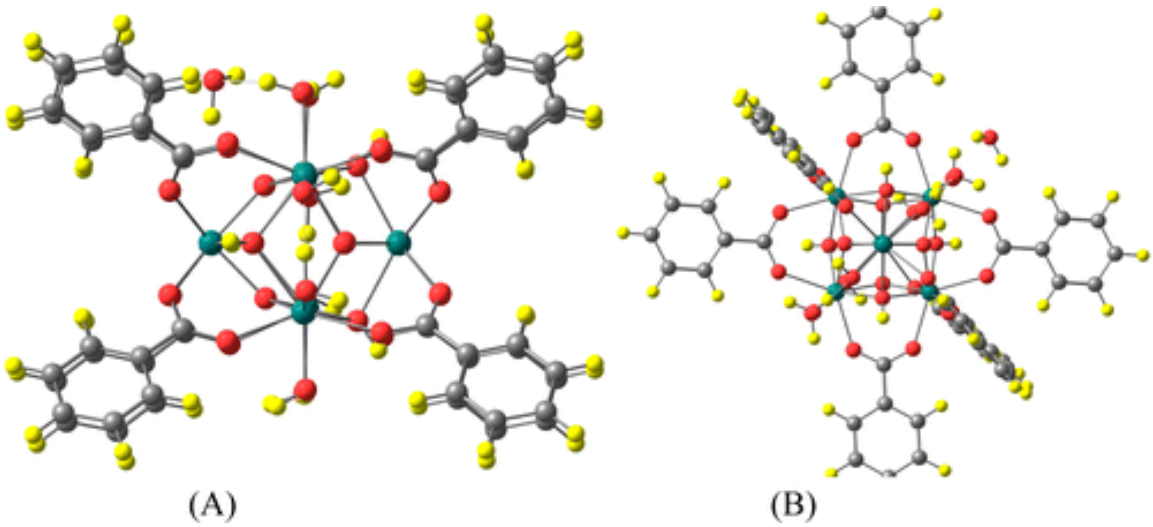

Figure 3.9. Optimized cluster models of water making hydrogen bonds with Zr_6 nodes.

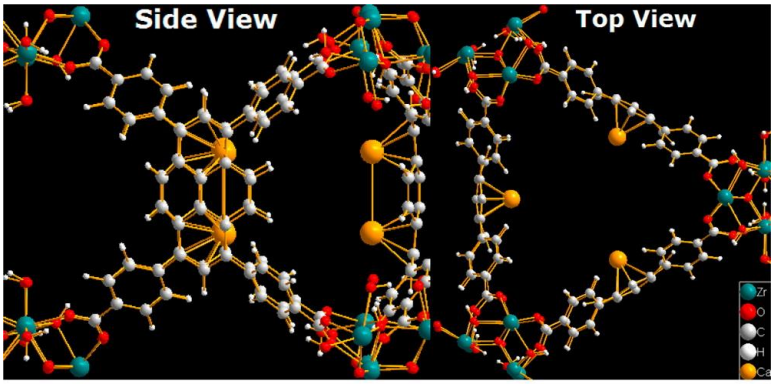

(A)

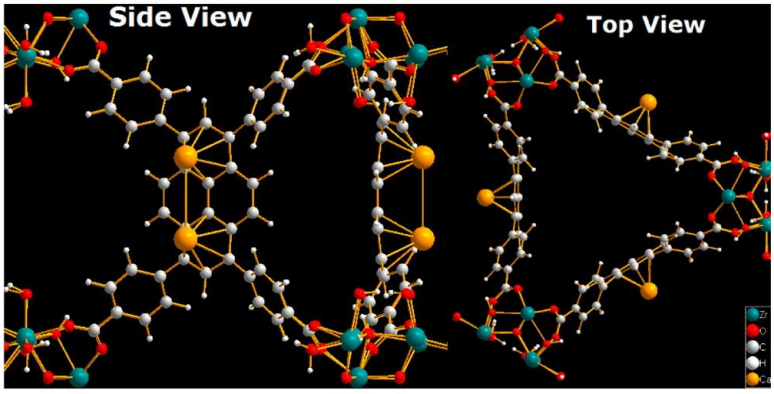

(B)

Figure 3.10. Two Ca atoms deposited on pyrene optimized in the periodic calculation (as listed in Table 3.1): (A) inside the triangular pore; and (B) outside the triangular pore.

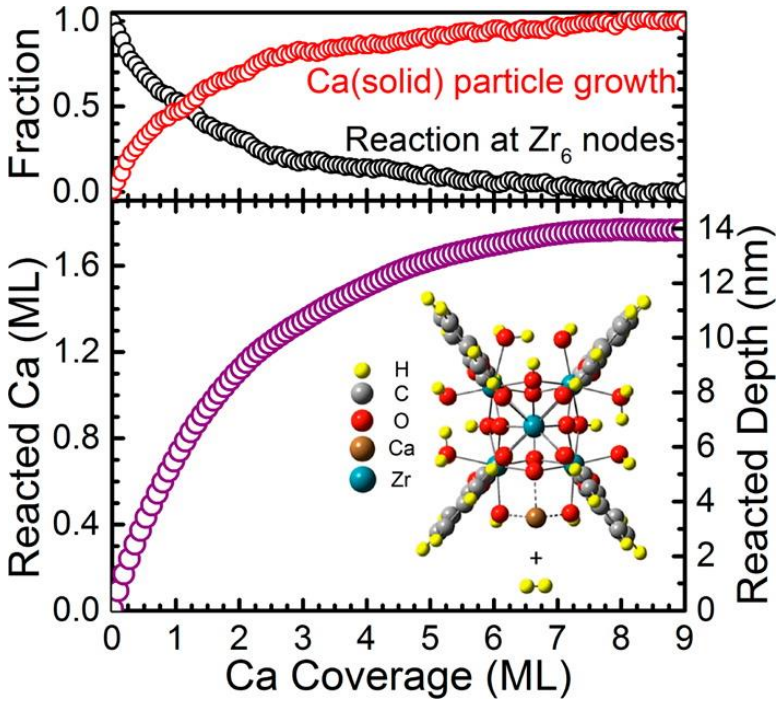

Figure 3.11. Top graph shows the fraction of Ca atoms that react with high heat (513 kJ/mol) within NU-1000 outgassed at 348 K (*f*, black points) and the fraction that grow as 3D Ca(solid) particles as a function of total Ca coverage at 300 K (*1 – f*, red points), estimated from the heat versus coverage data as analyzed with a simple two-state model (see text). The bottom graph shows the corresponding cumulative amount of Ca that reacts with the Zr_6 node of NU-1000; it is plotted as a function of total Ca coverage at 300 K, shown in ML of Ca (left axis) and reacted depth in nm (right axis), which is calculated by assuming that 4 Ca atoms react per Zr_6 node. These values for the "reacted" amount and depth are clearly lower limits because reactions that are much less exothermic than -513 kJ/mol are occurring among the highly exothermic "reactions".

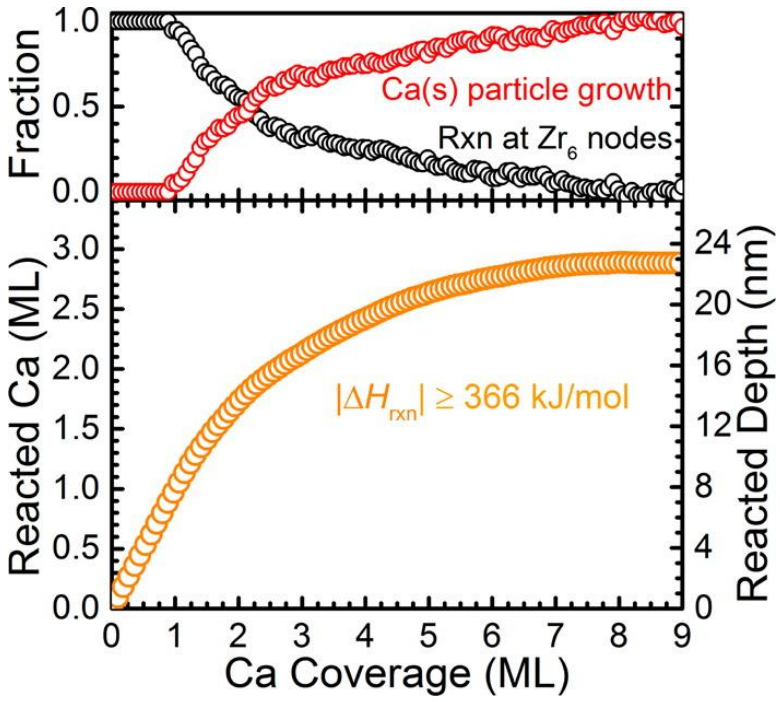

Figure 3.12. Top graph shows the fraction of Ca atoms that react at –OH and $–OH_2$ groups on the Zr_6 nodes with a reaction heat of $|\Delta H_{rxn}| \geq 366$ kJ/mol, (i.e., the average heat measure in the first 2 ML of Ca coverage) within NU-1000 outgassed at 348 K (*f*, black points), and the fraction that grow as 3D Ca(solid) particles as a function of Ca coverage at 300 K (*1 – f*, red points), as estimated from the heat versus coverage data analyzed with the same two-state model used for Figure 3.11, except the reaction heat was changed from 513 to ≥366 kJ/mol (see text). The bottom graph shows the corresponding cumulative amount of Ca that reacts with the Zr_6 node of NU-1000 with a reaction heat of ≥366 kJ/mol plotted as a function of total Ca coverage at 300 K, shown in ML of Ca (left axis) and reacted depth in nm (right axis) assuming 4 Ca atoms react per Zr_6 node.

Table 3.1. Heats of Reaction at T = 300 K for Ca Vapor Reacting with Different Functional Groups on the External and Internal Surfaces of NU-1000,[a] as Calculated with Periodic and Cluster-Based DFT Methods[b]

reactant	description	model type (figure number for product structure)	product	reaction enthalpy (kJ/mol)
benzoic acid	50% surface H	periodic (3.6B)	H_2+Ca^{2+}	-538
benzoic acid	100% surface H	periodic (3.6C)	H_2+Ca^{2+}	-500
benzoic acid	gas phase	cluster	H_2+Ca^{2+}	-531
–OH_x	1 Ca in large pore	periodic (3.8A)	H_2+Ca^{2+}	-421
–OH_x	1 Ca in small pore	periodic (3.8B)	H_2+Ca^{2+}	-421
–OH_x	1 Ca in large pore	cluster (3.5)	H_2+Ca^{2+}	-395
–OH_x	2 Ca in large pore, C_i sym	periodic (3.8C)	H_2+Ca^{2+}	-436
–OH_x	2 Ca in large pore, C_2 sym	periodic (3.8D)	H_2+Ca^{2+}	-419
–OH_x	2 Ca in small pore, C_i sym	periodic (3.8E)	H_2+Ca^{2+}	-424
–OH_x	2 Ca in small pore, C_2 sym	periodic (3.8F)	H_2+Ca^{2+}	-417
–OH_x	4 Ca, 1 Ca per face, C_i sym	periodic (3.8G)	H_2+Ca^{2+}	-459
–OH_x	4 Ca, 1 Ca per face, C_2 sym	periodic (3.8H)	H_2+Ca^{2+}	-417
–OH_x	4 Ca in large pore, C_i sym	periodic (3.8I)	H_2+Ca^{2+}	-382
–OH_x	4 Ca in large pore, C_2 sym	periodic (3.8J)	H_2+Ca^{2+}	-388
–OH_x	4 Ca in small pore, C_i sym	periodic (3.8K)	H_2+Ca^{2+}	-370
–OH_x	4 Ca in small pore, C_2 sym	periodic (3.8L)	H_2+Ca^{2+}	-379
–OH_x	8 Ca in both pores	periodic (3.8M)	H_2+Ca^{2+}	-393
-OH_x	hydride formation in large pore	periodic (3.8N)	Ca–H	-311
-OH_x	hydride formation in large pore	cluster	Ca–H	-349
pyrene	2 Ca inside small pore	periodic (3.9A)	Ca_2^+···$pyrene^-$	-49
pyrene	2 Ca outside small pore	periodic (3.9B)	Ca_2^+···$pyrene^-$	-45
pyrene	2 Ca on 1,3,6,8-tetrakis (phenyl)pyrene in gas phase	cluster	Ca_2^+···$pyrene^-$	-62

[a]Thermocorrections obtained from the frequency calculation in the cluster model were applied to the energy calculated in the periodic model to obtain the approximated reaction enthalpy. All results are in kJ per mole of Ca. [b]All of the groups represent internal surface sites except benzoic acid, which represent unreacted linkers on the external surfaces of MOF particles.

Chapter 4. Calorimetric Metal Vapor Adsorption Energies for Characterizing Industrial Catalyst Support Materials

This chapter is reprinted with permission from reference [157]:

Zhang, W.; Campbell, C. T. Calorimetric Metal Vapor Adsorption Energies for Characterizing Industrial Catalyst Support Materials. *ACS Catal*. submitted.

ABSTRACT

Many important catalysts and electro-catalysts for energy and environmental technologies involve late transition metal atoms and nanoparticles dispersed across the surface of some high-surface-area support materials, for example, oxide nanoparticles. The surface reactivity and long-term stability against deactivation of these materials depends strongly on the strength of bonding of the metal atom and nanoparticles to the support surface. Here, we introduce a novel calorimetry method that implements a $LiTaO_3$ crystal for heat detection and extends metal adsorption calorimetry to surfaces of nanomaterials that are deposited from liquid solutions, as is typical when preparing industrial catalyst materials. This allows one to measure the strength of metal atom bonding and the adhesion energy of metal nanoparticles to clean surfaces of technologically relevant catalyst support materials. We demonstrate that here by measuring the bond energies of Ag vapor onto the clean surfaces of high-surface-area TiO_2 anatase powdered support materials (i.e., 5-nm-diameter nanoparticles) of the type used industrially and the clean surfaces of calcium niobate perovskite nanosheets. This opens up the possibility of using metal adsorption calorimetry to screen catalyst support materials for the strengths with which they bind metal atoms and metal nanoparticles. These strengths are well-known to be crucial in determining both the long-term stability of transition metal catalysts and their catalytic reactivity when in the form of small metal

nanoparticles (i.e., <6 nm in size). This offers new opportunities for discovering better support materials and for basic scientific study of structure / function relationships with respect to metal / support bond energies. The calorimeter measures heats of Ag adsorption on clean surfaces of calcium niobate(001) with a pulse-to-pulse standard deviation of 5.5% for pulses containing only 0.013 monolayer of Ag atoms.

4.1 INTRODUCTION

Active industrial processes apply heterogeneous catalysts consisting of supported metal nanoparticles to a variety of catalytic and electrocatalytic reactions.[14,17,18,158-161] The catalytic activity and selectivity of these catalysts often varies dramatically with the size and shape of the metal nanoparticles, and, when smaller than ~6 nm, with the support materials.[20,162-164] In many cases, the supported metal nanoparticles are rendered inactive due to particle sintering (i.e., coarsening into fewer, larger particles) and the sintering kinetics also depends strongly on the particle size and support materials.[23,26,27] These properties have been proven to be closely correlated with the strength of bonding of the metal atom and nanoparticles to the support surface.[12] Here, we introduce a novel calorimeter to measure the strength of this bonding which extends metal adsorption calorimetry to surfaces of nanomaterials that are deposited from liquid solutions, as is typical when preparing industrial catalyst materials. This allows one to measure the strength of metal atom bonding and the adhesion energy of metal nanoparticles to clean surfaces of technologically relevant catalyst support materials.

We demonstrate the capabilities of this new calorimeter by measuring the bond energies of Ag vapor onto the clean surfaces of high-surface-area TiO_2 powdered support materials of the type used industrially and the clean surfaces of calcium niobate perovskite nanosheets. This calorimeter design opens up the possibility of using metal adsorption calorimetry to screen catalyst support

materials for the strengths with which they bind metal atoms and metal nanoparticles, properties which are well-known to be crucial in determining both the long-term stability of transition metal catalysts and their catalytic reactivity when in the form of small metal nanoparticles (i.e., <6 nm in size).[20,162-164] This offers new opportunities for discovering better support materials and for basic scientific study of structure / function relationships with respect to metal / support bond energies.

To clarify structure–activity relationship in such catalysts and their sintering kinetics, our group has previously measured the strength of the interaction between metal nanoparticles and the support surfaces using metal vapor adsorption calorimetry.[12,26-28] These metal adsorption calorimetry studies have been performed on thin, single-crystal oxide films grown on thin, single-crystal metal substrates and cleaned in ultra-high vacuum (UHV), in order to have very well-defined surface structures where the fundamental aspects of metal / support bonding can most easily be elucidated.[12,26-28] However, this "model catalyst" approach encounters the well-known "materials gap" with respect to the real industrial catalysts.[29,30] That is, these flat and well-ordered surfaces are quite different from the atomically-rough surfaces typically present on the high-surface-area materials needed for real industrial catalyst supports. To bridge this materials gap, we demonstrate here the similar ability to calorimetrically measure metal atom adsorption energies and metal nanoparticle adhesion energies but now onto nanoparticles of support materials with large specific surface areas instead. We further demonstrate that these high-area supports can be prepared for calorimetry by simple deposition from liquid solutions onto the heat detector (e.g., by drop-casting, spin-casting or Langmuir-Blodgett deposition), so that it includes methods similar to those typically used to prepare industrial catalyst materials. Finally, we demonstrate that these materials can be cleaned after deposition by heating to high temperatures (up to ~890 K theoretically) in ultrahigh vacuum or in controlled gases (e.g., O_2) to remove impurities present

after deposition, so that the adsorption properties of their *clean* surfaces can be studied by calorimetry. To our knowledge, this is the only metal adsorption calorimeter capable of measuring metal adsorption energies on the surfaces of solution-prepared high-surface-area samples.

To demonstrate this new calorimetry capability, we study here the heat of adsorption of Ag vapor as a detailed function of coverage on two very different types of nanoparticle support materials. The first support is a drop-casted film of 5 nm diameter anatase TiO_2 nanoparticles, which have been used in many catalytic studies and showed the unusual ability to stabilized single-atom metal catalyst through oxidation and reduction conditions.[57,165-167] For example, Christopher's group has recently reported a single Pt atom catalyst with high thermal stability by depositing isolated Pt atoms onto these TiO_2 nanoparticles, and this catalyst exhibited a 2-fold greater turnover frequency for CO oxidation than the 1 nm pre-reduced Pt clusters on the same TiO_2 nanoparticles.[57] Therefore, the strength of binding of transition metal atoms and nanoparticles to these surfaces of these TiO_2 nanoparticles is of significant interest.

We also applied this calorimeter to study Ag adsorption onto the surfaces of calcium niobate nanosheets. These are synthesized in liquid solution as crystalline, unilamellar $HCa_2Nb_3O_{10}$(001) nanosheets that are 1.45 nm thick and extend laterally for approximately 1 micrometer.[69,71,168,169] When deposited from solution and dehydrated by heating to make crystalline powders of stoichiometery $Ca_4Nb_6O_{19}$, these make an excellent support material from transition metal nanoparticle catalysts which imparts unusual thermal stability against their sintering.[170,171] We have used this calorimeter to study Ag adsorption on this same dehydrated form, but in this case the perovskite nanosheets were deposited in a layer-by-layer fashion (to four-layer or ~6 nm thickness) on the flat heat detector using Langmuir-Blodgett (LB) techniques. In this way, the surface is dominated by (001) facets, so that the calorimetry here is probing a well-

ordered mixed-oxide surface, of similar cleanliness and order to that typically used in studies of single-crystalline oxide surfaces. Those results are presented in detail in another paper.[172] They show that the differential heat of Ag adsorption is initially ~303 kJ/mol and increases slowly to ~338 kJ/mol by 0.8 monolayer (ML). This initial rise was attributed to an increase in the average size of growing 2-atom-thick Ag islands and the resulting increase in the average number of Ag−Ag nearest-neighbor bonds per added Ag atom. At higher coverages, Ag atoms mainly add on top of the 2D islands, growing 3D nanoparticles of increasing thickness. The heat decreased exponentially towards the heat of sublimation of bulk Ag (285 kJ/mol) at 4.5 ML. The adhesion energy of Ag(s) to this Ca niobate surface was estimated to be 4.33 J/m^2 from the integral heat at 4.5 ML. This is larger than previously reported for Ag on any other oxide surface, which we showed can explain the sinter resistance reported for metal nanoparticles on this support.[172]

4.2 CALORIMETER DESIGN

The ultrahigh vacuum (UHV) metal adsorption calorimetry apparatus, which also includes capabilities for XPS, LEIS and metal atomic-beam surface scattering with mass spectroscopic detection, was described previously.[60] The methods for metal adsorption calorimetry are quite similar to those reported previously with this apparatus, whereby 100 ms pulses of a 2-mm diameter atomic beam of metal vapor is impinged onto the surface of interest every 2 seconds, and the transient heat released upon metal adsorption in measured by a pyroelectric heat detector.[60,173] This approach has been applied extensively to study metal adsorption energies on single-crystal oxide surfaces.[12,26-28] Here, we introduce a new heat detector and sample mounting for adsorption calorimetry, implementing a metal-coated $LiTaO_3$ single crystal as the pyroelectric heat detector, onto which nanoparticles of the material whose surface is to be studied are *directly* deposited as a thin film from a liquid solution. For the two materials studied here, they were deposited from

colloidal dispersions, but other deposition methods could be used. Crucial to this new heat detector's design is that it allows heating these thin films to very high temperatures in UHV (or in controlled high-purity gases at low pressures) to clean their surfaces before calorimetry.

4.2.1 *Sample Platen for Sample Mounting, Heating and Calorimetric Heat Detection*

For the purpose of sample heating, we used $LiTaO_3$ single crystals as the heat detectors, which maintain high pyroelectric heat-signal response after heating to high temperatures.[58] We demonstrate this capability here by repeatedly heating different nanoparticle film types up to ~725 K for ~30 minutes in 2×10^{-7} mbar O_2 gas to clean them, and successfully performing adsorption calorimetry measurements after such heating. $LiTaO_3$ has a Curie point of 893 K,[58] theoretically allowing samples to be heated up to ~890 K before the heat detector loses its pyroelectric response, while the pyroelectric polymer heat detectors used previously in this calorimetry apparatus could only be heated up to ~350 K.[59,60]

The novel sample platen design that accomplishes this is shown in Figure 4.1. The $LiTaO_3$ heat detector (red) used here is 25 μm thick and in a 12 mm × 12 mm square shape, with both faces precoated with 100 nm thick $Ni_{80}Cr_{20}$ alloy which serve as the electrodes for electrical signal measurement. When struck with a pulse of metal vapor atoms, these heat detectors generate a charge (and thus transient current through the preamlifier) in response to heat input due to the heat of metal vapor adsorption.

Both the sample platen body and the face plate are made of aluminum for the purpose of easy machining and to reduce weight, and they make electrical contact with the electrode on the front face of the $LiTaO_3$ crystal. The $LiTaO_3$ crystal with a thin film of the nanoparticle material to be studied deposited on its front face will be referred to as the "sample" below. This sample is placed on a tantalum plate, which is 125 μm thick and has the same lateral dimensions as the

crystal. (Note that the $LiTaO_3$ crystal cannot be clearly seen in Figure 4.1b because of its tiny thickness.) The Ta plate not only supports the $LiTaO_3$ crystal mechanically but also serves as a uniformly heated "hot plate" for the crystal so that the crystal can be heated through thermal conduction. The Ta plate is in turn heated by radiation from a hot tungsten filament placed very near the back side of itself (i.e., from below in Figure 4.1b). The heating temperature and heating/cooling rate of the sample can be controlled by controlling that of the Ta plate. The Ta plate is placed in the square groove of a stainless steel (SS) cup bushing which makes electrical contact with the electrode on the back face of the sample. The SS cup bushing has an open cylindrical space on the back side where the sample heater can be positioned. The sample heater (i.e., the W filament and its mount) is movable through a precision port aligner, and the distance between the heater filament and the Ta plate/sample is adjustable. When mounted in the calorimetry position in ultrahigh vacuum (UHV), the platen provides electrical contacts between the electrodes on the front and back face of the sample and wires that lead outside the UHV chamber to a preamplifier whose components were shown schematically in ref. [60].

4.2.2 *Deposition of Oxide Thin Films Directly onto $LiTaO_3$ Heat-Detector Crystals*

We deposited TiO_2 nanoparticles directly onto the metal-coated $LiTaO_3$ crystals to form thin TiO_2 films. Briefly, five nanometer diameter anatase TiO_2 (99.5%) nanoparticles with a specific surface area of 480–650 m^2/g were purchased from US Research Nanomaterials (Stock no. US3838). 0.25 wt % of TiO_2 nanoparticles were well dispersed in H_2O (HPLC grade) after a 30-minute (5 minutes × 6 times) ultrasonication process to form a TiO_2 suspension, which then kept being magnetically stirred for deposition. Thin TiO_2 films were deposited by drop-casting from the agitated TiO_2 suspension directly onto the $LiTaO_3$ crystals (before mounting the crystal on its sample platen). The added droplets on each $LiTaO_3$ crystal was covered by a weighing boat

to prevent surrounding airflow from affecting solvent (H_2O) evaporation. The yielded TiO_2 films typically have a thickness of ~1–2 μm and uniformly coat the $LiTaO_3$ crystals with low surface roughness confirmed using a microscope. The procedures for depositing the calcium niobate(001) nanosheet films onto these heat detectors are described elsewhere.[172]

The deposited film must cover the full area of the metal atom beam (~2 mm diameter) and the area analyzed by the electron and ion spectroscopies (~3 mm x 1 mm), but not extend so far that it prevents the aluminum face plate from making good electrical contact to the metal coating on the front face of the pyroelectric crystal.

4.3 HEATING PROCEDURE AND SURFACE CLEANING

Up to ten such samples can be mounted onto such sample platens and stored in the sample preparation chamber with a base pressure of 2×10^{-9} torr. They are then transferred to the UHV analysis chamber with a base pressure of 4×10^{-10} mbar, where they are heated for cleaning just before experimental measurements, for example, metal vapor adsorption calorimetry or surface spectroscopies. For the drop-casted TiO_2 films, to remove H_2O and organic impurities from the surface, each sample was heated to ~725 K at a rate of 50 degrees per 10 minutes in an O_2 pressure of 2×10^{-7} mbar and was held at that temperature for 30 minutes. The sample was then cooled with the same rate. The O_2 pressure was maintained during both the heating and cooling processes, and evacuated after cooling. The temperature was ramped up/down slowly because faster heating/cooling rates sometimes cause the $LiTaO_3$ crystals to crack. The heat-cleaned sample was then used for silver vapor adsorption calorimetry and surface spectroscopy measurements, such as low-energy He^+ ion scattering spectroscopy (LEIS) and X-ray photoelectron spectroscopy (XPS).

XPS spectra before and after the heating procedure for the same TiO_2 film were measured and compared to verify the removal of surface impurities and the sample integrity (i.e., proper

elemental composition not being changed by heating), see Figure 4.2. On the broad scan spectra (Figure 4.2a), the major photoelectron peaks for titanium, oxygen, and carbon are labeled. Each narrow scan spectrum (Figure 4.2b-d) is fitted using the product of a Gaussian and Lorentzian function after subtraction of a Shirley baseline.[174,175]

The C 1s peak in Figure 4.2b was best fitted with two subpeaks which possibly correspond to different carbon species adsorbed on the sample surface (e.g., CH_x vs. C-O or COOH).[149,176] After the sample was heated to ~725 K for 30 minutes in an O_2 pressure of 2×10^{-7} mbar, the C 1s peak intensity markedly dropped, with the atomic ratio of C:Ti decreasing from 0.69:1 before heating to 0.27:1 calculated using the atomic sensitivity factors taken from Wagner et al.[149] and assuming a homogeneous distribution of elements within the total depth seen by XPS. Previous studies have shown that water and organic contaminants could be removed from Degussa P25 powders after being heated to above 673 K in air.[177,178] Here, ~40% of the carbon impurities (~7.4% atomic concentration in the TiO_2 film's surface) was still detected after the vacuum heating procedure, and we attribute this remaining carbon signal to carbon impurities below the surface but still within the total depth seen by XPS. For the Ti 2p XPS peak in Figure 4.2c, there is no broadening or line shape change which indicates no or negligible oxidation state change for Ti (i.e., Ti is not reduced from Ti^{4+} to Ti^{3+}). The O 1s peak in Figure 4.2d was best-fitted with two subpeaks which are labeled as O^1 and O^2. Here we assume that the O^1 subpeak corresponds to oxygen atoms in TiO_2 while the O^2 subpeak is ascribed to oxygen atoms in adsorbed impurities. With this assumption, the atomic ratio of Ti:O^1 is calculated to be 0.49:1 before heating and 0.50:1 after heating, which is exactly as expected based on the bulk chemical formula, TiO_2. Besides, the O^2 subpeak intensity dropped after the sample was heated, indicating the removal of adsorbed impurities containing oxygen.

In principal, we could have heated the nanoparticle support powders, after their deposition onto the pyroelectric heat detector, in a tube furnace in air, to remove more of the carbon impurity. We did not attempt that here, since our main focus here was to evaluate the practicality of this calorimetric technique. We note too that the metal coatings on the $LiTaO_3$ crystals visibly degraded upon heating in air to 773 K, but appeared stable (by visual inspection) up to 673 K.

4.4 HEAT SIGNAL CALIBRATION USING LASER PULSES

The metal vapor adsorption calorimetry procedure has been described previously.[97] The calorimetric heat released from metal vapor adsorption generates a transient temperature rise in the TiO_2 film, which is transferred by thermal diffusion to the $LiTaO_3$ heat detector. The resulting voltage response ("signal") is calibrated by the voltage response to pulses of know energy from stabilized He–Ne laser at 632.8 nm wavelength. Figure 4.3 shows the heat signal during laser calibration from a train of five laser pulses onto a 2-micron-thick film of TiO_2 nanoparticles on $LiTaO_3$ heat detector at 300 K. Each laser pulse is 102 ms wide with a repeat period of 2s and contains 2.2 μJ of adsorbed energy. The "peak-to-peak" signal intensity (i.e., the difference between the peak of the voltage response and the baseline of the voltage immediately before the pulse) gives the heat detector a contact sensitivity of ~720 V/J. The contact sensitivity of the heat detector depends strongly on the competition between the heat transfer from the heated portion of the sample to the heat detector and to other parts of the sample platen.[60,173] For the drop-casted TiO_2 films, to which different sample thicknesses and quality of thermal contact with the $LiTaO_3$ crystal could easily be introduced during sample preparation, we expect strong variations in contact sensitivities from sample to sample. At the adsorbed energy of Figure 4.3 (2.2 μJ), the "peak-to-peak" signal intensity from 50 individual pulses shows a pulse-to-pulse standard deviation of 2.6%.

4.5 CALORIMETRIC HEAT DETECTION DURING METAL ADSORPTION

Figure 4.4 shows the calorimetric heat signal generated when the surface of the above TiO_2 film was struck by pulses of Ag vapor atoms at 300 K. Each Ag pulse is 102 ms wide and repeats every 2 s. The TiO_2 film was precovered by 401 pulses or ~8 monolayer (ML) of Ag. One ML is defined as the number density of the surface oxygen atoms on anatase TiO_2(101), 5.19×10^{14} cm^{-2}, and each pulse contains ~0.020 ML Ag atoms. Silver vapor atoms were generated from a hot metal source which typically operates at temperatures above 1325 K and thus generates some thermal radiation impinging on the surface. Therefore, the calorimetric heat signal shown in Figure 4.4 includes a contribution (~85 %) from this optical radiation, which can be accurately measured and subtracted as described previously.[97] This correction was made in the heat data reported below.

As mentioned above, the calorimetric heat signal is calibrated by the laser signal from a stablized He–Ne laser at 632.8 nm. This is a accurate calibration for cases where heat is deposited instantly when the metal adsorbs on the surface, that is, the line shape of the heat signal matches that of the laser signal (laser deposits its energy on a very fast timescale). If there is a significant delay between the metal pulse and the deposition of heat, the lineshape of heat signal will change and the laser calibration is no longer accurate for such case, and corrections must be made.[179] To prove the accuracy of the laser calibration, the average laser signal of Figure 4.3 and the average heat signal of Figure 4.4 are compared and shown in Figure 4.5. The time window of the gray rectangular area indicates when the mechanical chopper is open. As seen, the steep rises for both the laser signal and the calorimetric heat signal match the chopper open time window well and do not show broadening. The average laser and heat signals are futher normalized based on the equation: $V_{avg,norm}(t) = (V_{avg}(t) - V_{min}) / (V_{max} - V_{min})$, where $V_{avg}(t)$ is the voltage response at time

t, V_{min} is the minimum of the voltage response, and V_{max} is the maximum of the voltage response. As seen in Figure 4.5 inset, the lineshape of the laser signal matches that of the calorimetric heat signal very well.

4.6 TYPICAL CALORIMETRY RESULTS: STICKING PROBABILITY AND DIFFERENTIAL HEATS OF ADSORPTION VERSUS COVERAGE

To determine the true Ag coverage and convert heats of adsorption measured by calorimetry into units of kJ per mole adsorbed, the sticking probability of Ag adsorption on the drop-casted, 2-micron-thick TiO_2 film was measured as described previously[97] as a function of Ag coverage at 300 K (see Figure 4.6a). The TiO_2 film was heated at ~725 K in an oxygen pressure of 2×10^{-7} mbar for 30 minutes to remove the adsorbed H_2O and organic impurities from the surface before the calorimetry run. The measured sticking probability of Ag on the drop-casted TiO_2 support is 0.988 in the limit of zero coverage, rises to 0.995 by 2 ML, and keeps increasing asymptotically towards unity at higher coverages.

Figure 4.6b shows the differential heat of adsorption of Ag on the drop-casted TiO_2 support as a function of Ag coverage at 300 K. Because the optical reflectivity (used in the laser calibration step) of the sample surface is unknown, we normalized the heat of adsorption at high coverages (>8 ML) equal to the known heat of sublimation of bulk Ag(s) (285 kJ/mol[61]) by adjusting the optical reflectivity of the starting surface. The adjusted optical reflectivity of the staring surface is 0.23. Because the contact sensitivity for the heat detector and the laser power at the sample are constant throughout the calorimetry run, the optical reflectivity of the sample surface covered by Ag can be determined. After the surface was covered by 9 ML of Ag, the optical reflectivity of the surface drops to 0.20. This 13% drop of the optical reflectivity indicates ~4% more adsorbed light by the surface covered by 9 ML of Ag. In the limit of zero Ag coverage, the heat of adsorption is

~206 kJ/mol. It then increases asymptotically to the heat of sublimation of bulk Ag(s) (285 kJ/mol) at higher Ag coverages. This increase is probably due to an increase in the average size of growing Ag nanoparticles in the range below 6 nm, which results in an increase in the average number of Ag−Ag nearest-neighbor bonds formed per added Ag atom. Similar increases in heat with coverage have been reported for Ag adsorption on all other oxide surface that have been studied,[13,172,180,181] except for the Ca niobate(001) surface that we studied with this same new calorimeter, which had a much higher initial heat of Ag adsorption, due to its unusually strong bonding to transition metals (see above). The initial heat of adsorption for Ag in those systems ranges from a low of 176 kJ/mol (on MgO(100) at 300 K)[181] to a high of 303 kJ/mol on Ca niobate(001).[172]

Note that these calorimetry results are from a single experimental run. The large scattering in the heat data is mainly due to the significant contribution of the thermal radiation form the hot metal source which accounts for ~85% of the calorimetric heat signal shown in Figure 4.4. The signal-noise ratio could be greatly approved by increasing the metal beam flux and by averaging over multiple experimental runs, as we usually do in metal adsorption calorimetry.[182,183] Since we were just testing this new calorimeter design in these experiments, we used a very old vacuum chamber here that now has a much lower metal atom flux than we typically use.

4.7 CONCLUSIONS AND PERSPECTIVES

A new metal adsorption calorimeter, with the capability for sample heating at high temperatures, is introduced to study metal vapor adsorption on solution-prepared high-surface-area support materials. It implements a pyroelectric $LiTaO_3$ crystal as the heat detector, which has a Curie point of 893 K,[58] thus theoretically allowing samples to be heated up to ~890 K to clean before use. Anatase TiO_2 nanoparticles (~5 nm diameter) were directly deposited onto the meal-coated $LiTaO_3$

crystal by simple drop-casting to form a 2-micron-thick TiO_2 film. Adsorbed H_2O and organic impurities were cleaned off the surface of the drop-casted TiO_2 film by heating the sample to ~725 K in a low oxygen pressure. The XPS results show that there is no or negligible oxidation state change of the TiO_2 support after being heated. The sticking probability and differential heat of adsorption of Ag vapor atoms on the drop-casted TiO_2 film were measured as a function of Ag coverage at 300 K using the new adsorption calorimeter. The measured sticking probability is above 0.988 for all Ag coverages. The initial heat of adsorption is ~206 kJ/mol. The heat then increases asymptotically to the heat of sublimation of bulk Ag(s), 285 kJ/mol, at higher Ag coverages. The line shape of the laser calibration signal well matches that of the Ag calorimetric heat signal, which proves the accuracy of our heat signal calibration method.

These results demonstrate clearly that this new calorimeter design if effective for studying metal adsorption on vacuum-annealed and cleaned surfaces of high-surface-area powders of support materials, which will enable screening such materials for the strengths with which they bond transition metal catalysts.

Besides the high-surface-area powdered supports, mixed or binary metal oxides (i.e., oxides with two metal elements) are often used as supports in industrial catalysis with the best-known example being ceria-zirconia in automotive exhaust treatment.[184] The presence of two metal elements in the mixed-oxides surely provides many opportunities for improvement in all aspects of support chemistry. As shown in a separate paper,[172] we also demonstrated the utility of this calorimeter for studying Ag adsorption energies on unilamellar calcium niobate(001) nanosheets that were deposited in a layer-by-layer fashion on the heat detector using Langmuir-Blodgett (LB) techniques to make thin, single-crystal mixed-oxide films following established procedures.[76,185]

Overall, this novel calorimeter design offers many new opportunities for surface science studies of industrially relevant high-surface-area support materials and allows to further bridge the well-known “materials gap” from model catalysts to real industrial catalysts.

4.8 FIGURES

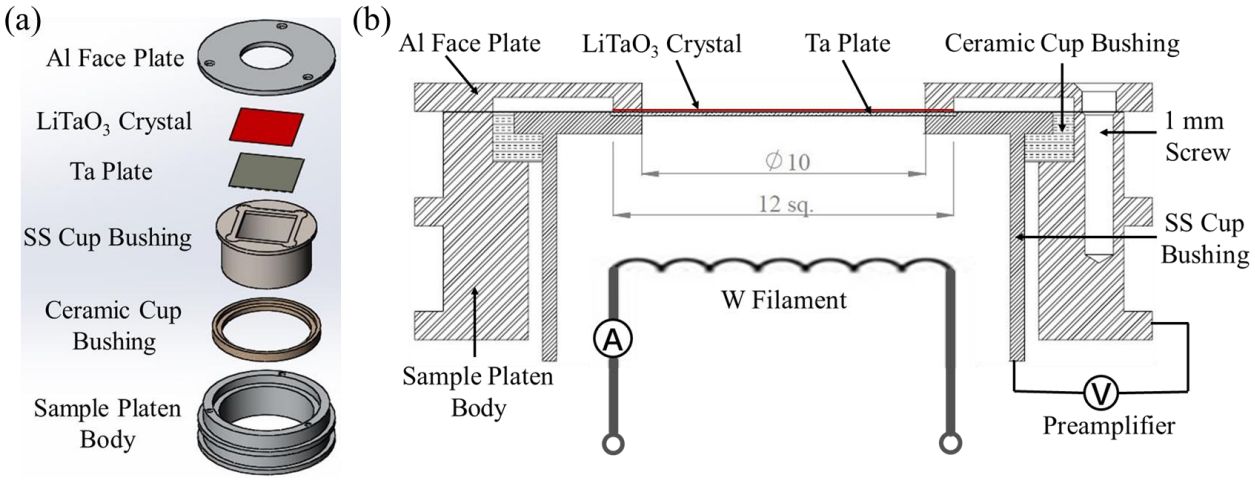

Figure 4.1. (a) A cartoon showing separate parts of the sample platen with built-in heat detector; and, (b) A cross-sectional view of the assembled sample platen. The heat detector (red) used here is a $LiTaO_3$ crystal (12 mm × 12 mm square, 25 μm thick) which is precoated on both sides with 100 nm thick $Ni_{80}Cr_{20}$ alloy. The heat detector sits on top of a 125 μm thick Ta plate which is then placed in the square groove of a stainless steel (SS) cup bushing. The SS cup bushing held by a ceramic cup bushing is isolated from the body of the sample platen. The front and back face of the heat detector are thus electrically isolated from each other, and the SS cup bushing and sample platen body act as the electrical leads to the preamplifier. A 10 mm diameter area centered on the front face of the heat detector is exposed for experimental measurements. A 10 mm × 10 mm square cut centered on the SS cup bushing is designed for sample heating. The sample heater (i.e., the W filament and its mount) is movable through a precision port aligner, and the distance between the heater filament and the Ta plate is adjustable.

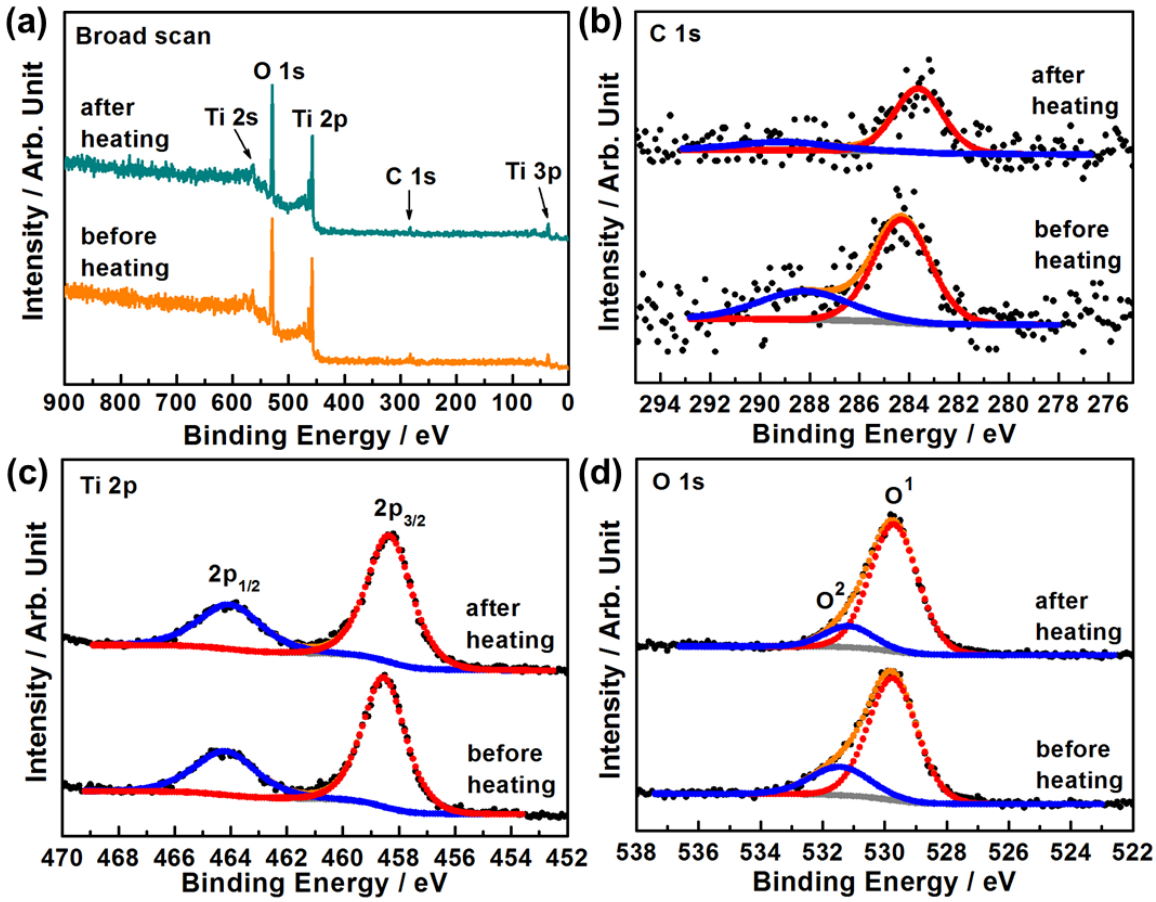

Figure 4.2. XPS spectra (Al Kα, *hv* = 1486.6 eV) and peak fits of a 2-micrometer-thick film of anatase TiO_2 nanoparticles deposited on the $LiTaO_3$ crystal before and after being heated to ~725 K for 30 minutes. The XPS spectra measured before the sample was heated have been normalized so that the average broad scan intensity at 850–900 eV before heating matches that after heating.

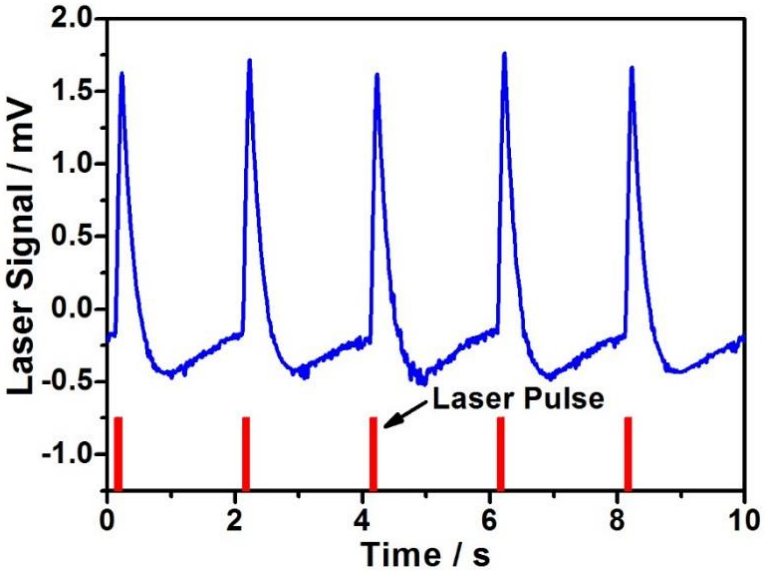

Figure 4.3. Heat signal during laser calibration from a train of He–Ne laser pulses (at 632.8 nm wavelength) onto a 2-micron-thick film of TiO_2 nanopartucles on the $LiTaO_3$ heat detector at 300 K. Each of the laser pulses contains 2.2 μJ of light energy with a ~720 V/J contact sensitivity for the $LiTaO_3$ heat detector. The time window of each laser pulse is 102 ms. These signals have been corrected by dividing by the preamplifier and postamplifier gain (100 × 10).

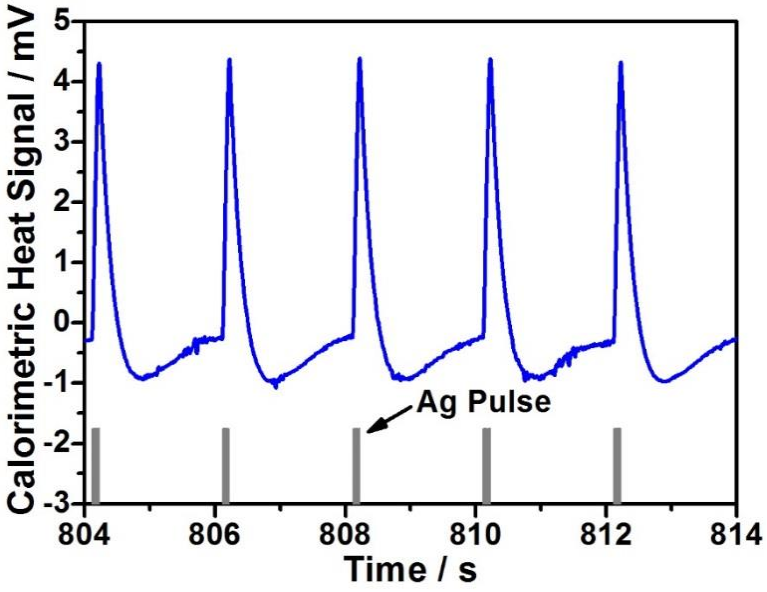

Figure 4.4. Calorimetric heat signal from a train of Ag pulses onto a 2-micron-thick film of TiO_2 nanoparticles on the $LiTaO_3$ heat detector at 300 K. The TiO_2 film surface here had been precovered with ~8 monolayer (ML) Ag. One ML here is taken as the number density of surface oxygen atoms on anatase TiO_2(101), 5.19×10^{14} cm^{-2}, and each pulse contains ~0.020 ML of Ag atoms. Besides the heat released from Ag adsorption, the heat signal also includes a significant radiation contribution from the hot metal source. The time window of each Ag pulse is 102 ms. These signals have been corrected by dividing by the preamplifier and postamplifier gain (100 × 10).

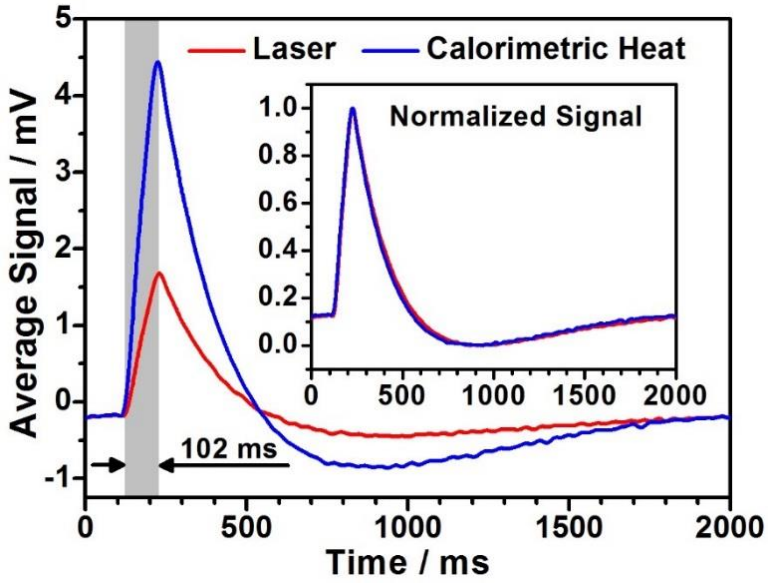

Figure 4.5. Comparison between the average laser signal of Figure 4.3 and the average calorimetric heat signal of Figure 4.4. The gray rectangular area has a width of 102 ms, indicating when the mechanical chopper is open to create the laser or gas pulse. Inset: The average laser and calorimetric heat signals after normalization (see text).

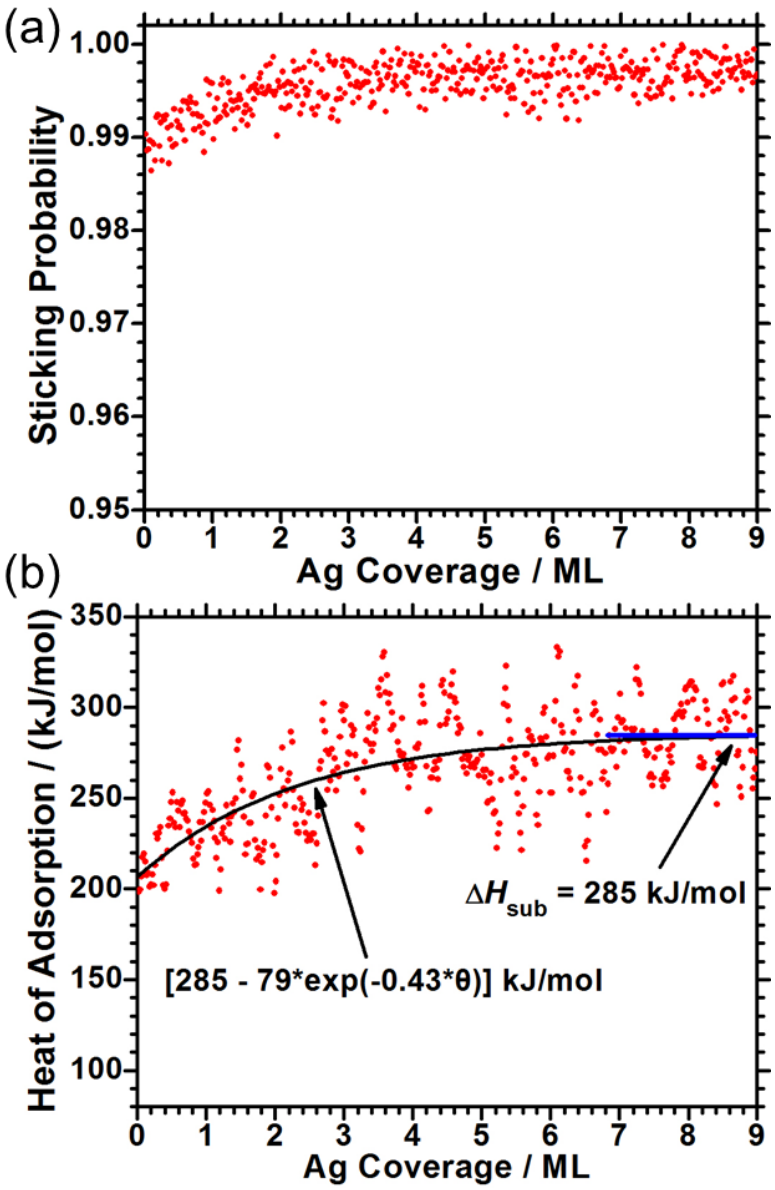

Figure 4.6. (a) Sticking probability and (b) differential heat of adsorption of Ag atoms on surface of 2-micron-thick film of anatase TiO_2 nanoparticles of 5 nm diameter (after heating at ~725 K for 30 minutes in an oxygen pressure of 2×10^{-7} mbar to clean) as a function of Ag coverage at 300 K, from a single calorimetry run. Each data point represents a pulse of ~0.020 ML. The black solid line in (b) is an exponential fit to the heat data.

Chapter 5. Silver Adsorption on Calcium Niobate(001) Nanosheets: Calorimetric Energies Explain Sinter-Resistant Catalyst Support

This chapter is reprinted with permission from reference [172]:

Zhang, W.; Uppuluri, R.; Mallouk, T. E.; Campbell, C. T. Silver Adsorption on Calcium Niobate(001) Nanosheets: Calorimetric Energies Explain Sinter-Resistant Catalyst Support. *J. Am. Chem. Soc.* submitted.

ABSTRACT

Metal nanoparticles dispersed across the surfaces of oxide supports are essential to many current and prospective technologies, including oxide-supported metal catalysts, fuel cells, photocatalysis, and nanoscale electronic contacts. Therefore, understanding the chemical bonding strength at the interface between the metal nanoparticles and oxide supports is of great interest. The adsorption energetics, adhesion energy and adsorbate structure of Ag on dehydrated $HCa_2Nb_3O_{10}$(001) nanosheets at 300 K have been studied using metal adsorption calorimetry and surface spectroscopies. These dehydrated ("dh") calcium niobate nanosheets, which we will refer to below as dh-$HCa_2Nb_3O_{10}$(001), have stoichiometry $Ca_4Nb_6O_{19}$**.** They are interesting since they impart unusual stability to metal nanoparticles when used as catalyst supports and are easy-to-prepare by Langmuir-Blodgett (LB) techniques, highly ordered, and essentially single-crystal surfaces of mixed oxides with a huge ratio of terrace to edge sites. Below monolayer coverage, Ag grows on dh-$HCa_2Nb_3O_{10}$(001) as 2D islands of thickness ~2 layers. The differential heat of Ag adsorption is initially ~303 kJ/mol and increases slowly to ~338 kJ/mol by 0.8 ML. This initial rise is attributed to an increase in the average Ag 2D island size and the resulting increase in the average

number of Ag−Ag nearest-neighbor bonds per added Ag atom. At higher coverages, Ag atoms mainly add on top of the 2D islands, growing 3D nanoparticles of increasing thickness. The heat decreases exponentially towards the heat of sublimation of bulk Ag (285 kJ/mol) at 4.5 ML. The adhesion energy of Ag(s) to this Ca niobate surface is estimated to be 4.33 J/m^2 from the integral heat at 4.5 ML. This is larger than previously reported for Ag on any other oxide surface, which explains the sinter resistance reported for metal nanoparticles on this support. The extent of electron transfer from the adsorbed Ag into the calcium niobate is also measured. These results using LB-deposited perovskite nanosheets demonstrate for the first time a new and easy way to apply surface science techniques derived for single-crystal surfaces to the complex surfaces of mixed oxides, whose study by such techniques have been limited so far to only a few systems.

5.1 INTRODUCTION

Late transition metal nanoparticles supported on high area oxide surfaces are the key ingredients of many catalysts and electrocatalysts with applications to future technologies in the energy, chemical, and environmental industries. The catalytic activity and selectivity of these catalysts are strongly dependent on the size and shape of the nanoparticles, and on the support material.[12,20,22,162,163] Mixed or binary metal oxides (i.e., oxides with two metal elements) are often used as supports in catalysis with considerable improvement on various aspects of catalyst performance. The best-known example is ceria-zirconia in automotive exhaust treatment and other reactions,[62-65,186] but many other mixed oxides are used industrially. The presence of two metals in the oxide surely offers ample opportunities for improvement on all aspects of support chemistry, including not only the strength of bonding to metal nanoparticles but also the extent of charge transfer, lattice stress/strain control, the shuttling of electrons or ions between the support and the metal as part of reaction mechanisms, etc. Thus, there is considerable motivation to understand

mixed metal oxides as supports. To our knowledge, nothing is known about how the second metal in such mixed oxides influences the strength of binding of metal nanoparticles to mixed-oxide surfaces. Here we measure for the first time how strongly metal adatoms and metal nanoparticles bond to a well-ordered mixed-oxide surface, using silver vapor adsorption calorimetry on the dehydrated $HCa_2Nb_3O_{10}$(001) surface. The results reveal larger adsorption energies than have ever been measured for any single-metal oxide surface previously studied.

There have been many metal atom adsorption calorimetry studies on thin, single-crystal oxide films grown on thin single-crystal metal substrates,[12,28,187] but those were all simple oxides of a single metal element. The preparation of atomically smooth single-crystal surfaces of mixed oxides (i.e., with two metal elements) in well-defined composition and a high degree of order is very seldom reported in the literature, and never on samples that would be applicable in our adsorption calorimetry, since preparing such samples is very challenging. Here we prove that we can measure adsorption energies on mixed metal oxide single crystals prepared in a simple new way that offers many exciting new possibilities for surface studies. Lamellar Nb- and Ta-perovskites which can be dispersed in solution as single-crystalline flat sheets which are only one layer thick but extend laterally for long distances (>1 μm).[68-73,188-190] These nanosheets can be deposited in a layer-by-layer fashion on flat substrates using Langmuir-Blodgett (LB) techniques to make a thin, single-crystal mixed-oxide film.[69,71,74-76] Here, we use this method to deposit such perovskite thin films *directly* onto pyroelectric heat detectors, and we perform metal adsorption calorimetry on these films in a similar way as reported for spin-coated films of polymers[97] and drop-cast films of metal–organic frameworks (MOFs),[99] except that those deposited films could not be heated to high temperatures as we do here. We find that this provides excellent signal-to-noise ratio, proving that this method should be broadly applicable. This LB-film method is far

easier than other methods that have been used to prepare clean single-crystal mixed-oxide surfaces, which required much more difficult sample preparations.

Perovskites, with the general formula ABO_3, represents probably the most studied mixed-oxide system in the field of heterogeneous catalysis. They are low-cost and easy to prepare, and show a large variation in their composition and structure, allowing tailoring of their chemical and physical properties to better suit their applications.[66] Unilamellar perovskite nanosheets can be deposited in a layer-by-layer fashion on flat substrates using LB techniques to make thin and well-ordered mixed-oxide films.[69,71,74-76] One of the most interesting of these with respect to use as a catalyst support material, and the one we study here, is the dehydrated form of $HCa_2Nb_3O_{10}(001)$ nanosheet. This dehydrated ('dh") form, which we will refer to below as dh-$HCa_2Nb_3O_{10}(001)$, actually has stoichiometry $Ca_4Nb_6O_{19}$.[168] Each nanosheet of this material consist of three NbO_6 octahedral layers, with Ca^{2+} in the center of the cube formed by Nb^{5+} (see Figure 5.1), and is 1.44–1.46 nm thick (i.e., the sheet-to-sheet repeat distance in the bulk, multilayer solid structure).[96,168,191-193] These and many other perovskites can be synthesized as single- and few-layer nanosheets in solution, with lateral dimensions ranging from several hundred nanometers to a few micrometers.[68-73] The long lateral dimension indicates that these nanosheets have a huge ratio of terrace sites to sheet-edge sites, much larger than the terrace : defect site ratio on the surfaces of single crystal oxides typically studied by surface science methods in recent years. This makes them promising model surfaces with very homogeneous and well-defined surface sites for studying adsorption, for example of metal atoms and nanoparticles if interested in their use as catalyst support materials, as we are here. These nanosheets offer an important advantage not present in normal single crystal surfaces: they can also be prepared as powders that have very high surface-to-volume ratio.[194-198] This means that their surface chemistry can be studied by many

methods not possible on most single crystal surfaces (e.g., volumetric adsorption, transient catalyst kinetics in normal-pressure flow reactors, etc.). It also means that they have many potential applications in real technology (e.g., as industrial catalysts or sorbents).

When used as supports for transition metal or oxide nanoparticles, powders of these dh-$HCa_2Nb_3O_{10}$(001) nanosheets impart unusual stability against sintering to these nanoparticles[170,171] and significantly enhance their catalytic activity for water splitting.[68,199] These layered perovskites are also temperature-stable up to ~825 K in powder form[168] and ~975 K in layered-film form[169] without obvious decomposition, so they hold significant promise as support materials for later transition metal nanoparticle catalysts.

In this work, we combine surface chemistry measurement methods developed for studying metal adsorption and nanoparticle growth on single-crystal oxide surfaces, particularly metal vapor adsorption calorimetry,[28] with this thin-film growth method for preparing much more complex perovskite mixed-oxide surfaces, to investigate the adsorption of Ag atoms on dh-$HCa_2Nb_3O_{10}$(001) nanosheet surfaces. Silver is chosen as the probe metal here because oxide-supported Ag catalysts are extensively used for selective oxidation reactions (e.g., for ethylene,[200] CO,[201] and methane[202] oxidation reactions), and show promise for a variety of other catalytic processes.[203,204] We use atomic force microscopy (AFM) to verify the lamellar sheet-like morphology of the $HCa_2Nb_3O_{10}$ nanosheet films. We report calorimetric measurements of the heat of adsorption and sticking probability of Ag atoms as a function of Ag coverage, which provide the strength of the chemical bonding interactions between Ag atoms and the dh-$HCa_2Nb_3O_{10}$(001) surface. The results show surprisingly strong bonding between Ag and this surface, which explains the unusual stability against sintering of metal and metal oxide nanoparticles when supported on this surface that was previously reported.[170,171] We also elucidate the particle-growth mechanism

and surface morphology of the evolving Ag nanoparticles using low-energy He^+ ion scattering spectroscopy (LEIS). The charge transfer associated with the strong chemical reaction between the Ag atoms and the dh-$HCa_2Nb_3O_{10}$ nanosheets is also elucidated using X-ray photoelectron spectroscopy (XPS).

As far as we know, this is the first adsorption calorimetry of metal gas atoms on any atomically smooth well-ordered *mixed-oxide* surface. The results demonstrate that thin LB films of layered perovskite nanosheets provide a powerful new approach to study surface chemistry on single-crystalline mixed-oxide surfaces.

5.2 EXPERIMENTAL METHODS

The ultrahigh vacuum (UHV) metal adsorption calorimetry apparatus, which also includes capabilities for XPS, LEIS and metal atomic-beam surface scattering, was described previously.[97] The heat detector, the mounting of the surface to be studied, and the way it is heated have been modified as described briefly below, and in more detail in another paper.[157]

Thin $LiTaO_3$ single crystals were used as the pyroelectric heat detectors for adsorption calorimetry. The $LiTaO_3$ heat detectors (purchased from DIAS Infrared GmbH) were 25 μm thick crystals with 12 mm × 12 mm square shape, with both faces pre-coated with 100 nm thick films of a $Ni_{80}Cr_{20}$ alloy which serve as the electrodes for electrical signal measurement. When struck with a pulse of metal vapor from the atomic beam of metal atoms, these detectors generate a charge (and thus transient current through the preamplifier) in response to heat input due to the heat of metal vapor adsorption.

The $HCa_2Nb_3O_{10}$(001) nanosheets whose surfaces we studied here were deposited directly onto these pyroelectric heat detectors used for adsorption calorimetry by Langmuir-Blodgett methods, as described below. In order to heat these niobate nanosheets to high temperatures in

order to dehydrate them (to $Ca_4Nb_6O_{19}$) and remove the hydrocarbon impurities from their surface, a new pyroelectric heat detector was required that could maintain a high pyroelectric heat-signal response after heating to high temperatures. (The heat detector used previously on this apparatus could only be heated up to about 350 K.[59,60,97]) Therefore, we used here $LiTaO_3$ single crystals as the heat detectors. $LiTaO_3$ has a Curie point of 893 K,[58] theoretically allowing samples to be heated up to ~875 K before the heat detector loses its pyroelectric response. Heating these niobate nanosheet coated lithium tantalate crystals ("samples") in UHV required a newly designed sample platen and sample heater, which are described elsewhere.[157] Briefly, the thin samples are heated by radiation from a hot tungsten filament that is placed very near the back side of the sample. The sample is mounted on a platen such that it can be moved to different positions in the UHV chamber depending upon whether it is being studied by surface spectroscopies (XPS, LEIS) or calorimetry, or is being heated for cleaning. When mounted in the calorimetry position, the platen provides electrical contacts between the electrodes on the front and back face of the sample and wires that lead outside the UHV chamber to a preamplifier.

Each heat detector was coated with four layers of $HCa_2Nb_3O_{10}$(001) nanosheets as described above. Five of these "samples" were then mounted onto the new sample platens and stored in the sample preparation chamber with a base pressure of 2×10^{-9} torr. Before the experimental measurements (i.e., sticking probability, differential heat of adsorption, LEIS, and XPS), each sample was transferred to the UHV analysis chamber with a base pressure of 1×10^{-9} mbar and heated at ~725 K for 10 minutes in an oxygen pressure of 2×10^{-7} mbar to dehydrate them and remove the hydrocarbon impurities from the surface. To prevent the heat detector from cracking due to thermal expansion, the temperature was ramped up/down slowly at ~50 degrees per 10 minutes. XPS spectra before and after the heating procedure for the same sample were also

collected and compared to verify the removal of hydrocarbon impurities and the sample integrity (i.e., proper elemental composition not being changed by heating).

Nanosheets of $HCa_2Nb_3O_{10}$(001) were first prepared as described previously.[170] Briefly, $KCa_2Nb_3O_{10}$ was prepared by solid state synthesis of a stoichiometric mixture of K_2CO_3 (40% excess), $CaCO_3$, and Nb_2O_5 at 1200 $^{\circ}$C for 12 h. The protonated form $HCa_2Nb_3O_{10}.0.5H_2O$ was obtained by acid-exchanging the potassium form ($KCa_2Nb_3O_{10}$(001)) with 1 M nitric acid for 3 days with the acid being replaced every day. The protonated form (0.1 g) was exfoliated by stirring in an aqueous solution of tetra(*n*-butylammonium) (TBA) hydroxide (25 mM, 100 mL) for 1 day and the nanosheets were decanted from the unexfoliated sheets after allowing the suspension to settle overnight. These nanosheets were deposited directly onto the pyroelectric heat detector used for adsorption calorimetry as follows. The heat detectors were first cleaned using UV-ozone and then pre-treated with Al Keggin ion[205] to anchor the negatively charged nanosheets. Langmuir-Blodgett deposition was performed by drop casting the nanosheet suspension onto a trough containing the heat detector filled with nanopure water and compressing the barriers to a surface tension of 15 mN/m. The heat detector was then lifted at a speed of 4 mm/min to ensure well-packed nanosheets. The heat detector was dipped into hydrochloric acid (0.1 mM) between each deposition to remove the surface-bound tetra-*n*-butylammonium cations.

Atomic Force Microscopy (AFM) images were acquired in peak-force tapping mode (Bruker Icon) using ScanAsyst-Air probe at a setpoint of 1 nN to verify the packing density of the nanosheets onto the pyroelectric heat detector.

The metal vapor adsorption calorimetry procedure used here has been described previously.[97] The sample platen was placed onto a large Cu thermal reservoir that was electrically connected to a pre-amplifier outside the UHV chamber. A 4.15 mm diameter, collimated atomic

beam of Ag gas atoms was produced by a high temperature effusion cell containing an alumina-lined tungsten crucible filled with Ag granules purchased from Alfa Aesar with 99.9% purity. The Ag beam was chopped into 100 ms pulses containing ~0.013 ML of Ag per pulse, repeating every two seconds. One monolayer (ML) is defined here as 1.38×10^{15} atoms/cm^2, which is the number of Ag surface atoms per unit area on the Ag(111) surface. This Ag atomic beam was then impinged onto the dh-$HCa_2Nb_3O_{10}$(001) surface. The heat released from metal atom adsorption generates a transient temperature rise in the dh-$HCa_2Nb_3O_{10}$ film, which is transferred by thermal diffusion to the $LiTaO_3$ heat detector. The resulting voltage response ("signal") was calibrated by the voltage response to pulses of known energy from stabilized He-Ne laser (632.8 nm wavelength). An average sensitivity of ~650 V/J (volts per joule of heat adsorbed by dh-$HCa_2Nb_3O_{10}$) from three experimental runs was found. The typical operating temperature of the effusion cell was 1375 K, which generates some thermal radiation that impinges on the sample surface. This radiation contribution was also measured by translating a BaF_2 window into the path of the Ag beam, which blocked all the Ag atoms before they impinged onto the sample but passed a known fraction (~94%) of the radiation, which was subtracted from the total measured heat. The radiation contribution typically accounts for ~65% of the total measured heat in the case of Ag adsorption on dh-$HCa_2Nb_3O_{10}$(001). To convert the experimentally measured internal energy changes into the standard enthalpy changes at the sample temperature (300 K), the excess translational energy of the metal gas atoms at the effusion cell temperature above that for a 300 K Maxwell-Boltzmann distribution was subtracted, and a small pressure-volume work term (RT) was added, as described elsewhere.[60]

The incident Ag beam flux was measured using a quartz crystal microbalance (QCM, Inficon). The sticking probability of Ag adsorption on dh-$HCa_2Nb_3O_{10}$(001) was measured by a

modified King-Wells method,[60,97,206] which uses a line-of-sight quadrupole mass spectrometer (QMS, UTI 100C) to measure the fraction of Ag atoms that strike the surface, but do not adsorb. This "non-sticking" signal was calibrated by a "zero-sticking" reference provided by measuring the integrated desorption signal of a known amount of multilayer Ag atoms on a hot Ta foil. A -500 V bias voltage was applied between the sample and the QMS to avoid electron damage to the dh-$HCa_2Nb_3O_{10}$ nanosheets.

The UHV analysis chamber is also equipped with a hemispherical electron energy analyzer (Leybold-Heraeus EA 11/100), ion gun (Leybold-Heraeus IQE 12/38), and Mg/Al Kα dual anode X-ray source (VG Scienta XR3E2) for low-energy He^+ ion scattering spectroscopy (LEIS) and X-ray photoelectron spectroscopy (XPS). The growth of Ag on dh-$HCa_2Nb_3O_{10}$(001) was studied by LEIS using He^+ ions with 1.00 keV primary energy. The sample was positioned perpendicular to the energy analyzer axis, and the ion beam was directed at 45° with respect to the surface normal. Ion fluxes were typically 15 nA/cm^2, and the sample was exposed to the He^+ ions only during spectrum acquisition. Each deposition of Ag atoms followed previous depositions consecutively, starting with a sample that had no adsorbed Ag atoms on its surface. All XPS spectra were collected using Al Kα ($h\upsilon$ = 1486.6 eV, 130 W) as the excitation source, with detection of photoelectrons normal to the surface. Each spectrum was fitted with the product of a Gaussian and Lorentzian function after subtraction of a Shirley baseline. The overlapping Ag 3d doublets and Nb 2p doublets were deconvoluted by fixing the peak splits of both doublets at values taken from Wagner et al.[149] The binding energy (BE) scale of the analyzer was calibrated to the expected BE of the Ag $3d_{5/2}$ peak for Ag(s) (367.9 eV),[149] as measured here for thick (6.8 ML) Ag films. All experiments were performed at 300 K.

5.3 RESULTS AND DISCUSSION

5.3.1 *Surface Structure and Morphology of $HCa_2Nb_3O_{10}$(001) Nanosheet Films*

Figure 5.1 shows polyhedral representations of $HCa_2Nb_3O_{10}$ structure in the [001] and [010] directions. The structural parameters used to draw this structure are from Chen et al.[96] The $HCa_2Nb_3O_{10}$(001) surface is O/OH-terminated with H atoms on every other O atom. Based on the structural optimization calculations done by Janik and co-workers,[171] there are three possible surface binding sites for metal atoms, all shown in Figure 5.1: (1) axial oxygen (AO), (2) equatorial oxygen (EO), and (3) interstitial space (IS) between NbO_6 polyhedra.

We deposited four layers of $HCa_2Nb_3O_{10}$(001) nanosheets on each $LiTaO_3$ heat detector. The sheet-like morphology of deposited $HCa_2Nb_3O_{10}$ nanosheets was confirmed by the sectional analysis of AFM images (Figure 5.2 top). The heat detectors were well covered, with a surface coverage of >95% and negligible nanosheet overlap. The deposited nanosheets were flat with an average lateral dimension of a few microns. The thickness of individual un-dehydrated $HCa_2Nb_3O_{10}$ nanosheets estimated from the c-axis lattice parameter measured from crystallographic data of the bulk 3D solid is ~1.44 nm.[168] Our AFM height profile of the as-deposited film (Figure 5.2 bottom) shows an overestimated thickness of 3.18 nm possibly due to (1) absorbed H_2O and hydrocarbon molecules in the interlayer space, (2) increased surface roughness of individual nanosheets and multilayers of nanosheets not being perfectly packed, and/or (3) systematic errors[207] in AFM height profile measurements. The overall thickness of the deposited nanosheet films indicate that these films show bulk-like characteristics with no or negligible film-thickness effects which have been reported previously for metals on oxide thin films, when the oxide film thickness drops to ∼1 nm.[180,208,209]

5.3.2 *$HCa_2Nb_3O_{10}$ Films before and after Heating*

These $HCa_2Nb_3O_{10}(001)$ nanosheet films were cleaned and dehydrated by heating to ~725 K in vacuum before use in studying Ag adsorption. These films are known to dehydrate upon heating at ~575K to form $Ca_4Nb_6O_{19}$ (i.e., 2 $HCa_2Nb_3O_{10}$ → $Ca_4Nb_6O_{19}$ + $H_2O(g)$).[168] The structure is still quite similar to Figure 5.1,[168] but all the H is removed (from the nanosheet's surface hydroxyl groups) and one surface O atom is removed for every two such H atoms. The Nb bonds to the lost O atom are replaced by Nb bonds to a surface O atom of the neighboring nanosheet, thereby linking together the parallel nanosheets (see Figure 5 in ref. [168]). This decreases the c-axis lattice parameter (nanosheet-to-nanosheet separation) slightly, to ~1.31 nm.[168] We refer to this dehydrated form as dh-$HCa_2Nb_3O_{10}(001)$ below. To produce this dehydrated calcium niobate, each sample was heated to ~725 K at a rate of 50 degrees per 10 minutes in an O_2 pressure of 2×10^{-7} mbar, and held there for 10 minutes. The sample was then cooled with the same rate in this same O_2 pressure. The heating/cooling rates were slow because faster rates sometimes caused the $LiTaO_3$ crystals to crack.

Figure 5.3 shows XPS spectra measured before and after the heating procedure for the 4-layer thick nanosheet films. On the broad scan spectrum (Figure 5.3a), the major photoelectron peaks for niobium, calcium, oxygen, carbon, and an oxygen Auger peak are labeled. Before the sample was heated, the ratio of the integrated XPS peak intensities gives atomic ratios of Ca:Nb:O = 1.00:1.6:10.5 and C:Nb = 5.1:1 using the atomic sensitivity factors taken from Wagner et al.,[149] and assuming a homogeneous distribution of elements within the total depth seen by XPS. The atomic concentrations of oxygen and carbon indicate the sample contains a significant amount of organics (CH_x, C-O, COOH).

After the sample was heated to a high temperature, the C concentration dropped markedly as shown in Figure 5.3a, with the ratio of C:Nb decreasing by seven-fold, to 0.71:1. The atomic

ratio of Ca:Nb:O also changed to 1.00:1.5:4.7, which is very close to that expected based on the bulk chemical formula, $Ca_4Nb_6O_{19}$. The comparison of O 1s, Nb 3d, and Ca 2p core level spectra before and after the heating procedure is also shown in Figure 5.3. Besides a small shift (~0.2 eV) to lower binding energy, there is no broadening or lineshape change for the Nb 3d and Ca 2p peaks, which indicates no or negligible oxidation state change for the two elements. The change for O 1s is however significant. The O 1s spectrum measured before the sample was heated is much broader, with a shoulder peak above 532 eV BE, while the O 1s spectrum measured after the sample was heated shows a much more symmetric lineshape. We attribute the change of the O 1s spectrum to the removal of adsorbed molecules containing O, which is also consistent with the decrease of relative atomic concentration of oxygen. (The O(1s) BE range for the part that was removed is consistent with C-O and COOH functionalities.[149,176]) Previously, it has been shown that hydrocarbon impurities could be removed from perovskite-type $SrRuO_3$ films after annealing to above 575 K in high oxygen pressure conditions.[210]

5.3.3 *Sticking Probability of Ag on dh-$HCa_2Nb_3O_{10}$(001)*

The amount of Ag atoms that chemically adsorb on the dh-$HCa_2Nb_3O_{10}$(001) surface must be known to determine the true Ag coverage and to convert heats of adsorption measured by calorimetry into units of kJ per mole adsorbed. Figure 5.4 shows the sticking probability of Ag atoms on dh-$HCa_2Nb_3O_{10}$(001) surface at 300 K as a function of Ag coverage. One Ag monolayer (ML) is defined throughout as 1.38×10^{15} atoms/cm^2, the number of Ag surface atoms per unit area on Ag(111) surface. In the limit of zero coverage, the sticking probability of Ag on $HCa_2Nb_3O_{10}$ is 0.955 and increases rapidly to 0.98 at 1 ML coverage. The sticking probability increases slowly towards unity at higher coverages. This is expected, since multilayer Ag films are known to have near unit sticking probability for Ag at 300 K.[13,180,181]

5.3.4 *LEIS Study of the Ag Film Morphology on dh-$HCa_2Nb_3O_{10}$(001)*

The method used here to detect the morphology and growth mode of the Ag film (such as the average thickness and number density of growing nanoparticles) is based on measurements of the intensities of He^+ LEIS peaks associated with the substrate and the Ag metal itself, which essentially provides quantitative elemental analysis of the topmost atomic layer of the solid.[13,142,143,180] Here, we used He^+ LEIS at a primary energy of 1 keV.

Figure 5.5a shows the LEIS spectra for the starting dh-$HCa_2Nb_3O_{10}$(001) surface (red dots) and for 1.1 ML adsorbed Ag (blue dots) at 300 K. For the starting dh-$HCa_2Nb_3O_{10}$(001) surface, only an oxygen peak at ~420 eV kinetic energy was detected above the baseline because the surface is O-terminated. (Hydrogen is too light to detect in LEIS.) After Ag was deposited on the surface, the intensity of oxygen peak decreased and a silver peak at ~860 eV kinetic energy appeared. Figure 5.5b shows the evolution of the integrated Ag and O LEIS intensities (normalized with respect to that from high Ag coverages and the starting dh-$HCa_2Nb_3O_{10}$(001) surface, respectively) as a function of Ag coverage on dh-$HCa_2Nb_3O_{10}$(001) surface at 300 K. This provides a *direct* measure of the fraction of the dh-$HCa_2Nb_3O_{10}$(001) surface covered by Ag particles (even if they are only one atom thick) because the He^+ ions are neutralized with essentially unit probability when they penetrate the electron density of a solid by an amount deeper than a small fraction of an atom, and are thus not detected as LEIS signal.[142] As seen in Figure 5.5b, the normalized LEIS intensities for both Ag and O change more slowly with Ag coverage than predicted by a layer-by-layer growth model on a flat substrate (shown by the dashed black line for Ag). Note that the blue and red dashed lines in Figure 5.5b are not best fits to the Ag and O LEIS signals, but just used to guide the reader's eye.

We tried to fit these LEIS signals using the hemispherical cap model first introduced by Diebold et al.,[211] which assumes that all the nanoparticles have hemispherical cap shape and the

same diameter at any coverage (which increases with coverage) and the same number density at all coverages, but as refined by Campbell's group.[143] This model cannot fit the data well. Specifically, it predicts that the LEIS signal for the metal would increase proportionally to the 2/3 power of the metal coverage up to ~35% of the surface being covered[143] whereas the Ag signal in Figure 5.5b increases linearly instead (as show better in expanded scale in Figure 5.6). The normalized Ag LEIS signal was fitted linearly with a slope of 0.41 in the first ML in Figure 5.6. The Ag layer-by-layer growth model in the first ML has a slope of 1. If Ag grew perfectly as flat 2-dimensional (2D) islands that are two atomic layers thick, with each layer having a packing density the same as our definition of 1 ML (i.e., the same as for bulk Ag(111)), one would expect a linear LEIS signal increase with a slope of 0.50, similar to what is observed. The straight-line fits in Figure 5.6 indicate that, on dh-$HCa_2Nb_3O_{10}$(001) at 300 K, Ag grows as flat 2D islands which are between 2 and 3 Ag layers thick until these cover ~50% of the surface. Above 1.5 ML, the Ag LEIS signal starts to curve down and no longer follows the linear fit. This indicates that, above 1.5 ML, Ag mostly adds on top of existing Ag islands to form 3D particles, but also adding (more slowly) to their edges, eventually making a continuous 3D Ag film.

To further prove that the 2D islands are two to three Ag layers thick at low coverages, we calculated the average Ag particle thickness versus coverage from these Ag LEIS data (i.e., by dividing the Ag coverage in ML by the fraction of the surface covered by Ag particles from LEIS). The resulting island thickness as a function of Ag coverage at 300 K is shown in Figure 5.7. The inset shows a close-up of the low Ag coverage region. Below 1.5ML coverage, the average Ag particle thickness increases slowly from 1.9 to 2.6 ML. Above 1.5 ML, the average Ag particle thickness increases faster, reaching 6.8 ML by 7 ML coverage when a continuous film first forms.

5.3.5 *Heat of Adsorption of Ag Vapor on dh-$HCa_2Nb_3O_{10}$(001)*

Figure 5.8 shows the differential heat of adsorption of Ag on dh-$HCa_2Nb_3O_{10}$(001) surface as a function of Ag coverage at 300 K, averaged over three experimental runs. We normalized the three runs individually by adjusting the absolute optical reflectivity of the starting surface (used in the heat signal calibration with heat from a He-Ne laser at 632 nm) to set the heat of adsorption at high coverages (>4 ML) equal to the known heat of sublimation of bulk Ag(s) (285 kJ/mol[61]). When individually normalized in this way, the three runs all showed the same coverage dependences of heats.

In Figure 5.8, Ag coverage was separated by two gray dashed lines into two regions corresponding to different adsorption behavior. In Region 1, the heat of adsorption is initially ~303 kJ/mol and increases slowly to ~338 kJ/mol by 0.8 ML. We attribute this initial rise to an increase in the average size (lateral dimension or effective diameter) of the Ag 2D islands (which were shown by LEIS above to have a nearly constant thickness of 2-3 atomic layers in this coverage range, increasing slightly with coverage). This increase in size results in an increase in the average number of Ag−Ag nearest-neighbor bonds formed per added Ag atom.[181] Above 0.8 ML, the heat decreases exponentially towards the heat of sublimation of bulk Ag (285 kJ/mol[61]) by 4.5 ML (see Region 2). We attribute this slow drop to the simple kinetic competition between Ag atoms which adsorb in a structure similar to that seen at ~0.6 to 0.8 ML (i.e., at the edges of large 2D islands of Ag that are 2-3 atoms thick with a heat near 338 kJ/mol) or in a structure more similar to adsorbing on top of a thick 3D film (i.e., on top of large 2D (and later, 3D) islands of Ag with a heat near 285 kJ/mol). As the coverage increases, the Ag atoms will naturally have a greater and greater probability to adsorb in the 2nd type structure, so the heat decreases asymptotically to 285 kJ/mol. The integral (i.e., coverage-averaged) heat of adsorption in the first ML is 320. kJ/mol.

The heats of adsorption of Ag atoms have been measured on MgO(100) and on reducible oxide surfaces (e.g., CeO_{2-x}(111) and Fe_3O_4(111)) previously.[13,180,181] For comparison, the initial heats of Ag adsorption were 176 kJ/mol, 200. kJ/mol, 220. kJ/mol, and 230. kJ/mol on MgO(100), $CeO_{1.9}$(111), $CeO_{1.8}$(111), and Fe_3O_4(111), respectively.[13,180,181] The much stronger binding strength of Ag atoms seen here on dh-$HCa_2Nb_3O_{10}$(001) surface (303 kJ/mol) indicates that this mixed-oxide support stablizes Ag nanoparticles better than those simple oxide supports. Strong interficial interactions between late transition metal/metal oxide nanoparticles and the layered dh-$HCa_2Nb_3O_{10}$(001) nanosheets have also been found by liquid-phase isothermal titration calorimetry (ITC), electron microscopy and density functional theory (DFT) calculations, showing that nanoparticles on supports with exothermic heats of interaction were stabilized against sintering.[170,171] Our high heats of adsorption at low coverages measured in UHV agrees with these findings.

5.3.6 *Chemical Reaction between Ag Atoms and dh-$HCa_2Nb_3O_{10}$(001)*

Figure 5.9 shows the XPS spectra and peak fits of Ag 3d for the adsorbed Ag nanoparticles and O 1s, Nb 3d, Ca 2p in the dh-$HCa_2Nb_3O_{10}$ support at 0 ML and 1.1 ML Ag coverages. Each peak was fitted with the product of a Gaussian and Lorentzian function after subtraction of a Shirley baseline.[174,175] The overlapping Ag 3d doublets (blue dots) and Nb 2p doublets (red dots) were deconvoluted in Figure 5.9a. No noticeable change in lineshape was detected for Nb 3d and Ca 2p peaks after Ag deposition, but they all shifted to higher binding energies (BE) by 0.3 to 0.4 eV (see Figure 5.10 below). For O 1s, a second peak at ~2 eV higher BE appeared after Ag was deposited on the surface. This Ag-induced component is labeled as O^2, and the original and main O 1s component at a lower BE is labeled as O^1.

Figure 5.10 shows the core-electron XPS BE shifts for Ag and for all the elements in the dh-$HCa_2Nb_3O_{10}$ support as a function of Ag coverage at 300 K. The BE shift of O 1s in Figure 5.10b is represented by the BE shift of the O 1s peak's centroid or "center line" (the integrated area is the same on both sides of the line). The BE of Ag $3d_{5/2}$ starts high after the first Ag dose (0.18 ML), but drops rapidly by 0.35 eV after the second Ag dose (0.36 ML), and then stays nearly constant at higher coverages, eventually decreasing slightly to reach the BE of 367.9 eV expected for bulk Ag(s)[149] at 6.8 ML. The high Ag BE at the lowest coverage is attributed mainly to electron transfer from Ag to the dh-$HCa_2Nb_3O_{10}$ support at very low coverage, which causes the Ag to be partially positively charged (i.e., higher XPS BE than at higher coverages where Ag becomes bulk-like). Janik and co-workers also discovered from DFT calculations and Bader charge analysis that for all the adsorbed transition metals they studied, there was significant transfer of electron density from the metal atoms to the $HCa_2Nb_3O_{10}$(001) support, with the metal adatom having a charge of +0.68 in the case of Ag,[171] consistent with our observation. As seen here, the Ag stops donating electrons to the oxide support at higher coverages, so the Ag BE stabilizes. The XPS BEs of metal nanoparticles (even when neutral) shift weakly to higher BE with decreasing particle size since there is less final-state relaxation of the core hole via screening by conduction electrons in smaller particles than in bulk metal.[25,212,213] (The strength of the screening increases with metal coverage or particle size.) This effect may be responsible for the small Ag BE shifts at higher coverages here.

The core-level BEs for all the support elements (and the residual C impurity) shift by ~0.3 eV to higher BE with the first Ag dose (Figure 5.10). As noted above, this Ag has significant positive charge. These uniform shifts of the support elements' XPS peaks indicate that at least some of the electron density from this $Ag^{\delta+}$ transfers deeper into the sample than the XPS probe

depth. This gives rise to a band-bending like effect, where all the atoms within the XPS probe depth feel this positive charge (of $Ag^{\delta+}$s nearby), and so all their electrons get stabilized, shifting to higher BEs by the same ~0.3 eV. This same effect has frequently been seen upon metal adsorption on thick semiconducting oxide crystals, where the electron donated from the metal is delocalized deep into the bulk of the oxide, so that the surface atoms of the oxide feel the nearby metal atom's positive charge and shift to higher BE upon metal adsorption.[25] After that first Ag dose, the new Ag is neutral, and the effect stops, so the BEs of the support elements nearly stabilize (increasing only slightly, by an additional ~0.1 eV for Nb and Ca, and ~0.2 eV for O). The O^2 component of the O 1s peak appeared after the first Ag dose (0.18 ML), and since it is ~2 eV higher in BE than the main peak, it dominates the overall shift of the O 1s centroid.

Figure 5.11 shows the XPS intensity of the O^2 component of the O 1s peak normalized to the total O 1s intensity of the Ag-free starting surface. As seen, the O^2 intensity almost plateaus already after the first dose of Ag (0.18 ML), just as the electron transfer from Ag to the support occurs mainly from the Ag in this first 0.18 ML, where the Ag takes the form of $Ag^{\delta+}$. This indicates that the O^2 atoms are those that are closest to this $Ag^{\delta+}$. This raises the question: How deeply are we measuring this O^2 component? The mean free path of the O 1s electrons at their kinetic energy measured here is estimated to be 1.67 nm based on Eq. 5 in ref. [214]. Since detection is normal to the surface, this equals the O 1s probe depth. There are ~8 layers of O atoms within this depth of the dh-$HCa_2Nb_3O_{10}$(001) surface (see Figure 5.1). The large contribution from the O^2 component (~16% after 0.18 ML) suggests that both of the first two layers of O atoms must be included in this component, since the first O layer includes only ~9% of the O atoms in this probe depth. The first two O layers hold 27%, since there are twice as many O atoms in the second layer. The observed 16% contribution from the O^2 component suggests that it corresponds to all the O

atoms in the first O layer and roughly half of those in the second layer. At the Ag coverage of 0.18 ML, this corresponds to roughly five O^2-type O atoms created for every $Ag^{\delta+}$ atom. An idealized c(2×2)-Ag overlayer on dh-$HCa_2Nb_3O_{10}$(001) (which corresponds to a similar coverage of 0.24 ML), would have one $Ag^{\delta+}$ for every two surface O atoms. It appears that both of these two surface oxygen atoms *plus* the two or three nearest O atoms in the second layer would need to have O 1s binding energies strongly affected by each $Ag^{\delta+}$ to explain the large XPS signal from this O^2 component. This does not seem unreasonable.

5.3.7 *Adhesion Energy and Sinter Resistance for Ag Adsorption on dh-$HCa_2Nb_3O_{10}$(001)*

The connection between adsorption and adhesion energies has been discussed in detail elsewhere[25,181] and their mathematical relationship is represented by:[181]

$$\sum_n \Delta H_{ads} = -n \cdot \Delta H_{sub} + (1 + f_r) \cdot A \cdot \gamma_{v/m} - A \cdot E_{adh} \quad (5.1)$$

where $\sum_n \Delta H_{ads}$ is the sum of adsorption enthalpies over n metal adatoms, ΔH_{sub} is the metal's bulk sublimation enthalpy, A is the area covered by the metal particles, f_r is the roughness factor to account for the surface roughness of the metal particles, $\gamma_{v/m}$ is the surface energy of the bulk metal solid ($\gamma_{v/m}$ is 1.22 J/m^2 for bulk Ag[12,13,181,215]), and E_{adh} is the metal's adhesion energy to the support. Our LEIS results show that Ag grows as 2D islands that cover most of the surface before thickening, and that ~96% of the surface is covered by Ag already by 4.4 ML. This indicates that the surface is very smooth at 4.5 ML, so we will assume f_r is 1.00 here.

To estimate the adhesion energy for Ag adsorption on dh-$HCa_2Nb_3O_{10}$(001) using Eq. $\sum_n \Delta H_{ads} = -n \cdot \Delta H_{sub} + (1 + f_r) \cdot A \cdot \gamma_{v/m} - A \cdot E_{adh}$ (5.1, we must integrate the heat of adsorption versus coverage up to a coverage where ΔH_{ads} is no longer different from ΔH_{sub}.[60] Using the data from Figure 5.8 and integrating up to 4.5 ML, the adhesion energy for Ag

adsorption on dh-$HCa_2Nb_3O_{10}$(001) is estimated to be 4.33 J/m^2. This is larger than twice the surface energy of Ag (2 × 1.22 J/m^2), which means that Ag wets this surface at equilibrium.[25]

For comparison, Ag growth on MgO(100), $CeO_{1.9}$(111), and Fe_3O_4(111) at 300 K give number densities of 2.5 × 10^{12}, 4.0 × 10^{12} and 4.0 × 10^{12} particles/cm^2 and adhesion energies of 0.3 ± 0.3, 2.3 ± 0.3 and 2.5 ± 0.3 J/m^2, respectively.[13,180,181,215] The higher adhesion energy of Ag to dh-$HCa_2Nb_3O_{10}$(001) indicates a very strong interaction between Ag(s) and the dh-$HCa_2Nb_3O_{10}$(001) surface.

This large adhesion energy of Ag to this Ca niobate(001) surface helps explain the stablization of Rh nanoparticles against sintering reported on this same Ca niobate support.[170] While Ag and Rh are different, we have found that the adhesion energies of late transition metals to a given oxide support surface strongly correlate with each other, and that when one such metal element has a higher adhesion energy to one given oxide surface compared to another, so too do all the late transition metals.[216] As we have also shown, the higher is E_{adh}, the lower is the metal atom's chemical potential at a given particle size, and the slower is the sintering rate.[216] This is qualitatively consistent with the earlier explanation for this unusually strong sinter-resistance imparted by this Ca niobate support based on solution-phase adsorption calorimetry and DFT calculations.[170,171] We can use the adhesion energy correlation mentioned above together with the value measured here for Ag on this Ca niobate(001) surface (4.33 J/m^2) to predict E_{adh} for other late transion metals to this mixed oxide surface. That correlation showed that E_{adh} increases linearly with $[(\Delta H_{sub,M} - \Delta H_{f,MOx})/N_A]/\Omega_M^{2/3}$, which is a measure of the oxophilicity of the metal element, per unit surface area.[216] Here, $\Delta H_{sub,M}$ is the bulk heat of sublimation of the metal M, $\Delta H_{f,MOx}$ is the heat of formation of its most stable bulk oxide (per mole of metal atoms), and Ω_M is the volume per atom in the bulk metal, so that $\Omega_M^{2/3}$ provides an estimate of the area per metal atom at the

interface. The slope is 0.146 for the two oxides that have been studied, and this x-axis value (oxophilicity per area) for Ag is 7.5 J/m^2.[216] For Rh, this x value is 23 J/m^2. Assuming the same slope as found for the other oxides, this correlation can be extrapolated from this E_{adh} value for Ag (4.33 J/m^2) to predict that E_{adh} equals ~6.6 J/ m^2 for Rh to this Ca niobate(001) surface. This is larger than twice the surface energy of Rh (2 × 2.33 J/m^2), which means that Rh is also predicted to wet this surface at equilibrium. (The surface energy of Rh used here is from ref. [217].)

5.4 CONCLUSIONS

Unilamellar $HCa_2Nb_3O_{10}$ nanosheets were easily deposited onto a $LiTaO_3$ heat detector as single-crystalline thin films using LB techniques. The AFM images show that these nanosheets are flat and have an average lateral dimension larger than 1 micron (the ratio of terrace to sheet-edge sites is huge). To obtain a relatively clean, dehydrated $HCa_2Nb_3O_{10}$(001) surface, the nanosheets were first heated to 725 K in a low oxygen pressure. These results demonstrate for the first time a new and easy way to apply surface science techniques derived for simple single-crystal surfaces to the complex surfaces of mixed oxides, using LB-deposited perovskite nanosheets. The He^+ LEIS and adsorption calorimetry results show that Ag grows on the dh-$HCa_2Nb_3O_{10}$(001) surface as 2D islands that are mostly two layers and some three layers thick with a coverage-averaged heat of adsorption of ~320 kJ/mol in the first monolayer. As the Ag coverage increases, Ag atoms add on top of the 2D islands, making 3D nanoparticles and eventually a continuous 3D film, with the heat of adsorption reaching the sublimation enthalpy of bulk Ag(s), 285 kJ/mol. A very high adhesion energy of Ag(s) to dh-$HCa_2Nb_3O_{10}$(001) of 4.33 J/m^2 is estimated from the heats of adsorption, and explains why this dh-$HCa_2Nb_3O_{10}$ support imparts unusual stability against sintering to transition metal nanoparticles. At very low coverages, Ag is in the form of $Ag^{\delta+}$, which causes a ~2 eV shift to higher binding energy of the O 1s XPS peaks of nearby O atoms in the first two

layers of the dh-$HCa_2Nb_3O_{10}$(001) support. Some of the electron density from this $Ag^{\delta+}$ transfers deeper into the sample than the XPS probe depth, causing an ~0.3 eV band-bending seen in all the support elements' core levels. Above 0.18 ML, Ag adsorbs in neutral form.

5.5 FIGURES

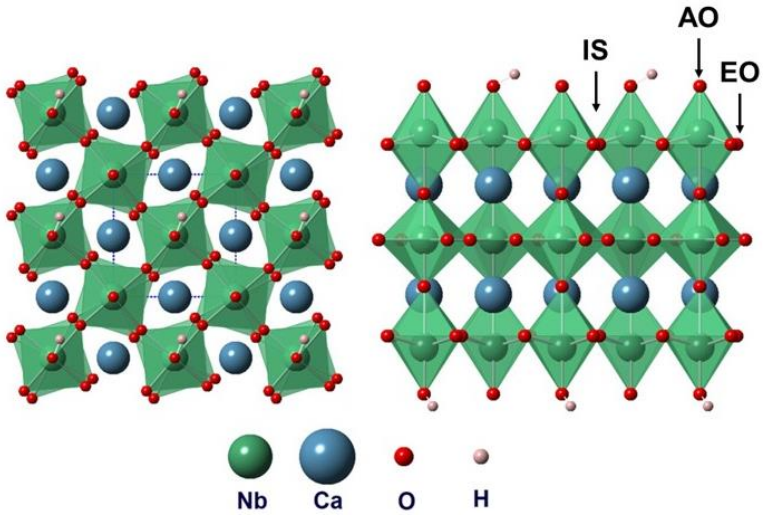

Figure 5.1. Polyhedral representations of the $HCa_2Nb_3O_{10}$ nanosheet structure, viewed from the [001] (left) and [010] (right) directions. The structure at left is the top view of the (001) surface being studied here. The dashed blue line indicates the unit cell. There are 6.74×10^{14} O atoms/cm^2 on this (001) surface, half of which are in the surface OH groups. All of these H atoms, and one O atom for every two such H atoms in this structure, is removed upon dehydration to produce the dehydrated (dh) form studied here (see text). The right structure shows one complete 'layer' of the nanosheet, which has a thickness (or repeat distance in the 3D bulk) of 1.44 nm (1.31 nm after dehydration). Labels indicate AO: axial oxygen, EO: equatorial oxygen, IS: interstitial space.

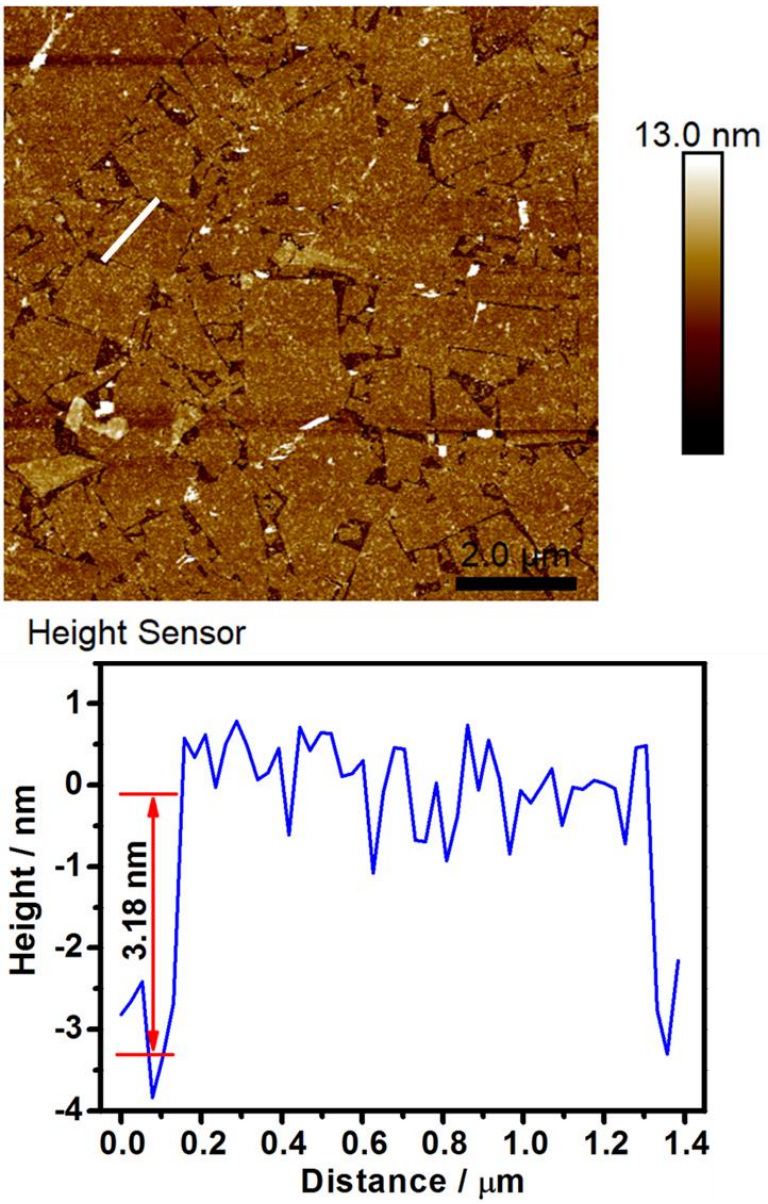

Figure 5.2. AFM image (top) of 4 layers of $HCa_2Nb_3O_{10}$(001) nanosheets deposited on a $LiTaO_3$ heat detector and height profile (bottom) across a single nanosheet along the white solid line in the image.

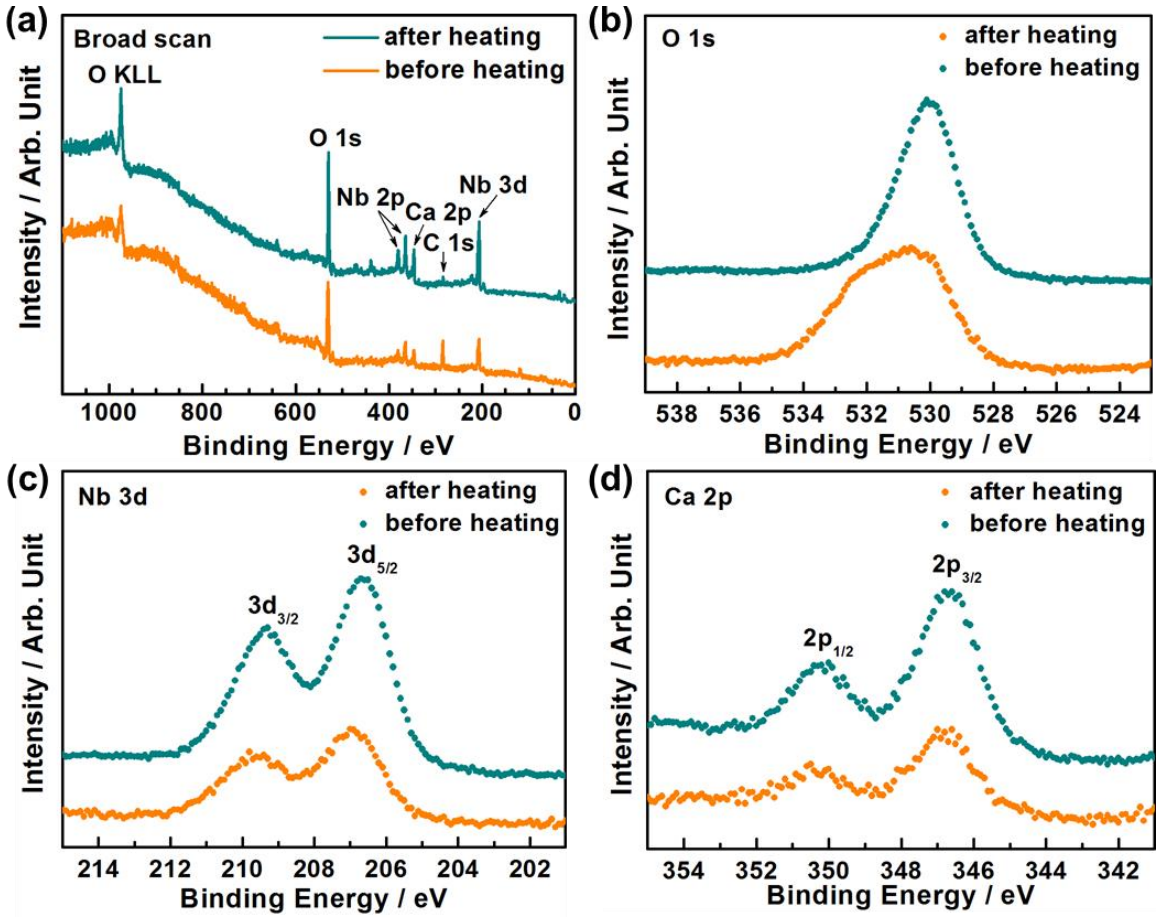

Figure 5.3. XPS spectra of 4 layers of $HCa_2Nb_3O_{10}$(001) nanosheets deposited on $LiTaO_3$ heat detectors before (orange) and after (dark cyan) heating to ~725 K, which produces its dehydrated form: (a) broad scan, (b) O 1s, (c) Nb 3d, and (d) Ca 2p. The orange spectra measured before the sample being heated have been normalized so that the average broad scan intensity at 1050–1100 eV before heating matches that after heating.

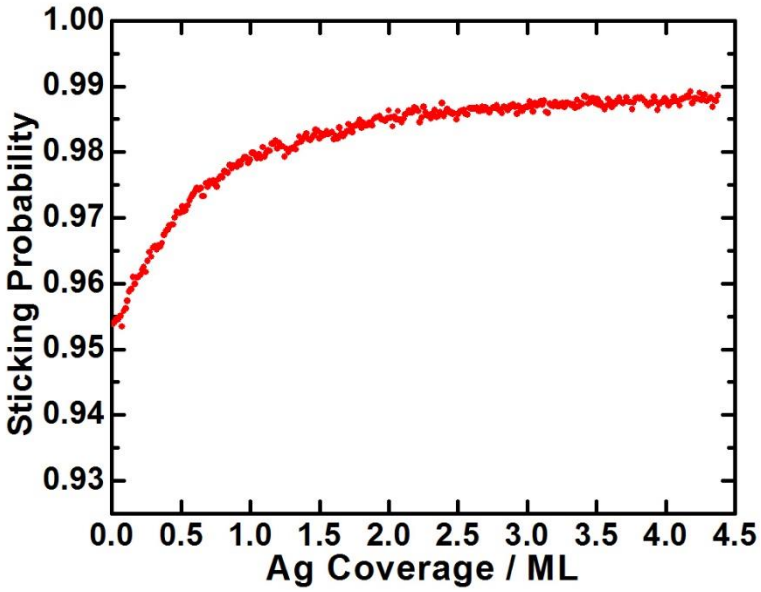

Figure 5.4. Sticking probability of Ag atoms on dh-$HCa_2Nb_3O_{10}$(001) surface (heated at ~725 K for 10 minutes in an oxygen pressure of 2×10^{-7} mbar) as a function of Ag coverage at 300 K. Each data point represents a pulse of ~0.013 ML. One ML is defined as the atom density of Ag(111), which is 2.05 times the number of O atoms per area on the dh-$HCa_2Nb_3O_{10}$(001) surface.

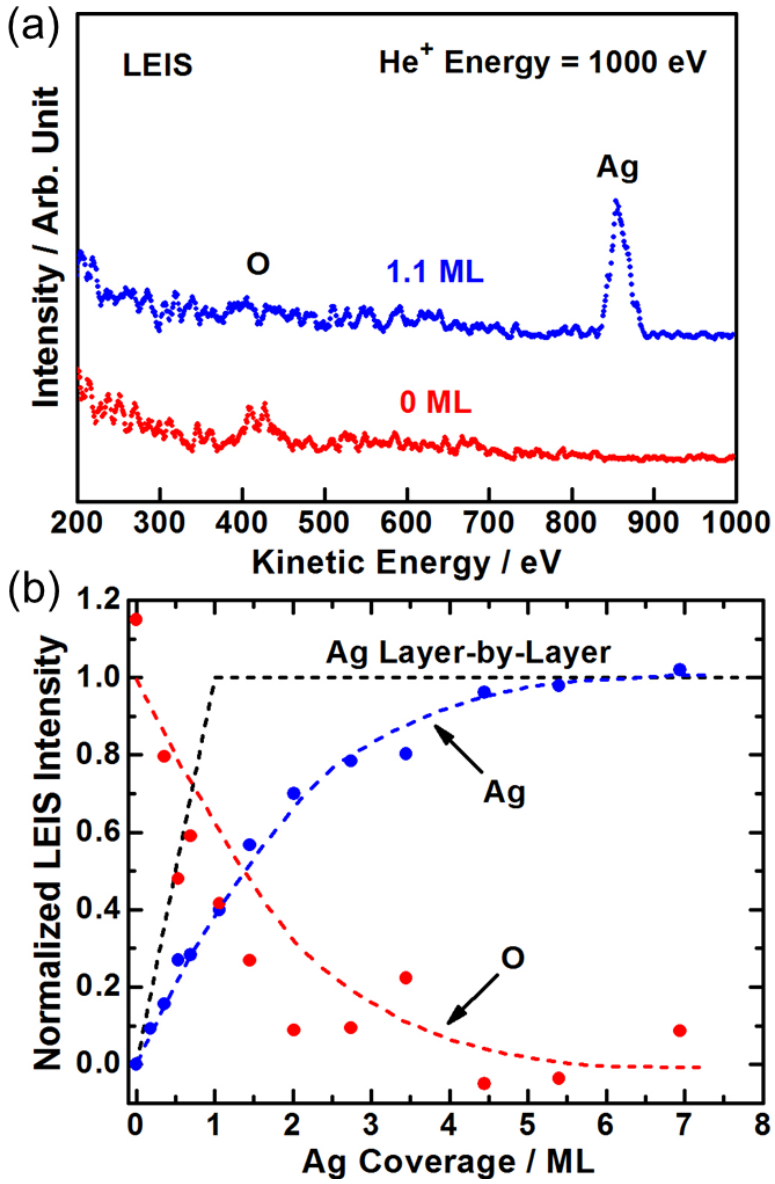

Figure 5.5. (a) He^+ LEIS spectra (at a primary energy of 1 keV) for the starting dh-$HCa_2Nb_3O_{10}$(001) surface (red dots) and for 1.1 ML adsorbed Ag (blue dots) at 300 K. (b) Integrated Ag (blue dots) and O (red dots) LEIS intensities as a function of Ag coverage at 300 K on dh-$HCa_2Nb_3O_{10}$(001) surface (heated at ~725 K for 10 minutes in an oxygen pressure of 2×10^{-7} mbar). Ag and O peak intensities were normalized with respect to that from high Ag coverages and the starting dh-$HCa_2Nb_3O_{10}$(001) surface, respectively. The black dashed lines correspond to the normalized LEIS intensities that would be observed if Ag grew in a layer-by-layer fashion on a flat substrate. Note that the blue and red dashed curves are only to guide the reader's eye.

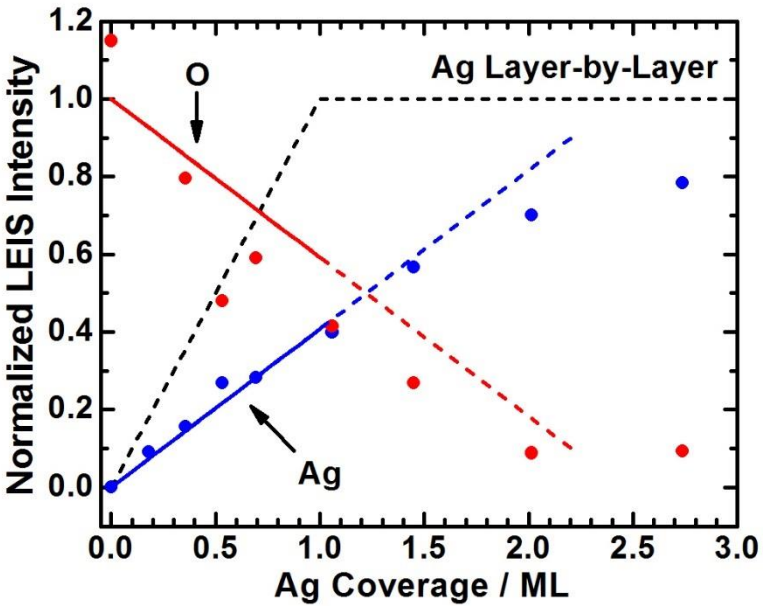

Figure 5.6. Integrated Ag (blue dots) and O (red dots) LEIS intensities versus Ag coverage up to 3 ML from Figure 5.5b. The blue solid line is a linear fit with a slope of 0.41 for the Ag LEIS signal up to 1 ML Ag coverage, above which the Ag LEIS signal starts to curve down so the blue dashed line after that is only a guide to the eye. The red line does not represent a best fit for the O LEIS signal but mirrors the blue line with respect to the normalized LEIS intensity at 50%. The black dashed lines correspond to the normalized LEIS intensities that would be observed if Ag grew in a layer-by-layer fashion on a flat substrate.

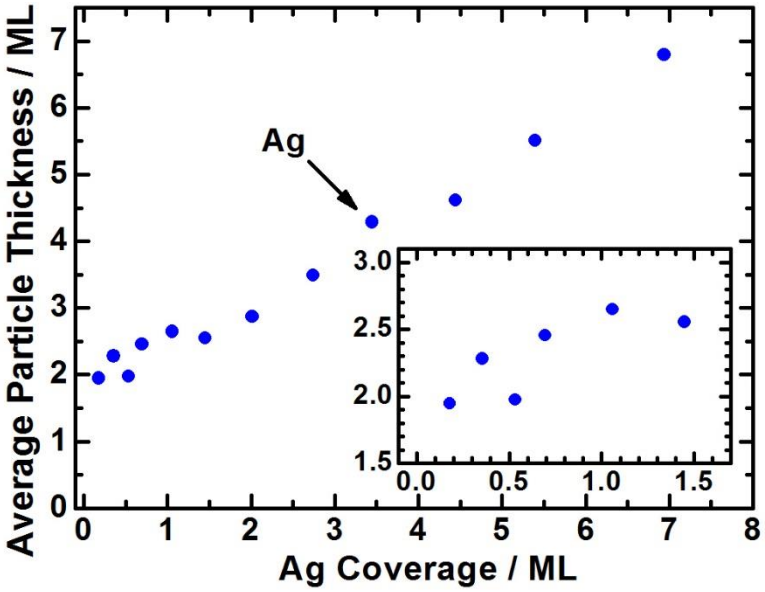

Figure 5.7. Average Ag nanoparticle thickness (as measured by LEIS) as a function of Ag coverage at 300 K. The inset shows a close-up of the low-coverage region. The thickness of 1 ML is 2.36 nm, the layer-to-layer separation between Ag(111) layers

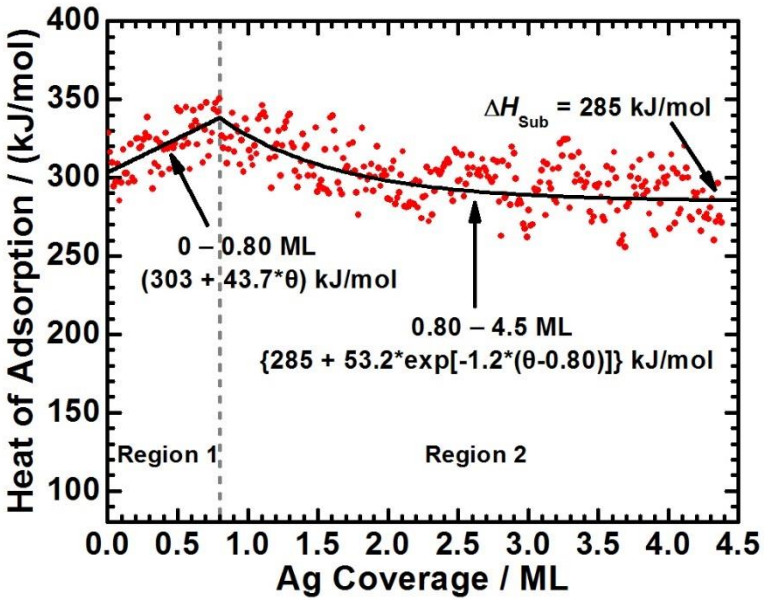

Figure 5.8. Differential heat of adsorption of Ag atoms on dh-$HCa_2Nb_3O_{10}$(001) surface (heated at ~725 K for 10 minutes in an oxygen pressure of 2×10^{-7} mbar) as a function of Ag coverage at 300 K. Ag coverage is separated by a gray dashed line into 2 regions, corresponding to different adsorption behaviors (see text). Note that the black lines are best fits to the data with a straight line in Region 1 and an exponential decay in Region 2.

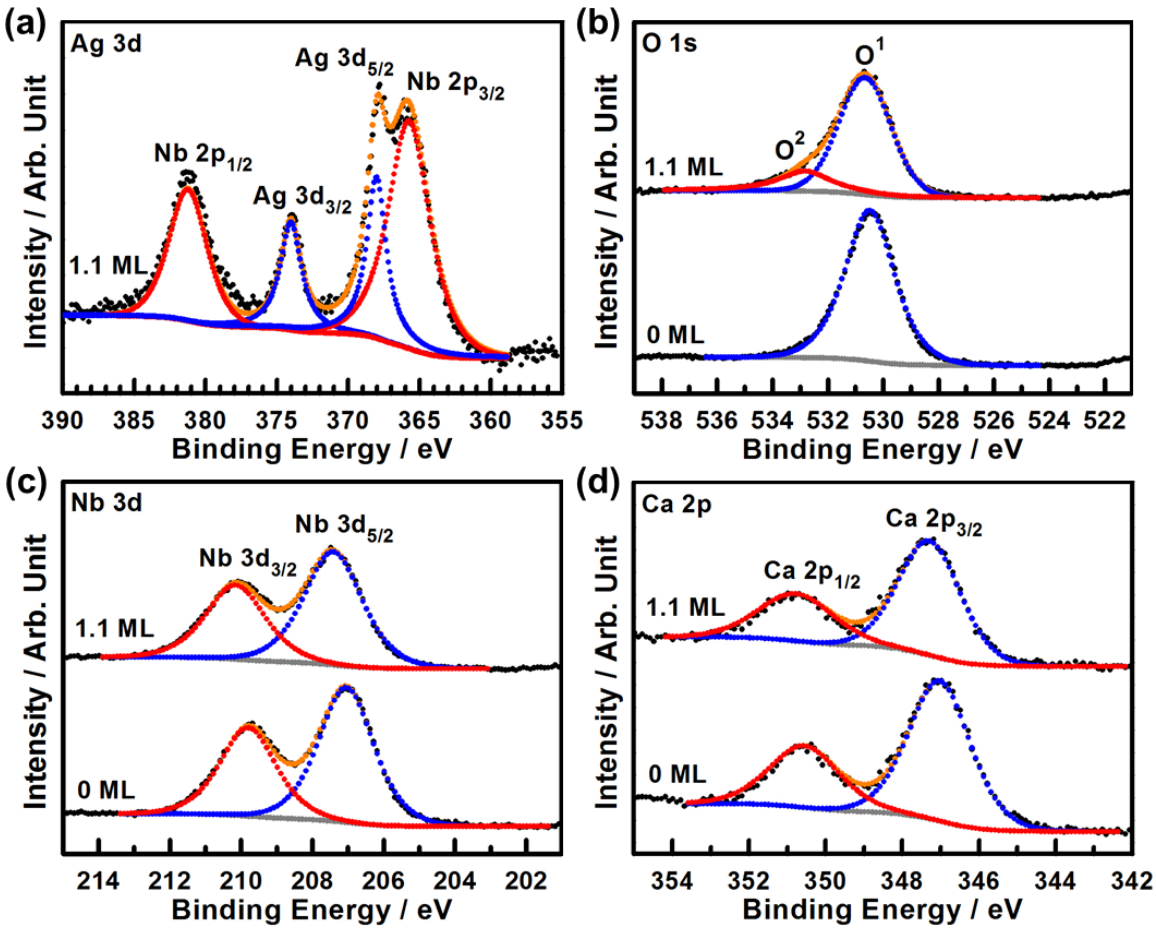

Figure 5.9. XPS spectra (hν = 1486.6 eV) and peak fits of the elements (a) Ag 3d for the adsorbed Ag nanoparticles and (b) O 1s, (c) Nb 3d, (d) Ca 2p in the dh-$HCa_2Nb_3O_{10}$ support, plotted for the starting clean dh-$HCa_2Nb_3O_{10}$(001) surface and after adsorbing 1.1 ML of Ag at 300 K. The O 1s peak at 1.1 ML Ag coverage was fitted with two components labelled as O^1, ascribed to the non-bonding O atoms (mostly subsurface O atoms) of the perovskite support, and O^2, the surface oxygen atoms that are in closer contact to the cationically adsorbed Ag. The overlapping Ag 3d doublets (blue dots) and Nb 2p doublets (red dots) were deconvoluted in (a).

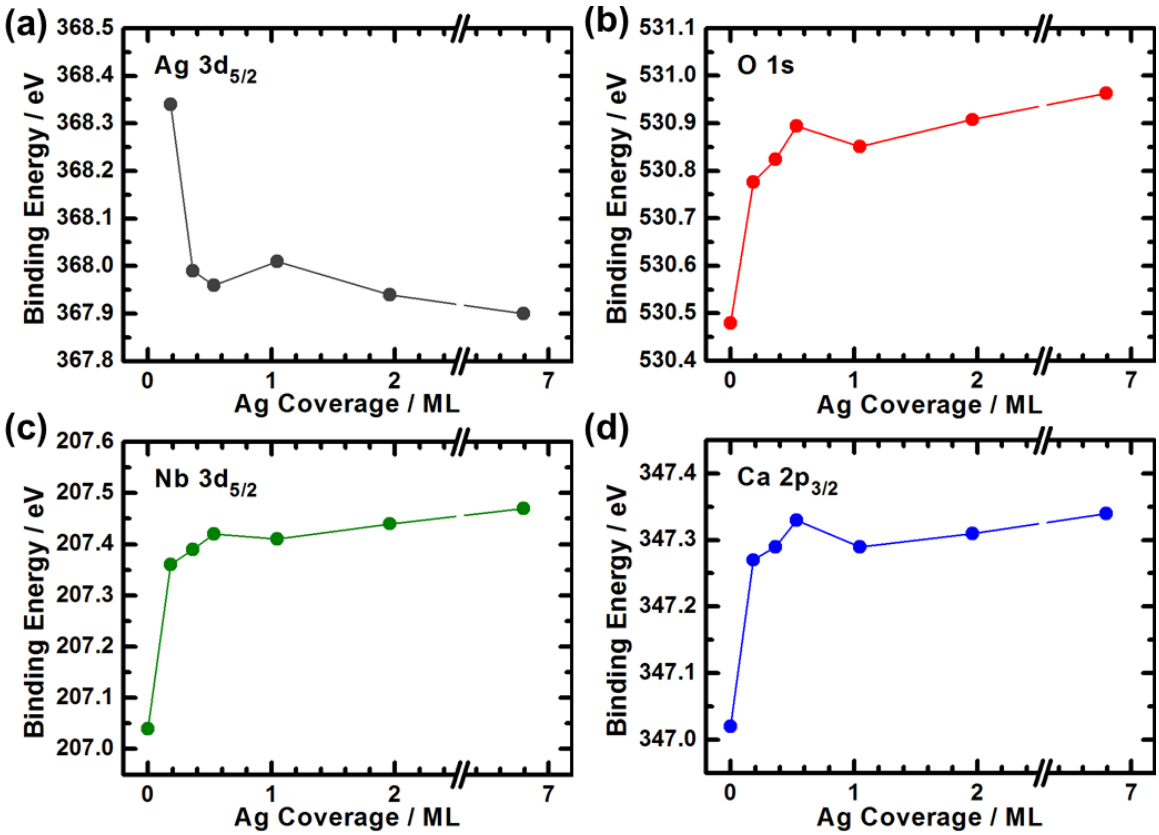

Figure 5.10. Core-electron XPS binding energy shifts with Ag coverage at 300 K for (a) Ag $3d_{5/2}$ for the adsorbed Ag nanoparticles and (b) O 1s, (b) Nb $3d_{5/2}$, (c) Ca $2p_{3/2}$ in the dh-$HCa_2Nb_3O_{10}$(001) support. The BE shift of O 1s peak in (b) is represented by the BE shift of the O 1s peak's centroid or "center line", on both sides of which the integrated area is the same. All spectra have been energy-referenced to Ag $3d_{5/2}$ peak for bulk Ag(s) (367.9 eV).[149]

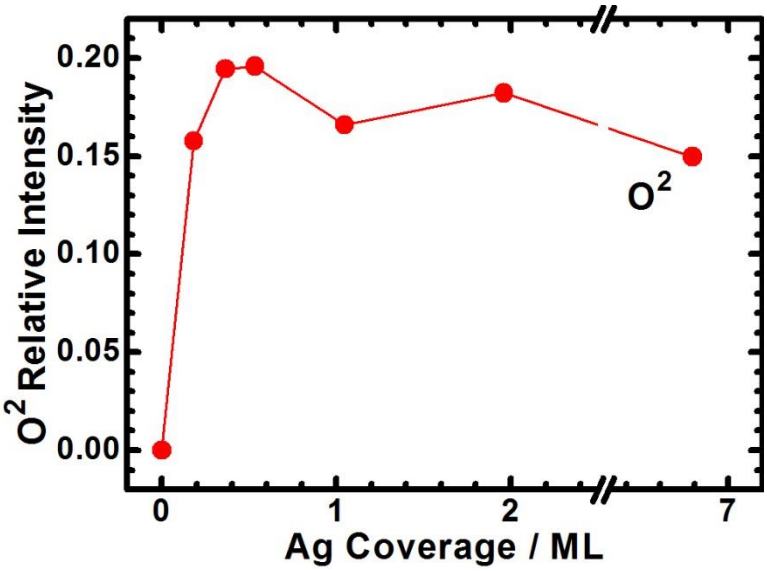

Figure 5.11. The integrated XPS intensity of the O^2 component of the O 1s peak, normalized to the total integrated O 1s peak for the starting surface (before dosing Ag).

Chapter 6. Energetics of van der Waals Adsorption on the Zr-based MOF NU-1000: Experimental Measurements and DFT Calculations

Metal−organic frameworks (MOFs) are a subclass of coordination polymers consisting of inorganic nodes containing metal ions, metal clusters, or metal oxide clusters joined by various types and lengths of organic linkers. Some of the recent developments and applications of MOFs are in the fields of hydrogen and methane storage,[33,77-79,83,85,86] toxic gas removal,[90-92] separation of propylene from propane,[218] and metalation for catalytic applications.[49,99,111,113-115] Most applications depend on the adsorption capacity and selectivity of a given MOF for the particular adsorbate or adsorbates of interest. As such, the measurements of adsorption isotherms and the determination of adsorption energies for gas molecules on MOF samples as a function of coverage are of great research interest. Here, a Zr-based MOF NU-1000 is chosen as a prototype system for this study.

This chapter describes the structure of NU-1000 in detail, reports the measurements of adsorption isotherms and the determination of isosteric heats of adsorption of many small gases (H_2, D_2, Ne, N_2, CO, CH_4, C_2H_6, Ar, Kr, and Xe) on NU-1000, correlates the adsorption energies as functions of coverage with the Lennard-Jones well depth (ε) where possible, compares the experimental results to the density functional theory (DFT) calculations of the single-atom/single-molecule adsorption enthalpies, and proposes a sequential-site-filling model (assuming gases are filled in a sequential order from the strongest to the weakest DFT-calculated adsorption site) to help understand gas molecule adsorption at low coverages.

This chapter splits into two subchapters. Subchapter 6.1 focuses on coverages from 0.1 ML up to the bulk three-dimensional phase, and Subchapter 6.2 extends to coverages below 0.1 ML.

6.1 Energetics of van der Waals Adsorption on the Metal−Organic Framework NU-1000 with Zr_6-oxo, Hydroxo, and Aqua Nodes

This subchapter is reprinted with permission from reference [94]:

Zhang, W.; Ma, Y.; Santos-López, I. A.; Lownsbury, J. M.; Yu, H.; Liu, W.-G.; Truhlar, D. G.; Campbell, C. T.; Vilches, O. E. Energetics of van der Waals Adsorption on the Metal–Organic Framework NU-1000 with Zr_6-oxo, Hydroxo, and Aqua Nodes. *J. Am. Chem. Soc.* **2018**, *140*, 328-338.

ABSTRACT

We report measurements of adsorption isotherms and the determination of the isosteric heats of adsorption of several small gases (H_2, D_2, Ne, N_2, CO, CH_4, C_2H_6, Ar, Kr, and Xe) on the metal-organic framework (MOF), NU-1000, which is one of the most thermally stable MOFs. It has transition-metal nodes of formula $Zr_6(\mu_3\text{-}OH)_4(\mu_3\text{-}O)_4(OH)_4(OH_2)_4$ that resemble hydrated ZrO_2 clusters and can serve as catalysts or catalyst supports. The linkers in this MOF are fused benzene rings linked to the nodes via the carboxylate groups of benzoates. The broad range of adsorbates studied here allows us to compare trends both with adsorption on other surfaces and with density functional calculations also presented here. The experimental isotherms indicate similar filling of the MOF surface by the different gases, starting with strong adsorption sites near the Zr atoms, a result corroborated by the density functional calculations. This adsorption is followed by the filling of other adsorption sites on the nodes and organic framework. Capillary condensation occurs in wide pores after completion of a monolayer. The total amount adsorbed for all the gases is the equivalent of two complete monolayers. The experimental isosteric heats of adsorption are nearly proportional to the atom-atom (or molecule-molecule) Lennard-Jones well-depth parameters of

the adsorbates but ~13-fold larger. The density functional calculations show a similar trend but with much more scatter and heats that are usually greater (by 30%, on average)

6.1.1 INTRODUCTION

Metal-organic frameworks (MOFs) are a class of coordination polymers that may be used as catalysts, catalytic support structures, and molecular sieves[31-33] with well controlled pores. They consist of nodes containing metal atoms, metal clusters, or inorganometallic clusters joined by various types and lengths of organic linkers. They can be synthesized in a variety of crystal structures and can be modeled in detail. Some of the recent developments and applications of MOFs are in the fields of hydrogen storage[219], metalation for catalytic applications[49], separation of propylene from propane[218], and micromotors[220]. Most applications depend on the adsorption capacity and selectivity of a given MOF for the particular adsorbate or adsorbates of interest. As such, the adsorption energies and the equilibrium adsorption capacities as functions of temperature and pressure are of great interest. Here we report experimental and theoretical studies of the low-temperature adsorption characteristics of one of the most stable and thus catalytically relevant Zr-based MOFs, NU-1000[49] (described below). We study ten inert, approximately spherical atoms and molecules, ranging from H_2 to Xe, thus reporting heats of adsorption over a large range of strengths of van der Waals interaction. In addition, single-atom or single-molecule enthalpies of adsorption on six possible sites at the metal nodes and one possible site on the organic linker were calculated using density functional theory (DFT) and compared with the low-coverage (0.1 monolayer) heats determined here from the experimental equilibrium adsorption isotherms. With these results, NU-1000 becomes a well understood MOF in terms of its adsorption behavior, and this information should be useful in guiding further applications on this or similar MOFs as well

as allowing NU-1000 to serve as a prototype system for studying the surface chemistry of MOFs in general.

Below, we describe the NU-1000 MOF structure, describe our measurement method and equipment used for adsorption isotherms, calculate the isosteric heats of adsorption from the pressure-temperature-coverage isotherms, describe the DFT methods and results, and compare the experimental results to the DFT calculations of the single-atom/single-molecule adsorption enthalpies. Where possible, we correlate adsorption energies as functions of coverage with the Lennard-Jones potential energy (ε) and size (σ) parameters of the pure gaseous adsorbates, and also with a quantum parameter (η= de Boer's parameter, defined below). Finally, we discuss possible reasons for a sharp rise in adsorption amount observed after monolayer completion for all the adsorbates, somewhat similar to the gate-opening[221,222] transition observed in zeolitic imidazolate framework MOFs (ZIFs).

NU-1000[49,99,221] contains $Zr_6(\mu_3\text{-}OH)_4(\mu_3\text{-}O)_4(OH)_4(OH_2)_4$ nodes separated by pyrene-based linkers. It has an open crystalline structure with *ab* planes shown in Figure 6.1(a), similar to a Kagome lattice. These planes are joined along the *c* axis by the organic linkers, as shown in Figure 6.1(b) and the lower insert. Each node has six Zr atoms in its structure connected by Zr-O-Zr bonds, so it resembles a tiny cluster of Zr oxide, Figure 6.1 (top insert). Adsorption studies on such cluster nodes promise to offer new insights into particle size effects in catalysis by metal oxide nanoparticles. The distance between nodes is approximately 15 Å; the hexagonal channels (large pores) seen in Figure 6.1(a) have a diameter of about 31 Å; and the pores seen in Figure 6.1(b) have diameters of 8.5 Å. The NU-1000 nodes offer several kinds of adsorption sites involving hydroxyl groups and Zr atoms on the nodes and carboxylates and aromatic rings on the linkers. Figure 6.2 shows the six locations near the nodes where the strongest adsorption sites were

found by density functional calculations. (The adsorption site on the pyrene linker will be shown in Figure 6.11 below.) While Ar is shown in Figure 6.2, similar figures were constructed for all other gases studied and will be referred to in Section 6.1.7 below; they are included in the Supporting Information.

The NU-1000 MOF has been studied by physical adsorption using N_2 and CO_2 as adsorbates, but the heat of adsorption was not determined.[49,50] A recent publication by Lownsbury et al. describes an extensive experimental and theoretical study of Ca adsorption on this MOF.[99,223] The Ca atoms adsorb on the inorganometallic nodes with adsorption energies in the 300 kJ/mol range. Close agreement was found between the experimentally determined differential heats of adsorption and theoretical DFT calculations of the same properties. Here we study the much weaker van der Waals binding of nine different atoms and molecules on the same material and correlate their adsorption energies with molecular properties, to establish benchmark energies for studies of adsorption on MOFs with multinuclear metal nodes. To our knowledge, there is no other MOF with isolated multinuclear metal nodes where adsorption energies have been measured for more than a few molecules.

6.1.2 EXPERIMENTAL TECHNIQUES

Our samples of NU-1000 were prepared at Northwestern University using a procedure described in ref [49] and kindly given to us by J. T. Hupp and O. K. Farha. Seven samples of NU-1000 powder were tested, each sample having up to 10 mg mass before vacuum and/or heat treatments. All samples were from the same batch. The Brunauer-Emmett-Teller (BET) specific surface area of this powder has been measured as 2,320 m^2/g.[49] The samples were placed in a 4 mm ID Pyrex glass tube with a wider(about 10 mm) flared flat bottom to make better thermal contact to the cooling system and to prevent powder migration when baked and/or evacuated. Samples 1, 2, 4,

and 5 were used to test different vacuum baking temperatures from 348 to 523 K, which were found to change the adsorbed volumes by less than 5% (i.e., within experimental error). After baking, they were submerged in liquid nitrogen and N_2 and/or Kr isotherms were measured. Sample 7 was used for a N_2 BET measurement at 77.4 K in a different apparatus; this measurement gave a specific surface area of 2,580 m^2/g, within error of values measured at Northwestern University.[49] Most of the results in this report come from samples 3 and 6. The BET areas per gram of samples 3 and 6 were not measured but are expected to be within experimental error of this value for sample 7, since all samples came from the same batch.

We adsorbed H_2, D_2, Ne, N_2, CH_4, C_2H_6, CO, Ar, Kr, and Xe. The weak dispersion and induced dipolar interactions of these species are well understood. The Lennard-Jones potential approximates this interaction. It is given by

$$V(r,\sigma,\epsilon) = -4\epsilon[\left(\frac{\sigma}{r}\right)^6 - \left(\frac{\sigma}{r}\right)^{12}] \tag{6.1}$$

where r is the distance between a pair of atoms (or molecules), ε is the depth of the pairwise attractive potential well, and σ corresponds to the hard core interaction distance. Table 6.1 shows the range of ε and σ encompassed[224] in the present study, the approximate atomic/molecular masses (m), and the dimensionless quantum parameter $\eta = \hbar^2/m\sigma^2\varepsilon$,[225,226] which has been extensively used to separate the "classical" and "quantum mechanical" regimes of liquid-vapor critical points (corresponding states) and solid-liquid-vapor triple points, both in two and three dimensions.[227-230]

Samples 3 and 6 were attached, at different times, to a cryo-mechanical refrigerator which could be operated within the regulated temperature range 11 K < T < 300 K, ±0.1 K. The refrigerator had two thermometers, one below and one above the adsorption cell, a heater attached to an electronic controller using the bottom thermometer, and an auxiliary heater which could be

turned on when running above 90 K to improve stability. Both samples were attached to a vacuum and gas handling manifold capable of pumping to 3×10^{-7} Torr and pressurizing up to 1 atm. Sample 3 was baked at 523 K in vacuum in a different vial, and then transferred to the cryocooler system and attached to the dosing system. During this transfer, some of the sample was lost. Sample 6 was baked at 348 K in vacuum on the cryocooler cell but outside the cryocooler system. It had an additional valve, which was closed after baking; it was opened only after being attached to the cryocooler and evacuated dosing system. Neither sample was further exposed to air.

Adsorption isotherms were measured using a point-by-point method. The dosing system had a calibrated volume of 87 cm^3, and two MKS Baratron capacitance absolute pressure gauges with 1000 Torr and 10 Torr ranges. The 10 Torr gauge could be used with reasonable stability to about 4×10^{-4} Torr. The calibration of this gauge was checked against the vapor pressure of Ar after condensing this gas into a tube identical to the one used for the NU-1000 experiments but without the sample. A thermo-molecular correction of the room temperature readout using an equation and coefficients for each gas published by Takaishi and Sensui[231] was done for all pressures below 2 Torr.

We used the CH_4 coefficients for C_2H_6, and the N_2 coefficients for CO since we could not find them in the literature. The maximum possible thermo-molecular correction for all gases in the limit of pressures low enough that the mean free path of atoms/molecules in the residual gas is much larger than the diameter of the tube between room and experimental temperatures is $(T_{experiment}/T_{room})^{1/2}$. The correction for all of the gases follows a rather universal curve. We calibrated the dead volume of the empty adsorption cells between 12 K and room temperature using helium gas.

We measured isotherms of H_2, D_2, N_2, and CO on sample 3 and of H_2, Ne, N_2, CO, CH_4, Ar, Kr, Xe and C_2H_6 on sample 6. Details of how many isotherms were measured and how they were measured are given below.

6.1.3 EXPERIMENTAL RESULTS

6.1.3.1 *Adsorption Isotherms and Analysis Method*

Figure 6.3 shows the N_2 surface area calibration isotherm measured at 77.4 K on sample 7. The inset shows the linear plot of the same isotherm following the BET equation in the form[232,233]

$$\frac{1}{\{V_{ads}[(P_0/P-1)]\}} = \frac{c-1}{cV_{ML}}(P/P_0) + \frac{1}{cV_{ML}} \tag{6.2}$$

where V_{ads} is the adsorbed volume of gas, P_0 is the bulk adsorbate saturated vapor pressure (760 Torr), P is the thermomolecular corrected measured pressure, $c = exp[(E_0 - E_L)/(RT)]$ is a constant related to the binding energy to the substrate (E_0, assumed constant) and the latent heat of condensation (E_L) of the bulk liquid or solid adsorbate, and V_{ML} is the BET monolayer coverage. The slope and intercept of the linearized BET graph yield V_{ML} and c. From the inset graph, V_{ML} = 5.93 ccSTP, or a specific area of 2,580 m^2/g when using 16.2 $Å^2$ for the area of a single N_2 molecule, a value estimated from its three-dimensional bulk liquid density.[232] This specific area is 11% larger than that reported in ref [49]. The BET V_{ML} is shown in Figure 6.3, as well as the inflexion point where the curvature of the isotherms changes from concave to convex. Adsorption above V_{ML} leads to a large, essentially constant jump, Δ, in the volume adsorbed when the pressure reaches a certain value, and finally bulk condensation at $P = P_0$.

Figure 6.4 and Figure 6.5 show measured isotherms of CO and CH_4 to illustrate two different approaches. For the CO isotherms, Figure 6.4, the temperatures were set, and all points were taken keeping the temperature constant. All pressures were within the range of the 10 Torr

and 1000 Torr pressure gauges. Multiple CH_4 isotherms, Figure 6.5, were started at constant temperatures between 91.8 K and 113.5 K in order to get to low coverages at equilibrium pressures accessible with the 10 Torr pressure gauge. The 91.8 K isotherm was continued until reaching the bulk liquid vapor pressure. The higher *T* isotherms were continued only to about half a monolayer, after which the temperature was lowered in steps. The single equilibrium points obtained at each lower *T* where used to check reproducibility. When the desired lower *T* was reached, the isotherm was then continued to the bulk vapor pressure.

Graphs for all measured isotherms for the other gases are presented in the SI. The pressure could not be accurately measured at low coverages of ethane due to non-condensable impurities in that gas.

6.1.3.2 *Monolayer Coverage*

Figure 6.4 and Figure 6.5 above show all the total and partial isotherms of CO and CH_4 measured on sample 6. In Figure 6.6 and Figure 6.7 we show one isotherm for each gas, measured on samples 3 and 6 respectively. The vertical axis in all the figures is the actual amount of gas adsorbed converted to standard pressure and temperature. The horizontal axis in Figure 6.6 and Figure 6.7 has been normalized to the saturated vapor pressure of each gas at the temperature of the isotherm. These figures clearly show the change in monolayer capacity with the size of the atom or molecule adsorbed.

H_2 and D_2 have the same Lennard-Jones interaction parameters, but their quantum parameters are different by a factor of 2 due to their different masses. The slight increase in the adsorption of D_2 over H_2 seen in Figure 6.6 is due to this difference since D_2's effective footprint is smaller. This effect is also seen on adsorption on exfoliated graphite,[234] where the molecular surface densities at monolayer completion on the (0001) surface are 0.099 $Å^{-2}$ (D_2) and 0.094 $Å^{-2}$

(H_2). The arrows in Figure 6.6 and Figure 6.7 indicate our estimated monolayer adsorbed volumes on samples 3 and 6. It is important to note that for H_2 and D_2 there is considerable adsorption on another layer or site past monolayer completion and before the Δ condensation jump. The same effect can be seen in Ne adsorption, and to a lesser extent in N_2 and CO. This extra adsorption has an effect on the Δ-jump as discussed below (Section 6.1.6.2).

Figure 6.6 and Figure 6.7 also show that the vertical condensation jump, Δ, occurs at about the same relative vapor pressure (P/P_0) for all adsorbates.

6.1.3.3 *Area of Sample Occupied by the Different Gases*

We present in Table 6.2 our determination of the volume of gas adsorbed at monolayer coverage, V_{ML}, from one particular isotherm of each species at the temperatures shown in Figure 6.6 and Figure 6.7. The accuracy of this determination is about 5%.

A linearized BET plot of the N_2 isotherms on samples 3 and 6, similar to Figure 6.3, gave BET monolayer completion volumes of 3.21 cm^3 STP (sample 3) and 4.66 cm^3 STP, similar to the monolayer coverages determined by the inflexion point in these isotherms. These coverages translate, respectively, into areas of 14.0 m^2 and 20.3 m^2 using 16.2 $Å^2$ for the N_2 molecular area.

We used the monolayer capacities for all gases in this study to check if all atoms or molecules occupied essentially the same effective total surface area of this MOF. From the ideal gas equation of state, the number of atoms/molecules adsorbed at monolayer completion is

$$N_{ML} = (P_{st}/RT_{st})V_{ML}N_A \tag{6.3}$$

where $P_{st} = 1.013 \times 10^5$ Pa, $T_{st} = 273.15$ K, and $R = 0.0831$ L bar/(mol K) is the gas constant, and N_A is Avogadro's number. V_{ML} is taken from Table 6.2. The total effective area of our NU-1000 samples for each adsorbate is

$$A = N_{ML} a \tag{6.4}$$

where a is the area of the atom or molecule adsorbed. One uniform way of estimating a is to assume that the full monolayer forms a close packed structure of spheres "touching" at the minimum of the Lennard-Jones potential, $r = 2^{1/6}\sigma$. Thus, each atom or molecule occupies a hexagon of area $a = 1.09\sigma^2$. Using this approximation and the V_{ML} data from Table 6.2, Figure 6.8 shows the calculated "Lennard-Jones area" of our samples 3 and 6 (normalized to the value for N_2 for that sample) versus the gas's quantum parameter, both calculated using the Lennard-Jones potential and other constants of Table 6.1.

We conclude from Figure 6.8 that, within the experimental uncertainty in the determination of V_{ML}, all adsorbates, except perhaps C_2H_6, occupy essentially the same sites or effective total area on the surface of the NU-1000 substrate.

Table 6.2 also lists the number of molecules adsorbed in this first monolayer per formula unit of NU-1000 (i.e., per Zr_6 node), n_{ML}. The BET specific surface area for N_2 molecules, 2,580 m^2/g, combined with the molar mass of NU-1000 (2,177 g/mol) and the area per N_2 molecule (16.2 $Å^2$, see above) gives n_{ML} = 58 N_2 molecules per Zr_6 node for N_2. For the other gases, n_{ML} is just n_{ML}(for N_2) times V_{ML}/V_{ML}(for N_2) with the same MOF sample. For comparison, one Zr_6O_{12} unit with the same density as bulk ZrO_2(solid) would have a radius of 0.38 nm if spherical, with an area of 1.8×10^{-14} cm^2. This simple spherical model for a node would adsorb ~11 N_2 molecules.

6.1.3.4 *Isosteirc Heat of Adsorption*

The isosteric (constant coverage) heat of adsorption is given by

$$Q_{st} = RT^2[\partial(lnP)/\partial T] = -R[\partial(lnP)/\partial(1/T)] \tag{6.5}$$

where R is the gas constant. Pairs of P and T were extracted from horizontal lines (isosteres) drawn across isotherms like those of Figure 6.4 and Figure 6.5, and graphs of ln P vs. $1/T$ at constant coverage were made from those pairs. Over a narrow range of temperature (such that Q_{st} is constant) these graphs yield straight lines through the data points. The slope of each of these lines gives Q_{st} at that coverage. Figure 6.9 shows the resulting Q_{st} for all the adsorbates versus coverage (relative to the monolayer coverage of each gas from Table 6.2). The bottom part of this figure shows the same data, with the heats normalized to the heat for each gas at 0.1 ML coverage. These are differential heats of adsorption. Table 6.2 lists the isosteric heats at 0.1 ML coverage, $Q_{st}(0.1)$, estimated from fitting curves to heats versus coverages near 0.1 ML.

Although the accuracy for Q_{st} of applying this analysis is reasonably good for those gases where we measured several isotherms, the values for Ar, Kr, and C_2H_6 were extracted from only two isotherms for each gas and less reliable. The low coverage H_2 and D_2 regions were measured via several isotherms between 25 K and 37.5 K, but results for these two molecules above monolayer coverage were calculated from only two isotherms at 16 K and 19 K.

Figure 6.9(top) shows the same trend for all the adsorbates. There is strong binding at very low coverages, followed by a general decrease to almost the bulk latent heat of each substance at monolayer completion. Past monolayer completion there is a small increase in Q_{st} during the condensation step Δ, easily visible in the Xe and CH_4 data in Figure 6.9 before the 3d latent heat of condensation (or sublimation) is reached.

The bottom half of Figure 6.9 normalizes the isosteric heats to 0.1 monolayer coverages. As seen, the heat of adsorption decreases strongly with coverage in the first ML, with a relative decrease that is faster for light gases (H_2, D_2, CH_4 and Ne).

The zero-coverage isosteric heat of adsorption is related to the single atom/molecule binding energy (E_0) on the strongest adsorption site at temperature T by

$$Q_{st} = E_0 + \alpha RT \tag{6.6}$$

where α is a constant that depends on the degree of localization of the atoms/molecules on the surface (3/2 for an ideal monatomic 2D gas[232,235]). The strongest adsorption site is usually a site near the Zr atoms, as discussed below.

Figure 6.10 shows these isosteric heats at a coverage of 0.1 monolayer, $Q_{st}(0.1)$, plotted against the atom-atom (or molecule-molecule) Lennard-Jones energy parameter (well-depth, ε) from Table 6.1. Data at lower coverages (like the "zero coverage" limit) are not as reliable due to the very low equilibrium vapor pressure of the films at the temperature of our experiments and due to the possible role of defect sites. Figure 6.10 shows that the heat increases nearly proportionally to ε of the adsorbates, with a best-fit slope of 12.9. For comparison to adsorption of these same gases on a uniform substrate, we also plot in Figure 6.10 the best estimates of the binding energy, E_0, to graphite (0001) at 0 K, from Vidali et al.'s review[236]. As seen, graphite shows a very similar trend to NU-1000, but usually with weaker binding (best-fit proportionality of slope = 9.3, 28% less than on NU-1000).

6.1.4 DENSITY FUNCTIONAL THEORY CALCULATION METHODS

We adopted the cluster model of NU-1000 that was used in our previous study of Ca adsorption on NU-1000.[99] For the geometry optimizations and normal-mode frequency calculations, we used the M06-L[129] exchange-correlation functional with the 6-31G(d,p)[135] basis for all atoms except Zr, Kr, and Xe, for which the SDD[138,237] effective core potential and corresponding basis sets were used. The M06-L functional has been well validated for van der Waals interactions in small-

molecule tests,[238-240] for molecule–surface adsorption,[241,242] and by applications to problems in MOFs where damped dispersion is essential.[243-245]

The frequencies were scaled by a factor of 0.977 calculated by the method described elsewhere.[140] The energies were refined by single-point calculations with a larger basis set,[246] 6-311++G(d,p) and corrected for basis set superposition error (BSSE) using the counterpoise method.[247]

We placed each of the ten adsorbates at each of the seven numbered adsorption sites of Figure 6.11, and we optimized the structures. Figure 6.12 provides a view from the triangular pore of Figure 6.1(a) to illustrate six of the sites around the Zr_6 node. In each case we found a local energy minimum. Site 1 is near the μ_3-OH, and site 2 is near the μ_3-O. These sites are each sandwiched between two benzene rings. Sites 3 and 4 are chemically equivalent to sites 1 and 2, respectively, except that sites 1 and 2 are in the large pore whereas site 3 and 4 are in the small pore of NU-1000. Site 5 is near four O atoms of four carboxylate groups, and site 6 is close to an –OH group and an $–OH_2$ group. In addition to the adsorption sites around the Zr_6 node, we also examined the gas adsorption on pyrene, which is the major structural component of the organic linker of NU-1000.

6.1.5 ENTHALPIES OF ADSORPTION FROM DFT

The adsorption enthalpies of various gas molecules at 77 K for each site are listed in Table 6.3. The average heat of adsorption at 77 K in the limit of low coverage was calculated using the following formula:

$$\langle Q \rangle_{0,DFT} = -\frac{\sum_{i=1-7} H_i d_i q_i e^{-E_i/kT}}{\sum_{i=1-7} d_i q_i e^{-E_i/kT}} \tag{6.7}$$

where d_i is the number of equivalent sites of type i in the crystal structure (which is 2 for sites 1–5 and 4 for site 6), E_i is the single-point potential energy at the equilibrium geometry of structure i relative to the overall zero of energy, q_i is the vibrational partition function of structure i with zero of energy at E_i, and H_i is the adsorption enthalpy for site i. The negative sign converts from reaction enthalpy to heat.

From Table 6.3, we can see that all gas species except C_2H_6 have larger adsorption enthalpy for sites in the small pore (sites 3 and 4) than for the corresponding sites in the large channel (sites 1 and 2). Sites 1, 2, 3, and 4 are in bowl-like structures surrounded by benzene rings, as shown in Figure 6.12. For sites in the small pores, the small benzene-benzene distance results in large attractive van der Waals interaction, in agreement with the previous finding for comparative binding energies in the two kinds of pores.[244] The large size of C_2H_6 makes it unable to reach the atomically dense metal-oxide node for site 4 in the small pore, resulting in almost the same adsorption enthalpy as in the large pore. Although it has more π electrons than the benzoates, the pyrene (site 7) has a smaller adsorption enthalpy than sites 1–4, which indicates the importance of the pocket-like structure to the adsorption enthalpy.

Table 6.3 also lists the differential enthalpy of adsorption of the site expected to be populated at 0.1 ML coverage, assuming that the sites are populated sequentially starting from the strongest to the weakest. Since there are 2 sites of most types, this is generally equal to H_i for the nth strongest site, where $n = 0.1\ n_{ML}/2$, and n_{ML} is the number of molecules per ML per Zr_6 node listed in Table 6.2. We refer to this enthalpy as $H_{DFT}(0.1)$. This enthalpy makes the most appropriate direct comparison to our differential isosteric heat of adsorption measurements at 0.1 ML coverage listed here. For the example of N_2, it is the enthalpy at the 3rd strongest site. At these nth strongest sites, all the gases are binding to the O, OH and/or H_2O groups of the Zr_6 nodes. These $H_{DFT}(0.1)$

values are plotted in Figure 6.10 for comparison to the experiments. The agreement with experiment at 0.1 ML coverage is much better for these DFT values than the thermally-averaged heat of adsorption calculated for the limit of zero coverage ($<Q>_{0,DFT}$). The increasing DFT heat with well depth is quite similar to experiments, although with much more scatter than the experiments. On average, the $H_{DFT}(0.1)$ values are 30% larger than the experimental isosteric heats at 0.1 ML, with the largest difference (69%) seen for D_2. (The large relative differences for the lightest gases (H_2 and D_2) dominate this average relative error, although their absolute errors are quite small (a few kJ/mol).)

6.1.6 DISCUSSION

6.1.6.1 *Monolayer Heats of Adsorption*

Comparison of the saturation adsorption amounts in the first layer indicates that the whole area of the NU-1000 samples is available to all the gases (Figure 6.8).

Table 6.3 and Figure 6.10 compare experimental Q_{st} results at low coverage (0.1 ML) to the theoretical enthalpies from the DFT calculations. The experimental isosteric heats of adsorption increase nearly proportionally to the atom-atom (or molecule-molecule) Lennard-Jones parameters of the adsorbates. The DFT calculations show a similar trend but with more scatter. The $H_{DFT}(0.1)$ values agree well with the experimental heats at 0.1 ML, except for N_2, CO and CH_4, which have DFT values that are too high, on average by 42%. The average absolute value of the relative difference between $-H_{DFT}(0.1)$ and $Q_{st}(0.1)$ for all the gases except ethane is ~30%.

An interesting feature of the experimental Q_{st} results at 0.1 ML in Figure 6.10 is their almost linear dependence on the adsorbate's ε parameter. This also seen in the initial heats of adsorption for many of these same gases reported for graphite(0001) surfaces,[236] also plotted in Figure 6.10 for comparison to NU-1000. On average, the gases bind more strongly to NU-1000

than to graphite at the coverages compared in Figure 6.10. The gases with the largest ε bind 30-40% less strongly to graphite, whereas the relative difference decreases as ε decreases. The average difference would be even larger if compared at the same low coverage, since heat drops with coverage. Indeed, this coverage effect partially explains why this relative difference appears to decrease with decreasing ε. By 10% of a ML, the smallest gases have already populated 9 sites per node, whereas the other gases except Ne have only populated 4 to 7 sites per node (i.e., compare n_{ML} values in Table 6.2). The DFT calculated adsorption enthalpies on NU-1000 show this same trend of increasing with ε, but usually with higher adsorption energies and more scatter.

To our knowledge, this linear dependence of the adsorption energy on ε seen in Figure 6.10 has never been recognized before for any MOF. However, when some early results on other MOFs are plotted in this way, we noticed that they follow the same trend. This is seen, for example, in adsorption measurements for N_2, Ar, Kr and Xe performed at 273 K and 292 K on the open-frame MOF-74-x (also called M-MOF-74, with M being the metal = Mg, Co, Ni or Zn). Simulations were performed for the same combinations.[248] A set of DFT calculations for the adsorption of Kr and Xe on M-MOF-74, where M stands for 10 different metals (but not Zr), has been performed by Vazhappilly et al.[249] The MOF-74 with M being Ni, Fe, and Co as the metal has been used to demonstrate quantum sieving between H_2 and D_2 with higher pressure isotherms than ours in the temperature range of 77K to 150K.[250] Our results for Q_{st} for the rare gases on samples of NU-1000 with Zr as the metal (experiment and theory) are in excellent agreement with the isosteric heats measured and calculated by Perry et al. for the Zn-based MOF, MOF-74-Zn. It should be noted though that different metals produce a wide range of Q_{st} values, as seen on Table 6.3 of Perry et al., and close to factors of two discrepancies in calculated and measured values of the N_2 isosteric heat with Mg (23.57 kJ/mol experimental, 12.82 kJ/mol simulation) and Ni (23.22 kJ/mol

experimental, 13.99 kJ/mol simulation), as the metals, while for Zn as the metal their experimental and simulation results are quite close (11.82 kJ/mol experimental, 14.99 kJ/mol simulation). Our discrepancy in the N_2 isosteric heat between measurement and calculation in our Table 6.3 and Figure 6.10 though is reversed to that on MOF-74-Ni or -Mg.

The calculations of Vazhappilly et al. on Cr-MOF-74 with six Kr or Xe atoms on the pore give binding energies of -12.83 kJ/mol for Kr and -21.02 kJ/mol for Xe, and for Zn-MOF-74 they give, respectively, -11.95 kJ/mol and -22.87 kJ/mol. These values are similar to our measured and calculated values for the same two gases in Table 6.3. We also obtained a slightly larger heat of adsorption of D_2 than H_2 as measured by FitzGerald et al., but our Q_{st} values are more than a factor of three lower than the ones in their measurements on that Cr-based MOF.

6.1.6.2 *Second Layer and Growth to Saturated Bulk Vapor Pressure*

The isosteric heats in the 2nd ML in Figure 6.9 show similar trends versus mass as do the latent heats of bulk condensation (listed in Table 6.2), for which quantum effects are known to cause gases with large quantum parameters to have much lower heats (relative to the Lennard-Jones well-depth, ε, see Table 6.2, last column.

The growth in coverage from one monolayer (V_{ML}) to the volume of adsorbed gas required to reach bulk (three-dimensional) condensation at the bulk saturated vapor pressure occurs, (V_{3d}), shows interesting and common characteristics amongst all of adsorbates. The arrows in the N_2 isotherm in Figure 6.3 show where the first statistical layer is completed. Increasing the coverage past V_{ML}, a second layer begins to form, soon followed by an increase in coverage, labeled Δ, at essentially constant pressure. Once this step has been completed, a further small increase in adsorbed (or condensed) gas is needed to reach the saturated bulk vapor pressure at the temperature of the isotherm. The Δ-step is common to all the gases used in our isotherms, as can be seen in the

normalized isotherms of Figure 6.6 and Figure 6.7. A constant pressure and temperature adsorption step is indicative of some form of condensation and phase coexistence (two- or three-dimensional). We have observed that the Δ-step occurs at a relative pressure $0.11 < (P/P_0) < 0.37$, with $P/P_0 = 0.11$ for CH_4 at 67 K and C_2H_6 at 127.4 K, and $P/P_0 = 0.37$ for Ne at 18 K, see Table 6.4 below, column 6. Furthermore, Figure 6.6 and Figure 6.7 clearly show that H_2, D_2 and Ne complete a monolayer well before reaching the Δ-step relative pressure. Thus, a second layer of these substances begins to form before the Δ step, reducing the two- or three-dimensional space available in the NU-1000 matrix for further adsorption or condensation. A smaller (or partial) 2nd layer forms also for N_2, CO, CH_4, and Ar, but may not exist for C_2H_6, Kr and Xe.

Column 4 of Table 6.4 shows the ratio of the volumes of gas required to reach the bulk vapor pressure and to reach one monolayer (V_{3d}/V_{ML}), calculated at the temperature shown in Column 5; the phase of the bulk condensed phase (S, solid; L, liquid) is also indicated. This ratio is higher for the more quantum gases (H_2, D_2, and Ne), where the overlayer capacity is approximately equivalent to a monolayer, than for the larger adsorbates (especially C_2H_6 and Xe). We know from many heat capacity and neutron diffraction studies of H_2 on uniform surfaces like graphite[234] that even at 19 K, well above its bulk triple point temperature, a full monolayer forms a rather compressible solid. Addition of a second layer increases the first layer density above that determined by an isotherm. The same effect occurs for adsorbed D_2, but its monolayer is less compressible than the H_2 one. The larger ratios of V_{3d}/V_{ML} we observe for these two molecules are likely due to this effect. The large ratio for Ne may be due to its small size and the way it can fill the pores. We note that the apparent area occupied by Ne in Figure 6.8 is larger than for the other adsorbates. In between the small and large quantum parameter gases though, the volume adsorbed above a monolayer is between 80% and 90% of the monolayer capacity with differences likely due

to details of their adsorption process and uncertainties in the experimental data. We note that for an idealized perfect cylindrical pore of 15Å radius, a uniform monolayer of thickness σ (from Table 6.1) will reduce its adsorption area from 81% (for H_2) to 73% (for Xe) of the initial pore area.

To quantify the adsorption at the Δ-step, we used the adsorbed amount in the Δ-step for both samples 3 and 6 (V_Δ), used the ideal gas low to calculate the number of atoms or molecules at the Δ-step, multiplied them by the close-packed Lennard-Jones volume (σ^3) and divided the result by the mass of the NU-1000 samples to obtain the volume of the voids per unit mass of the adsorbent for each one of the gases used. The resulting void volumes per mass are shown in Table 6.4, Column 2, for the temperature and condensed phase of the bulk adsorbate listed in Column 3. We would expect that if the actual void space left after the first monolayer is formed were the same for all the gases, about the same volume would be occupied by all the condensed gases. It is obvious from Table 6.4 that this is not the case. The volume of H_2 in the phase condensed in the pores is the smallest. The next smallest is D_2, followed by Ne. This effect reinforces our observation above that the equivalent of another partial layer of these gases forms on top of the first layer in the available surface or pore before the Δ-step.

We also observe in Table 6.4 that the calculated void volume of the pores is larger for those atoms or molecules that condense into a solid phase at the temperature in the table. This effect is largely due to using the same Lennard-Jones σ for both the liquid and solid state at the temperature of the isotherm; using the molecular volumes of the actual three-dimensional phases would make the liquid and solid values closer (although not identical). These results should be useful for future modeling of the complete isotherms, including quantum effects for H_2 and D_2.

Our isotherms at the Δ-step look similar to those measured at the gate opening transition on a commercially available zeolite, the Zn imidazolate framework, ZIF-8: N_2 by Fairen-Jimenez

et al.,[221] Xe by Gallaba et al.,[222] O_2 by Russell et al.,[251] N_2, Ar, CO and O_2 by Ania et al.,[252] and Ar by Tanaka et al.[253] The imidazolate ($C_4H_3N_2^-$) linkers join Zn atoms to form a macroscopic crystalline structure of "quasi-spheres". The inner surface of these quasi-spheres is not available when adsorption starts, but at a certain relative pressure, P/P_0, the linkers bend to allow for gas to penetrate into the cavities. This phenomena (gate opening) suddenly increases the adsorption capacity of the framework (the vertical step), and produces a small measurable increase in the heat of adsorption. The Ar, CO and O_2, and some of the N_2 measurements show significant hysteresis between adsorption and desorption isotherms (gate closing). Furthermore, simulations for the Ar isotherms on ZIF-8 corroborate the general form of the isotherms, the significant hysteresis and the structural transition of opening and closing the gate.[253]

We find some differences between our isotherms on NU-1000 and the Ar isotherms[253] and Xe isotherms[222] on ZIF-8. The ratio P/P_0 for the gate opening in the ZIF-8 Ar isotherms grows from about 0.15 at 79 K to about 0.62 at 91 K as the 3d triple point of Ar is approached.[253] The ratio for the Xe isotherms also increases rapidly from 0.45 at 95 K to 1 at the 3d solid-liquid-vapor triple point, T_t.[222] Our isotherms for CO and CH_4 span T_t and don't show a tendency for the Δ-step to disappear. In fact, Table 6.4 shows the rather narrow range of changes of the ratio P_Δ/P_0. We adsorbed and desorbed CO at 64 K through the Δ-step on Sample 3 and found at most a 0.1 Torr hysteresis at 9.1 Torr. This is well within our uncertainties but deserves to be studied carefully.

We believe capillary condensation in the small pores is responsible for the Δ-step seen here. This fills the volume of the small pores of NU-1000 remaining after one monolayer of adsorbate has been deposited on the NU-1000 (or, after a partial second layer, as seen for most of the gases). In a study of N_2 adsorption at 77.4 K on well characterized siliceous molecular sieves (MCM-41), Kruk et al.[254] measured adsorption and desorption isotherms on samples with pore diameters

between 2.83 nm and 6.59 nm. They used a modified Kelvin equation to calculate the pore radius from the relative pressure at capillary condensation, which could be compared to the pore radius measured by X-ray diffraction. Kruk et al used the Kelvin equation with additional terms[254] to estimate their pore radius from pressures at the condensation step (P_Δ) relative to the 3d bulk vapor pressure:

$$r(P_\Delta/P_0) = \frac{2\gamma V_L}{RT}\ln(P_\Delta/P_0) + t(P_\Delta/P_0) \qquad (6.8)$$

where

We have used the data from the Table 6.4 isotherms of H_2(19.6 K), D_2(19.7 K), N_2(65.2 K) and CO(77 K) on Sample 3, and CO(78.6 K) and CH_4(91.8 K) from Sample 6, all leading to a 3d liquid phase, in $r(P_\Delta/P_0) = \frac{2\gamma V_L}{RT}\ln(P_\Delta/P_0) + t(P_\Delta/P_0)$ (6.8 above to estimate the effective radius of the open condensing space. We used $\gamma = 2.2 \times 10^{-3}$ N/m[255] and $V_L = 28.6 \times 10^{-6}$ m^3/mol[256] for H_2 at 19 K, $\gamma = 3.6 \times 10^{-3}$ N/m[255] and $V_L = 23.4 \times 10^{-6}$ m^3/mol[256] for D_2 at 19.7 K , $\gamma = 11.7 \times 10^{-3}$ N/m[257], $V_L = 32.6 \times 10^{-6}$ m^3/mol[258] for N_2 at 65.2 K, $\gamma = 10.2 \times 10^{-3}$ N/m[259], $V_L = 34.7 \times 10^{-6}$ m^3/mol[260] at 77.7 K for CO and $\gamma = 16.62 \times 10^{-3}$ N/m[257] and $V_L = 35.6 \times 10^{-6}$ m^3/mol[261] for CH_4. The calculated apparent radius of the pores using the normal Kelvin equation (i.e., $t(P_\Delta/P_0) = 0$ in $r(P_\Delta/P_0) = \frac{2\gamma V_L}{RT}\ln(P_\Delta/P_0) + t(P_\Delta/P_0)$ (6.8), are: 5.5 Å (H_2), 5.6 Å (D_2), 8.2 Å (N_2), 7.0 Å (CO, Sample 3), 6.3 Å (CO, sample 6) and 9.2 Å (CH_4). If we consider the hexagonal pores of Figure 6.1 as an idealized tube of radius 15 Å and use as an estimate of a monolayer thickness the Lennard-Jones σ from Table 6.1, adding a monolayer of CH_4, somewhat more than a layer of N_2 and CO, and almost two layers of H_2 and D_2 on the walls of the pore would account for the reduced volume of the pores on going from CH_4

to H_2, which is consistent with our findings on the pore volume from the volume adsorbed at the Δ-step.

6.1.7 CONCLUSIONS

We have measured an extended set of adsorption isotherms of 10 small gases on a relatively open frame Zr-MOF, namely NU-1000. Our objective was to obtain for each adsorbate the isosteric heat of adsorption, Q_{st}, both at low coverage as a function of the pair interaction energy of the different adsorbates, and as a function of amount of gas adsorbed from zero coverage to bulk three-dimensional condensation. The heats at 0.1 ML increase nearly proportional to the Lennard-Jones 6−12 pair potential energy parameter (ε) for the interaction between adsorbates (Figure 6.10). The same area of the NU-1000 samples is available to all the gases (Figure 6.8). We present DFT calculations of the enthalpy of adsorption on seven different sites associated with the NU-1000 Zr-MOF crystal for the individual gases studied (Figure 6.2, Figure 6.11, Figure 6.12, and Table 6.3). Favorable agreement is achieved when the differential heat at 0.1 ML is compared to DFT results after appropriate filling of more stable (lower-coverage) sites Figure 6.10. The filling of the pores above the statistical first layer occurs via adsorption of a significant partial second layer for the small mass quantum gases (H_2, D_2, Ne), a lower amount of second layer for the intermediate-mass gases, and no apparent second layer for C_2H_6 and Xe. For all the gases though there is a sizable adsorption step (increase in adsorption at constant *P* and *T*) that we interpret as capillary condensation in the voids left after the first (and partial second) statistical layer is formed.

6.1.8 FIGURES AND TABLES

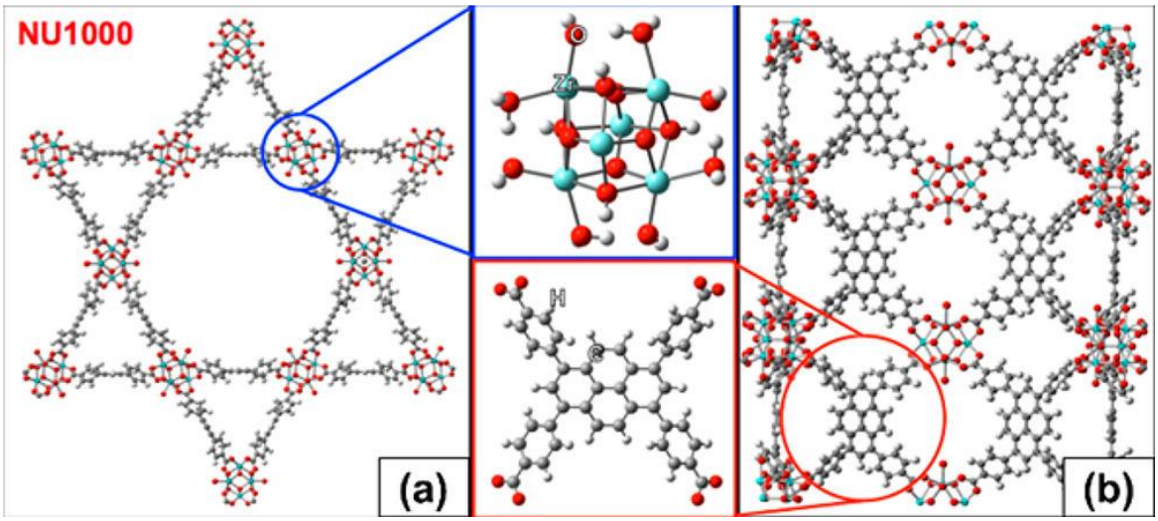

Figure 6.1. Cartoon of the NU-1000 MOF lattice: (a) Cross sectional view of the lattice (along the *c* axis) and an amplified view of one of the nodes containing the metal of interest. This view shows the large channel and six triangular channels. (b) Side view of the linkers joining the nodes and an enlarged view of the organic linkers. This view, from perpendicular to the view in part (a), along the direction bisecting the *a* and *b* axes, shows the small pores.

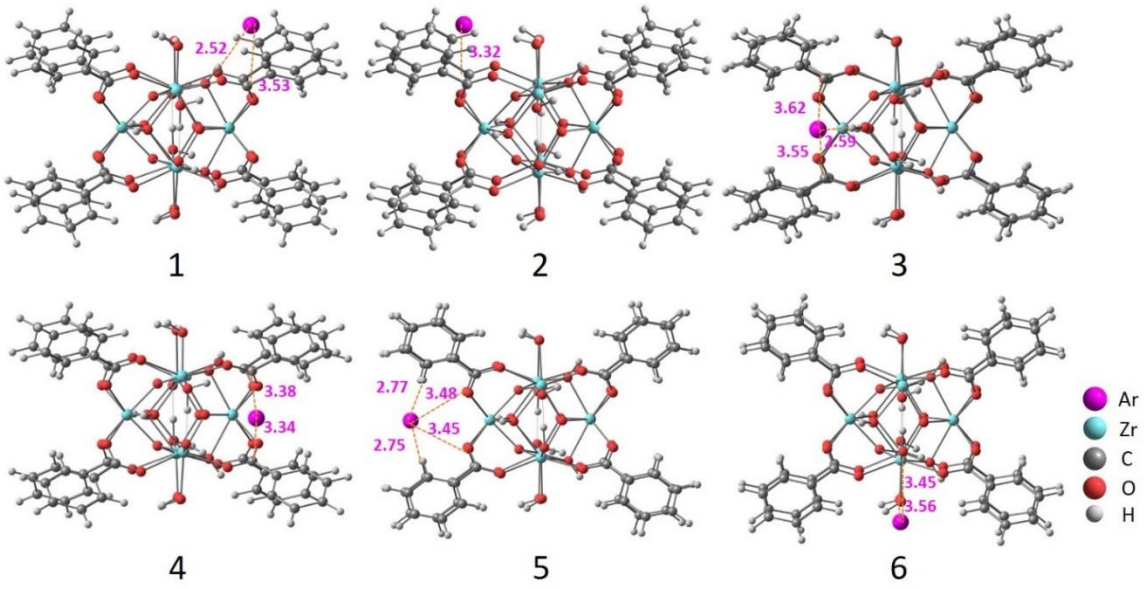

Figure 6.2. Cartoon of the node model used to identify six adsorption sites for each atom or diatomic molecule on the NU-1000 lattice. The figure illustrates the locations of the six most stable sites for Ar atoms, additional similar figures for all other atoms/molecules in this study can be found in the Supporting Information.

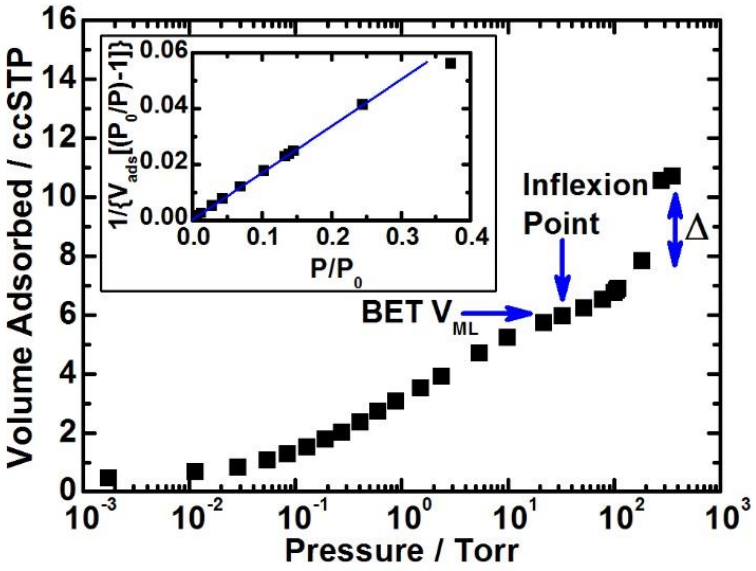

Figure 6.3. N_2 adsorption isotherm (i.e., total amount adsorbed versus pressure) on a 10.0 mg sample 7 of NU-1000, measured at 77.4 K (liquid N_2 temperature, where P_0 = 760 torr). Inset: linearized BET isotherm, $\frac{1}{\{V_{ads}[(P_0/P-1)]\}} = \frac{c-1}{cV_{ML}}(P/P_0) + \frac{1}{cV_{ML}}$ (6.2. The slope of the straight line (S) and intercept on the vertical axis (I) give a BET monolayer volume V_{ML} = 1/(S + I) = 5.93 ccSTP (horizontal arrow). Δ: condensation jump after completion of the first BET layer.

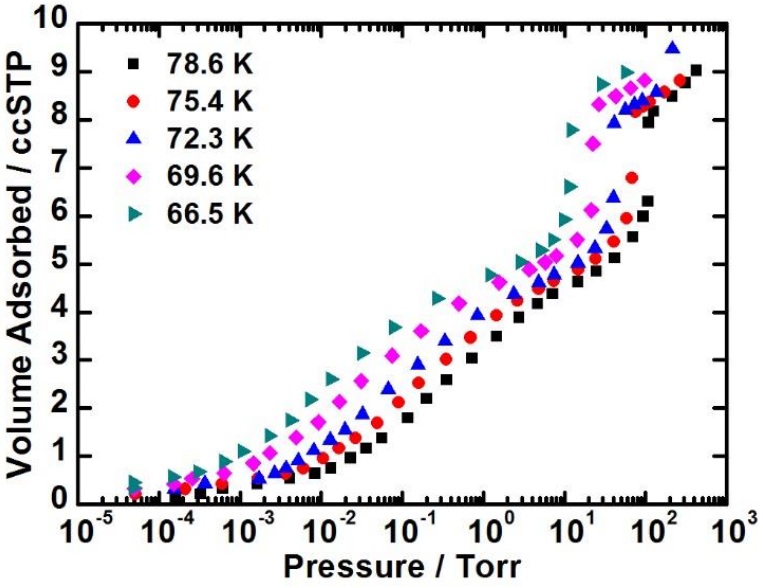

Figure 6.4. CO isotherms on NU-1000 MOF, Sample 6.

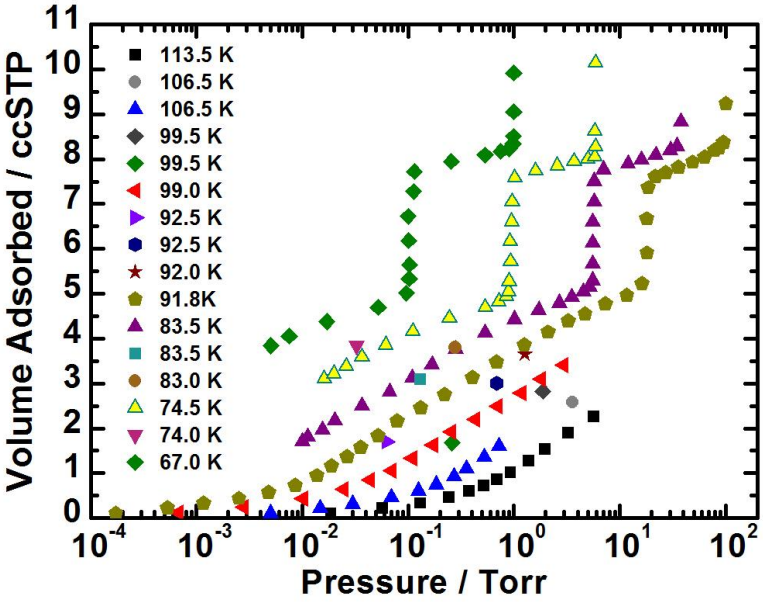

Figure 6.5. CH_4 isotherms on NU-1000 MOF, sample 6.

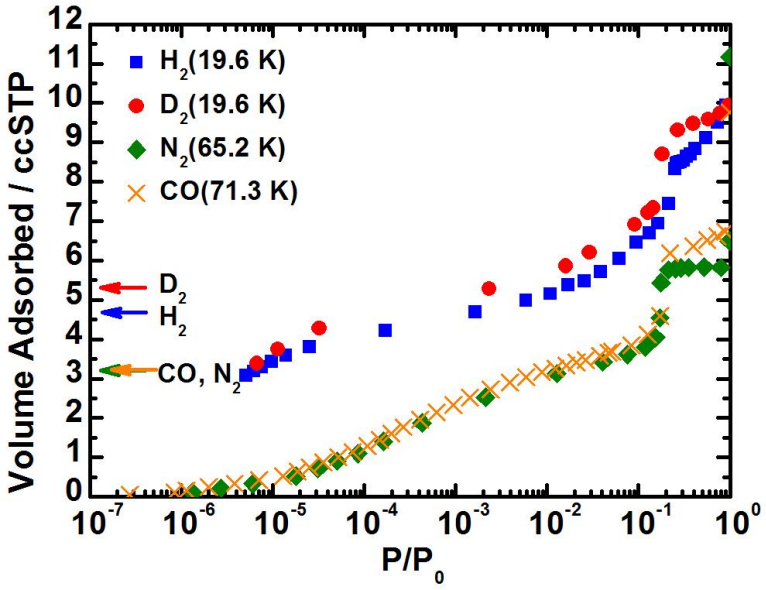

Figure 6.6. One reduced isotherm for each one of the four gases adsorbed on Sample 3 at temperatures indicated. Horizontal arrows indicate monolayer completion as listed on Table 6.2. To view all the isotherms for each gas, please see the Supporting Information.

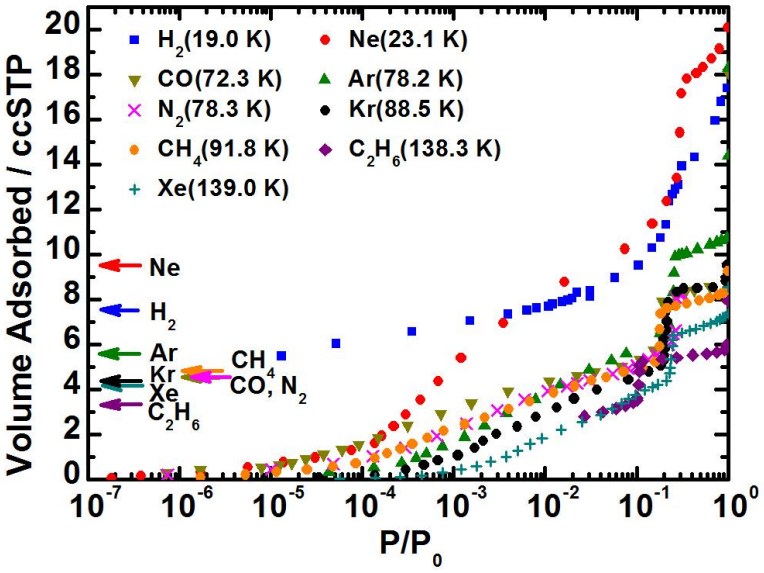

Figure 6.7. One reduced isotherm for each gas adsorbed on Sample 6 at temperatures indicated. Horizontal arrows show monolayer completion for some of the adsorbed gases. Table 6.2 lists V_{ML} for all the gases. To view all isotherms for each gas, please go to Supporting Information.

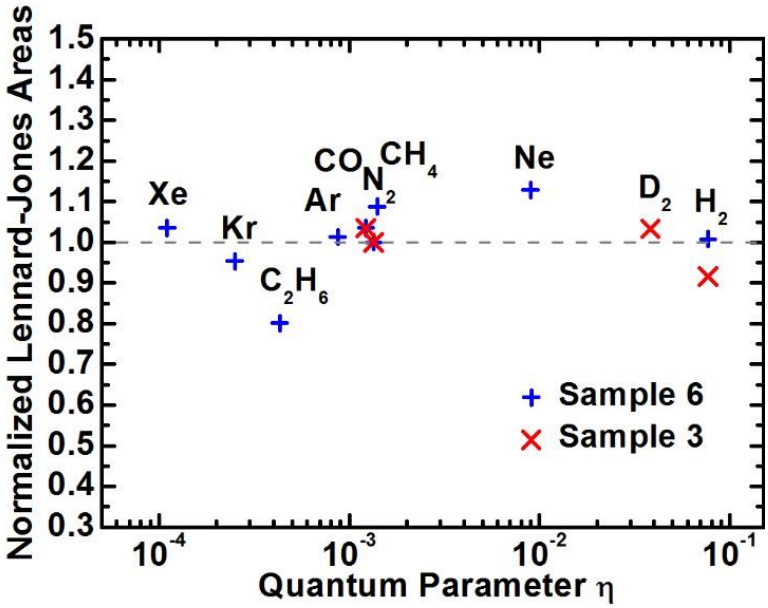

Figure 6.8. Lennard-Jones areas of Samples 3 and 6 based on the monolayer adsorption capacities for different gases, calculated using data from Table 6.1 and Table 6.2 (and normalized to that from N_2 adsorption, which gives a BET area of 2,580 m^2/g) versus the quantum parameter η for the gas, as defined in text.

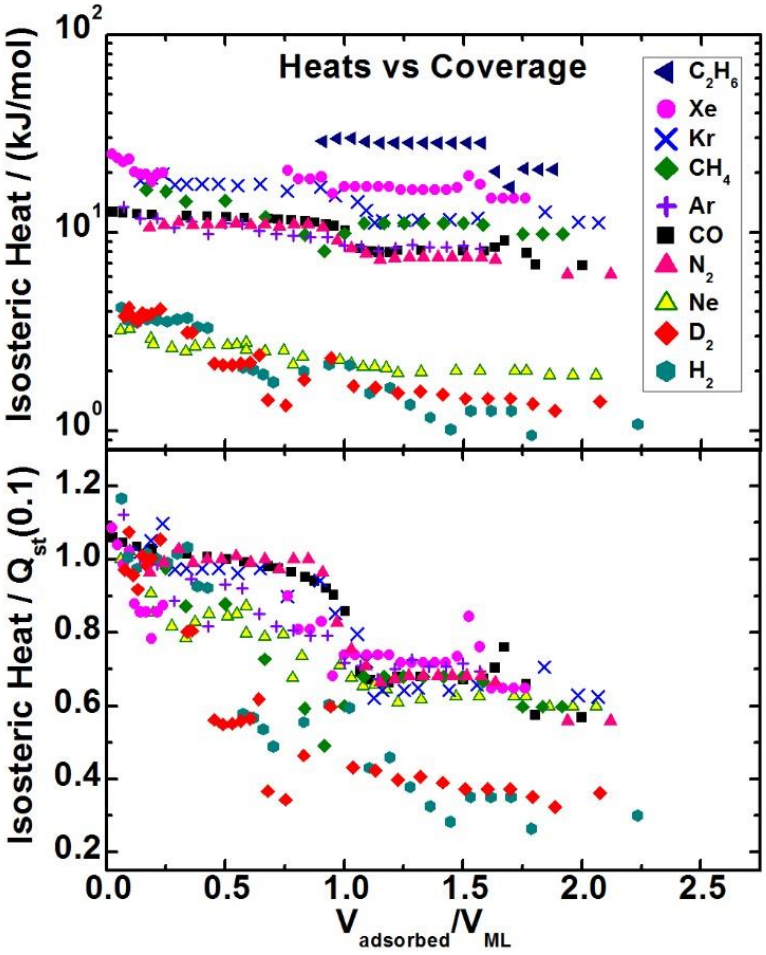

Figure 6.9. Top: Isosteric heats of adsorption versus coverage determined from analyzing isotherms at multiple temperatures. Bottom: Same data with heats normalized to value at 0.1 ML. Experimental average temperature for each gas: CO, 72.5 K; Xe, 134 K; CH_4, 95.2 K (1st layer), 79.2 K (2nd layer); Ar, 74.1 K; Ne, 26.3 K (1st third of 1st layer), 20.7 K (rest of 1st and 2nd layers); H_2 and D_2, 34 K (initial half of 1st layer), 17.5 K (2nd layer); N_2, 72 K; Kr, 84 K; C_2H_6, 142 K.

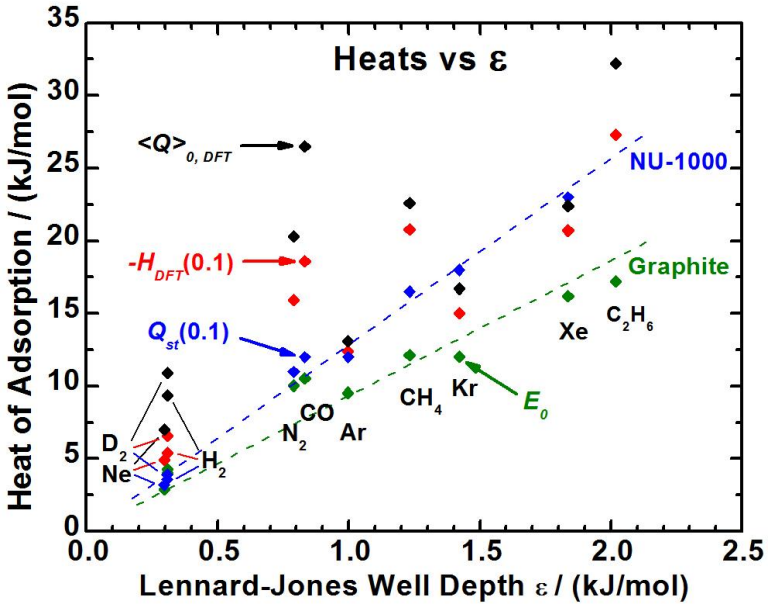

Figure 6.10. Differential isosteric heat of adsorption at 0.1 ML coverage versus the Lennard-Jones well depth, ε, for all the gases where measurements could be carried to that low coverage. Also shown are two adsorption enthalpies calculated with DFT: the thermally-averaged value at 77 K in the limit of low coverage, $\langle Q \rangle_{0,\,\mathrm{DFT}}$, and the adsorption enthalpy of the site expected to be being populated at 0.1 ML, $-H_{\mathrm{DFT}}(0.1)$, are also shown. For comparison, experimental values of the binding energy of the adsorbates on graphite(0001) in the low-coverage limit at 0 K, E_0, are also shown from Vidali et al[236].

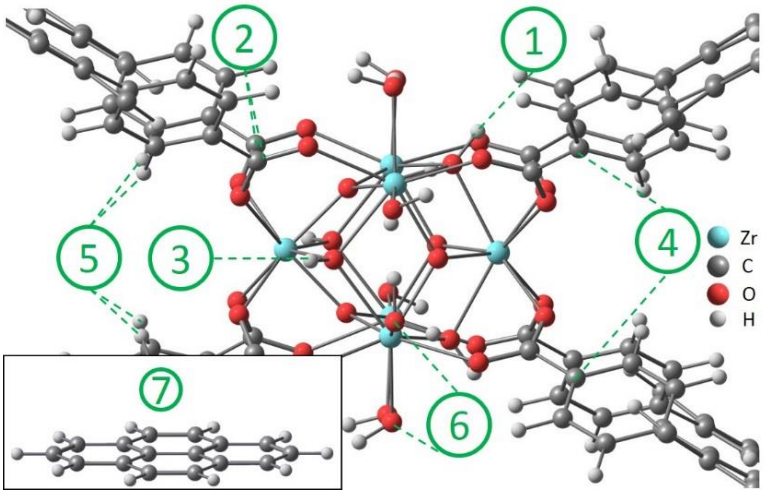

Figure 6.11. Six adsorption sites on the hexazirconium node of NU-1000, and one adsorption site on the pyrene linker (#7). Dashed lines indicate the shortest distances between adsorbates and MOF atoms. This is a view from the hexagonal pore of Figure 6.1(a).

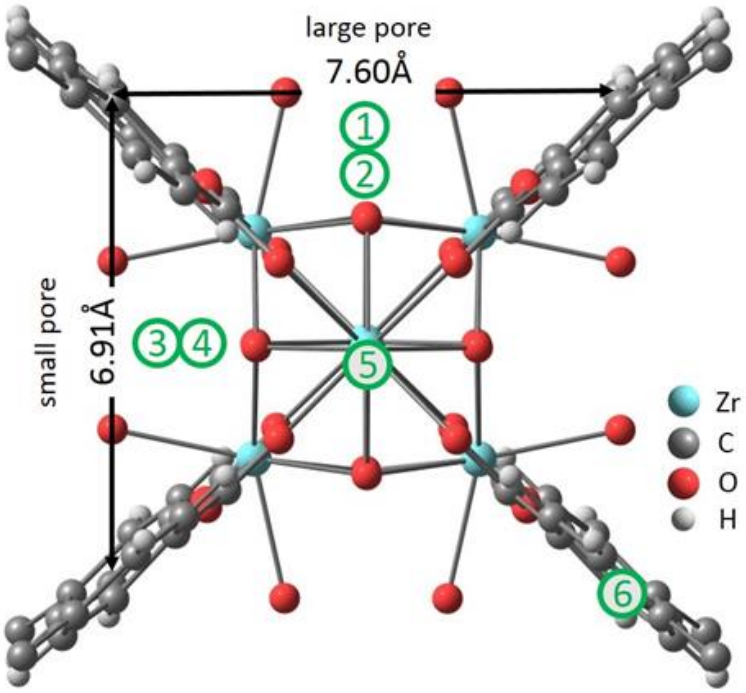

Figure 6.12. Illustration of the relation between the node and benzene rings, and six site locations. Hydrogens on the nodes are not shown for simplicity. This is a view from the triangular pore of Figure 6.1(a). Site 7 is not shown because it is farther away from the node.

Table 6.1. Gases adsorbed, Lennard-Jones potential parameters (σ, ε), molecular masses (m), quantum parameters (η), sample number used for quantitative measurements (#), and range of temperatures at which isotherms were measured (T).

gas	σ	ε	m	$\eta \times 10^3$	#	T
	Å	kJ/mol	g/mol			K
H_2	2.92	0.31	2.01	76.65	3, 6	16.5-37.5
D_2	2.92	0.31	4.03	38.23	3	16.5-37.5
Ne	2.75	0.30	20.18	8.95	6	18.0-29.0
CH_4	3.82	1.23	16.04	1.40	6	67.0-113.5
N_2	3.70	0.79	28.01	1.34	2, 3, 6, 7	65.2-78.3
CO	3.76	0.83	28.01	1.22	3, 6	66.5-78.6
Ar	3.41	1.00	39.95	0.87	6	70.0-78.2
C_2H_6	3.95	2.02	30.03	0.43	6	127.4-145.0
Kr	3.65	1.42	83.80	0.25	6	79.5-88.5
Xe	3.98	1.84	131.29	0.11	6	128.3-139.0

Table 6.2. Monolayer coverage from samples 3 and 6, and isosteric heats of adsorption at 0.1 monolayer coverage, $Q_{st}(0.1)$, measured at average temperature, $\langle T \rangle$. Such low-coverage C_2H_6 isotherms could not be measured. Also listed are the average number of molecules per Zr_6 node (per formula unit of NU-1000) in the monolayer, n_{ML}, the bulk latent heat of condensation (E_L)[256,262-268], and the ratio E_L/ε.

gas	#	V_{ML} ccSTP	n_{ML}	$\langle T \rangle$ K	$Q_{st}(0.1)$ kJ/mol	E_L kJ/mol	E_L/ε
H_2	3, 6	4.7, 7.6	86, 93	34	3.6	0.964	3.11
D_2	3	5.3	95	34	3.9	1.47	4.74
Ne	6	9.6	118	26.3	3.2	2.14	7.13
CH_4	6	4.8	59	95.2	16.5	10	8.13
N_2	3, 6	3.2, 4.7	58, 58	72	11	5.88	7.44
CO	3, 6	3.2, 4.7	58, 58	72.5	12	6.43	7.74
Ar	6	5.6	69	74.1	12	7.91	7.91
C_2H_6	6	3.3	40	142	-	15.8	7.82
Kr	6	4.6	56	84	18	11.2	7.89
Xe	6	4.2	51	134	23	15.5	8.42

Table 6.3. The adsorption enthalpies at the numbered sites, H_i, average heat of adsorption in the limit of low coverage, $\langle Q \rangle_{0,DFT}$, at 77 K and differential enthalpy of adsorption at 0.1 ML coverage in a sequential-site model, $H_{DFT}(0.1)$, all based on DFT calculations (see text), compared to the experimental isosteric heats at 0.1 ML coverage, $Q_{st}(0.1)$ (at temperatures from 26 to 142 K, see Table 6.2). All values in kJ/mol. Negative signs are omitted for all H values.

site	1	2	3	4	5	6	7	$\langle Q \rangle_{0,DFT}$	$-H_{DFT}(0.1)$	$Q_{st}(0.1)$
d_i*	2	2	2	2	2	4	4			
H_2	8.6	8.1	9.6	9.0	5.4	4.2	4.4	9.3	5.4	3.6
D_2	10.0	10.0	11.1	11.0	6.6	5.6	4.6	10.9	6.6	3.9
Ne	3.0	7.3	6.8	7.3	6.1	4.9	2.4	7.0	4.9	3.2
CH_4	21.4	19.9	23.0	20.8	6.8	11.6	8.2	22.6	20.8	16.5
N_2	15.9	15.8	20.3	16.1	3.4	9.0	3.6	20.3	15.9	11
CO	20.9	18.6	26.5	17.9	4.3	7.0	8.3	26.5	18.6	12
Ar	12.7	12.4	13.5	13.2	4.6	6.3	6.1	13.2	12.4	12
Kr	15.0	14.4	16.9	15.5	6.0	8.7	7.4	16.5	15.0	18
Xe	21.2	18.8	23.0	20.7	8.0	8.8	10.6	22.4	20.7	23
C_2H_6	27.3	27.0	32.2	27.0	15.0	11.4	11.6	32.2	27.3	-

*The number of equivalent sites of type i per node.

Table 6.4. Measured properties of adsorbed gases beyond the first layer. Column 2: Volume of voids at the Δ-step ($N_\Delta \times \sigma^3/m_{sample}$) where N_Δ is the number of atoms derived from the volume adsorbed at the Δ-step; Column 3: temperature of isotherm and phase of 3d substance, used to calculate Column 2; Column 4: ratio of full volume adsorption capacity, V_{3d}, to volume of adsorbed monolayer; Column 5: temperature of isotherm used, phase of 3d substance, and sample number, used to calculate Column 4; Column 6: ratio of measured pressures at the Δ-step (P_Δ) to the saturated vapor pressure of the bulk 3d adsorbate at the temperature (T) and 3d phase (L or S) of the isotherm. S = solid; L = liquid; (#) Sample number.

gas	V_Δ (cm^3/g)	T (K), phase	$<V_{3d}/V_{ML}>$	T (K), phase (#)	P_Δ/P_o, T (K), phase
H_2	0.095	19.6, L	2.08	19.6, L (3)	0.19, 19.6, L
D_2	0.17	19.6, L	1.96	19.6, L (3)	0.16, 17.1, S; 0.19, 19.6, L
Ne	0.3	18.0, S	2.08	23.1, S (6)	0.37, 18.0; 0.32, 21; 0.29, 23.1, S
CH_4	0.49	67.0, S	1.82	91.8, L (6)	0.11, 67.0; 0.16, 74.5; 0.14, 83.5, S; 0.18, 91.8, L
N_2	0.265	78.3, L	1.85	65.2, L (3)	0.16, 65.2; 0.22, 71.2; 0.25, 78.3, L
CO	0.335	78.6, L	1.94	78.6, L (6)	0.16, 66.5, S; 0.18, 69.6; 0.20, 72.3; 0.22, 75.4; 0.22, 78.6, L
Ar	0.43	78.2, S	1.93	78.2, S (6)	0.20, 70.0; 0.26, 78.2, S
C_2H_6	0.36	138.3, S	1.76	138.3, S (6)	0.11, 127.4; 0.11, 138.3; 0.13, 145.0, S
Kr	0.5	79.5, S	1.91	88.5, S (6)	0.20, 79.5; 0.21, 88.5, S
Xe	0.41	128.3, S	1.69	149.8, S (6)	0.20, 128.3; 0.23, 139.0, S

6.2 Heats of Adsorption of N_2, CO, Ar, and CH_4 versus Coverage on the Zr-Based MOF NU-1000: Measurements and DFT Calculations

This subchapter is reprinted with permission from reference [95]:

Vissers, G. O.; Zhang, W.;Vilches, O. E.; Liu, W.-G.; Yu, H. S.; Truhlar, D. G.; Campbell, C. T. Heats of Adsorption of N_2, CO, Ar, and CH_4 versus Coverage on the Zr-Based MOF NU-1000: Measurements and DFT Calculations. *J. Phys. Chem. C* **2019**, *123*, 6586-6591.

ABSTRACT

Equilibrium adsorption isotherms at very low coverage (0 to ~0.1 monolayer) have been measured for four simple gases, N_2, CO, Ar and CH_4, above 98 K on the metal-organic framework (MOF) NU-1000 (which has $Zr_6(\mu_3\text{-}OH)_4(\mu_3\text{-}O)_4(OH)_4(OH_2)_4$ nodes linked by pyrenes with $–COO^-$ end groups). From these, the differential isosteric heats of adsorption (Q_{st}) were determined versus coverage. These were compared to density functional calculations of the adsorption enthalpies on different sites, assuming that they are filled in a sequential order from strongest to weakest binding. This comparison shows excellent quantitative agreement on the trends for the four gases, as well as reasonable agreement in the absolute magnitude of the adsorption energies. This agreement indicates that the sites predicted by the density functional calculations to be populated at different coverages for the different gases are correct, thus further increasing our understanding of adsorption on this prototype MOF.

6.2.1 INTRODUCTION

Metal-organic frameworks (MOFs) represent an important new class of adsorbent materials and catalysts. As such, it is important to fundamentally understand the adsorption of simple gases on these materials, and to quantitatively evaluate the accuracy of density functional theory (DFT) in

predicting their adsorption energies at the different sites on the MOFs. Our team recently reported measurements of adsorption isotherms and the calculation of the isosteric (differential) heat of adsorption, Q_{st}, versus coverage from the isotherms for ten different small gases adsorbed on a Zr-based metal-organic framework (MOF) called NU-1000.[94] Those measurements were performed for ten gases (H_2, D_2, Ne, CH_4, N_2, CO, Ar, C_2H_6, Kr, and Xe) at various temperatures, from low sub-monolayer coverages (0.1 ML) up to condensation of the bulk three-dimensional phase.

NU-1000 is one of the most thermally stable MOFs[49] and has been demonstrated to have interesting catalytic applications.[48,269-275] NU-1000 has transition-metal nodes of formula $Zr_6(\mu_3\text{-}OH)_4(\mu_3\text{-}O)_4(OH)_4(OH_2)_4$ that resemble hydrated ZrO_2 clusters and can serve as catalysts or catalyst supports, and the linkers in this MOF are pyrenes (fused benzene rings) linked to the nodes via the carboxylate groups of benzoates. The monolayer completion coverages in our adsorption study were found to correspond to a large number of adsorbed molecules per Zr_6 node (58 to 69 molecules per node for the four gases studied in this present paper), and the heats of adsorption were found to decrease strongly with coverage, which is explained by the varying chemical character of the sites in a unit cell. These measurements were accompanied by density functional theory (DFT) calculations of enthalpies of adsorption at 77 K for the zero-coverage adsorption of the same gases at seven different types of sites (i) of the MOF lattice, each of which has two or four identical sites per node within each unit cell of NU-1000. The structure of NU-1000 and the DFT-calculated site locations are shown in Figure 6.13(a); the site-type multiplicities (M_i) are listed in Table 6.5.

A summary of some of the experimental results from Zhang et al.[94] is shown in Figure 6.13(b) (Figure 10 of that article) and in Table 6.5. As shown, at 10% monolayer (ML) coverage (the lowest coverages for which reliable Q_{st} values were obtained in ref [94]) the measured $Q_{st}(0.1)$

for the different gases followed an almost linear dependence on the Lennard-Jones well depth ε for the atom-atom or molecule-molecule interaction of the substances being studied. As also shown, the zero-coverage DFT adsorption enthalpies ($<Q>_{0,DFT}$) for the noble gases were close in magnitude to the measured $Q_{st}(0.1)$, while for the diatomic and polyatomic molecules the DFT enthalpies were much larger than the experimental $Q_{st}(0.1)$. Much better agreement with the experimental $Q_{st}(0.1)$ was obtained with a model assuming sequential filling of DFT adsorption sites, from high to low adsorption energies, up to 10% of a monolayer ($-H_{DFT}(0.1)$, shown in Figure 6.13(b)).

Although the previous experiments did not extend to coverages below 0.1 ML, the DFT calculated energies gave a large change in heat with coverage even below 0.1 ML within this sequential site-filling model. This stimulated the current study, where we report experimental heats of adsorption of four of these gases (N_2, CO, Ar, and CH_4) extended to much lower coverage with better resolution. The results agree well with the trends predicted by the DFT calculations, including the higher adsorption energy magnitude for the diatomic and polyatomic molecules than for the rare gas. This combination of experimental and calculated heats at different sites gives a nearly complete understanding of the adsorption of these gases on NU-1000, making this perhaps the best understood MOF in terms of adsorption properties. Furthermore, it provides confidence in the ability of DFT to predict relative adsorption energies at the many different sites in MOFs when van der Waals interactions dominate, as they do here.

6.2.2 METHODS

6.2.2.1 *Experimental Methods*

Details of the synthesis of the NU-1000 studied here and its structural characterization are presented in ref. [94], with more details in the original synthesis paper.[49] That structural

characterization is summarized below. The N_2 adsorption isotherm measured for the sample of NU-1000 studied here (Figure 6.14) is indistinguishable from that presented in the original synthesis paper[49] (i.e., within tiny run-to-run differences seen on the same sample). This further verifies that we studied the same structure here, at least with respect to gas adsorption.

As we stated in ref [94], the NU-1000 samples studied here were synthesized and activated by the same group (Farha, Hupp et al.) following the same procedures as outlined in their original paper,[49] and further outgassed by us as described in ref [94]. A great deal of structural analysis of the material we used here was provided in that original synthesis paper,[49] including X-ray diffraction (XRD), scanning electron microscopy (SEM) and diffuse reflectance infrared fourier transform spectroscopy (DRIFTS). The crystallite sizes are large, so the fraction of defect sites due to crystal terminations should be lower than 0.5%. We had published a previous paper about the adsorption energy of calcium vapor onto this same type of NU-1000 sample synthesized by that same group, in which they were coauthors.[99] The Experimental section of that joint paper with them says regarding defects: "^{1}H NMR of the digested material confirmed that activation was complete, with the only carbon-containing component being the tetra-acid of the MOF organic linker, pyrene-tetraphenylcarboxylate. Nitrogen adsorption measurements of the activated MOF yielded the BET surface area, the pore volume, and the isotherm shape expected for a clean and undamaged sample. Powder X-ray diffraction (XRD) measurements yielded the pattern expected for NU-1000, with no evidence of the formation of polymorphs such as NU-901. The MOF crystallites are necessarily terminated with linkers, nodes, or both, with the identity of the terminating units possibly being crystal-face dependent. A linker-terminated face will present unreacted carboxylic acid groups. We have been unable to observe these by DRIFTS, which is not unexpected even if they are present, as the detection limit is about 1%. A node-terminated face will present excess aqua and

hydroxo ligands. These additional ligands, if present, are likely to be indistinguishable by DRIFTS from aqua and hydroxo ligands present within the crystallites." This NU-1000 also contains a secondary framework seen in residual electron density plots in powder XRD which was estimated to be present in ~20% of the mesopores of NU-1000 (in excellent agreement with the 25% modeled in N_2 adsorption simulations).[49] The nodes and linkers in that secondary framework are nearly identical to those in the main framework, and thus provide essentially the same types of adsorption sites as we have modelled here with DFT based on the main framework crystal structure. That same synthesis team (Farha, Hupp et al.) also used potentiometric acid–base titrations to look for defects in this same material, and were unable to find any defects except for the type already expected from this secondary framework structure.[276]

The methods and apparatus are essentially the same as those we reported previously,[94] with some minor modifications in methods. This study focusses on coverages in the region below 0.1 monolayer, and thus required using higher temperatures (T) than those reported in ref [94]. We used the Langmuir isotherm equation to estimate the temperature of the isotherm at which to measure the adsorption pressure of the calculated strongest site (called Site 3 in Figure 6.13(a)), compatible with our absolute pressure measurement system. Pressures were measured with a 10 Torr range or 1000 Torr range MKS Baratron capacitance manometer, accurate to 1% at full range and chosen for best accuracy.

We measured a N_2 adsorption isotherm at approximately 77 K for a new sample of NU-1000 (Sample 8, prepared as we reported previously[94]), as shown in Figure 6.14. We used the BET equation to determine the BET monolayer capacity V_{ML} of this sample (5.11 ccSTP). Considering the mass-loading difference between samples, we scaled this monolayer capacity to the value

reported by ref [94] for Sample 6 of the NU-1000 (4.7 ccSTP) to compare data from different samples. Sample 8 was used for the new experiments reported here.

Before each isotherm measurement, the sample was pumped at 23 °C to about 10^{-6} Torr, then cooled to the desired temperature. At coverages below 0.1 ML, we either added (or removed) gas at a fixed *T* or changed *T* with the fixed amount dosed. We repeatedly verified that we reached the same volume adsorbed at a given temperature and pressure whether approaching from lower of higher coverage (i.e., that our procedure allowed us to reach true equilibrium). The adsorption cell volume was calibrated as a function of temperature using He gas.

6.2.2.2 *Theoretical Methods*

Full details about the theoretical methods were provided previously;[94] here we just give a brief summary. For the DFT calculations, we adapted the cluster model that had been used in a previous study.[99] The geometry optimizations employed the M06-L density functional[129] and 6-31G(d,p) basis set.[135] The enthalpies were then calculated based on interaction energies evaluated with a larger basis set, 6-311++G(d,p),[246] and a counterpoise correction.[277]

6.2.3 RESULTS AND DISCUSSION

Figure 6.15 shows the DFT calculated differential heat of adsorption, $-H_i$, versus coverage at 77K, taken from Table 6.5, assuming sequential filling of sites from the strongest to the weakest and no lateral interactions between adsorbates as sites fill. If we use N_2 as an example, Site 3 of Figure 6.13(a) is the strongest site with multiplicity of 2, so the first two "sequential sites" in Figure 6.15 both correspond to a structure like Site 3 of Figure 6.13(a). We will compare newly measured heats below to this aspect of our previously reported DFT calculations.

Adsorption isotherms for the four gases in the central range of adsorption energies of Figure 6.13(b), i.e., the gases N_2, CO, Ar, and CH_4, were measured versus temperature to determine

heats of adsorption versus coverage, with emphasis on the region below 0.1 monolayer. Figures S2 through S5 in the Supporting Information show for each gas the expanded low-coverage isotherms. For each gas, we measured one complete isotherm, lowering the temperature and adding gas until we reached liquid- or solid-vapor coexistence at saturated vapor pressure, P_0. Once P_0 was reached, lowering T allowed us to check the thermometer readings vs. tabulated saturated vapor pressures. The differential isosteric heats of adsorption, Q_{st}, were calculated from these isotherms using the equilibrium pressure (P) versus temperature (T) at constant coverage (θ) in the standard relation:[235]

$$Q_{st}(\theta) = -R[\partial(lnP)/\partial(1/T)]_{\theta} \tag{6.9}$$

where R is the gas constant. The isotherms have no singularities in the range measured. They were smoothed and digitized every 0.02 ccSTP adsorbed. From the table of data for each gas, graphs of ln P vs. 1/T were constructed. Straight lines were drawn through the constant coverage points, their slopes (multiplied by -R) giving Q_{st} as a function of coverage. The amount of gas adsorbed was converted to site occupancy assuming a sequential filling of sites from strongest to weakest adsorption energies. From Table 6.2 of ref. [94], the measured number of adsorbed atoms or molecules per Zr-node at monolayer completion are n_{ML} = 58, 58, 69, and 59 for N_2, CO, Ar and CH_4, respectively. The number of sites being occupied as coverage increases is given by

$$\text{no. of sites occupied} = n_{\text{ML}}(V_{\text{ads}}/V_{\text{ML}}) \tag{6.10}$$

where V_{ML} is the monolayer adsorbed quantity and V_{ads} is the actual amount adsorbed. Thus, if there is a sequential filling of sites, 0.1 monolayer corresponds, in the same order, to roughly 6, 6, 7, and 6 molecules per node being adsorbed. The resulting plots of differential heat of adsorption versus coverage or site occupancy for N_2, CO, Ar, and CH_4 are shown in Figure 6.16. The DFT results from Figure 6.15 are added for comparison.

The heats of adsorption of N_2 and CO on NU-1000 in Figure 6.16 decrease strongly with coverage in the initial stages of adsorption (below 10% of saturation coverage) due to the sequential filling of different types of adsorption sites present on the NU-1000, as is remarkably well predicted by DFT. The heats of adsorption of Ar and CH_4, on the other hand, decrease more slowly with coverage, as also predicted by the DFT calculations. The average temperature of the current measurements is about 40 K higher than the 77 K of the DFT calculations, so the new measurements should be higher by about $R \times \Delta T \approx 0.33$ kJ/mol.

As seen in Figure 6.16, there is very good agreement between these measured heats of adsorption versus coverage in this low-coverage regime and the differential heats calculated with DFT assuming sequential site filling for all four gases, especially in the magnitude of the decrease in heat with coverage. This suggests that the sites and binding energies predicted by DFT represent a very accurate reflection of reality, making these adsorbates on NU-1000 some of the best understood of all adsorbate-on-MOF systems. The DFT calculations also reproduce the faster decreases in heat of adsorption with coverage seen for N_2 and CO than for Ar and CH_4, which is probably associated with the stronger interaction between adsorbate pi bonds (present in CO and N_2 only) and Site 3 on the node. The DFT calculations overestimate the heats of adsorption by 2-5 kJ/mol for all the molecular gases, with less disagreement (2-3 kJ/mol) for the single-element molecule (N_2), but larger disagreement (~5 kJ/mol) for the other molecular gases (CO and CH_4). This overestimate of the heats is probably due to an intrinsic error in the DFT method. The DFT heats show almost no difference with our measurement for the monatomic noble gas (Ar). It is clear that the M06-L functional is particularly well suited for this study, probably because it takes advantage of the ability of meta functionals to account for damped dispersion at van der Waals distances.[238,244]

The temperatures for the DFT energies (77 K) were chosen to match the average of the experiments in our previous paper where they were published. They are lower than in the current experiments, which used higher temperatures to achieve lower equilibrium coverages. However, since the heat-capacity effect on the heat is small (~$R\Delta T$), this temperature difference is not considered important. (The heat capacity effect was estimated from the vibrational partition functions as described earlier,[94] using frequencies provided by normal-mode analyses.)

The range of coverages studied in Figure 6.16 (~0.5% to 10 % of a ML) is so low that one must consider whether the results might be dominated by defects. As noted in the Experimental Methods section, structural analyses of the NU-1000 synthesized exactly as the samples used here (and showing identical N_2 adsorption isotherms as measured here) have <1% defects, except for a secondary framework that has nodes and linkers arranged in a way that is nearly identical to those in the main framework. This secondary framework thus provides essentially the same types of adsorption sites as we have modelled here with DFT based on the main framework crystal structure. The excellent agreement in Figure 6.16 between the DFT-calculated heats and those measured here also strongly suggests that defects are not a significant problem here.

Figure 6.17 is the same type plot as Figure 6.16, but now extended all the way up to 1.0 ML using data from our prior study.[94] It is very clear in this comparison to experiments that the assumption in these DFT-based estimates of adsorption heats that adsorbate-adsorbate interactions are negligible breaks down severely soon after filling 8 sites per node with adsorbates. The measured heats stay much higher than predicted, which we attribute to adsorbate-adsorbate van der Waals (vdW) attractions. The importance of these vdW attractions has been clearly observed in studies of CH_4 adsorption on other MOFs,[243,278,279] and they are expected to be important for all four of these gases when adsorbed on surfaces to which they are very weakly bonded.

However, it is also clear in Figure 6.17 that at coverages below 8 adsorbates per node (i.e., ~0.1 ML and below), that these adsorbate-adsorbate attractions are not yet important. This is because the sites that are available here bind these adsorbates so strongly to well-separated sites that it would be uphill in energy to move two adsorbates closer together where they could enjoy these vdW attractions. For example, when 8 sites per node are filled, the closest CH_4−CH_4 separation is greater than 0.60 nm (based on our DFT geometries for isolated adsorbates), compared to the CH_4−CH_4 van der Waals bond distance of 0.43 nm from its Lennard-Jones parameters.[94] This low-coverage region is perhaps most interesting from the point-of-view of benchmarking comparisons to theory, since the lack of adsorbate-adsorbate interactions removes many of the assumptions needed for theoretical modeling of higher coverages,, and thus makes a far simpler and more direct comparison. Heats of adsorption in this low-coverage regime are rarely reported on any MOFs with such high coverage resolution as we do in Figure 6.16 on NU-1000 with four different gases. The heats of adsorption of CH_4 and N_2 have been measured at low coverages on Fe-MOF-74.[245]

In contrast to the case above with 8 or fewer adsorbates per node, when 9 or more adsorbates per node are sequentially populated, the minimum adsorbate-adsorbate distance gets very close to the Lennard-Jones bond distance. The resulting vdW attractions explain why the heats at this coverage in Figure 6.17 suddenly get larger than predicted by this sequential-site-filling model, which neglects adsorbate-adsorbate interactions.

Figure 6.18 compares the results from our present measurements to the previous DFT results and previous measurements reported by ref. [94]. The results are shown in the order of increasing Lennard-Jones well depth, ε. The present measurements at 0.1 ML agree with previous measurements to within <2 kJ/mol. The magnitude of heats calculated by DFT (in the limit of

zero coverage at 77 K, $<Q>_{0,DFT}$) is somewhat larger for the molecules than the measured values, whereas for the monoatomic gas (Ar) these values agree within uncertainties.

The data show that at zero coverage the adsorption energies do not follow a linear dependence on the Lennard-Jones well depth, ε, but rather each molecule has its own adsorption characteristic dependence on coordination and accommodation on the MOF nodes and linkers. The strongest adsorption site is situated near a Zr atom but aided by two organic rings as shown in Figure 6.13(a) (Site 3). The origin of the discrepancy in the magnitude between the DFT enthalpy calculations and the Q_{st} measurements is not resolved. On the experimental side, it is possible that the NU-1000 sample has impurities adsorbed on the strongest site that cannot be removed by simple baking in vacuum. We have baked samples of NU-1000 up to 300 °C at 7×10^{-7} Torr and immediately run N_2 isotherms. Only very small changes were seen in the monolayer capacity up to 250 °C. Baking at 300 °C decreased the effective substrate area significantly. We have not explored the zero-coverage limit in detail.

6.2.4 CONCLUSOINS

In summary, the heats of adsorption of N_2, CO, Ar, and CH_4 on NU-1000 decrease strongly with coverage in the initial stages of adsorption (below 10% of saturation coverage), due to the sequential filling of different types of adsorption sites present on NU-1000, as is remarkably well predicted by DFT. The heat decreases more strongly with coverage for the less symmetric gases (CO and N_2) than for Ar and CH_4, as also predicted by DFT. These agreements strongly support the nature of the sites predicted by DFT for the adsorption of the ten different gases reported in our previous study,[94] especially for this subset of four. These adsorbates on NU-1000 are now some of the best understood of all adsorbates on any MOF system.

6.2.5 FIGURES AND TABLES

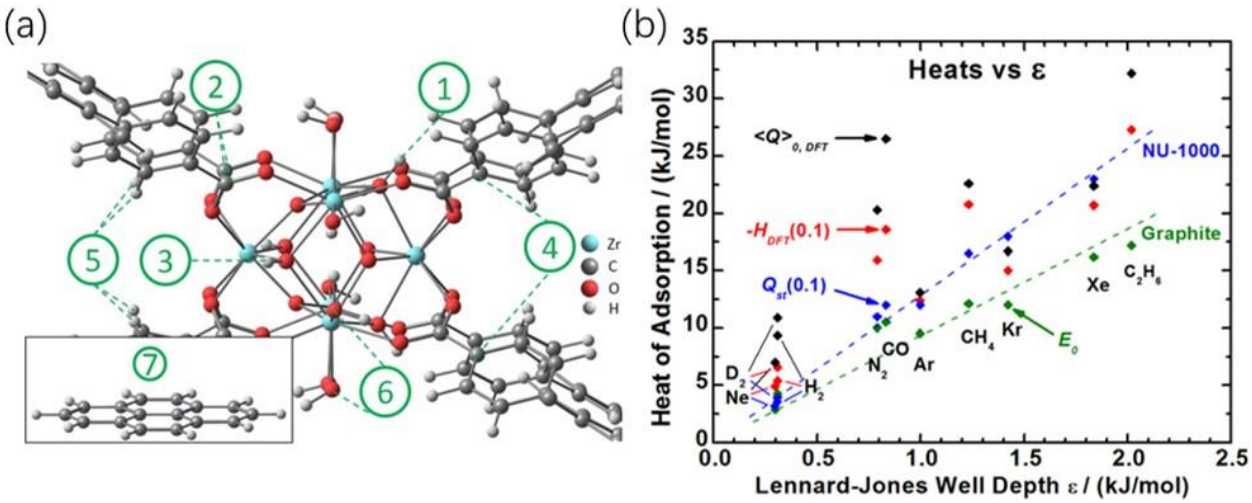

Figure 6.13. (a) Six adsorption sites on the hexazirconium node of NU-1000 and one adsorption site (#7) on the pyrene linker. Dashed lines indicate the shortest distances between adsorbates and MOF atoms. (b) Differential isosteric heat of adsorption at 0.1 ML coverage versus the Lennard-Jones well depth, ε, for all the gases for which measurements could be carried to that low coverage. Also shown are two adsorption enthalpies calculated with DFT: the thermally-averaged value at 77 K in the limit of low coverage, which is labeled as $<Q>_{0,\,\mathrm{DFT}}$, and the adsorption enthalpy of the site expected to be populated at 0.1 ML, which is labeled as $-H_{\mathrm{DFT}}(0.1)$. For comparison, experimental values of the binding energy of the adsorbates on graphite(0001) in the low-coverage limit at 0 K, E_0, are also shown from Vidali et al.[236] Reprinted with permission from ref [94]. Copyright 2017 American Chemical Society.

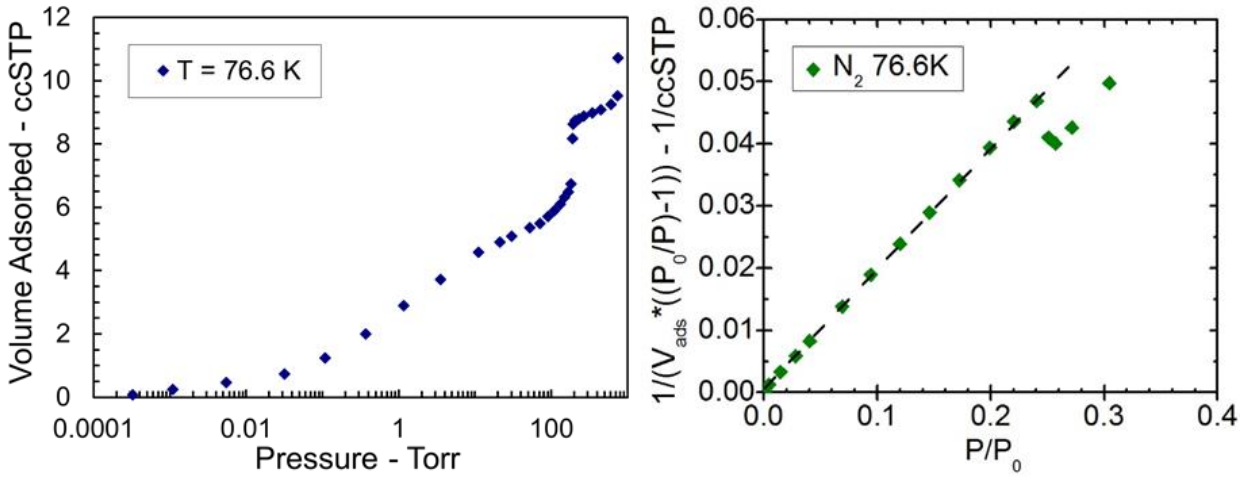

Figure 6.14. Left: N_2 equilibrium adsorption isotherm on Sample 8 of NU-1000 measured at approximately 77 K in the cryocooler system after baking for several hours at 75 °C and 10^{-6} Torr. Right: BET plot of this same N_2 isotherm. Here, V_{ads} is the volume of gas adsorbed (if measured at STP), P is the pressure and P_0 is the equilibrium vapor pressure of the bulk liquid at the measurement temperature. The BET linearized best-fit equation shown gives V_{ML} = 5.11 ccSTP. This value was used to scale coverages to those of Sample 6 for which V_{ML} = 4.7 ccSTP (i.e., ~8% smaller sample size).

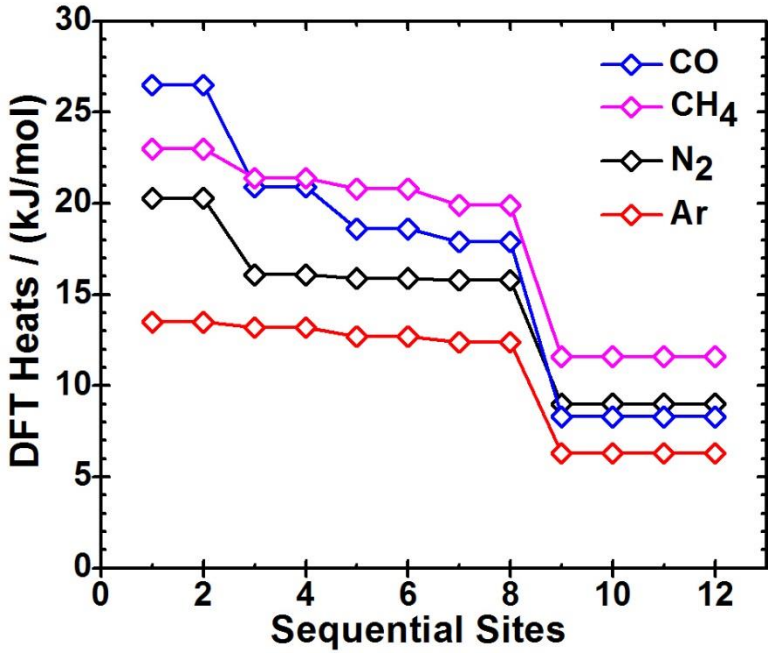

Figure 6.15. Calculated isosteric heats of adsorption at 77 K versus coverage using the DFT enthalpies calculated at zero coverage in the different sites, $-H_i$, assuming that the sites are filled sequentially with no adsorbate-adsorbate interactions. The five strongest structurally-distinct sites found from DFT have multiplicities 2, 2, 2, 2 and 4, from strongest to weakest (with a total of 12 sites shown here).

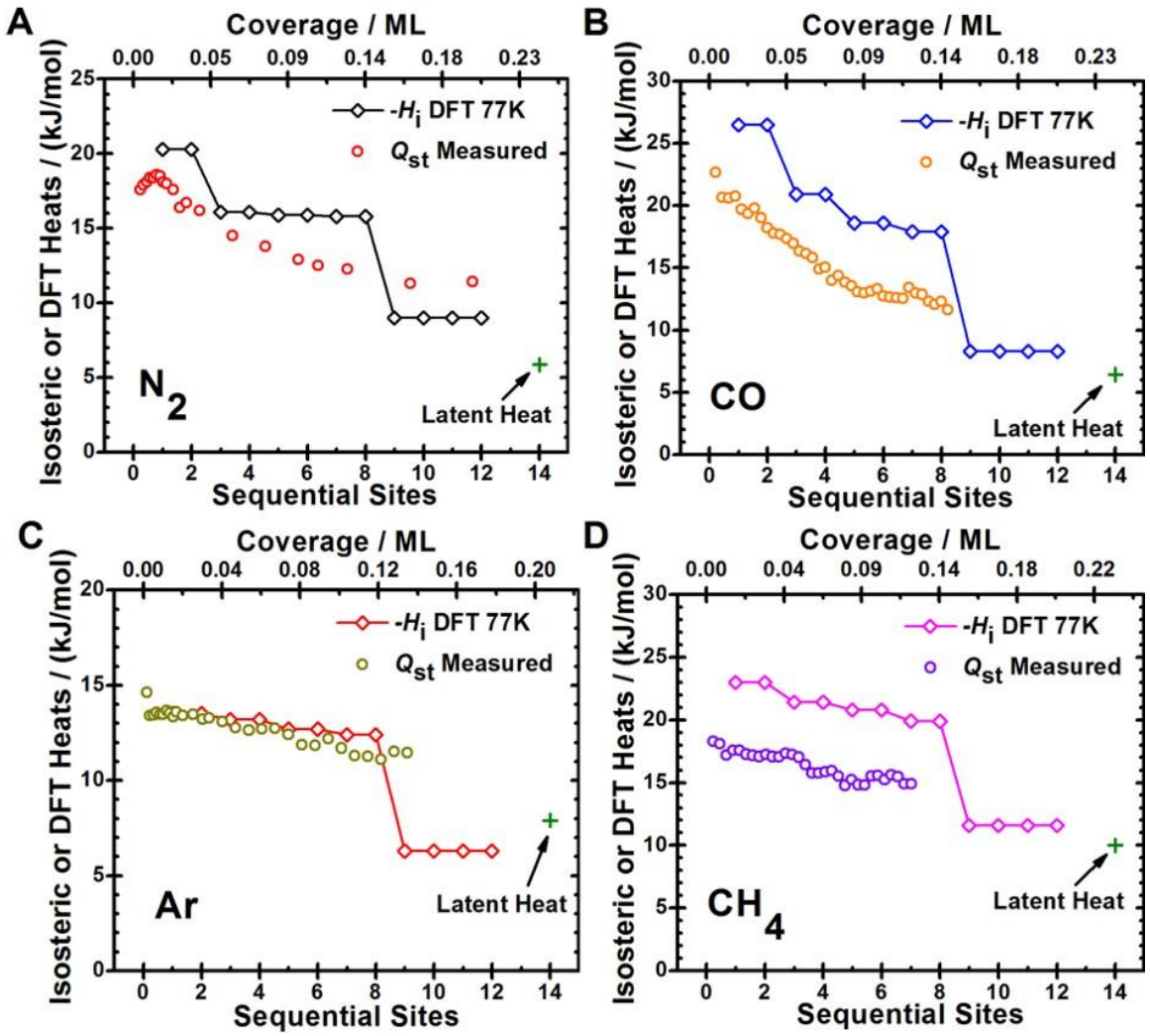

Figure 6.16. The very low coverage isosteric heats (Q_{st}) of N_2, CO, Ar, and CH_4 adsorption as functions of the amount adsorbed as determined from the measured isotherms. Also shown is the DFT estimate at 77 K ($-H_i$) assuming sequential filling of sites, taken from Figure 6.15 and Table 6.5. The bulk latent heats of vaporization from the literature[262,264,267] are also shown (green crosses).

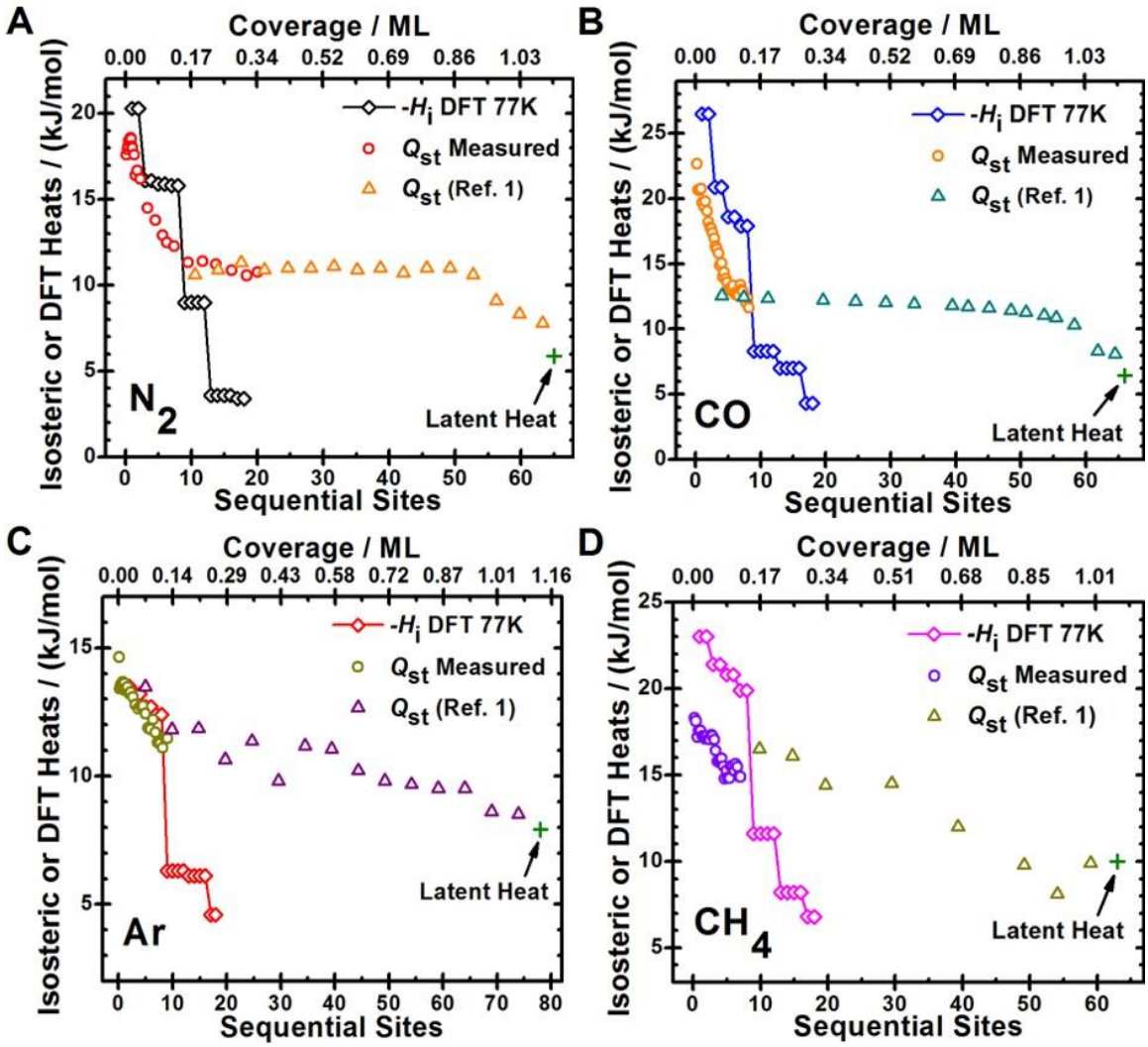

Figure 6.17. The same as Figure 6.16, but now extended to much higher coverage (1.0 ML) using experimental heats from our prior study[94] (open triangles) and the DFT estimate at 77 K ($-H_i$) assuming sequential filling of sites, taken from Table 6.5 (just as in Figure 6.16, but now going to the highest coverage, or weakest binding site, studied by DFT).

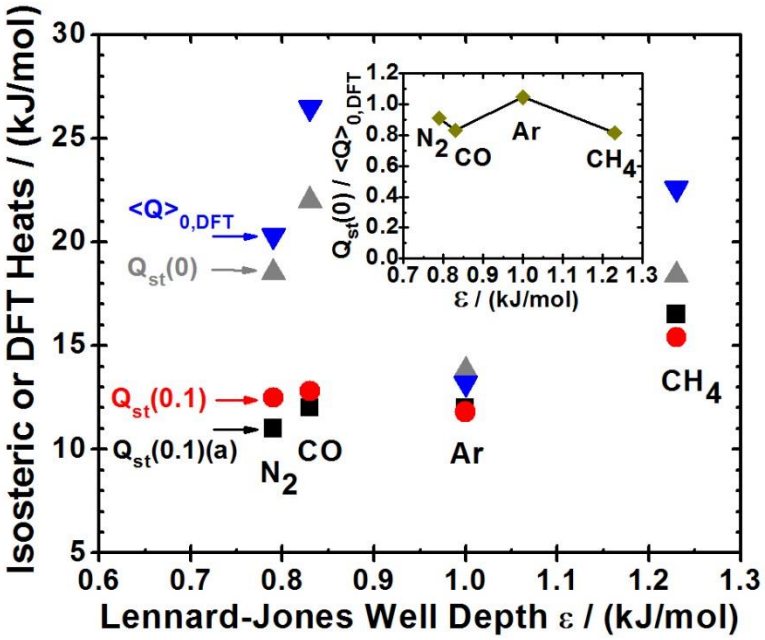

Figure 6.18. Calculated (DFT) heat of adsorption at zero coverage and 77 K ($<Q>_{0,DFT}$) from ref. [94], measured differential Isosteric heat of adsorption at 0 and 0.1 ML coverage ($Q_{st}(0)$ and $Q_{st}(0.1)$) from this experiment, and $Q_{st}(0.1)$ from ref. [94] (labelled with "(a)") for all four gases studied here, plotted as a function of increasing Lennard-Jones well depth. Inset is the ratio between $Q_{st}(0)/<Q>_{0,DFT}$ as a function of increasing Lennard-Jones well depth.

Table 6.5. Four Gases Used in this Study, their Experimental Lennard-Jones Well Depth (ε), their Enthalpy of Adsorption at Site *I* Calculated by DFT[b] (H_i) at the Seven Adsorption Sites Shown in Figure 6.13 (from ref. [94]), their Experimental Isosteric Heats of Adsorption at 0.1 ML ($Q_{st}(0.1)$) from the Same Reference (Labelled with "(a)"), their Experimental $Q_{st}(0.1)$ and $Q_{st}(0)$ from the Present Work, and the Range of Temperatures over which the Isotherms Used to Calculate the Q_{st} Values were Measured[a]

gas	ε	calculated adsorption enthalpies at 77 K							$Q_{st}(0.1)$ (a)	$Q_{st}(0.1)$	$Q_{st}(0)$	temperature range (K)
		$-H_1$	$-H_2$	$-H_3$	$-H_4$	$-H_5$	$-H_6$	$-H_7$				
N_2	0.79	15.9	15.8	20.3	16.1	3.4	9	3.6	11	12.5	18.5	98-128
CO	0.83	20.9	18.6	26.5	17.9	4.3	7	8.3	12	12.8	22	113-154
Ar	1	12.7	12.4	13.5	13.2	4.6	6.3	6.1	12	11.8	13.8	98-118
CH_4	1.23	21.4	19.9	23	20.8	6.8	11.6	8.2	16.5	15.4	18.4	118-137
M_i		2	2	2	2	2	4	4				

[a]All energies and enthalpies are in kJ/mol. The table also shows the multiplicities (M_i) of the sites. [b]The DFT methods are described in detail in ref. [94]. (a) From measurements in ref. [94].

CONCLUSION

To sum up, this dissertation provides deeper and systematic understandings of metal and gas adsorption on high-surface-area catalyst support materials, in the fields of heterogeneous catalysis and gas storage/separation relevant to energy and environmental industries.

Chapter 2 describes the standard procedure and experimental setup for metal vapor adsorption calorimetry and equilibrium adsorption isotherm (EAI). The metal vapor adsorption calorimeter described in Section 2.1 has been applied to drop-cast films of metal–organic frameworks (MOFs) NU-1000 described in Chapter 3. The Brunauer–Emmett–Teller (BET) system described in Section 2.2 has been used to measure equilibrium adsorption isotherms for many small gas molecules on NU-1000 in Chapter 6.

Chapter 3 describes the study of Ca vapor adsorption on a Zr-based metal–organic framework (MOF) NU-1000 at 300 K. Calcium vapor reacts initially with a high exothermicity (~ -513 and ~ -570 kJ/mol for samples outgassed at 348 and 378 K, respectively), attributed to Ca reacting with carboxylic acid groups, free water, or both on the internal surfaces. The exothermicity slowly drops to −280 kJ/mol by 2 ML, attributed to a gradual switch to reaction of Ca with $-OH_x$ on Zr_6 nodes deep below the external surface, with an average enthalpy of reaction equal to -366 kJ per mole of Ca. The very slow growth of Ca LEIS and XPS signals shows that these reactions proceed to ~20 nm below the external surface before the diffusion of transiently adsorbed Ca atoms becomes too slow to find unreacted sites on the internal surfaces. Beyond 2 ML, the exothermicity of adsorption decreases exponentially to the sublimation enthalpy of Ca (178 kJ/mol), reaching this limit by 5 ML; this is attributed to the formation of Ca(solid) nanoparticles near and on the MOF's external surface.

Chapter 4 introduces a novel calorimetry method that implements a metal-coated $LiTaO_3$ crystal for heat detection and extends metal adsorption calorimetry to surfaces of nanomaterials that are deposited from liquid solutions, as is typical when preparing industrial catalyst materials. We demonstrate the capabilities of this new calorimeter by measuring the bond energies of Ag vapor onto the clean surfaces of anatase TiO_2 nanoparticles (5 nm diameter) at 300 K, which were directly deposited onto the $LiTaO_3$ heat detector by simple drop-casting to form a 2-micron-thick TiO_2 film. Adsorbed H_2O and organic impurities were cleaned off the surface of the drop-casted TiO_2 film by heating the sample to ~725 K in a low oxygen pressure. The measured sticking probability is above 0.988 for all Ag coverages. The initial heat of adsorption is ~206 kJ/mol. The heat then increases asymptotically to the heat of sublimation of bulk Ag(s), 285 kJ/mol, at higher Ag coverages. To our knowledge, this is the <u>only</u> metal adsorption calorimeter capable of measuring metal adsorption energies on the surfaces of solution-prepared high-surface-area catalyst support materials.

Chapter 5 describes the <u>first</u> adsorption calorimetry of metal gas atoms on any atomically smooth well-ordered <u>mixed</u> oxide surface, using the new metal adsorption calorimeter introduced in Chapter 4. Unilamellar $HCa_2Nb_3O_{10}$ nanosheets were easily deposited onto the $LiTaO_3$ heat detector as single-crystalline mixed-oxide thin films using Langmuir-Blodgett (LB) techniques. A clean, dehydrated ("dh") $HCa_2Nb_3O_{10}(001)$ surface was obtained after heating the nanosheets to ~725 K in a low oxygen pressure. The He^+ LEIS and adsorption calorimetry results show that Ag grows on the dh-$HCa_2Nb_3O_{10}(001)$ surface as 2D islands that are mostly two layers and some three layers thick with a coverage-averaged heat of adsorption of ~320 kJ/mol in the first monolayer. As the Ag coverage increases, Ag atoms add on top of the 2D islands, making 3D nanoparticles and eventually a continuous 3D film, with the heat of adsorption reaching the sublimation enthalpy of

bulk Ag(s), 285 kJ/mol. A very high adhesion energy of Ag(s) to dh-$HCa_2Nb_3O_{10}$(001) of 4.33 J/m^2 is estimated from the heats of adsorption and explains why this dh-$HCa_2Nb_3O_{10}$ support imparts unusual stability against sintering to transition metal nanoparticles. At very low coverages, Ag is in the form of $Ag^{\delta+}$, which causes a ~2 eV shift to higher binding energy of the O 1s XPS peaks of nearby O atoms in the first two layers of the dh-HCa2Nb3O10(001) support. Above 0.18 ML, Ag adsorbs in neutral form.

Chapter 6 reports the adsorption isotherms for many small gases on NU-1000 from zero coverage up to the condensation of bulk three-dimensional phase, together with density functional theory (DFT) calculations of the single-atom/single-molecule adsorption enthalpies at 77 K. At coverage below 0.1 monolayer (ML) when the adsorbate-adsorbate attractions are not yet important, the heats of adsorption of N_2, CO, Ar, and CH_4 on NU-1000 decrease strongly with coverage, due to the sequential filling of different types of adsorption sites present on NU-1000, as is remarkably well predicted by DFT. The heats at 0.1 ML for Ne, H_2, D_2, N_2, CO, Ar, CH_4, Kr, and Xe increase nearly proportional to the Lennard-Jones 6−12 pair potential energy parameter (ε) for the interaction between adsorbates. The same area of the NU-1000 samples is available to all the gases. For all the gases there is a sizable adsorption step (increase in adsorption at constant *P* and *T*) that we interpret as capillary condensation in the voids left after the first (and partial second) statistical layer is formed.

Here, I want to emphasize the importance of the new metal adsorption calorimeter introduced in **Chapter 4**. To clarify the structure–activity relationships in supported metal nanoparticle catalysts and their sintering kinetics, researchers have adopted a model catalysts approach whereby structurally well-defined samples are prepared by vapor deposition of the metal onto single-crystal oxide surfaces, which encounters the well-known “materials gap” with respect

to real industrial catalysts. To bridge this materials gap, this calorimeter allows one to measure the strength of metal atom bonding and the adhesion energy of metal nanoparticles to clean surfaces of technologically relevant catalyst support materials, e.g., metal oxide nanoparticles and perovskite nanosheets. This opens up new opportunities for discovering better support materials and for basic scientific study of structure / function relationships with respect to metal / support bond energies.

REFERENCES

(1) *BP Statistical Review of World Energy 2018*.
(2) Suplee, C. *What You Need to Know About Energy*; The National Academies Press: Washington, DC, 2008.
(3) Vlachos, D. G.; Caratzoulas, S. The roles of catalysis and reaction engineering in overcoming the energy and the environment crisis. *Chem. Eng. Sci.* **2010**, *65*, 18-29.
(4) Thomas, J. M.; Thomas, W. J. *Principles and practice of heterogeneous catalysis*; Wiley-VCH: Weinheim, Germany, 2014.
(5) Erisman, J. W.; Sutton, M. A.; Galloway, J.; Klimont, Z.; Winiwarter, W. How a century of ammonia synthesis changed the world. *Nat. Geosci.* **2008**, *1*, 636.
(6) Friend, C. M.; Xu, B. Heterogeneous Catalysis: A Central Science for a Sustainable Future. *Acc. Chem. Res.* **2017**, *50*, 517-521.
(7) Foreword for the Gerhard Ertl Festschrift. *J. Phys. Chem. B* **2004**, *108*, 14183-14186.
(8) Freund, H. Gerhard Ertl: Congratulations! *Surf. Sci. Rep.* **2008**, *63*, iii-iv.
(9) Ertl, G. Surface Science and Catalysis—Studies on the Mechanism of Ammonia Synthesis: The P. H. Emmett Award Address. *Catal. Rev.* **1980**, *21*, 201-223.
(10) Ertl, G. Reactions at Surfaces: From Atoms to Complexity (Nobel Lecture). *Angew. Chem. Int. Ed.* **2008**, *47*, 3524-3535.
(11) Cuenya, B. R. Synthesis and catalytic properties of metal nanoparticles: Size, shape, support, composition, and oxidation state effects. *Thin Solid Films* **2010**, *518*, 3127-3150.
(12) Campbell, C. T. The Energetics of Supported Metal Nanoparticles: Relationships to Sintering Rates and Catalytic Activity. *Acc. Chem. Res.* **2013**, *46*, 1712-1719.
(13) Sharp, J. C.; Yao, Y. X.; Campbell, C. T. Silver Nanoparticles on Fe_3O_4(111): Energetics by Ag Adsorption Calorimetry and Structure by Surface Spectroscopies. *J. Phys. Chem. C* **2013**, *117*, 24932-24936.
(14) Abad, A.; Concepción, P.; Corma, A.; García, H. A Collaborative Effect between Gold and a Support Induces the Selective Oxidation of Alcohols. *Angew. Chem. Int. Ed.* **2005**, *44*, 4066-4069.
(15) Topsøe, H.; Clausen, B. S.; Massoth, F. E. In *Catalysis: Science and Technology*; Anderson, J. R., Boudart, M., Eds.; Springer-Verlag: Berlin, Heidelberg, 1996, p 1-269.
(16) Twigg, M. V. *Catalyst Handbook*; Manson: London, 1996.
(17) Rostrup-Nielsen, J. R. In *Catalysis: Science and Technology Volume 5*; Anderson, J. R., Boudart, M., Eds.; Springer-Verlag: Berlin, Heidelberg, 1984, p 1-117.
(18) Aika, K.-i.; Christiansen, L.; Dybkjaer, I.; Hansen, J.; Nielsen, P. H.; Nielsen, A.; Stoltze, P.; Tamaru, K. *Ammonia: catalysis and manufacture*; Springer-Verlag: Berlin, Heidelberg, 1995.
(19) Rodriguez, J. A.; Liu, P.; Wang, X.; Wen, W.; Hanson, J.; Hrbek, J.; Pérez, M.; Evans, J. Water-gas shift activity of Cu surfaces and Cu nanoparticles supported on metal oxides. *Catal. Today* **2009**, *143*, 45-50.
(20) Valden, M.; Lai, X.; Goodman, D. W. Onset of Catalytic Activity of Gold Clusters on Titania with the Appearance of Nonmetallic Properties. *Science* **1998**, *281*, 1647-1650.
(21) Haruta, M. Catalysis of Gold Nanoparticles Deposited on Metal Oxides. *CATTECH* **2002**, *6*, 102-115.
(22) Goodman, D. W. Model Studies in Catalysis Using Surface Science Probes. *Chem. Rev.* **1995**, *95*, 523-536.

(23) Bartholomew, C. H. In *Studies in Surface Science and Catalysis*; Bartholomew, C. H., Fuentes, G. A., Eds.; Elsevier: 1997; Vol. 111, p 585-592.
(24) Parker, S. C.; Campbell, C. T. Kinetic model for sintering of supported metal particles with improved size-dependent energetics and applications to Au on TiO_2(110). *Phys. Rev. B* **2007**, *75*, 035430.
(25) Campbell, C. T. Ultrathin metal films and particles on oxide surfaces: structural, electronic and chemisorptive properties. *Surf. Sci. Rep.* **1997**, *27*, 1-111.
(26) Campbell, C. T.; Parker, S. C.; Starr, D. E. The Effect of Size-Dependent Nanoparticle Energetics on Catalyst Sintering. *Science* **2002**, *298*, 811-814.
(27) Parker, S. C.; Campbell, C. T. Reactivity and sintering kinetics of Au/TiO_2(110) model catalysts: particle size effects. *Top. Catal.* **2007**, *44*, 3-13.
(28) Campbell, C. T.; Sellers, J. R. V. Enthalpies and Entropies of Adsorption on Well-Defined Oxide Surfaces: Experimental Measurements. *Chem. Rev.* **2013**, *113*, 4106-4135.
(29) Chen, S.; Xiong, F.; Huang, W. Surface chemistry and catalysis of oxide model catalysts from single crystals to nanocrystals. *Surf. Sci. Rep.* **2019**, *74*, 100471.
(30) Somorjai, G. A.; Park, J. Y. Concepts, instruments, and model systems that enabled the rapid evolution of surface science. *Surf. Sci.* **2009**, *603*, 1293-1300.
(31) Farha, O. K.; Hupp, J. T. Rational Design, Synthesis, Purification, and Activation of Metal-Organic Framework Materials. *Acc. Chem. Res.* **2010**, *43*, 1166-1175.
(32) Férey, G. Hybrid porous solids: past, present, future. *Chem. Soc. Rev.* **2008**, *37*, 191-214.
(33) Zhou, H.-C.; Long, J. R.; Yaghi, O. M. Introduction to Metal–Organic Frameworks. *Chem. Rev.* **2012**, *112*, 673-674.
(34) Katz, M. J.; Brown, Z. J.; Colón, Y. J.; Siu, P. W.; Scheidt, K. A.; Snurr, R. Q.; Hupp, J. T.; Farha, O. K. A facile synthesis of UiO-66, UiO-67 and their derivatives. *Chem. Commun.* **2013**, *49*, 9449-9451.
(35) Shekhah, O.; Wang, H.; Kowarik, S.; Schreiber, F.; Paulus, M.; Tolan, M.; Sternemann, C.; Evers, F.; Zacher, D.; Fischer, R. A.; Wöll, C. Step-by-Step Route for the Synthesis of Metal−Organic Frameworks. *J. Am. Chem. Soc.* **2007**, *129*, 15118-15119.
(36) Farha, O. K.; Eryazici, I.; Jeong, N. C.; Hauser, B. G.; Wilmer, C. E.; Sarjeant, A. A.; Snurr, R. Q.; Nguyen, S. T.; Yazaydın, A. Ö.; Hupp, J. T. Metal–Organic Framework Materials with Ultrahigh Surface Areas: Is the Sky the Limit? *J. Am. Chem. Soc.* **2012**, *134*, 15016-15021.
(37) Furukawa, H.; Ko, N.; Go, Y. B.; Aratani, N.; Choi, S. B.; Choi, E.; Yazaydin, A. Ö.; Snurr, R. Q.; O'Keeffe, M.; Kim, J.; Yaghi, O. M. Ultrahigh Porosity in Metal-Organic Frameworks. *Science* **2010**, *329*, 424.
(38) Deria, P.; Gómez-Gualdrón, D. A.; Bury, W.; Schaef, H. T.; Wang, T. C.; Thallapally, P. K.; Sarjeant, A. A.; Snurr, R. Q.; Hupp, J. T.; Farha, O. K. Ultraporous, Water Stable, and Breathing Zirconium-Based Metal–Organic Frameworks with ftw Topology. *J. Am. Chem. Soc.* **2015**, *137*, 13183-13190.
(39) Férey, G.; Mellot-Draznieks, C.; Serre, C.; Millange, F. Crystallized Frameworks with Giant Pores: Are There Limits to the Possible? *Acc. Chem. Res.* **2005**, *38*, 217-225.
(40) Fletcher, A. J.; Thomas, K. M.; Rosseinsky, M. J. Flexibility in metal-organic framework materials: Impact on sorption properties. *J. Solid State Chem.* **2005**, *178*, 2491-2510.
(41) Vermoortele, F.; Ameloot, R.; Alaerts, L.; Matthessen, R.; Carlier, B.; Fernandez, E. V. R.; Gascon, J.; Kapteijn, F.; De Vos, D. E. Tuning the catalytic performance of metal–organic frameworks in fine chemistry by active site engineering. *J. Mater. Chem.* **2012**, *22*, 10313-10321.

(42) Zhao, D.; Timmons, D. J.; Yuan, D.; Zhou, H.-C. Tuning the Topology and Functionality of Metal−Organic Frameworks by Ligand Design. *Acc. Chem. Res.* **2011**, *44*, 123-133.
(43) Moon, S.-Y.; Liu, Y.; Hupp, J. T.; Farha, O. K. Instantaneous Hydrolysis of Nerve-Agent Simulants with a Six-Connected Zirconium-Based Metal–Organic Framework. *Angew. Chem. Int. Ed.* **2015**, *54*, 6795-6799.
(44) Mondloch, J. E.; Katz, M. J.; Isley Iii, W. C.; Ghosh, P.; Liao, P.; Bury, W.; Wagner, G. W.; Hall, M. G.; DeCoste, J. B.; Peterson, G. W.; Snurr, R. Q.; Cramer, C. J.; Hupp, J. T.; Farha, O. K. Destruction of chemical warfare agents using metal–organic frameworks. *Nat. Mater.* **2015**, *14*, 512-516.
(45) Yang, D.; Odoh, S. O.; Borycz, J.; Wang, T. C.; Farha, O. K.; Hupp, J. T.; Cramer, C. J.; Gagliardi, L.; Gates, B. C. Tuning Zr_6 Metal–Organic Framework (MOF) Nodes as Catalyst Supports: Site Densities and Electron-Donor Properties Influence Molecular Iridium Complexes as Ethylene Conversion Catalysts. *ACS Catal.* **2016**, *6*, 235-247.
(46) Valvekens, P.; Vermoortele, F.; De Vos, D. Metal–organic frameworks as catalysts: the role of metal active sites. *Catal. Sci. Technol.* **2013**, *3*, 1435-1445.
(47) Lee, J.; Farha, O. K.; Roberts, J.; Scheidt, K. A.; Nguyen, S. T.; Hupp, J. T. Metal–organic framework materials as catalysts. *Chem. Soc. Rev.* **2009**, *38*, 1450-1459.
(48) Yang, D.; Odoh, S. O.; Wang, T. C.; Farha, O. K.; Hupp, J. T.; Cramer, C. J.; Gagliardi, L.; Gates, B. C. Metal–organic framework nodes as nearly ideal supports for molecular catalysts: NU-1000-and UiO-66-supported iridium complexes. *J. Am. Chem. Soc.* **2015**, *137*, 7391-7396.
(49) Mondloch, J. E.; Bury, W.; Fairen-Jimenez, D.; Kwon, S.; DeMarco, E. J.; Weston, M. H.; Sarjeant, A. A.; Nguyen, S. T.; Stair, P. C.; Snurr, R. Q.; Farha, O. K.; Hupp, J. T. Vapor-Phase Metalation by Atomic Layer Deposition in a Metal-Organic Framework. *J. Am. Chem. Soc.* **2013**, *135*, 10294-10297.
(50) Deria, P.; Mondloch, J. E.; Tylianakis, E.; Ghosh, P.; Bury, W.; Snurr, R. Q.; Hupp, J. T.; Farha, O. K. Perfluoroalkane Functionalization of NU-1000 via Solvent-Assisted Ligand Incorporation: Synthesis and CO_2 Adsorption Studies. *J. Am. Chem. Soc.* **2013**, *135*, 16801-16804.
(51) Planas, N.; Mondloch, J. E.; Tussupbayev, S.; Borycz, J.; Gagliardi, L.; Hupp, J. T.; Farha, O. K.; Cramer, C. J. Defining the proton topology of the Zr_6-based metal–organic framework NU-1000. *J. Phys. Chem. Lett.* **2014**, *5*, 3716-3723.
(52) Mondloch, J. E.; Katz, M. J.; Planas, N.; Semrouni, D.; Gagliardi, L.; Hupp, J. T.; Farha, O. K. Are Zr_6-based MOFs water stable? Linker hydrolysis vs. capillary-force-driven channel collapse. *Chem. Commun.* **2014**, *50*, 8944-8946.
(53) Deria, P.; Bury, W.; Hupp, J. T.; Farha, O. K. Versatile functionalization of the NU-1000 platform by solvent-assisted ligand incorporation. *Chem. Commun.* **2014**, *50*, 1965-1968.
(54) Haruta, M.; Daté, M. Advances in the catalysis of Au nanoparticles. *Appl. Catal. A: Gen.* **2001**, *222*, 427-437.
(55) Subramanian, V.; Wolf, E. E.; Kamat, P. V. Catalysis with TiO_2/Gold Nanocomposites. Effect of Metal Particle Size on the Fermi Level Equilibration. *J. Am. Chem. Soc.* **2004**, *126*, 4943-4950.
(56) Hoffmann, M. R.; Martin, S. T.; Choi, W.; Bahnemann, D. W. Environmental Applications of Semiconductor Photocatalysis. *Chem. Rev.* **1995**, *95*, 69-96.
(57) DeRita, L.; Dai, S.; Lopez-Zepeda, K.; Pham, N.; Graham, G. W.; Pan, X.; Christopher, P. Catalyst Architecture for Stable Single Atom Dispersion Enables Site-Specific Spectroscopic and Reactivity Measurements of CO Adsorbed to Pt Atoms, Oxidized Pt Clusters, and Metallic Pt Clusters on TiO_2. *J. Am. Chem. Soc.* **2017**, *139*, 14150-14165.

(58) Kovář, M.; Dvořák, L.; Černý, S. Application of pyroelectric properties of $LiTaO_3$ single crystal to microcalorimetric measurement of the heat of adsorption. *Appl. Surf. Sci.* **1994**, *74*, 51-59.
(59) Silva, M.; Costa, C. M.; Sencadas, V.; Paleo, A.; Lanceros-Méndez, S. Degradation of the dielectric and piezoelectric response of β-poly(vinylidene fluoride) after temperature annealing. *J. Polym. Res.* **2011**, *18*, 1451-1457.
(60) Stuckless, J.; Frei, N. A.; Campbell, C. T. A novel single-crystal adsorption calorimeter and additions for determining metal adsorption and adhesion energies. *Rev. Sci. Instrum.* **1998**, *69*, 2427-2438.
(61) Haynes, W. M. *CRC Handbook of Chemistry and Physics, 96th Edition*; CRC Press, 2015.
(62) Zhu, H.; Razzaq, R.; Li, C.; Muhmmad, Y.; Zhang, S. Catalytic Methanation of Carbon Dioxide by Active Oxygen Material $Ce_xZr_{1-x}O_2$ Supported Ni–Co Bimetallic Nanocatalysts. *AIChE J.* **2013**, *59*, 2567-2576.
(63) Kambolis, A.; Matralis, H.; Trovarelli, A.; Papadopoulou, C. Ni/CeO_2-ZrO_2 catalysts for the dry reforming of methane. *Appl. Catal. A: Gen.* **2010**, *377*, 16-26.
(64) Deshpande, P. A.; Hegde, M. S.; Madras, G. Pd and Pt ions as highly active sites for the water–gas shift reaction over combustion synthesized zirconia and zirconia-modified ceria. *Applied Catalysis B: Environmental* **2010**, *96*, 83-93.
(65) He, Q.; Mukerjee, S.; Zeis, R.; Parres-Esclapez, S.; Illán-Gómez, M. J.; Bueno-López, A. Enhanced Pt stability in MO_2 (M=Ce, Zr or $Ce_{0.9}Zr_{0.1}$)-promoted Pt/C electrocatalysts for oxygen reduction reaction in PAFCs. *Appl. Catal. A: Gen.* **2010**, *381*, 54-65.
(66) Royer, S.; Duprez, D.; Can, F.; Courtois, X.; Batiot-Dupeyrat, C.; Laassiri, S.; Alamdari, H. Perovskites as Substitutes of Noble Metals for Heterogeneous Catalysis: Dream or Reality. *Chem. Rev.* **2014**, *114*, 10292-10368.
(67) Halwidl, D.; Stöger, B.; Mayr-Schmölzer, W.; Pavelec, J.; Fobes, D.; Peng, J.; Mao, Z.; Parkinson, G. S.; Schmid, M.; Mittendorfer, F.; Redinger, J.; Diebold, U. Adsorption of water at the SrO surface of ruthenates. *Nat. Mater.* **2016**, *15*, 450-455.
(68) Compton, O. C.; Carroll, E. C.; Kim, J. Y.; Larsen, D. S.; Osterloh, F. E. Calcium niobate semiconductor nanosheets as catalysts for photochemical hydrogen evolution from water. *J. Phys. Chem. C* **2007**, *111*, 14589-14592.
(69) Fang, M.; Kim, C. H.; Saupe, G. B.; Kim, H.-N.; Waraksa, C. C.; Miwa, T.; Fujishima, A.; Mallouk, T. E. Layer-by-layer growth and condensation reactions of niobate and titanoniobate thin films. *Chem. Mater.* **1999**, *11*, 1526-1532.
(70) Li, B.-W.; Osada, M.; Ozawa, T. C.; Ebina, Y.; Akatsuka, K.; Ma, R.; Funakubo, H.; Sasaki, T. Engineered interfaces of artificial perovskite oxide superlattices via nanosheet deposition process. *ACS Nano* **2010**, *4*, 6673-6680.
(71) Schaak, R. E.; Mallouk, T. E. Self-assembly of tiled perovskite monolayer and multilayer thin films. *Chem. Mater.* **2000**, *12*, 2513-2516.
(72) Song, Y.; Iyi, N.; Hoshide, T.; Ozawa, T. C.; Ebina, Y.; Ma, R.; Miyamoto, N.; Sasaki, T. Accordion-like swelling of layered perovskite crystals via massive permeation of aqueous solutions into 2D oxide galleries. *Chem. Commun.* **2015**, *51*, 17068-17071.
(73) Xu, P.; Milstein, T. J.; Mallouk, T. E. Flat-Band Potentials of Molecularly Thin Metal Oxide Nanosheets. *ACS Appl. Mater. Interfaces* **2016**, *8*, 11539-11547.
(74) Keller, S. W.; Kim, H.-N.; Mallouk, T. E. Layer-by-Layer Assembly of Intercalation Compounds and Heterostructures on Surfaces: Toward Molecular "Beaker" Epitaxy. *J. Am. Chem. Soc.* **1994**, *116*, 8817-8818.

(75) Ma, R.; Sasaki, T. Two-Dimensional Oxide and Hydroxide Nanosheets: Controllable High-Quality Exfoliation, Molecular Assembly, and Exploration of Functionality. *Acc. Chem. Res.* **2015**, *48*, 136-143.
(76) Muramatsu, M.; Akatsuka, K.; Ebina, Y.; Wang, K.; Sasaki, T.; Ishida, T.; Miyake, K.; Haga, M.-a. Fabrication of Densely Packed Titania Nanosheet Films on Solid Surface by Use of Langmuir−Blodgett Deposition Method without Amphiphilic Additives. *Langmuir* **2005**, *21*, 6590-6595.
(77) Ma, S.; Zhou, H.-C. Gas storage in porous metal–organic frameworks for clean energy applications. *Chem. Commun.* **2010**, *46*, 44-53.
(78) Ma, S.; Collier, C. D.; Zhou, H.-C. In *Design and Construction of Coordination Polymers*; Hong, M., Chen, L., Eds.; Wiley-VCH: Hoboken, New Jersey, USA, 2009.
(79) Collins, D. J.; Ma, S.; Zhou, H.-C. In *Metal Organic Frameworks: Design and Application*; MacGillivray, L. R., Ed.; Wiley-VCH: Hoboken, New Jersey, USA, 2009.
(80) Talu, O. In *Studies in Surface Science and Catalysis*; Suzuki, M., Ed.; Elsevier: 1993; Vol. 80, p 655-662.
(81) Lozano-Castelló, D.; Alcañiz-Monge, J.; de la Casa-Lillo, M. A.; Cazorla-Amorós, D.; Linares-Solano, A. Advances in the study of methane storage in porous carbonaceous materials. *Fuel* **2002**, *81*, 1777-1803.
(82) Celzard, A.; Fierro, V. Preparing a Suitable Material Designed for Methane Storage: A Comprehensive Report. *Energy Fuels* **2005**, *19*, 573-583.
(83) Mason, J. A.; Veenstra, M.; Long, J. R. Evaluating metal–organic frameworks for natural gas storage. *Chem. Sci.* **2014**, *5*, 32-51.
(84) *World Energy Outlook 2011 Special Report: Are We Entering a Golden Age of Gas*, International Energy Agency.
(85) He, Y.; Zhou, W.; Qian, G.; Chen, B. Methane storage in metal–organic frameworks. *Chem. Soc. Rev.* **2014**, *43*, 5657-5678.
(86) Li, H.; Wang, K.; Sun, Y.; Lollar, C. T.; Li, J.; Zhou, H.-C. Recent advances in gas storage and separation using metal–organic frameworks. *Mater. Today* **2018**, *21*, 108-121.
(87) Furukawa, H.; Go, Y. B.; Ko, N.; Park, Y. K.; Uribe-Romo, F. J.; Kim, J.; O'Keeffe, M.; Yaghi, O. M. Isoreticular Expansion of Metal–Organic Frameworks with Triangular and Square Building Units and the Lowest Calculated Density for Porous Crystals. *Inorg. Chem.* **2011**, *50*, 9147-9152.
(88) Sanz-Pérez, E. S.; Murdock, C. R.; Didas, S. A.; Jones, C. W. Direct Capture of CO_2 from Ambient Air. *Chem. Rev.* **2016**, *116*, 11840-11876.
(89) Sumida, K.; Rogow, D. L.; Mason, J. A.; McDonald, T. M.; Bloch, E. D.; Herm, Z. R.; Bae, T.-H.; Long, J. R. Carbon Dioxide Capture in Metal–Organic Frameworks. *Chem. Rev.* **2012**, *112*, 724-781.
(90) Allan, P. K.; Wheatley, P. S.; Aldous, D.; Mohideen, M. I.; Tang, C.; Hriljac, J. A.; Megson, I. L.; Chapman, K. W.; De Weireld, G.; Vaesen, S.; Morris, R. E. Metal–organic frameworks for the storage and delivery of biologically active hydrogen sulfide. *Dalton Trans.* **2012**, *41*, 4060-4066.
(91) Khan, N. A.; Hasan, Z.; Jhung, S. H. Adsorptive removal of hazardous materials using metal-organic frameworks (MOFs): A review. *J. Hazard. Mater.* **2013**, *244-245*, 444-456.
(92) Barea, E.; Montoro, C.; Navarro, J. A. R. Toxic gas removal – metal–organic frameworks for the capture and degradation of toxic gases and vapours. *Chem. Soc. Rev.* **2014**, *43*, 5419-5430.

(93) Kerry, F. G. *Industrial Gas Handbook: Gas Separation and Purification*; CRC press: Boca Raton, FL, 2007.
(94) Zhang, W.; Ma, Y.; Santos-López, I. A.; Lownsbury, J. M.; Yu, H.; Liu, W.-G.; Truhlar, D. G.; Campbell, C. T.; Vilches, O. E. Energetics of van der Waals Adsorption on the Metal–Organic Framework NU-1000 with Zr_6-oxo, Hydroxo, and Aqua Nodes. *J. Am. Chem. Soc.* **2018**, *140*, 328-338.
(95) Vissers, G. O.; Zhang, W.; Vilches, O. E.; Liu, W.-G.; Yu, H. S.; Truhlar, D. G.; Campbell, C. T. Heats of Adsorption of N_2, CO, Ar, and CH_4 versus Coverage on the Zr-Based MOF NU-1000: Measurements and DFT Calculations. *J. Phys. Chem. C* **2019**, *123*, 6586-6591.
(96) Chen, Y.; Zhao, X.; Ma, H.; Ma, S.; Huang, G.; Makita, Y.; Bai, X.; Yang, X. Structure and dehydration of layered perovskite niobate with bilayer hydrates prepared by exfoliation/self-assembly process. *J. Solid State Chem.* **2008**, *181*, 1684-1694.
(97) Diaz, S.; Zhu, J.; Harris, J.; Goetsch, P.; Merte, L.; Campbell, C. T. Heats of adsorption of Pb on pristine and electron-irradiated poly(methyl methacrylate) by microcalorimetry. *Surf. Sci.* **2005**, *598*, 22-34.
(98) Pauls, S. W.; Campbell, C. T. Magic-angle thermal desorption mass spectroscopy. *Surf. Sci.* **1990**, *226*, 250-256.
(99) Lownsbury, J. M.; Santos-Lopez, I. A.; Zhang, W.; Campbell, C. T.; Yu, H. Y. S.; Liu, W. G.; Cramer, C. J.; Truhlar, D. G.; Wang, T.; Hupp, J. T.; Farha, O. K. Calcium Vapor Adsorption on the Metal-Organic Framework NU-1000: Structure and Energetics. *J. Phys. Chem. C* **2016**, *120*, 16850-16862.
(100) Gomez-Gualdron, D. A.; Gutov, O. V.; Krungleviciute, V.; Borah, B.; Mondloch, J. E.; Hupp, J. T.; Yildirim, T.; Farha, O. K.; Snurr, R. Q. Computational Design of Metal–Organic Frameworks Based on Stable Zirconium Building Units for Storage and Delivery of Methane. *Chem. Mater.* **2014**, *26*, 5632-5639.
(101) Wilmer, C. E.; Leaf, M.; Lee, C. Y.; Farha, O. K.; Hauser, B. G.; Hupp, J. T.; Snurr, R. Q. Large-scale screening of hypothetical metal–organic frameworks. *Nat. Chem.* **2012**, *4*, 83-89.
(102) Li, J.-R.; Kuppler, R. J.; Zhou, H.-C. Selective gas adsorption and separation in metal–organic frameworks. *Chem. Soc. Rev.* **2009**, *38*, 1477-1504.
(103) Seo, J. S.; Whang, D.; Lee, H.; Jun, S. I.; Oh, J.; Jeon, Y. J.; Kim, K. A homochiral metal–organic porous material for enantioselective separation and catalysis. *Nature* **2000**, *404*, 982-986.
(104) Farha, O. K.; Wilmer, C. E.; Eryazici, I.; Hauser, B. G.; Parilla, P. A.; O'Neill, K.; Sarjeant, A. A.; Nguyen, S. T.; Snurr, R. Q.; Hupp, J. T. Designing Higher Surface Area Metal–Organic Frameworks: Are Triple Bonds Better Than Phenyls? *J. Am. Chem. Soc.* **2012**, *134*, 9860-9863.
(105) Peng, Y.; Krungleviciute, V.; Eryazici, I.; Hupp, J. T.; Farha, O. K.; Yildirim, T. Methane Storage in Metal–Organic Frameworks: Current Records, Surprise Findings, and Challenges. *J. Am. Chem. Soc.* **2013**, *135*, 11887-11894.
(106) Eddaoudi, M.; Kim, J.; Rosi, N.; Vodak, D.; Wachter, J.; O'Keeffe, M.; Yaghi, O. M. Systematic Design of Pore Size and Functionality in Isoreticular MOFs and Their Application in Methane Storage. *Science* **2002**, *295*, 469-472.
(107) Rosi, N. L.; Eckert, J.; Eddaoudi, M.; Vodak, D. T.; Kim, J.; O'Keeffe, M.; Yaghi, O. M. Hydrogen Storage in Microporous Metal-Organic Frameworks. *Science* **2003**, *300*, 1127-1129.
(108) Kreno, L. E.; Leong, K.; Farha, O. K.; Allendorf, M.; Van Duyne, R. P.; Hupp, J. T. Metal–Organic Framework Materials as Chemical Sensors. *Chem. Rev.* **2012**, *112*, 1105-1125.
(109) Allendorf, M. D.; Bauer, C. A.; Bhakta, R. K.; Houk, R. J. T. Luminescent metal–organic frameworks. *Chem. Soc. Rev.* **2009**, *38*, 1330-1352.

(110) Horcajada, P.; Serre, C.; Vallet-Regí, M.; Sebban, M.; Taulelle, F.; Férey, G. Metal–Organic Frameworks as Efficient Materials for Drug Delivery. *Angew. Chem. Int. Ed.* **2006**, *45*, 5974-5978.
(111) Hermes, S.; Schröter, M.-K.; Schmid, R.; Khodeir, L.; Muhler, M.; Tissler, A.; Fischer, R. W.; Fischer, R. A. Metal@MOF: Loading of Highly Porous Coordination Polymers Host Lattices by Metal Organic Chemical Vapor Deposition. *Angew. Chem. Int. Ed.* **2005**, *44*, 6237-6241.
(112) Schröder, F.; Esken, D.; Cokoja, M.; van den Berg, M. W. E.; Lebedev, O. I.; Van Tendeloo, G.; Walaszek, B.; Buntkowsky, G.; Limbach, H.-H.; Chaudret, B.; Fischer, R. A. Ruthenium Nanoparticles inside Porous $[Zn_4O(bdc)_3]$ by Hydrogenolysis of Adsorbed [Ru(cod)(cot)]: A Solid-State Reference System for Surfactant-Stabilized Ruthenium Colloids. *J. Am. Chem. Soc.* **2008**, *130*, 6119-6130.
(113) Houk, R. J. T.; Jacobs, B. W.; Gabaly, F. E.; Chang, N. N.; Talin, A. A.; Graham, D. D.; House, S. D.; Robertson, I. M.; Allendorf, M. D. Silver Cluster Formation, Dynamics, and Chemistry in Metal−Organic Frameworks. *Nano Lett.* **2009**, *9*, 3413-3418.
(114) Meilikhov, M.; Yusenko, K.; Esken, D.; Turner, S.; Van Tendeloo, G.; Fischer, R. A. Metals@MOFs – Loading MOFs with Metal Nanoparticles for Hybrid Functions. *Eur. J. Inorg. Chem.* **2010**, *2010*, 3701-3714.
(115) Kim, I. S.; Borycz, J.; Platero-Prats, A. E.; Tussupbayev, S.; Wang, T. C.; Farha, O. K.; Hupp, J. T.; Gagliardi, L.; Chapman, K. W.; Cramer, C. J.; Martinson, A. B. F. Targeted Single-Site MOF Node Modification: Trivalent Metal Loading via Atomic Layer Deposition. *Chem. Mater.* **2015**, *27*, 4772-4778.
(116) Peters, A. W.; Li, Z.; Farha, O. K.; Hupp, J. T. Atomically Precise Growth of Catalytically Active Cobalt Sulfide on Flat Surfaces and within a Metal–Organic Framework via Atomic Layer Deposition. *ACS Nano* **2015**, *9*, 8484-8490.
(117) Klet, R. C.; Wang, T. C.; Fernandez, L. E.; Truhlar, D. G.; Hupp, J. T.; Farha, O. K. Synthetic Access to Atomically Dispersed Metals in Metal–Organic Frameworks via a Combined Atomic-Layer-Deposition-in-MOF and Metal-Exchange Approach. *Chem. Mater.* **2016**, *28*, 1213-1219.
(118) Campbell, C. T.; Lytken, O. Experimental measurements of the energetics of surface reactions. *Surf. Sci.* **2009**, *603*, 1365-1372.
(119) Zhu, J.; Farmer, J. A.; Ruzycki, N.; Xu, L.; Campbell, C. T.; Henkelman, G. Calcium Adsorption on MgO(100): Energetics, Structure, and Role of Defects. *J. Am. Chem. Soc.* **2008**, *130*, 2314-2322.
(120) Sharp, J. C.; Feng, X. F.; Farmer, J. A.; Guo, Y. X.; Bebensee, F.; Baricuatro, J. H.; Zillner, E.; Zhu, J. F.; Steinrück, H. P.; Gottfried, J. M.; Campbell, C. T. Calcium Thin Film Growth on Polyfluorenes: Interface Structure and Energetics. *J. Phys. Chem. C* **2014**, *118*, 2953-2962.
(121) Ju, H.; Feng, X.; Ye, Y.; Zhang, L.; Pan, H.; Campbell, C. T.; Zhu, J. Ca Carboxylate Formation at the Calcium/Poly(methyl methacrylate) Interface. *J. Phys. Chem. C* **2012**, *116*, 20465-20471.
(122) Ju, H.; Ye, Y.; Feng, X.; Pan, H.; Zhu, J.; Ruzycki, N.; Campbell, C. T. Low-Temperature Growth Improves Metal/Polymer Interfaces: Vapor-Deposited Ca on PMMA. *J. Phys. Chem. C* **2014**, *118*, 6352-6358.
(123) Lownsbury, J. M.; Sharp, J. C.; Mann, E. J.; Campbell, C. T. Calcium Thin Film Growth on Phenyl-C_{61}-Butyric Acid Methyl Ester (PCBM): Interface Structure and Energetics. *J. Phys. Chem. C* **2015**, *119*, 18444-18451.

(124) Zhu, J.; Goetsch, P.; Ruzycki, N.; Campbell, C. T. Adsorption Energy, Growth Mode, and Sticking Probability of Ca on Poly(methyl methacrylate) Surfaces with and without Electron Damage. *J. Am. Chem. Soc.* **2007**, *129*, 6432-6441.
(125) Kung, C.-W.; Wang, T. C.; Mondloch, J. E.; Fairen-Jimenez, D.; Gardner, D. M.; Bury, W.; Klingsporn, J. M.; Barnes, J. C.; Van Duyne, R.; Stoddart, J. F.; Wasielewski, M. R.; Farha, O. K.; Hupp, J. T. Metal–Organic Framework Thin Films Composed of Free-Standing Acicular Nanorods Exhibiting Reversible Electrochromism. *Chem. Mater.* **2013**, *25*, 5012-5017.
(126) Pandey, A. K.; Shaw, P. E.; Samuel, I. D. W.; Nunzi, J.-M. Effect of metal cathode reflectance on the exciton-dissociation efficiency in heterojunction organic solar cells. *Applied Physics Letters* **2009**, *94*, 103303.
(127) Frisch, M. J.; Trucks, G. W.; Schlegel, H. B.; Scuseria, G. E.; Robb, M. A.; Cheeseman, J. R.; Scalmani, G.; Barone, V.; Mennucci, B.; Petersson, G. A.; Nakatsuji, H.; Li, X.; Caricato, M.; Marenich, A.; Bloino, J.; Janesko, B. G.; Gomperts, R. Gaussian Inc., Wallingford, CT, USA, 2009.
(128) Dovesi, R.; Orlando, R.; Erba, A.; Zicovich-Wilson, C. M.; Civalleri, B.; Casassa, S.; Maschio, L.; Ferrabone, M.; De La Pierre, M.; D'Arco, P.; Noël, Y.; Causà, M.; Rérat, M.; Kirtman, B. CRYSTAL14: A program for the ab initio investigation of crystalline solids. *Int. J. Quantum Chem.* **2014**, *114*, 1287-1317.
(129) Zhao, Y.; Truhlar, D. G. A new local density functional for main-group thermochemistry, transition metal bonding, thermochemical kinetics, and noncovalent interactions. *J. Chem. Phys.* **2006**, *125*, 194101.
(130) Zhao, Y.; Truhlar, D. G. The M06 suite of density functionals for main group thermochemistry, thermochemical kinetics, noncovalent interactions, excited states, and transition elements: two new functionals and systematic testing of four M06-class functionals and 12 other functionals. *Theor. Chem. Acc.* **2008**, *120*, 215-241.
(131) Yu, H.; Truhlar, D. G. What Dominates the Error in the CaO Diatomic Bond Energy Predicted by Various Approximate Exchange–Correlation Functionals? *J. Chem. Theory Comput.* **2014**, *10*, 2291-2305.
(132) Binkley, J. S.; Pople, J. A. Self‐consistent molecular orbital methods. XIX. Split‐valence Gaussian‐type basis sets for beryllium. *J. Chem. Phys.* **1977**, *66*, 879-880.
(133) Ditchfield, R.; Hehre, W. J.; Pople, J. A. Self‐Consistent Molecular‐Orbital Methods. IX. An Extended Gaussian‐Type Basis for Molecular‐Orbital Studies of Organic Molecules. *J. Chem. Phys.* **1971**, *54*, 724-728.
(134) Francl, M. M.; Pietro, W. J.; Hehre, W. J.; Binkley, J. S.; Gordon, M. S.; DeFrees, D. J.; Pople, J. A. Self‐consistent molecular orbital methods. XXIII. A polarization‐type basis set for second‐row elements. *J. Chem. Phys.* **1982**, *77*, 3654-3665.
(135) Hehre, W. J.; Ditchfield, R.; Pople, J. A. Self-consistent molecular-orbital methods 12. Further extensions of gaussian-type basis sets for use in molecular-orbital studies of organic-molecules. *J. Chem. Phys.* **1972**, *56*, 2257-2261.
(136) Hehre, W. J.; Pople, J. A. Self‐Consistent Molecular Orbital Methods. XIII. An Extended Gaussian‐Type Basis for Boron. *J. Chem. Phys.* **1972**, *56*, 4233-4234.
(137) Andrae, D.; Häußermann, U.; Dolg, M.; Stoll, H.; Preuß, H. Energy-adjusted ab initio pseudopotentials for the second and third row transition elements. *Theoret. Chim. Acta* **1990**, *77*, 123-141.

(138) Martin, J. M.; Sundermann, A. Correlation consistent valence basis sets for use with the Stuttgart–Dresden–Bonn relativistic effective core potentials: The atoms Ga–Kr and In–Xe. *J. Chem. Phys.* **2001**, *114*, 3408-3420.
(139) Kaupp, M.; Schleyer, P. v. R.; Stoll, H.; Preuss, H. Pseudopotential approaches to Ca, Sr, and Ba hydrides. Why are some alkaline earth MX_2 compounds bent? *J. Chem. Phys.* **1991**, *94*, 1360-1366.
(140) Alecu, I. M.; Zheng, J. J.; Zhao, Y.; Truhlar, D. G. Computational Thermochemistry: Scale Factor Databases and Scale Factors for Vibrational Frequencies Obtained from Electronic Model Chemistries. *J. Chem. Theory Comput.* **2010**, *6*, 2872-2887.
(141) Yu, H. S.; Fiedler, L. J.; Alecu, I. M.; Truhlar, D. G. Computational thermochemistry: Automated generation of scale factors for vibrational frequencies calculated by electronic structure model chemistries. *Comput. Phys. Commun.* **2017**, *210*, 132-138.
(142) Brongersma, H. H.; Draxler, M.; de Ridder, M.; Bauer, P. Surface composition analysis by low-energy ion scattering. *Surf. Sci. Rep.* **2007**, *62*, 63-109.
(143) Campbell, C. T.; James, T. E. Ion scattering spectroscopy intensities for supported nanoparticles: The hemispherical cap model. *Surf. Sci.* **2015**, *641*, 166-169.
(144) Bebensee, F.; Zhu, J.; Baricuatro, J. H.; Farmer, J. A.; Bai, Y.; Steinrück, H.-P.; Campbell, C. T.; Gottfried, J. M. Interface Formation between Calcium and Electron-Irradiated Poly(3-hexylthiophene). *Langmuir* **2010**, *26*, 9632-9639.
(145) Sharp, J. C.; Bebensee, F.; Baricuatro, J. H.; Steinrück, H. P.; Gottfried, J. M.; Campbell, C. T. Calcium Thin Film Growth on a Cyano-Substituted Poly(p-phenylene vinylene): Interface Structure and Energetics. *J. Phys. Chem. C* **2013**, *117*, 23781-23789.
(146) Zhu, J.; Bebensee, F.; Hieringer, W.; Zhao, W.; Baricuatro, J. H.; Farmer, J. A.; Bai, Y.; Steinrück, H.-P.; Gottfried, J. M.; Campbell, C. T. Formation of the Calcium/Poly(3-Hexylthiophene) Interface: Structure and Energetics. *J. Am. Chem. Soc.* **2009**, *131*, 13498-13507.
(147) Tanuma, S.; Powell, C. J.; Penn, D. R. Calculations of electorn inelastic mean free paths. II. Data for 27 elements over the 50–2000 eV range. *Surf. Interface Anal.* **1991**, *17*, 911-926.
(148) Ertl, G.; Küppers, J. *Low energy electrons and surface chemistry*; VCH: Weinheim, Germany, 1985.
(149) Wagner, C. D.; Riggs, W. M.; Davis, L. E.; Moulder, J. F.; Muilenberg, G. E. *Handbook of X-ray Photoelectron Spectroscopy*; Perkin-Elmer Corp., Physical Electronics Division: Eden Prairie, MN, 1979.
(150) Platero-Prats, A. E.; Mavrandonakis, A.; Gallington, L. C.; Liu, Y.; Hupp, J. T.; Farha, O. K.; Cramer, C. J.; Chapman, K. W. Structural Transitions of the Metal-Oxide Nodes within Metal–Organic Frameworks: On the Local Structures of NU-1000 and UiO-66. *J. Am. Chem. Soc.* **2016**, *138*, 4178-4185.
(151) Wietelmann, U.; Felderhoff, M.; Rittmeyer, P. In *Ullmann's Encyclopedia of Industrial Chemistry*; Wiley-VCH: Weinheim, Germany, 2016.
(152) Franzosini, P.; Sanesi, M. *Thermodynamic and Transport Properties of Organic Salts: International Union of Pure and Applied Chemistry*; 1st ed.; Pergamon Press Inc.: New York, 1980.
(153) Marenich, A. V.; Jerome, S. V.; Cramer, C. J.; Truhlar, D. G. Charge Model 5: An Extension of Hirshfeld Population Analysis for the Accurate Description of Molecular Interactions in Gaseous and Condensed Phases. *J. Chem. Theory Comput.* **2012**, *8*, 527-541.
(154) Mulliken, R. S. Electronic Population Analysis on LCAO–MO Molecular Wave Functions. I. *J. Chem. Phys.* **1955**, *23*, 1833-1840.

(155) Nanda, K. K.; Maisels, A.; Kruis, F. E.; Fissan, H.; Stappert, S. Higher Surface Energy of Free Nanoparticles. *Phys. Rev. Lett.* **2003**, *91*, 106102.
(156) Murdey, R.; Stuckless, J. T. Calorimetry of Polymer Metallization: Copper, Calcium, and Chromium on PMDA-ODA Polyimide. *J. Am. Chem. Soc.* **2003**, *125*, 3995-3998.
(157) Zhang, W.; Campbell, C. T. Calorimetric Metal Vapor Adsorption Energies for Characterizing Industrial Catalyst Support Materials. *ACS Catal.* **submitted**.
(158) de Oliveira, A. L.; Wolf, A.; Schüth, F. Highly selective propene epoxidation with hydrogen/oxygen mixtures over titania-supported silver catalysts. *Catal. Lett.* **2001**, *73*, 157-160.
(159) Matsumura, Y.; Shen, W.-J.; Ichihashi, Y.; Okumura, M. Low-Temperature Methanol Synthesis Catalyzed over Ultrafine Palladium Particles Supported on Cerium Oxide. *J. Catal.* **2001**, *197*, 267-272.
(160) Rodriguez, J. A.; Liu, G.; Jirsak, T.; Hrbek, J.; Chang, Z.; Dvorak, J.; Maiti, A. Activation of Gold on Titania: Adsorption and Reaction of SO_2 on Au/TiO_2(110). *J. Am. Chem. Soc.* **2002**, *124*, 5242-5250.
(161) Iglesia, E. Design, synthesis, and use of cobalt-based Fischer-Tropsch synthesis catalysts. *Appl. Catal. A: Gen.* **1997**, *161*, 59-78.
(162) Haruta, M. Size-and support-dependency in the catalysis of gold. *Catal. Today* **1997**, *36*, 153-166.
(163) Mostafa, S.; Behafarid, F.; Croy, J. R.; Ono, L. K.; Li, L.; Yang, J. C.; Frenkel, A. I.; Cuenya, B. R. Shape-dependent catalytic properties of Pt nanoparticles. *J. Am. Chem. Soc.* **2010**, *132*, 15714-15719.
(164) Xu, X.; Goodman, D. W. The effect of particle size on nitric oxide decomposition and reaction with carbon monoxide on palladium catalysts. *Catal. Lett.* **1994**, *24*, 31-35.
(165) DeRita, L.; Resasco, J.; Dai, S.; Boubnov, A.; Thang, H. V.; Hoffman, A. S.; Ro, I.; Graham, G. W.; Bare, S. R.; Pacchioni, G.; Pan, X.; Christopher, P. Structural evolution of atomically dispersed Pt catalysts dictates reactivity. *Nat. Mater.* **2019**, *18*, 746-751.
(166) Resasco, J.; Yang, F.; Mou, T.; Wang, B.; Christopher, P.; Resasco, D. E. Relationship between Atomic Scale Structure and Reactivity of Pt Catalysts: Hydrodeoxygenation of m-Cresol over Isolated Pt Cations and Clusters. *ACS Catal.* **2020**, *10*, 595-603.
(167) Thang, H. V.; Pacchioni, G.; DeRita, L.; Christopher, P. Nature of stable single atom Pt catalysts dispersed on anatase TiO_2. *J. Catal.* **2018**, *367*, 104-114.
(168) Fang, M.; Kim, C. H.; Mallouk, T. E. Dielectric properties of the lamellar niobates and titanoniobates $AM_2Nb_3O_{10}$ and $ATiNbO_5$ (A = H, K, M = Ca, Pb), and their condensation products $Ca_4Nb_6O_{19}$ and $Ti_2Nb_2O_9$. *Chem. Mater.* **1999**, *11*, 1519-1525.
(169) Li, B.-W.; Osada, M.; Ebina, Y.; Akatsuka, K.; Fukuda, K.; Sasaki, T. High thermal robustness of molecularly thin perovskite nanosheets and implications for superior dielectric properties. *ACS Nano* **2014**, *8*, 5449-5461.
(170) Strayer, M. E.; Binz, J. M.; Tanase, M.; Kamali Shahri, S. M.; Sharma, R.; Rioux, R. M.; Mallouk, T. E. Interfacial bonding stabilizes rhodium and rhodium oxide nanoparticles on layered Nb oxide and Ta oxide supports. *J. Am. Chem. Soc.* **2014**, *136*, 5687-5696.
(171) Strayer, M. E.; Senftle, T. P.; Winterstein, J. P.; Vargas-Barbosa, N. M.; Sharma, R.; Rioux, R. M.; Janik, M. J.; Mallouk, T. E. Charge transfer stabilization of late transition metal oxide nanoparticles on a layered niobate support. *J. Am. Chem. Soc.* **2015**, *137*, 16216-16224.
(172) Zhang, W.; Uppuluri, R.; Mallouk, T. E.; Campbell, C. T. Silver Adsorption on Calcium Niobate(001) Nanosheets: Calorimetric Energies Explain Sinter-Resistant Catalyst Support. *J. Am. Chem. Soc.* **submitted**.

(173) Stuckless, J. T.; Frei, N. A.; Campbell, C. T. Pyroelectric detector for single-crystal adsorption microcalorimetry: analysis of pulse shape and intensity. *Sens. Actuators B* **2000**, *62*, 13-22.
(174) Shirley, D. A. High-Resolution X-Ray Photoemission Spectrum of the Valence Bands of Gold. *Phys. Rev. B* **1972**, *5*, 4709-4714.
(175) Ansell, R. O.; Dickinson, T.; Povey, A. F.; Sherwood, P. M. A. X-ray photoelectron spectroscopic studies of electrode surfaces using a new controlled transfer technique: Part II. Results for a molybdenum electrode and the curve fitting procedure. *J. Electroanal. Chem.* **1979**, *98*, 79-89.
(176) Beamson, G.; Briggs., D. *High Resolution XPS of Organic Polymers: The Scienta ESCA300 Database* Wiley: New York, NY, 1992.
(177) Zhang, D.; Yoshida, T.; Oekermann, T.; Furuta, K.; Minoura, H. Room-Temperature Synthesis of Porous Nanoparticulate TiO_2 Films for Flexible Dye-Sensitized Solar Cells. *Adv. Funct. Mater.* **2006**, *16*, 1228-1234.
(178) Rossi, P. F.; Busca, G. Microcalorimetric and FT-IR spectroscopic study of the adsorption of methanol on TiO_2 (anatase). *Colloids Surf.* **1985**, *16*, 95-102.
(179) Lytken, O.; Lew, W.; Harris, J. J. W.; Vestergaard, E. K.; Gottfried, J. M.; Campbell, C. T. Energetics of Cyclohexene Adsorption and Reaction on Pt(111) by Low-Temperature Microcalorimetry. *J. Am. Chem. Soc.* **2008**, *130*, 10247-10257.
(180) Farmer, J. A.; Baricuatro, J. H.; Campbell, C. T. Ag Adsorption on Reduced CeO_2(111) Thin Films. *J. Phys. Chem. C* **2010**, *114*, 17166-17172.
(181) Larsen, J. H.; Ranney, J. T.; Starr, D. E.; Musgrove, J. E.; Campbell, C. T. Adsorption energetics of Ag on MgO(100). *Phys. Rev. B* **2001**, *63*, 195410.
(182) James, T. E.; Hemmingson, S. L.; Ito, T.; Campbell, C. T. Energetics of Cu Adsorption and Adhesion onto Reduced CeO_2(111) Surfaces by Calorimetry. *J. Phys. Chem. C* **2015**, *119*, 17209-17217.
(183) Sellers, J. R. V.; James, T. E.; Hemmingson, S. L.; Farmer, J. A.; Campbell, C. T. Adsorption calorimetry during metal vapor deposition on single crystal surfaces: Increased flux, reduced optical radiation, and real-time flux and reflectivity measurements. *Rev. Sci. Instrum.* **2013**, *84*, 123901.
(184) Gandhi, H.; Graham, G.; McCabe, R. W. Automotive exhaust catalysis. *J. Catal.* **2003**, *216*, 433-442.
(185) Schaak, R. E.; Mallouk, T. E. Perovskites by Design: A Toolbox of Solid-State Reactions. *Chem. Mater.* **2002**, *14*, 1455-1471.
(186) Zhao, M.; Wang, H.; Cai, L.; Zhu, Y.; Gong, M.; Chen, Y. Effect of Different Supports on Performance of Palladium Methanol Decomposition Catalyst. *Rare Metal Mat. Eng.* **2010**, *39*, 519-522.
(187) James, T. E.; Hemmingson, S. L.; Campbell, C. T. Energy of Supported Metal Catalysts: From Single Atoms to Large Metal Nanoparticles. *ACS Catal.* **2015**, *5*, 5673-5678.
(188) Schaak, R. E.; Mallouk, T. E. Prying apart Ruddlesden−Popper phases: Exfoliation into sheets and nanotubes for assembly of perovskite thin films. *Chem. Mater.* **2000**, *12*, 3427-3434.
(189) Wang, T.; Henderson, C. N.; Draskovic, T. I.; Mallouk, T. E. Synthesis, Exfoliation, and Electronic/Protonic Conductivity of the Dion–Jacobson Phase Layer Perovskite $HLa_2TiTa_2O_{10}$. *Chem. Mater.* **2014**, *26*, 898-906.

(190) Treacy, M. M. J.; Rice, S. B.; Jacobson, A. J.; Lewandowski, J. T. Electron microscopy study of delamination in dispersions of the perovskite-related layered phases $K[Ca_2Na_{n-3}Nb_nO_{3n-1}]$: evidence for single-layer formation. *Chem. Mater.* **1990**, *2*, 279-286.
(191) Hata, H.; Kobayashi, Y.; Bojan, V.; Youngblood, W. J.; Mallouk, T. E. Direct Deposition of Trivalent Rhodium Hydroxide Nanoparticles onto a Semiconducting Layered Calcium Niobate for Photocatalytic Hydrogen Evolution. *Nano Lett.* **2008**, *8*, 794-799.
(192) Gao, H.; Shori, S.; Chen, X.; zur Loye, H.-C.; Ploehn, H. J. Quantitative analysis of exfoliation and aspect ratio of calcium niobate platelets. *J. Colloid Interface Sci.* **2013**, *392*, 226-236.
(193) Jacobson, A. J.; Lewandowski, J. T.; Johnson, J. W. Ion exchange of the layered perovskite $KCa_2Nb_3O_{10}$ by protons. *J. Less-Common Met.* **1986**, *116*, 137-146.
(194) Ebina, Y.; Sasaki, T.; Harada, M.; Watanabe, M. Restacked perovskite nanosheets and their Pt-loaded materials as photocatalysts. *Chem. Mater.* **2002**, *14*, 4390-4395.
(195) Liang, S. J.; Zhu, S. Y.; Chen, Y.; Wu, W. M.; Wang, X. C.; Wu, L. Rapid template-free synthesis and photocatalytic performance of visible light-activated $SnNb_2O_6$ nanosheets. *J. Mater. Chem.* **2012**, *22*, 2670-2678.
(196) Ma, X. D.; Jiang, D. L.; Xiao, P.; Jin, Y.; Meng, S. C.; Chen, M. 2D/2D heterojunctions of WO_3 nanosheet/$K^+Ca_2Nb_3O_{10}^-$ ultrathin nanosheet with improved charge separation efficiency for significantly boosting photocatalysis. *Catal. Sci. Technol.* **2017**, *7*, 3481-3491.
(197) Park, S.; Song, H. J.; Lee, C. W.; Hwang, S. W.; Cho, I. S. Enhanced Photocatalytic Activity of Ultrathin $Ba_5Nb_4O_{15}$ Two-Dimensional Nanosheets. *ACS Appl. Mater. Interfaces* **2015**, *7*, 21860-21867.
(198) Wang, Y.; Ren, Y.; Luo, J. J.; Hao, Q. Y.; Li, B.; Gao, Z.; Hu, Y. W.; Lin, D.; Tang, K. B. Preparation of ultrathin perovskite nanosheets by the exfoliation of $H_2CaTa_2O_7$ for high-performance lead removal from water. *RSC Adv.* **2016**, *6*, 113671-113680.
(199) Oshima, T.; Lu, D.; Ishitani, O.; Maeda, K. Intercalation of highly dispersed metal nanoclusters into a layered metal oxide for photocatalytic overall water splitting. *Angew. Chem. Int. Ed.* **2015**, *54*, 2698-2702.
(200) Campbell, C. T.; Paffett, M. T. Model studies of ethylene epoxidation catalyzed by the Ag(110) surface. *Surf. Sci.* **1984**, *139*, 396-416.
(201) Imamura, S.; Yamada, H.; Utani, K. Combustion activity of Ag/CeO_2 composite catalyst. *Appl. Catal. A: Gen.* **2000**, *192*, 221-226.
(202) Kundakovic, L.; Flytzani-Stephanopoulos, M. Cu-and Ag-modified cerium oxide catalysts for methane oxidation. *J. Catal.* **1998**, *179*, 203-221.
(203) Zhang, D.-H.; Li, H.-B.; Li, G.-D.; Chen, J.-S. Magnetically recyclable Ag-ferrite catalysts: general synthesis and support effects in the epoxidation of styrene. *Dalton Trans.* **2009**, 10527-10533.
(204) Subramanian, V.; Roeder, R. K.; Wolf, E. E. Synthesis and UV−Visible-Light Photoactivity of Noble-Metal−$SrTiO_3$ Composites. *Ind. Eng. Chem. Res.* **2006**, *45*, 2187-2193.
(205) Hara, M.; Lean, J. T.; Mallouk, T. E. Photocatalytic Oxidation of Water by Silica-Supported Tris(4,4‘-dialkyl-2,2‘-bipyridyl)ruthenium Polymeric Sensitizers and Colloidal Iridium Oxide. *Chem. Mater.* **2001**, *13*, 4668-4675.
(206) King, D. A.; Wells, M. G. Molecular beam investigation of adsorption kinetics on bulk metal targets: Nitrogen on tungsten. *Surf. Sci.* **1972**, *29*, 454-482.

(207) Okamoto, Y.; Ida, S.; Hyodo, J.; Hagiwara, H.; Ishihara, T. Synthesis and Photocatalytic Activity of Rhodium-Doped Calcium Niobate Nanosheets for Hydrogen Production from a Water/Methanol System without Cocatalyst Loading. *J. Am. Chem. Soc.* **2011**, *133*, 18034-18037.
(208) Giordano, L.; Baistrocchi, M.; Pacchioni, G. Bonding of Pd, Ag, and Au atoms on MgO(100) surfaces and MgO/Mo(100) ultra-thin films: A comparative DFT study. *Phys. Rev. B* **2005**, *72*, 115403.
(209) Freund, H.-J. Metal-supported ultrathin oxide film systems as designable catalysts and catalyst supports. *Surf. Sci.* **2007**, *601*, 1438-1442.
(210) Shin, J.; Kalinin, S. V.; Lee, H. N.; Christen, H. M.; Moore, R. G.; Plummer, E. W.; Baddorf, A. P. Surface stability of epitaxial $SrRuO_3$ films. *Surf. Sci.* **2005**, *581*, 118-132.
(211) Diebold, U.; Pan, J. M.; Madey, T. E. Growth mode of ultrathin copper overlayers on TiO_2(110). *Phys. Rev. B* **1993**, *47*, 3868-3876.
(212) Wertheim, G. K.; DiCenzo, S. B.; Buchanan, D. N. E. Noble- and transition-metal clusters: The d bands of silver and palladium. *Phys. Rev. B* **1986**, *33*, 5384-5390.
(213) Wertheim, G. K.; DiCenzo, S. B. Cluster growth and core-electron binding energies in supported metal clusters. *Phys. Rev. B* **1988**, *37*, 844-847.
(214) Seah, M. P.; Dench, W. A. Quantitative electron spectroscopy of surfaces: A standard data base for electron inelastic mean free paths in solids. *Surf. Interface Anal.* **1979**, *1*, 2-11.
(215) Farmer, J. A.; Campbell, C. T. Ceria Maintains Smaller Metal Catalyst Particles by Strong Metal-Support Bonding. *Science* **2010**, *329*, 933-936.
(216) Campbell, C. T.; Mao, Z. Chemical Potential of Metal Atoms in Supported Nanoparticles: Dependence upon Particle Size and Support. *ACS Catal.* **2017**, *7*, 8460-8466.
(217) Tyson, W. R.; Miller, W. A. Surface free energies of solid metals: Estimation from liquid surface tension measurements. *Surf. Sci.* **1977**, *62*, 267-276.
(218) Cadiau, A.; Adil, K.; Bhatt, P. M.; Belmabkhout, Y.; Eddaoudi, M. A metal-organic framework-based splitter for separating propylene from propane. *Science* **2016**, *353*, 137-140.
(219) Gygi, D.; Bloch, E. D.; Mason, J. A.; Hudson, M. R.; Gonzalez, M. I.; Siegelman, R. L.; Darwish, T. A.; Queen, W. L.; Brown, C. M.; Long, J. R. Hydrogen Storage in the Expanded Pore Metal-Organic Frameworks M_2(dobpdc) (M = Mg, Mn, Fe, Co, Ni, Zn). *Chem. Mat.* **2016**, *28*, 1128-1138.
(220) Li, J. X.; Yu, X.; Xu, M. L.; Liu, W. J.; Sandraz, E.; Lan, H.; Wang, J.; Cohen, S. M. Metal-Organic Frameworks as Micromotors with Tunable Engines and Brakes. *J. Am. Chem. Soc.* **2017**, *139*, 611-614.
(221) Fairen-Jimenez, D.; Moggach, S. A.; Wharmby, M. T.; Wright, P. A.; Parsons, S.; Duren, T. Opening the Gate: Framework Flexibility in ZIF-8 Explored by Experiments and Simulations. *J. Am. Chem. Soc.* **2011**, *133*, 8900-8902.
(222) Gallaba, D. H.; Albesa, A. G.; Migone, A. D. Evidence of Gate-Opening on Xenon Adsorption on ZIF-8: An Adsorption and Computer Simulation Study. *J. Phys. Chem. C* **2016**, *120*, 16649-16657.
(223) Lownsbury, J. M. Ph.D. Dissertation, University of Washington, 2016.
(224) Hirschfelder, J. O.; Curtiss, C. F.; Bird, R. B. *Molecular Theory of Gases and Liquids*; John Wiley & Sons: New York, 1954.
(225) de Boer, J.; Bird, R. B. In *Molecular Theory of Gases and Liquids*; Hirschfelder, J. O., Curtiss, C. F., Bird, R. B., Eds.; John Wiley & Sons: New York, 1954, p 392-438.
(226) Stwalley, W. C.; Nosanow, L. H. Possible New Quantum Systems. *Phys. Rev. Lett.* **1976**, *36*, 910-913.

(227) Nosanow, L., H. Quantum Theorem of Corresponding States and Spin-Polarized Quantum Systems. *J. Phys. Colloques* **1980**, *41*, 1-12.
(228) Ma, J.; Sullivan, T. S.; Vilches, O. E. Critical and Triple Points of Films of Quantum Gases. *Japanese J. Appl. Phys.* **1987**, *26*, 263-264.
(229) Liu, Y. M.; Ebey, P. S.; Vilches, O. E.; Dash, J. G.; Bienfait, M.; Gay, J. M.; Coddens, G. Heat capacity, adsorption isotherms, and quasielastic neutron scattering measurements of bilayer deuterium hydride adsorbed on graphite. *Phys. Rev. B* **1996**, *54*, 6307-6314.
(230) Bruch, L. W.; Cole, M. W.; Zaremba, E. M. *Physical Adsorption: Forces and Phenomena*; Clarendon Press: Oxford, 1997.
(231) Takaishi, T.; Sensui, Y. Thermal Transpiration Effect of Hydrogen, Rare Gases and Methane. *Trans. Farad. Soc.* **1963**, *59*, 2503-2514.
(232) Young, D. M.; Crowell, A. D. *Physical Adsorption of Gases*; Butterworths: London, 1962.
(233) Gomez-Gualdron, D. A.; Moghadam, P. Z.; Hupp, J. T.; Farha, O. K.; Snurr, R. Q. Application of Consistency Criteria To Calculate BET Areas of Micro- And Mesoporous Metal-Organic Frameworks. *J. Am. Chem. Soc.* **2016**, *138*, 215-224.
(234) Wiechert, H. In *Landolt-Bornstein New Series*; Bonzel, H. P., Ed.; Springer-Verlag Berlin Heidelberg: Germany, 2003; Vol. 42A3, p 166-300.
(235) Dash, J. G. *Films on Solid Surfaces*; Academic Press: New York, 1975.
(236) Vidali, G.; Ihm, G.; Kim, H.-Y.; Cole, M. W. Potentials of physical adsorption. *Surf. Sci. Reports* **1991**, *12*, 135-181.
(237) Andrae, D.; Häußermann, U.; Dolg, M.; Stoll, H.; Preuß, H. Energy-adjusted *ab initio* pseudopotentials for the second and third row transition elements: Molecular test for M_2 (M = Ag, Au) and MH (M = Ru, Os). *Theoret. Chim. Acta* **1991**, *78*, 247-266.
(238) Zhao, Y.; Truhlar, D. G. Applications and validations of the Minnesota density functionals. *Chem. Phys. Lett.* **2011**, *502*, 1-13.
(239) Peverati, R.; Truhlar, D. G. Improving the accuracy of hybrid meta-GGA density functionals by range separation. *J. Phys. Chem. Lett.* **2011**, *2*, 2810-2817.
(240) Peverati, R.; Truhlar, D. G. Quest for a universal density functional: the accuracy of density functionals across a broad spectrum of databases in chemistry and physics. *Phil. Trans. R. Soc. A* **2014**, *372*, 20120476.
(241) Luo, S.; Zhao, Y.; Truhlar, D. G. Improved CO Adsorption energies, site preferences, and surface formation energies from a meta-generalized gradient approximation exchange–correlation functional, M06-L. *J. Phys. Chem. Lett.* **2012**, *3*, 2975-2979.
(242) Duanmu, K.; Truhlar, D. G. Validation of Density Functionals for Adsorption Energies on Transition Metal Surfaces. *J. Chem. Theory Comput* **2017**, *13*, 835-842.
(243) Verma, P.; Xu, X.; Truhlar, D. G. Adsorption on Fe-MOF-74 for C1–C3 hydrocarbon separation. *J. Phys. Chem. C* **2013**, *117*, 12648-12660.
(244) Gallington, L. C.; Kim, I. S.; Liu, W. G.; Yakovenko, A. A.; Platero-Prats, A. E.; Li, Z. Y.; Wang, T. C.; Hupp, J. T.; Farha, O. K.; Truhlar, D. G.; Martinson, A. B. F.; Chapman, K. W. Regioselective Atomic Layer Deposition in Metal-Organic Frameworks Directed by Dispersion Interactions. *J. Am. Chem. Soc.* **2016**, *138*, 13513-13516.
(245) Lee, K.; Isley, W. C.; Dzubak, A. L.; Verma, P.; Stoneburner, S. J.; Lin, L.-C.; Howe, J. D.; Bloch, E. D.; Reed, D. A.; Hudson, M. R.; Brown, C. M.; Long, J. R.; Neaton, J. B.; Smit, B.; Cramer, C. J.; Truhlar, D. G.; Gagliardi, L. Design of a Metal–Organic Framework with Enhanced Back Bonding for Separation of N_2 and CH_4. *J. Am. Chem. Soc.* **2014**, *136*, 698-704.

(246) Frisch, M. J.; Pople, J. A.; Binkley, J. S. Self-consistent molecular-orbital methods 25. Supplementary functions for gaussian-basis sets. *J. Chem. Phys.* **1984**, *80*, 3265-3269.
(247) Boys, S. F.; Bernardi, F. The calculation of small molecular interactions by the differences of separate total energies. Some procedures with reduced errors (Reprinted from Molecular Physics, vol 19, pg 553-566, 1970). *Mol. Phys.* **2002**, *100*, 65-73.
(248) Perry IV, J. J.; Teich-McGoldrick, S. L.; Meek, S. T.; Greathouse, J. A.; Haranczyk, M.; Allendorf, M. D. Noble gas adsorption in metal–organic frameworks containing open metal sites. *J. Phys. Chem. C* **2014**, *118*, 11685-11698.
(249) Vazhappilly, T.; Ghanty, T. K.; Jagatap, B. Computational Modeling of Adsorption of Xe and Kr in M-MOF-74 Metal Organic Frame Works with Different Metal Atoms. *J. Phys. Chem. C* **2016**, *120*, 10968-10974.
(250) FitzGerald, S. A.; Pierce, C. J.; Rowsell, J. L.; Bloch, E. D.; Mason, J. A. Highly selective quantum sieving of D_2 from H_2 by a metal–organic framework as determined by gas manometry and infrared spectroscopy. *J. Am. Chem. Soc.* **2013**, *135*, 9458-9464.
(251) Russell, B.; Villaroel, J.; Sapag, K.; Migone, A. D. O2 adsorption on ZIF-8: temperature dependence of the gate-opening transition. *J. Phys. Chem. C* **2014**, *118*, 28603-28608.
(252) Ania, C. O.; García-Pérez, E.; Haro, M.; Gutiérrez-Sevillano, J.; Valdés-Solís, T.; Parra, J.; Calero, S. Understanding gas-induced structural deformation of ZIF-8. *J. Phys. Chem. Lett.* **2012**, *3*, 1159-1164.
(253) Tanaka, H.; Ohsaki, S.; Hiraide, S.; Yamamoto, D.; Watanabe, S.; Miyahara, M. T. Adsorption-Induced Structural Transition of ZIF-8: A Combined Experimental and Simulation Study. *J. Phys. Chem. C* **2014**, *118*, 8445-8454.
(254) Kruk, M.; Jaroniec, M.; Sayari, A. Application of Large Pore MCM-41 Molecular Sieves To Improve Pore Size Analysis Using Nitrogen Adsorption Measurements. *Langmuir* **1997**, *13*, 6267-6273.
(255) Grigorev, V.; Rudenko, N. Surface Tension of Liquid Hydrogen Isotopes and Hydrogen-Deuterium Solutions. *Soviet Phys. JETP* **1965**, *20*, 63-66.
(256) Woolley, H. W.; Scott, R. B.; Brickwedde, F. Compilation of thermal properties of hydrogen in its various isotopic and ortho-para modifications. *J. Res. Nat. Bur. Standards* **1948**, *41*, 379-475.
(257) Ostromoukhov, V.; Ostronov, M. Surface Tension of Liquid Solutions O_2-N_2 at 54-77 K. *Zh. Fiz. Khim.* **1994**, *68*, 39-43.
(258) Jacobsen, R. T.; Stewart, R. B. Thermodynamic properties of nitrogen including liquid and vapor phases from 63K to 2000K with pressures to 10,000 bar. *J. Phys. Chem. Ref. Data* **1973**, *2*, 757-922.
(259) Sprow, F.; Prausnitz, J. Surface tensions of simple liquids. *Trans. Farad. Soc.* **1966**, *62*, 1097-1104.
(260) Terry, M.; Lynch, J.; Bunclark, M.; Mansell, K.; Staveley, L. The densities of liquid argon, krypton xenon, oxygen, nitrogen, carbon monoxide methane, and carbon tetrafluoride along the orthobaric liquid curve. *J. Chem. Thermodynamics* **1969**, *1*, 413-424.
(261) Setzmann, U.; Wagner, W. A new equation of state and tables of thermodynamic properties for methane covering the range from the melting line to 625 K at pressures up to 100 MPa. *J. Phys. Chem. Ref. Data* **1991**, *20*, 1061-1155.
(262) Jones, A. H. Sublimation Pressure Data for Organic Compounds. *J. Chem. Eng. Data* **1960**, *5*, 196-200.

(263) Hoare, F. E.; Jackson, L. C.; Kurti, N. *Experimental Cryogenics: Liquid Helium II*; Butterworths: London, 1961.
(264) Ziegler, W. T.; Mullins, J. C.; Kirk, B. S. Technical Report No. 2, Project A-460, Georgia Inst. Tech., *NBS Reference Data Program*, 1962.
(265) Ziegler, W. T.; Yarbrough, D. W.; Mullins, J. C. Technical Report No. 1, Project A-764, Georgia Inst. Tech., *NBS Reference Data Program*, 1964.
(266) Ziegler, W. T.; Mullins, J. C.; Berquist, A. R. Technical Report No. 3, Project A-764, E-115, Georgia Inst. Tech., *NBS Reference Data Program*, 1966.
(267) Zemansky, M. W.; Dittman, R. H. *Heat and Thermodynamics*; Mcgraw-Hill Book Company, 1981.
(268) Friend, D. G.; Ingham, H.; Fly, J. F. Thermophysical properties of ethane. *J. Phys. Chem. Ref. data* **1991**, *20*, 275-347.
(269) Yuan, S.; Chen, Y.-P.; Qin, J.-S.; Lu, W.; Zou, L.; Zhang, Q.; Wang, X.; Sun, X.; Zhou, H.-C. Linker Installation: Engineering Pore Environment with Precisely Placed Functionalities in Zirconium MOFs. *J. Am. Chem. Soc.* **2016**, *138*, 8912-8919.
(270) Li, Z.; Schweitzer, N. M.; League, A. B.; Bernales, V.; Peters, A. W.; Getsoian, A. B.; Wang, T. C.; Miller, J. T.; Vjunov, A.; Fulton, J. L.; Lercher, J. A.; Cramer, C. J.; Gagliardi, L.; Hupp, J. T.; Farha, O. K. Sintering-Resistant Single-Site Nickel Catalyst Supported by Metal–Organic Framework. *J. Am. Chem. Soc.* **2016**, *138*, 1977-1982.
(271) Li, Z.; Peters, A. W.; Platero-Prats, A. E.; Liu, J.; Kung, C.-W.; Noh, H.; DeStefano, M. R.; Schweitzer, N. M.; Chapman, K. W.; Hupp, J. T.; Farha, O. K. Fine-Tuning the Activity of Metal–Organic Framework-Supported Cobalt Catalysts for the Oxidative Dehydrogenation of Propane. *J. Am. Chem. Soc.* **2017**, *139*, 15251-15258.
(272) Li, Z.; Peters, A. W.; Bernales, V.; Ortuño, M. A.; Schweitzer, N. M.; DeStefano, M. R.; Gallington, L. C.; Platero-Prats, A. E.; Chapman, K. W.; Cramer, C. J.; Gagliardi, L.; Hupp, J. T.; Farha, O. K. Metal–Organic Framework Supported Cobalt Catalysts for the Oxidative Dehydrogenation of Propane at Low Temperature. *ACS Cent. Sci.* **2017**, *3*, 31-38.
(273) Ikuno, T.; Zheng, J.; Vjunov, A.; Sanchez-Sanchez, M.; Ortuño, M. A.; Pahls, D. R.; Fulton, J. L.; Camaioni, D. M.; Li, Z.; Ray, D.; Mehdi, B. L.; Browning, N. D.; Farha, O. K.; Hupp, J. T.; Cramer, C. J.; Gagliardi, L.; Lercher, J. A. Methane Oxidation to Methanol Catalyzed by Cu-Oxo Clusters Stabilized in NU-1000 Metal–Organic Framework. *J. Am. Chem. Soc.* **2017**, *139*, 10294-10301.
(274) Noh, H.; Cui, Y.; Peters, A. W.; Pahls, D. R.; Ortuño, M. A.; Vermeulen, N. A.; Cramer, C. J.; Gagliardi, L.; Hupp, J. T.; Farha, O. K. An exceptionally stable metal–organic framework supported molybdenum(VI) oxide catalyst for cyclohexene epoxidation. *J. Am. Chem. Soc.* **2016**, *138*, 14720-14726.
(275) Bernales, V.; Ortuño, M. A.; Truhlar, D. G.; Cramer, C. J.; Gagliardi, L. Computational design of functionalized metal–organic framework nodes for catalysis. *ACS Cent. Sci.* **2017**, *4*, 5-19.
(276) Klet, R. C.; Liu, Y.; Wang, T. C.; Hupp, J. T.; Farha, O. K. Evaluation of Brønsted acidity and proton topology in Zr- and Hf-based metal–organic frameworks using potentiometric acid–base titration. *J. Mater. Chem. A* **2016**, *4*, 1479-1485.
(277) Boys, S. F.; Bernardi, F. The calculation of small molecular interactions by the differences of separate total energies. Some procedures with reduced errors. *Mol. Phys.* **1970**, *19*, 553-566.

(278) Hulvey, Z.; Vlaisavljevich, B.; Mason, J. A.; Tsivion, E.; Dougherty, T. P.; Bloch, E. D.; Head-Gordon, M.; Smit, B.; Long, J. R.; Brown, C. M. Critical factors driving the high volumetric uptake of methane in $Cu_3(btc)_2$. *J. Am. Chem. Soc.* **2015**, *137*, 10816-10825.
(279) Sillar, K.; Sauer, J. Ab Initio Prediction of Adsorption Isotherms for Small Molecules in Metal–Organic Frameworks: The Effect of Lateral Interactions for Methane/CPO-27-Mg. *J. Am. Chem. Soc.* **2012**, *134*, 18354-18365.

VITA

Wei Zhang is from a coastal city of Qingdao, China, where the Tsingtao Beer is rich. After passing the College Entrance Examination, he was enrolled in Department of Chemistry, Nankai University in September 2010. While at Nankai University, Wei participated in two research projects. In April 2012, he joined the group of Prof. Xinge Zhang and conducted research about the antibacterial properties of antimicrobial peptides functionalized Ag nanoparticles. Afterwards, he joined the group of Prof. Shurong Wang in April 2013 and conducted research about the gas sensing properties of ZnO@ZnS core/shell microrods. As an undergraduate researcher, Wei published three peer-reviewed articles, including one as a first author. Wei received a bachelor's degree in Chemistry (A National "Project of Elite Students Cultivation for Fundamental Disciplines") from Nankai University in June 2014.

Wei became a graduate student, majoring in Physical Chemistry, at Department of Chemistry, University of Washington in September 2014. He conducted his Ph.D. research under the supervision of Prof. Charles Campbell. His research includes using a unique ultra-high vacuum (UHV) technique, metal vapor adsorption calorimetry, to study model systems of heterogeneous catalysts and learn how the fundamental thermodynamic properties and structure of model systems can provide insight for the catalytic properties of more complex real catalysts such as activity, selectivity, and resistance to sintering. Wei was particularly interested in the system of transition metal nanoparticles dispersed across high-area oxide support surfaces and designed a novel metal adsorption calorimeter so that surface science study could be performed on solution-prepared high-surface-area catalyst support nanomaterials. His research and academic accomplishments earned him the Lloyd E. and Florence M. West Fellowship in Chemistry in 2017. He was also awarded the AVS

65 Dorothy M. and Earl S. Hoffman Travel Grant and chosen as a finalist for the Graduate Student Presentation Award in Heterogeneous Catalysis Focus Topic at AVS 65th International Symposium & Exhibition in Long Beach, CA in 2018. Additionally, Wei's research also includes gas adsorption properties on a porous adsorbent materials, a Zr-based metal–organic framework (MOF) NU-1000.

During his Ph.D. life, Wei mentored two undergraduate students, John E. Eichler and Graeme O. Vissers. He trained John on maintaining and troubleshooting a UHV system for a year and a half, who is still working on UHV as a graduate student at UT Austin. He also instructed Graeme on his first publication of peer-reviewed article. Wei also served as a teaching assistant at University of Washington for General Chemistry (142, 143, 162, 165), Physical Chemistry (456), and Statistical Mechanics (552), and as a tutor in the Chemistry Study Center for all the 100-level courses.

Out of lab, Wei enjoys a variety of outdoor sports including hiking, camping, rock climbing and skiing. He has very strong self-learning capability with respect to sports. He learned how to ski by simply watching YouTube videos for 30 minutes and was able to handle many of the blue chairs at the ski resort after the third time he went to ski. Wei is also a big fan for basketball, and he likes to watch basketball games more than any other games or shows.